

Three-Dimensional Morphanalysis of the Face

Bernard Tiddeman

October 8, 1998

A THESIS SUBMITTED TO HERIOT-WATT UNIVERSITY
FOR THE DEGREE OF DOCTOR OF PHILOSOPHY
IN THE DEPARTMENT OF COMPUTING AND ELECTRICAL ENGINEERING

Copyright Notice

This copy of the thesis has been supplied on condition that anyone who consults it is understood to recognize that the copyright rests with its author and that no quotation from the thesis and no information derived from it may be published without the prior written consent of the author or the University (as may be appropriate).

Contents

I	Introduction	1
1	Introduction	2
1.1	Introduction	2
1.2	Motivation	3
1.3	Background	5
1.4	Objectives	7
1.5	Thesis Overview	8
II	Universally Relatable Surface Data	10
2	Universally Relatable Images	11
2.1	Introduction	11
2.2	Universal Relatability	12
2.3	Cartesian Reference Frames	14
2.4	Literature Review	15
2.4.1	Craniofacial Invariant Registration	15
2.4.2	Best fit registration of matched points	16
2.4.3	Best fit registration of unmatched points	18
2.4.4	Best fit registration of surfaces	19
2.4.5	Best fit registration of volumes	20
2.4.6	Traditional Cephalostatic Registration	20
2.4.7	Fixed Relations Principle	21

CONTENTS

2.5	Discussion	24
2.6	Conclusions	26
3	Surface Data Capture Methods	28
3.1	Introduction	28
3.2	Triangulation-based methods	29
3.2.1	Stereophotogrammetry	29
3.2.2	Moiré Fringe Scanners	31
3.2.3	Phase Measurement	32
3.2.4	Laser light scanners	33
3.3	Time-of-Flight based methods	35
3.3.1	Sonic scanners	35
3.3.2	Holography	35
3.4	Choice of Method	36
4	Calibration of the Interface Laser Scanner	38
4.1	Introduction	38
4.2	System Description	39
4.3	Calibration Methods	39
4.3.1	Camera Calibration Based Methods	39
4.3.2	Geometry Based Methods	41
4.4	New Model Based Method	42
4.4.1	Overview	42
4.4.2	The System Model	42
4.4.3	Calibration Methods	47
4.4.4	Calibration Data Collection	51
4.4.5	Results	52
4.5	Conclusions	55
III	Inter-Subject Relation	56
5	Inter-Patient Comparison Methods	57

CONTENTS

5.1	Introduction	57
5.2	Literature Review	59
5.2.1	The original morphanalytic solution.	59
5.2.2	Depth Averaging	62
5.2.3	Feature based warping	63
5.2.4	Template Fitting Methods	65
5.2.5	Automatic Ridge Line Matching	70
5.2.6	Intensity Based Matching	74
5.3	Discussion	76
5.4	Conclusions	78
6	Image Processing Methods	79
6.1	Introduction	79
6.2	Basic Image Processing	79
6.2.1	Introduction	79
6.2.2	Convolution and Image Filtering	80
6.2.3	Regularisation	81
6.3	Differential Geometry	83
6.3.1	Introduction	83
6.3.2	Methods	84
6.4	Edge detection and contour extraction	89
6.4.1	Introduction	89
6.4.2	Active Contours Methods	90
6.4.3	Bayesian Methods	92
6.4.4	Graph Searching Methods	93
6.4.5	Choice of Method	94
6.5	Two-dimensional Interpolation	94
6.5.1	Introduction	94
6.5.2	Energy minimisation methods	94
6.5.3	Triangulation based methods	97
6.5.4	Weighted average approaches	98

CONTENTS

6.5.5	Grid based methods	98
6.5.6	Multilevel B-splines	100
6.6	A New Multiscale Method	100
6.6.1	Introduction	100
6.6.2	Method	101
6.6.3	Results	103
6.6.4	Conclusions	104
6.7	Feature based two-dimensional image warping	106
6.7.1	Introduction	106
6.7.2	The one-to-one property	107
6.7.3	Previous solutions	109
6.7.4	A new general solution	110
6.7.5	Results	112
6.7.6	Conclusion	112
7	Inter-Surface Comparison Study	115
7.1	Introduction	115
7.2	Data Capture	117
7.3	Method 1: Automatic surface matching	119
7.3.1	Method Overview	119
7.3.2	Implementation	121
7.3.3	Results	125
7.4	Method 2: Automatic edge based warping	125
7.4.1	Method Overview	125
7.4.2	Implementation	130
7.4.3	Results	131
7.5	Method 3: Feature based warping with interactive labelling	135
7.5.1	Method overview	135

CONTENTS

7.5.2	Implementation	136
7.5.3	Results	139
7.6	Conclusions and Choice of Method	139
IV	Statistics, Results and Applications	143
8	Surface Statistics	144
8.1	Introduction	144
8.2	Method 1: Probability histomorphogram	145
8.2.1	Method description	145
8.2.2	Results	147
8.3	Method 2: Warping based averaging	149
8.3.1	Method overview	149
8.3.2	Multivariate Statistical Methods	151
8.3.3	Implementation	154
8.3.4	Results	155
8.4	Conclusion and Choice of Method	156
9	Results and Applications	160
9.1	Introduction	160
9.2	Patient Assessment	161
9.3	Assessing averages	162
9.4	Assessing surgical models	164
9.4.1	Background	164
9.4.2	Mass Spring Models	165
9.4.3	Finite element models	167
9.4.4	A New Method	169
9.4.5	The model	170
9.4.6	Results	173
9.4.7	Validation of Surgical Models	174
9.5	Face Space Transformations	177

CONTENTS

9.5.1	Growth Studies	177
9.5.2	Background	177
9.5.3	A New Method	178
9.5.4	Results	179
 V Conclusions		184
 10 Conclusions and Future Directions		185
10.1	Summary	185
10.2	New Advances	188
10.3	Future Work	189
10.3.1	Introduction	189
10.3.2	Clinical Trials	190
10.3.3	Computer Graphic and Imaging Enhancements	191
10.4	Concluding Remarks	192

Acknowledgements

The work reported in this thesis would not have been possible without the generous support of Sir James Savile, via the Jimmy Savile Stoke Mandeville Hospital Trust.

I would like to thank the staff of the Radiology Department, Stoke Mandeville Hospital, Aylesbury, Bucks, for their hospitality and kind collaboration and the many staff of the hospital generally who participated as volunteers in the scanner trial.

Finally I would like to thank my supervisors, Dr Graham Rabey and Mr Neil Duffy for their support and encouragement.

Abstract

The aim of the work reported in this thesis was to determine the extent to which orthogonal two-dimensional morphanalytic (universally relatable) craniofacial imaging methods can be extended into the realm of computer-based three-dimensional imaging.

New methods are presented for capturing universally relatable laser-video surface data, for inter-relating facial surface scans and for constructing probabilistic facial averages. Universally relatable surface scans are captured using the fixed relations principle combined with a new laser-video scanner calibration method. Inter-subject comparison of facial surface scans is achieved using interactive feature labelling and warping methods. These methods have been extended to groups of subjects to allow the construction of three-dimensional probabilistic facial averages.

The potential of universally relatable facial surface data for applications such as growth studies and patient assessment is demonstrated. In addition, new methods for scattered data interpolation, for controlling overlap in image warping and a fast, high-resolution method for simulating craniofacial surgery are described.

The results demonstrate that it is not only possible to extend universally relatable imaging into three dimensions, but that the extension also enhances the established methods, providing a wide range of new applications.

Part I

Introduction

Chapter 1

Introduction

1.1 Introduction

The work reported in this thesis was carried out as part of the Interface Project, and builds on the methods that have been developed over the Project's 35 year history. The Interface Project is concerned with morphanalytic imaging of the human head and face, to assist in the research, treatment planning and diagnosis of craniofacial abnormalities. Morphanalytic imaging uses standardised images of patients aligned to a Cartesian reference frame. The use of this independent reference convention allows the universal comparison of patients, irrespective of their age, sex or facial shape.

The previous work of the Interface Project involved the development of methods for capturing orthogonal two-dimensional morphanalytic (universally relatable) images, the extraction and comparison of outline tracings from these

CHAPTER 1. INTRODUCTION

images and the construction of average and standard deviation outline tracings.

The aim of the work reported in this thesis was to extend these established methods into three-dimensional imaging using laser-scanned facial surface data. New methods are presented for capturing universally relatable laser-video surface data, for inter-relating different facial surface scans and for constructing three-dimensional probabilistic facial averages. The potential for applications such as growth studies and patient assessment is demonstrated. In addition, new methods for scattered data interpolation, for controlling overlap in image warping and a fast, high-resolution method for simulating craniofacial surgery are described.

1.2 Motivation

Craniofacial anomalies sufficient to justify surgery affect at least 1 in every 100 people at some time in their lives. The reason can be a genetic disorder, an injury or a disease but in many cases the root cause is not known. The condition may result in abnormal development or growth of all or part of the craniofacial complex. Most people affected are otherwise perfectly normal. The psychological impact of growing up with a craniofacial abnormality is well documented (1). Any improvement in the quality of treatment can have a major influence on the quality of patients' lives.

Surgery is an important treatment for many craniofacial abnormalities, but it is performed in conjunction with many other treatments such as orthodontics,

CHAPTER 1. INTRODUCTION

dental correction, speech therapy and counselling for the patients and their families. Treatment for congenital abnormalities is usually started early in the patient's life. Some conditions demand urgent treatment, for example if the patient cannot breathe or eat sufficiently well. For other less serious conditions, the surgeon is free to choose the most appropriate time for surgery.

Surgical treatment for undergrowth or overgrowth of all or part of the craniofacial skeleton involves the dissection, repositioning and fixing of hard tissue fragments. Craniofacial surgery has advanced to the stage where almost any part of the skull can be dissected and repositioned. With care and ingenuity this can often be performed with minimal disruption to other facial anatomy (muscles, nerves etc) and without externally visible scarring (e.g. by accessing the hard tissues via the mouth, the orbits or from above the hairline).

In order to maximise the benefits of treatment and to minimise the need for further surgery, a clinician needs to plan major craniofacial treatment carefully. This planning will usually involve the qualitative assessment of the patient directly and indirectly via medical images. Quantitative measurements can enhance the diagnosis and lead to improved treatment planning.

Early attempts to quantify facial shape derived from the anthropological study of dry skulls. Known as cephalometrics, this method involved the measurement of lines, triangles and other Euclidean constructions drawn between landmark points on patient X-rays. While such measurements give some useful information about the structure of the craniofacial complex, the limited information contained in landmark data and a lack of standardisation and rigorous

CHAPTER 1. INTRODUCTION

mathematical theory leaves a great deal to be desired. Any improvement in the quality of quantitative tools for craniofacial assessment leads to an improvement in the quality of research, diagnosis and treatment planning and hence to an improvement in the treatment of craniofacial patients.

1.3 Background

Dr Graham Rabey started the Craniofacial Morphanalysis Project (later renamed the Interface Project) in 1963, partly because of a general dissatisfaction with traditional cephalometrics. Dr Rabey's solution to the traditional problems essentially involves three main parts, which are referred to collectively as *morphanalysis* (2) (3) (4) (5). Morphanalysis is the application of analytic (Cartesian) geometry to the study of form. In contrast, *morphosynthesis* (of which most traditional cephalometrics is a subset) is the application of synthetic (Euclidean) geometry to the study of form.

The first stage in morphanalysis is to register all the forms under study (in this case human heads) to a three-dimensional Cartesian reference frame. This required the development of a rigid-body registration system that could define a unique orientation for each form, while allowing for the enormous variations in size and shape that exist in biology. The solution became known as the fixed relations principle, because it does not depend upon allegedly 'fixed' positions, angles or distances that do not exist in organic forms, but only on exploiting certain fixed relations that do exist in all biological forms. This registration

CHAPTER 1. INTRODUCTION

system allows the referral of three-dimensional features to an external reference system directly, rather than to other biological landmarks. In the linguistic conventions of traditional mathematics this represents a general shift of approach from the 2300 year old 'synthetic' mathematics of Euclid to the 350 year old 'analytic' mathematics of Descartes.

The second stage was to standardise the images of the forms registered to the Cartesian reference frame. The result was the *Analytic Morphograph*, a machine that could capture mutually orthogonal radiographic and photographic two-dimensional images. The morphograph contains a pressure sensitive cephalostat and marked axes for implementing the fixed relations principle. The imaging equipment has been designed with carefully standardised projections for accurate interrelation of patient images.

The third stage was the development of methods for the study of the standardised images. Three-dimensional points and lines captured from mutually orthogonal projections could be compared between patients. By tracing outlines of patient images and comparing the tracings, measurement of much of the craniofacial complex was made possible. Average outlines of large samples were constructed and used to formulate new diagnoses and to improve treatment planning.

The analytic morphograph has been used to capture standardised orthogonal photographic and radiographic images. These images have been used to compare and contrast individual patients and to construct average facial outlines (4). The average outlines have subsequently been used to assess individual patients,

CHAPTER 1. INTRODUCTION

providing a clinical assessment service and allowing previously unknown facial anomalies to be diagnosed and treated (7). Methods were developed for comparing different average outlines and for applying techniques such as Student's t-test to assess the significance of the difference between averages. Later studies used computer graphic techniques to construct the average outlines, allowing larger samples to be used (8). The current study is concerned with extending the previous orthogonal two-dimensional methods into the new three-dimensional modality of surface range data.

1.4 Objectives

In the spirit of the Interface Project, the Project's collaborators were not satisfied with studying only orthogonal two-dimensional images, and wished to extend their studies of the human head in a truly three-dimensional fashion. The installation of a laser-stripe surface scanner designed by Neil Duffy of Heriot-Watt University within the analytic morphograph at Stoke Mandeville Hospital and the development of early scanner controlling software by Jamie Lokier signalled the first moves in this direction.

This thesis reports the continuing development of new methods for capturing and using morphanalytic laser-range data. The goals of this work are

- a) to demonstrate that morphanalytic methods can be applied to three-dimensional data (in the form of laser-video range data),
- b) to validate the individual methods used for registration, image cap-

CHAPTER 1. INTRODUCTION

ture and inter-subject comparison in the light of recent advances in medical image processing,

- c) to develop new methods where necessary and
- d) to demonstrate the possibilities for practical clinical application.

1.5 Thesis Overview

In recent years the advances in three-dimensional medical imaging equipment and rapid increases in computer power have led to a great deal of research activity in several areas related to this project. New techniques have been developed for three-dimensional image registration, three-dimensional imaging, and inter-subject matching.

The development of many new three-dimensional registration methods since the development of the fixed relations principle justifies a review, given in chapter 2. The new methods are compared with the fixed relations principle to ensure its continuing validity.

In order to use scanned surface data for patient research or treatment planning it is vital to ensure that the captured data truly reflect the shape of the subject's anatomy. It is also important that the coordinate system of the captured data is properly registered to the morphograph's coordinate system. Chapter 3 reviews the available surface capture methods and explains the choice of the laser-video scanning system chosen. Chapter 4 describes the Interface laser-scanner and a new method for its calibration.

CHAPTER 1. INTRODUCTION

Many methods for matching anatomical points between subjects have also been developed in recent years and they are reviewed in chapter 5. Three of these methods are adapted for the modality of laser-range data and evaluated in chapter 7. Because the three tested methods all require a collection of similar mathematical and image processing techniques, these are described separately in chapter 6.

The construction of average three-dimensional facial data would equip clinicians and researchers with new tools to aid diagnosis, research and treatment planning. Two methods for constructing mean and distribution facial data are described and evaluated in chapter 8.

In chapter 9, several of the potential applications are tested. Probabilistic assessment of individual patients and significance testing of two averages is performed using colour-coded texture mapping. These can aid in the diagnosis of individual patients and in the identification of the differences between statistical facial groups. The analysis of surgical simulations using the probabilistic assessment method can help to quantify the results of the proposed surgical treatment. The transformation of individual faces between different statistical groups has applications in growth studies and pre-surgical predictions.

Part II

Universally Relatable

Surface Data

Chapter 2

Universally Relatable Images

2.1 Introduction

Chapter 1 drew attention to the need for the quantitative assessment of facial shape and presented an overview of morphanalysis. Previous morphanalytic methods have involved three fundamental stages: registration, standardised image capture and inter-subject matching. In this chapter, various modern methods for rigid-body registration are reviewed and compared with the original morphanalytic registration method, the fixed relations principle.

2.2 Universal Relatability

The potential value of comprehensive standardisation in medical imaging may be illustrated by a typical clinical and research ‘wish list’. Ideally, clinicians and researchers would like to have confidence in relating (in some *clinically and mathematically valid* way) every single image of every single patient with every other image,

- a) of the same and different patients,
- b) of the same and different views (e.g. frontal, lateral, basal),
- c) of the same and different modalities (e.g. photographs, radiographs, laser-range data, CT and MRI data) and
- d) made at the same and different times (e.g. before and after treatment or at 2 years and 20 years).

To underline the general impetus of the wish-list, it may be said that in time it is hoped and expected that clinicians and researchers will be able to make medically meaningful and mathematically valid comparisons between all medical images. For example, standardised comparisons between the 2D craniofacial photographs of a day-old Canadian baby born with a cleft palate and the 3D craniofacial CT scans of an adult Welsh sufferer from mandibulofacial dysostosis could help in investigations of the nature of the many links between these two conditions. Currently such comparisons are not possible.

CHAPTER 2. UNIVERSALLY RELATABLE IMAGES

Thus far, the two main approaches to relatability in medical imaging mirror their counterparts in traditional mathematics.

Medical morphosynthetic methods apply the techniques of synthetic (Euclidean) geometry to human forms and their images and thus entail *no requirement* to relate the organic points, lines, surfaces and volumes being compared to any *independent* reference frame. There is thus no provision for *universal relatability* and therefore no possibility of fulfilling the above wish-list.

Medical morphanalysis applies the techniques of analytic (Cartesian) geometry to human forms and their images and this entails a requirement to relate the organic points, lines, surfaces and volumes to an independent reference frame. In short, there is a provision for universal relatability and the potential for fulfilling the above wish-list.

Analytic geometry reduces a shape into infinitesimal or (in the approximate world of digital imaging) finite points for independent study. The problem is that a single point does not possess any property that can be measured. It has no length, area or volume and there are no angles or ratios that can be measured. Measurement of a single point requires a reference frame, to give it a single vector value denoting its position.

The choice of reference frame is difficult because biological forms do not possess intrinsic coordinate systems. Further, a convention must be defined that facilitates inter-subject comparison. Such a convention should possess certain properties. The position defined by the registration system should be unique, i.e. identical shapes should always be registered in the same way. The registration

CHAPTER 2. UNIVERSALLY RELATABLE IMAGES

system should leave shape and size unchanged, a condition that is equivalent to restricting the allowed registration operations to rotations and translations. Furthermore, the registration must be applicable to every human head and its images.

Universally relatable images have the potential to facilitate increased communication between clinicians and researchers. Research projects, patients or specific conditions could be compared universally, in an analytically valid way, irrespective of the narrower aims of a particular project. Universal relatability has already been achieved for radiographic and photographic images in the context of orthogonal morphanalysis. The aim of this work is to extend the scope of universally relatable images to laser-scanned surface data.

2.3 Cartesian Reference Frames

In three dimensions a Cartesian reference frame is composed of three mutually perpendicular direction vectors and a single point defined as the origin. An important question when performing registration is ‘what is the minimum information required to define a Cartesian reference frame?’ Any two vectors will have a unique orthogonal vector defined by their cross product. Hence the problem can be reduced to defining any two mutually orthogonal vectors and the origin. Furthermore, any two vectors (not necessarily perpendicular) define a plane containing those two vectors. A vector in the two dimensional plane will have a single unique orthogonal vector in the plane. Hence the problem can

CHAPTER 2. UNIVERSALLY RELATABLE IMAGES

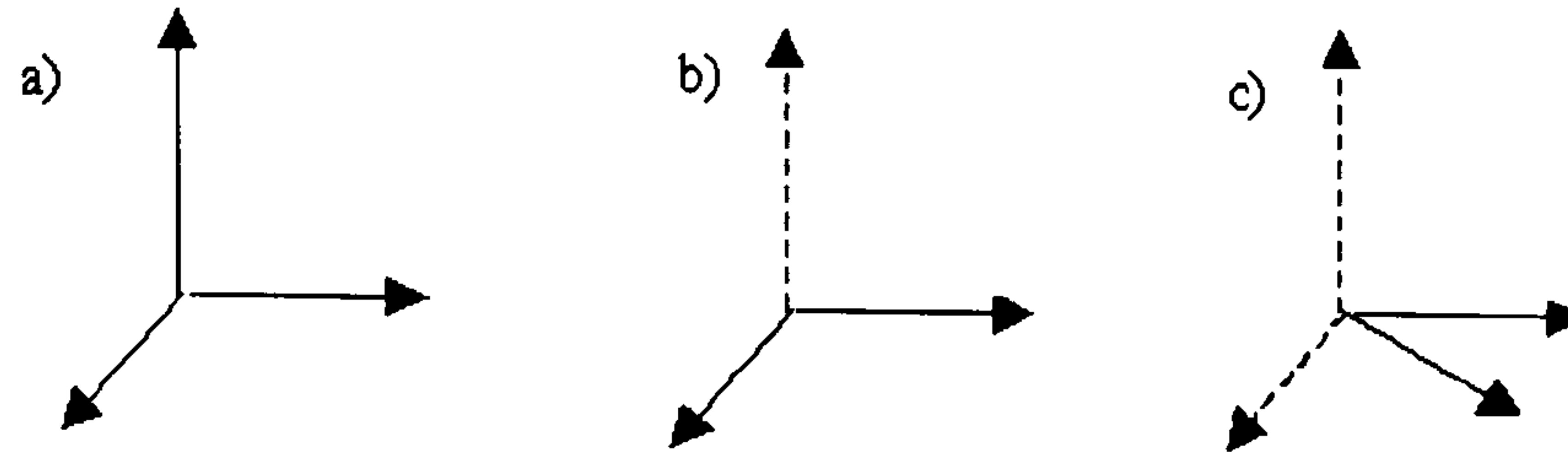


Figure 2.1: Deducing the minimum information required to define a 3D Cartesian reference frame. The three orthogonal directions (a) can be reduced to two orthogonal directions (b) and then to two non-orthogonal directions (c). Together with the origin this leaves three vectors.

be further reduced to finding any two vectors and defining the origin. Thus the minimum information required to define a reference frame is three vectors, one to define the origin and two non-parallel direction vectors (Figure 2.1).

2.4 Literature Review

2.4.1 Craniofacial Invariant Registration

Many authors have attempted to register patient images using anatomical point landmarks that are considered invariant in an individual scanned at different times (e.g. during different periods of growth) or in different modalities (e.g. CT and MR). Because regions of the human craniofacial complex grow in different ways and at different rates, there are no points that can be considered invariant from the cradle to the grave. Furthermore, no landmark points exist in the human craniofacial complex that can be considered invariant for registration purposes throughout the population, between people of different age, sex, race and medical condition. In human anatomy, no such ‘fixed’ points exist.

In general image processing, two-dimensional images can be registered by

CHAPTER 2. UNIVERSALLY RELATABLE IMAGES

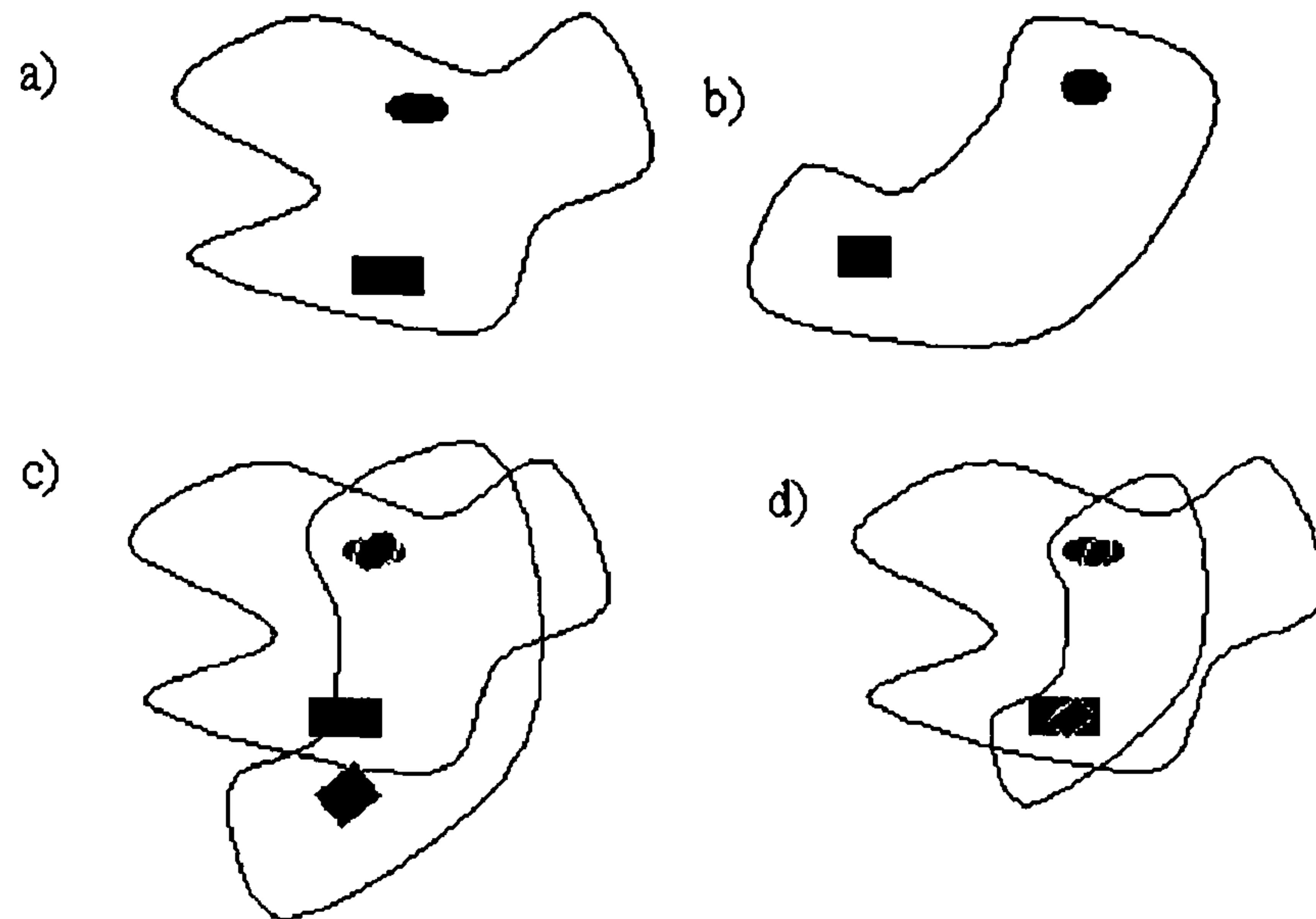


Figure 2.2: A two-dimensional registration problem. The two forms (a) and (b) cannot be registered using only translations and rotations (c) but can be registered with the additional operation of scaling (d).

fixing two points if scaling is allowed in addition to rotation and translation (Figure 2.2). In medical imaging the same principle applies (for example in clinical radiographs and photographs) but the introduction of scaling prevents the use of the images for the study of size. As explained earlier, the registration of three-dimensional images requires at least three points, and these can only be made coincident (in general) if additional non-rigid operations such as non-uniform scaling or shearing are allowed (Figure 2.3). The introduction of a non-rigid operation such as shearing changes the shape of the study object and so removes the medical meaning from the images.

2.4.2 Best fit registration of matched points

With the advent of affordable computer technology and digital three-dimensional imaging systems such as CT and MRI, several techniques for registering three-

CHAPTER 2. UNIVERSALLY RELATABLE IMAGES

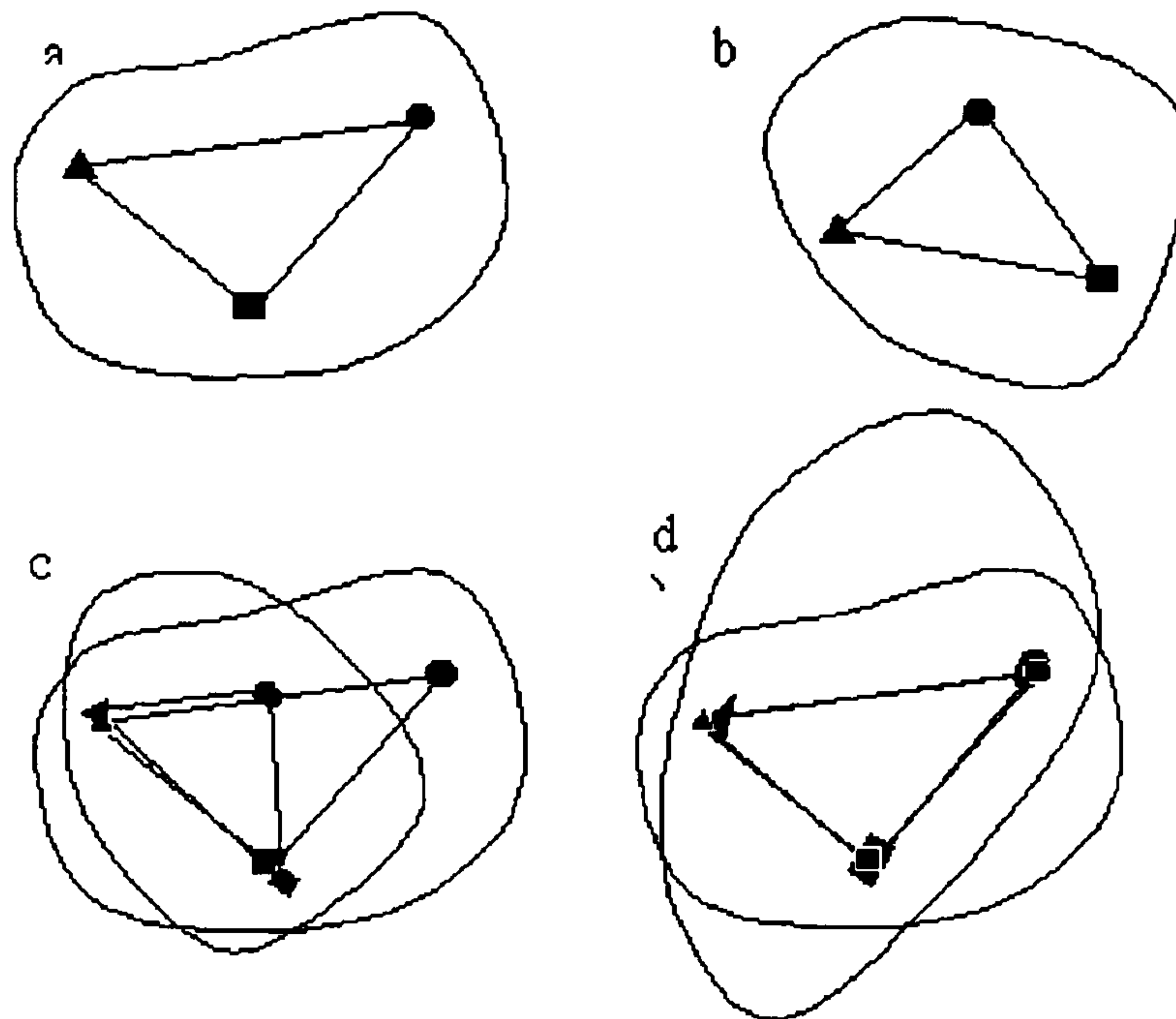


Figure 2.3: A three-dimensional registration problem. The three points in the two objects (a) and (b) cannot be registered using only translations, rotations and uniform scaling (c) but require additional non-rigid operations such as shearing (d).

dimensional data have been developed. The applications include pose estimation in robot vision and registration of medical images from different modalities. A number of techniques have been devised for the case where corresponding points can be found and labelled in each of the study forms. The problem can be stated as finding the 3 components of the rotation, expressed as a 3x3 rotation matrix \mathbf{R} , and the 3 components of the translation vector \mathbf{T} that minimise the sum of the squared errors χ^2 for the point sets p_i and p'_i i.e.

$$\chi^2 = \sum_{i=0}^N (p_i - (\mathbf{R}p'_i + \mathbf{T}))^2 \quad (2.1)$$

It has been shown (9) that the least-squares solution to the above problem,

CHAPTER 2. UNIVERSALLY RELATABLE IMAGES

$(Rp'_i + T)$, will have the same centroid as p_i . Hence the problem can be reduced to finding the three components of the rotation. Three approaches to the solution of this minimisation problem have been proposed in the literature. The first method involved the use of quaternions, 4x1 vectors used to describe and manipulate rotations efficiently (10) (11). The second approach is to use an iterative scheme such as Newton's method for finding the roots (9) (12) (13). The third method uses singular valued decomposition to find the rotation matrix (14) (15) (16). Procrustes analysis (17) (18) is a least-squares method that first applies uniform scaling to normalise the squared sum of displacements from the centroid to 1, and then uses singular valued decomposition to find the rotation. Several authors have applied these methods to medical data, usually for combining two or more 3D scans of the same patient from different modalities (19) (20) (21). Bookstein has used Procrustes registration for normalising orientation and scale when constructing synthetic averages (22) and McCance et al (23) have used the method of Fright and Linney (12) for registering laser-range scans for comparison and average construction.

2.4.3 Best fit registration of unmatched points

One drawback to the algorithms described above is the need to label corresponding points prior to registration. For many problems there is no pre-defined correspondence between points in each data set, e.g. a point cloud captured from a surface scanner or the most highly curved points extracted from a CT data set. The problem is to define a measure of the registration error between the

CHAPTER 2. UNIVERSALLY RELATABLE IMAGES

two data sets. One measure is the distance from each point in one data set to its closest point in the other data set, which gives rise to the iterative closest point (ICP) algorithm (24) (25). During each iteration, points are matched with their closest counterparts in the other data set and then the least-squares registration is computed and applied to improve the registration. The algorithm is terminated when the change in the mean-squared error between iterations falls below a pre-defined threshold. The ICP algorithm can also be used to register higher order structures such as contours and surfaces provided a parametric description of the structure exists. Subsol et al have used the ICP algorithm for registration of CT skull data (26) and MRI brain data (27) using automatically extracted crest lines to aid in the construction of averages.

2.4.4 Best fit registration of surfaces

Other methods present the problem explicitly as one of matching corresponding (28) (29) or adjacent (30) surfaces. These improve the robustness of the registration using knowledge of the anatomical correspondence or adjacency of the matched surfaces. This requires extraction and labelling of the desired surfaces. Although some of the surfaces in craniofacial images are easy to segment automatically, many require considerable user interaction for delineation and labelling.

2.4.5 Best fit registration of volumes

In order to overcome the problems associated with manual and interactive labelling of features, registration methods based on the intensity correlation between entire volumes have been developed. These algorithms require two components: one to measure the voxel similarity and the other to optimise this similarity using rotations and translations. Measures of voxel similarity include soft-tissue correlation (31), correlation of intensity variance (32) (33), joint entropy of the combined images (34) (35) and mutual information (36) (37) (38). The optimisation routines used include the gradient descent method (32) (39), Powell's method (36), multi-resolution exhaustive searches (31), a genetic algorithm (33) and stochastic optimisation (37). Studholme et al (39) compared the different voxel similarity measures and found that all gave reliable results for data sets with a large axial field of view but were less robust for data sets with a short axial extent.

2.4.6 Traditional Cephalostatic Registration

In the 19th century, anthropologists developed cephalostatic registration systems for the study of dry human and animal skulls. Their methods were later adapted for clinical use using radiographic imaging equipment. A cephalostat is a head holding device that uses rods placed in the patient's ears to provide a standardised position for capturing radiographic images. The patient's head is free to rotate about the horizontal axis, and so it is rotated so that the Frankfort plane (through the porions and the left orbitale) lies horizontally. It is a long-

CHAPTER 2. UNIVERSALLY RELATABLE IMAGES

standing registration method (40) and is still popular with craniofacial surgeons and orthodontists in spite of detailed criticism of the methods employed (2) (5) (41).

Cephalostatic registration does not aim to provide a coordinate system, and so no origin or orthogonal axes are defined explicitly. Cephalostatic registration only implies a coordinate system with one axis through the porions and a plane through the porions and the left orbitale. The major drawback in attempting to define a coordinate system using traditional cephalostatic registration is inaccuracy. Inaccuracies can result from errors in locating the desired landmarks, especially those used in registration such as the orbitale and from variations in the imaging equipment used. The cephalostat's axis passes through the centre of the ear rods and not through the porions, so the coordinate system is incorrectly defined.

2.4.7 Fixed Relations Principle

An alternative to traditional cephalostatic methods is to use the fixed relations principle (2) (3) (4) (5). The fixed relations principle defines a coordinate system based on the relative positions of three points, without requiring those points to have a specific 3D location (Figure 2.4). First the y -axis is defined as passing through two of the points, and their mid-point defines the origin. A third non-collinear point defines the xy -plane. The x -axis lies in this plane and extends from the origin perpendicular to the y -axis. The z -axis is orthogonal to both of these axes, extending out of the plane from the origin. Any two points define

CHAPTER 2. UNIVERSALLY RELATABLE IMAGES

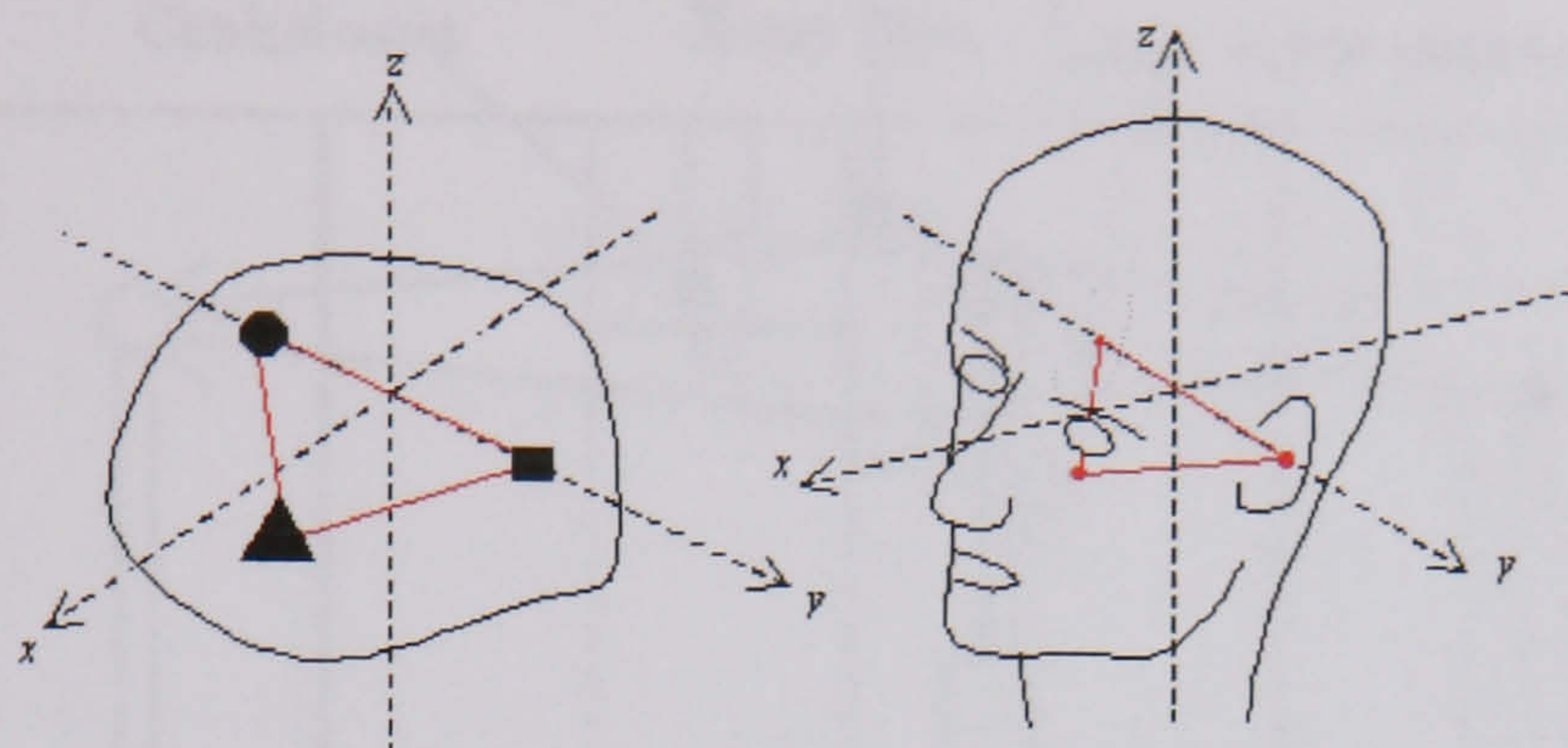


Figure 2.4: The fixed relations principle can be applied to any form with three identifiable points. For the human head it is implemented using a cephalostat and an orbitale marker.

an axis and any three non-collinear points define a plane, and so no constraints have been placed on the nature or relative positions of the registration points. Any three labelled, non-collinear points in a three-dimensional object can be used to define a Cartesian coordinate system using the fixed relations principle.

For craniofacial studies, the fixed relations principle is implemented in a recording machine called the *analytic morphograph* (Figure 2.5). The analytic morphograph contains a pressure sensitive cephalostat, with the axis through the centre of its ear rods defining the y -axis. These rods are placed in the subject's ears until the pressures are equalised to standard values. At the pointed tip of each of the cephalostat's ear rods is a piece of lead-shot, and the midpoint between these two points defines the origin. This eliminates the inaccuracies in traditional cephalostatic systems due to the rotation of the porions about the cephalostat's y -axis and the variability and deformity of the external acoustic meatus. The third registration point is a lead-shot marker placed on the skin over the subject's left orbitale, located by a clinician by palpation. This reduces

CHAPTER 2. UNIVERSALLY RELATABLE IMAGES

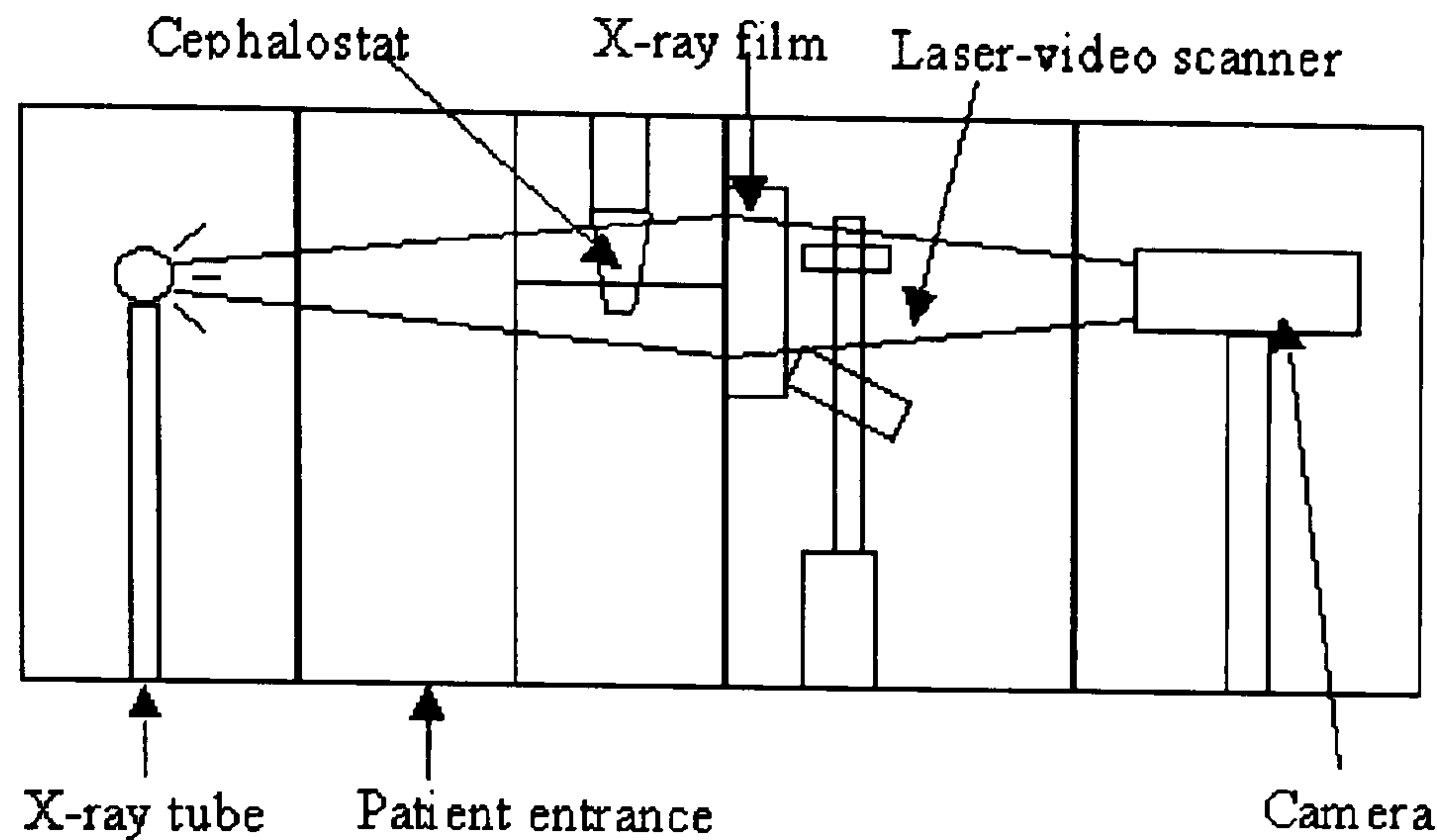


Figure 2.5: A simplified diagram of the analytic morphograph

the error incurred in trying to accurately locate the orbitale on images. The subject is placed in the cephalostat and then asked to rotate their head until the orbitale marker lies in the xy -plane. This plane is visible as a horizontal line in the morphograph's window superimposed on its reflection in a mirror opposite.

Although the fixed relations principle is implemented using a cephalostat, the registration differs from traditional cephalostatic registration in two principal ways: validity and accuracy. The redefinition of the coordinate system to pass through the centre of the cephalostat's ear rods rather than the porions ensures the registration remains valid when the head is rotated to other recording positions. Accuracy is improved in several ways. Pressure sensitive ear rods, the marker on the left orbitale and the marked coordinate lines and mirrors improve the registration accuracy. Imaging equipment with precisely defined positions and projection characteristics ensures standardisation of the radiographic and photographic data.

2.5 Discussion

The solution of the registration problem can be seen from a mathematical perspective as solving a set of simultaneous equations for the unknown registration parameters in terms of known image properties. The solution of simultaneous equations can produce three types of result. If insufficient data are available, the equations are under-defined and an infinite number of possible solutions exist. If too much information is given then several conflicting solutions may exist and so the problem is over-defined. If the input data are sufficient to give a single unique solution then the problem is well-defined.

The inappropriate and inaccurate registration inherent in traditional cephalometrics was part of the motivation for the development of morphanalysis, and has already been discussed. Because these inherent inaccuracies open the solution to ambiguity, traditional cephalometrics is an under-defined solution to the registration problem.

This leaves a choice of registration techniques between the fixed relations principle and various least-square error methods. The best-fit schemes over-define the registration problem and attempt to find the ‘best’ solution in the least square error sense. They are accurate and robust within their limited contexts, but they do not satisfy all of the requirements for universally relatability. Firstly, it is not possible to analytically inter-relate two-dimensional (e.g. radiographic and photographic), two-and-a-half dimensional (e.g. laser-range) and three-dimensional (e.g. CT and MRI) data. As researchers in a field rapidly advancing into 3D imaging, we should not lose sight of the fact that

CHAPTER 2. UNIVERSALLY RELATABLE IMAGES

approximately 90% of all clinical images are still two-dimensional. Although least-squares fitting methods are frequently applied to individual CT or MRI slices, little attention is usually given to how the particular slices are chosen. The situation is similar with photographic and radiographic data. Although some form of 2D registration can be applied, it is meaningless as a standard because of the loss in information associated with capturing a projection of a 3D object.

A second problem with using best-fit methods to define a standard is that the same data (points, surfaces or volumes) are not available in all modalities and all scans. For example, a least-squares surface fit of a facial scan will give very different results from a least-squares fit of the whole head surface. The same is true of volumetric least-squares registration of a few CT slices as compared to a complete head scan. With landmark point based registration the problems are similar e.g. bony landmarks are usually not available in MR images and lateral radiographic landmarks might not be visible on a frontal photograph.

Finally, the best-fit methods do not provide a simple way of defining a standard registration target and the improvements in communication that accompany it. For a single study, the usual method is to register the subjects to a single subject's image or to the average landmark configuration. This means that every study will define its own coordinate system. Constructing a universal convention would require either

- a) selection of a particular individual image as the universal registration target,

CHAPTER 2. UNIVERSALLY RELATABLE IMAGES

which might bias the registration in an unpredictable way, or

- b) continually updating and backdating the coordinate convention,

which is impractical.

The fixed relations principle uses only three points to define a coordinate system and hence the registration of the form containing those points. The registration so defined is unique and can therefore be thought of as a well-defined solution to the registration problem. Because the registration is applied before the images are captured it is not limited to only three-dimensional images, but is equally valid for all imaging modalities. Finally, the fixed relations principle does not require a registration target, other than the reference frame itself, and so avoids the problems discussed above.

2.6 Conclusions

In summary, the choice of registration system is between three principal contenders: traditional cephalometrics, the fixed relations principle and a range of best-fit methods. Traditional cephalometric methods are inaccurate and ill-defined. Theoretically, best-fit methods have the potential to define a universal reference convention, but not practically. Because these methods can only be applied after imaging, they are only appropriate to full three-dimensional data in which the same anatomical information (points, surfaces or regions) required is always present. Additionally, the definition of a universal target shape for the registration is difficult and may have an impact on the results.

CHAPTER 2. UNIVERSALLY RELATABLE IMAGES

In contrast, the fixed relations principle is accurate, robust and universally applicable. The drawback to the fixed relations principle is the need for accurately constructed (and therefore relatively expensive) registration and imaging apparatus. For this project, the necessary equipment was already available in the form of the analytic morphograph and so expense did not present a problem. This chapter can therefore end with the bold statement that the fixed relations principle remains the only method currently available for the registration of patients in an *analytically valid and universally relatable* way in pursuit of the clinical and research wish-list mentioned at the beginning of the chapter.

Chapter 3

Surface Data Capture

Methods

3.1 Introduction

Various methods exist for the measurement of 3D facial surfaces (42) (43) (44), from simple approaches using calipers to highly complex ones involving computationally intensive reconstruction. Most modern methods are based on triangulation (Figure 3.1), time-of-flight (Figure 3.2), or a variety of single image methods. Single image methods such as depth-from-shading, depth-from-focus and depth-from-texture can only produce approximate surface data and have not been used for medical examination. In this chapter the other modern, non-contact, 3D surface acquisition systems are reviewed and the reasons for our

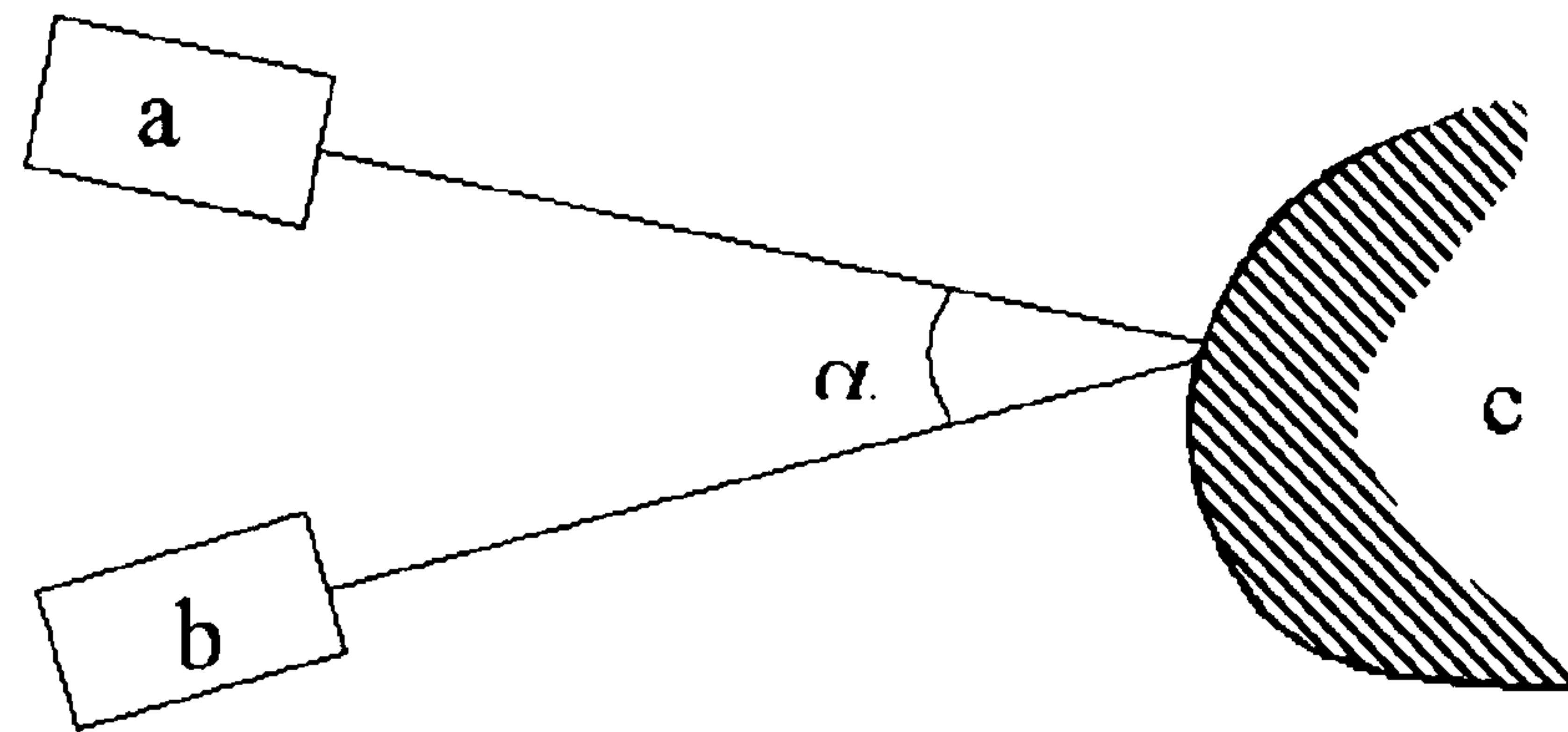


Figure 3.1: The principle of triangulation is the basis of most surface scanning systems. The surface c is intersected by two rays of light that also pass through positions a and b . Using the angle of separation of the rays and the location of a and b the position of the point on c can be calculated.

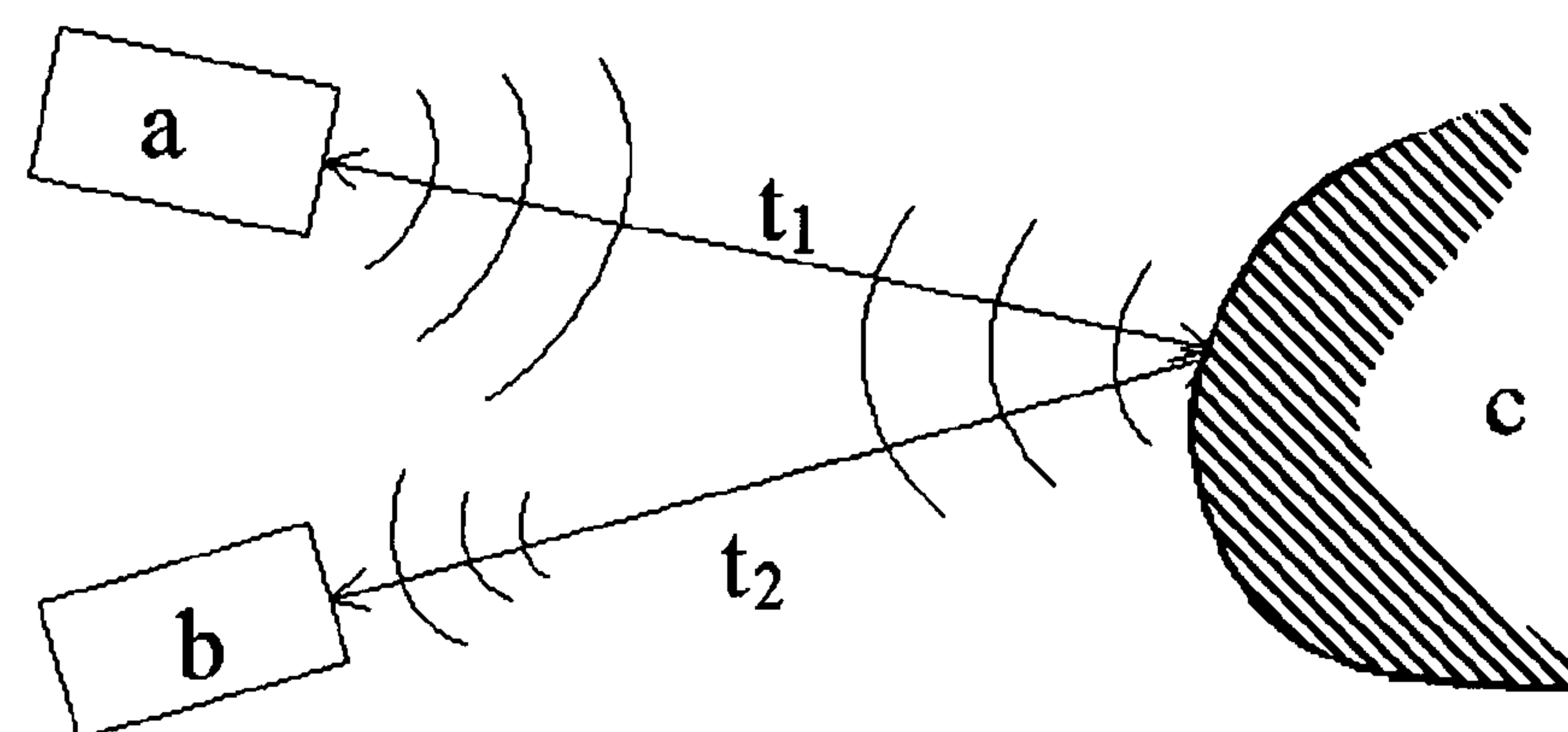


Figure 3.2: Time-of-flight surface measurement systems calculate the distance to an object (c) using the time ($t_1 + t_2$) between transmission of a signal from (a) and the reception of the reflected signal at (b).

choice of a laser-video scanning system are explained.

3.2 Triangulation-based methods

3.2.1 Stereophotogrammetry

Human vision uses the combination of two images to provide three-dimensional information about the environment and so is a natural place to start when look-

CHAPTER 3. SURFACE DATA CAPTURE METHODS

ing at 3D measurement systems. Given two images of an object taken simultaneously from slightly different angles, the 3D location of any point identifiable in both scenes can be calculated using triangulation, provided the position and optical details of the cameras involved are known. This approach has been used extensively in aerial surveying and for measuring the human body.

The first to realise the potential of stereophotogrammetry for facial measurement was Mansbach (45) in 1922, but it was not until 1939 that Zeller (46) demonstrated the principle in practice. Zeller encouraged Thalmaan-Degan (47) to apply his method clinically. She studied the changes in facial morphology due to orthodontic treatment, using contour plots derived from stereophotogrammetry to illustrate her findings. Since then many studies have been carried out e.g. Bjorn et al 1954 (48), Haga et al 1964 (49), Burke and Beard 1967 (50), Dixon and Newton, 1972 (51) and Berkawitz and Cuzzi 1977 (52), Ras et al 1995 (53) and 1996 (54) and Stevens 1997 (55).

In order to identify points on the surface some kind of grid or pattern is generally projected onto the face. Manual identification of points is a time consuming process, and prone to inaccuracies. This limits the methods cited above to landmarks or, when a simple pattern is projected, very low resolution data. Many approaches to automating the matching have been researched, largely in the fields of robot vision and aerial surveying (56). Recently, the Turing Institute at Glasgow University has produced a commercial system capable of capturing 3D data using stereophotogrammetry and reconstructing the 3D surface in a few minutes (57). This system projects a fractal pattern onto the face

CHAPTER 3. SURFACE DATA CAPTURE METHODS

and then uses a fast, multiscale matching algorithm to reproduce the 3D data. Unfortunately, due to the commercial nature of the work, published results are not available, although another group at the University of Central Lancashire is beginning to publish results of a similar method (58).

3.2.2 Moiré Fringe Scanners

When a light source is projected through a grid onto a surface it produces a set of shadows. If these are viewed through a second grid, a set of contours or fringe patterns is seen. These are called Moiré fringes, and were first used to study the shape of surfaces by Takasaki in 1970 (59) . Many studies have been carried out using Moiré topography to map the shape of parts of the human body, particularly the back (60) (61) (62) (63) and face (59) (60) (64). More recently a system capable of capturing 360,000 3D coordinates in under 2 seconds and automatically processing facial data has been built (65).

In spite of the fast capture time and recent advances in automation of the reconstruction process, Moiré fringe topography suffers from several drawbacks. The contours are highly sensitive to positioning and orientation of both the patient and the projectors (66) (67) (68). Hence for accuracy Moiré systems require special measures to combat expansion of the hardware due to changes in temperature, leading to a significant increase in cost. Ambiguity in the fringe order and sign and corruption of the image due to noise and non-uniformity of the sampling mean that a large amount of computer processing is required to segment the 3D data from the fringe pattern (69) (70). The poor reflectivity of

CHAPTER 3. SURFACE DATA CAPTURE METHODS

the facial surface produces blurring of the contours, thus makeup often has to be used before the scan takes place.

In order to overcome some of these difficulties a reconstruction method has been devised using the Fourier transform (71). Analysing the Moiré fringes in the frequency domain avoids the need for determining the order of the fringes or interpolating between them, and is sensitive to variations in depth within fringes. However, problems remain in terms of the computer processing required and the difficulties in extracting data from steep contours(69).

3.2.3 Phase Measurement

Phase measuring profilometry (69) (72) (73) is a simple method for capturing three-dimensional data using a projected intensity pattern and a single camera. Three or more images of a scene illuminated by a sinusoidally varying intensity pattern are captured. The intensity of the incident light along a profile is constant, but the reflectivity and orientation of the surface affect the intensity of the reflected light. To segment profiles from the images, the pattern is shifted by a fraction of a phase between each frame. This allows the reflective properties of the surface to be eliminated and so the intensity of the incident light in any single image can be calculated in terms of the phase. The variation in the incident signal's intensity produces constant intensity profiles across the face. The images are captured at an angle to the incident light source, so three-dimensional information can be extracted from the profiles using triangulation. Because only a few frames need to be captured this method has a fast acquisi-

CHAPTER 3. SURFACE DATA CAPTURE METHODS

tion time (under 1 second), high precision (RMS error of 0.65mm on the back) and low cost. Aliasing of the phase due to repeated cycling of the intensity distribution requires extra processing and could lead to occasional large errors.

3.2.4 Laser light scanners

Structured light scanners using laser light were first described by Will and Pennington (74) in 1971 and are now commonly used for machine vision applications. The simplest such scanner uses a laser to project a single spot onto the surface. This is viewed with a video camera, aligned to view the spot at an angle to the direction of the laser. The 3D location of the spot can be calculated using triangulation. In order to capture an entire surface with this method it is necessary to scan the spot across the whole surface. To improve speed, the laser can be passed through a cylindrical lens that fans the beam out into a stripe. Viewing this profile at a small angle to the laser plane with a video camera produces a distorted profile on a video monitor. The 2D coordinates in the video image of the laser-stripe are stacked up into a 3D surface (depth map) by advancing the laser-stripe and camera using a translation stage, driven by a stepper motor.

Capturing a complete image frame for each position of the laser stripe requires large amounts of storage and a fast video capture board. To overcome these problems, purpose-built hardware can be used to automatically segment the stripe during the course of one video frame (75) (76) (77). This calculates the time between the start of each video line (signalled by the line-sync pulse)

CHAPTER 3. SURFACE DATA CAPTURE METHODS

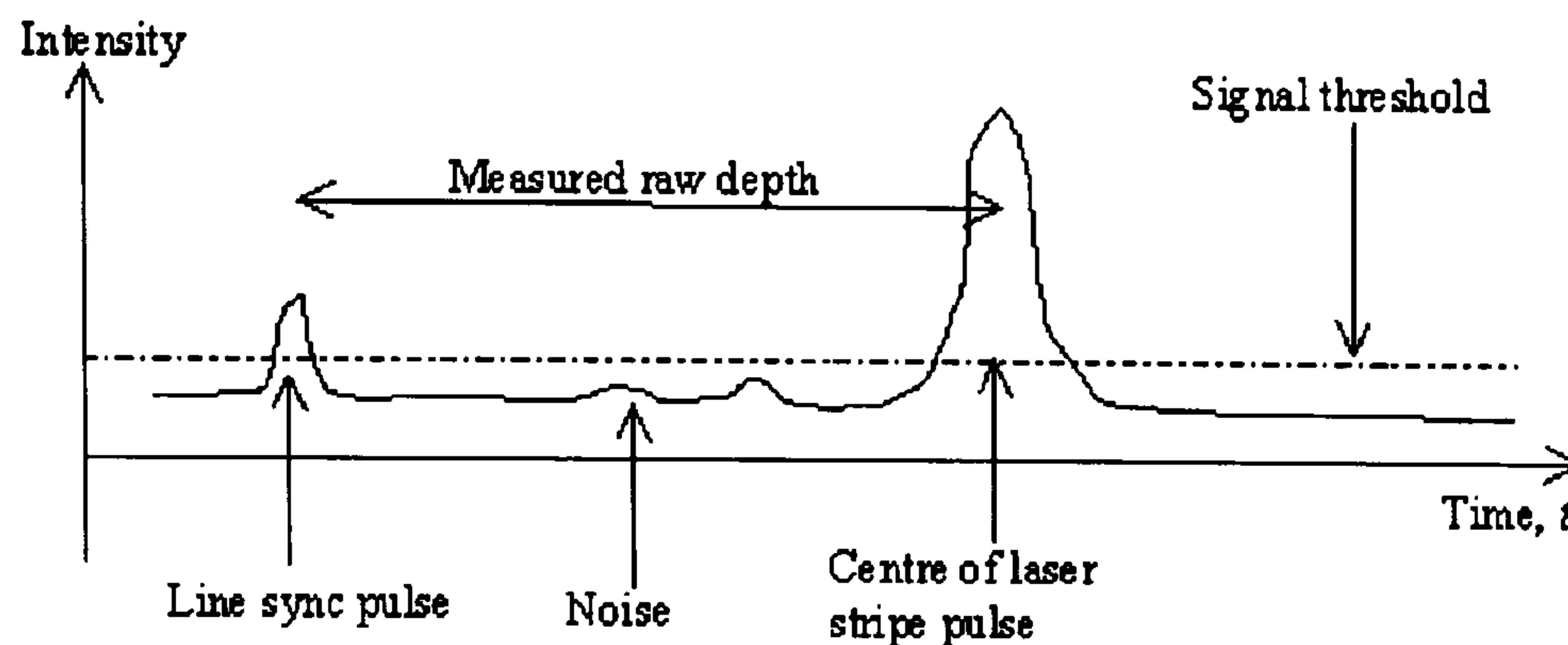


Figure 3.3: The video processing hardware measures the time between the line sync pulse and the centre of the laser stripe pulse in real time, eliminating the need for a frame store.

and the peak due to the laser stripe (Figure 3.3). This allows one stripe to be captured per video frame (1/50s).

Several laser-stripe systems have been developed for measuring the facial surface for medical applications (78) (79) and animation (80) (77). These systems use either a radial movement for capturing the 360° head surface data or a linear movement to concentrate on the facial area. Although some have raised questions regarding the safety of lasers for scanning, there is no evidence to support this. Our own safety audit (81) concluded that in the worst case scenario, with mechanical breakdown at eye level and dislodgement of the fanning lenses, the subject would have complete eye protection provided by their natural blink reflex.

3.3 Time-of-Flight based methods

3.3.1 Sonic scanners

A change in acoustic impedance between two tissues will reflect a large proportion of an incident ultrasound wave. The reflected wave can be detected and used to calculate the structure of the reflective surface. The use of this technique for measuring internal body structures has long been established, and is now in routine clinical use. The first to suggest its use for measuring the body surface was Short et al in 1974 (82). Their work was enhanced by Lindstrom et al (83) who reported an accuracy of between 1.0 and 0.1mm. Later work by Gallup et al (84) had difficulty in reproducing this level of accuracy, with a measurement error close to 3mm. Another drawback is the slow acquisition speed (between 6 and 10 minutes) which is too long to expect a patient to maintain position and facial expression.

3.3.2 Holography

When a scene is illuminated by a coherent light source (i.e. a laser) the phase of the light reflected on to a photographic film will depend on the length of the path travelled from the source. The phase therefore contains 3D information about the scene, which it imparts to the film to produce a hologram. Ansley (85) was the first to describe the use of holography to image the face in 1970, achieving an accuracy of 2mm in a test with a dummy head (86). The technique has a fast capture rate of approximately 30 nanoseconds, but the high burst of

CHAPTER 3. SURFACE DATA CAPTURE METHODS

energy (1-3 Joules) raised concerns about possible tissue damage, and so the method was not applied to live subjects.

3.4 Choice of Method

The choice of facial scanning system must take into account the cost, accuracy, speed and safety of the equipment, the availability of necessary expertise and the proven clinical effectiveness of the proposed system. The Moiré fringe method has high cost and processing requirements. Stereophotogrammetry requires sophisticated processing for dense surface reconstruction and the accuracy of these algorithms for facial surface reconstruction remains clinically untested. Phase-measuring profilometry is a simpler system that has been tested clinically but ambiguity in the phase order due to aliasing requires additional processing and could lead to errors.

Laser-stripe scanners have been widely used for medical facial scanning applications(79) (78). Unlike other systems there is no ambiguity in the profile segmentation and little additional processing is required. Such systems are reasonably low cost and are safe for patients. The speed of a single scan is limited to one stripe per video refresh (i.e. 50 per second). This means that a stripe moving at 50mm/s can scan an area the size of the face in approximately 5 seconds at 1mm resolution. This is slower than some of the other systems, but is still quite a reasonable length of time to expect a subject to remain stationary. In addition, one of the Interface Project collaborators, Neil Duffy, has

CHAPTER 3. SURFACE DATA CAPTURE METHODS

expertise in the design and construction of laser scanning systems. This important human factor, when combined with the foregoing technical factors made laser-stripe triangulation our choice for a facial scanning system.

Chapter 4

Calibration of the Interface Laser Scanner

4.1 Introduction

This chapter describes the Interface laser scanner and a new calibration method (87) designed for it. The video scanner hardware outputs the time between the video line sync pulse and the laser stripe, at each point along the stripe at each translation stage position. Calibration is required to convert these unprocessed time measurements into 3D coordinates relative to the analytic morphograph's Cartesian reference frame.

4.2 System Description

The Interface scanner is installed within the analytic morphograph as shown in Figure 2.5. The scanner is a dual-laser plus video scanning system that uses hardware-based measurement of the illuminated line position (Figure 3.3). The scanner uses a vertical, linear motion of the horizontal laser plane so that the captured range-image shares the same coordinate system as the previous 2D records (Figure 4.1). Hardware-based stripe segmentation (75) (76) (77) eliminates the storage and processing overheads imposed by capturing an image of each scan line using a large frame store. This was particularly important in previous versions of the scanner which were capable of capturing changing surface profiles in real time over extended periods (88). The disadvantage of not having a frame store is that standard model-based camera calibration methods that involve the capture of a single image frame cannot be used. This has provided the motivation for a new calibration method.

4.3 Calibration Methods

4.3.1 Camera Calibration Based Methods

Calibration methods for laser-video scanners that use a frame store are most frequently based on a camera model with pinhole perspective (89) (78) with the possible inclusion of radial, tangential or other non-linear distortion terms (90) (91). These methods can achieve very accurate camera calibration but they do not calibrate the laser stripe or the translation stage movement, which are fre-

CHAPTER 4. CALIBRATION OF THE INTERFACE LASER SCANNER

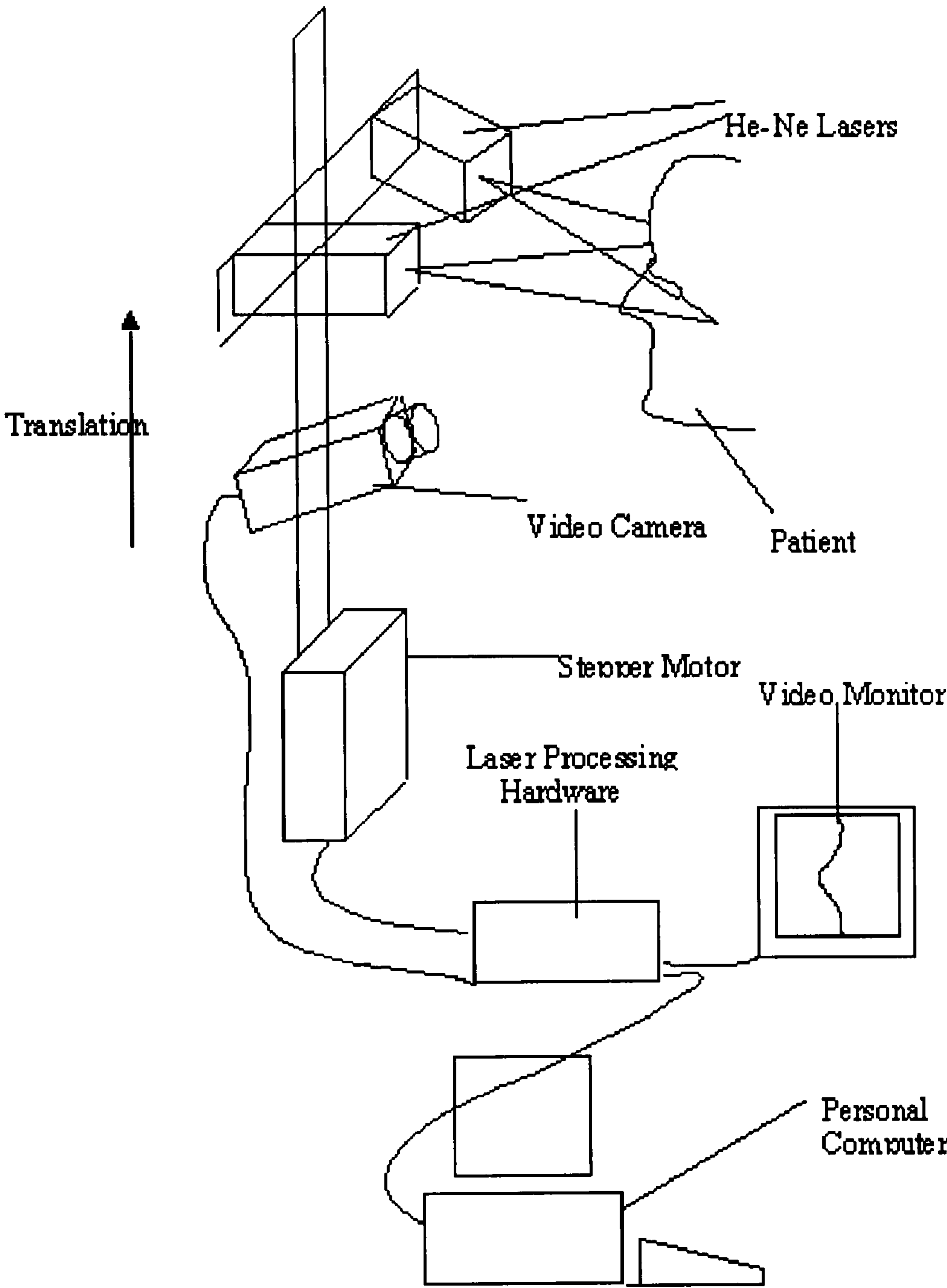


Figure 4.1: The Interface Laser Video Scanner Architecture.

CHAPTER 4. CALIBRATION OF THE INTERFACE LASER SCANNER

quently left to alignment by sight. Theodoracatos and Calkins (92) include laser stripe and camera calibration in a single model, but do not include translation stage alignment. This is because they only require calibration to the camera's internal reference frame and not to an externally defined reference frame.

4.3.2 Geometry Based Methods

Calibration methods that do not require a frame-store are more varied and have been less widely adopted by the imaging community. The simplest such method is to measure all of the extrinsic parameters of the system and to rely on the manufacturer's data for the intrinsic parameters. This is inaccurate and time consuming and thus unsatisfactory.

A more promising approach is to scan a suitable 3D target and derive the necessary information from the known geometry and the imaged geometry. Manthey, Knapp and Lee (94) attempted to fit values to a model by scanning two geometrical objects - a sphere and a plane. They used a simple linear model that does not include camera perspective distortion or radial distortion. Trucco and Fisher (95) used a look-up table of the translations between the known and expected locations of points in a scanned calibration jig. This ensured that all systematic errors were accounted for but required an expensive and accurately machined calibration jig and interpolation of the table's values.

4.4 New Model Based Method

4.4.1 Overview

The new method presented here is based on Tsai's camera model (90) (91), extended to include the full laser scanning system and modified for implementation on a system without a frame store. Parameters are fitted to one of two scanner models by scanning a target of points. The first model includes camera perspective, translation stage movement and laser-plane alignment. The resulting equations are solved using a linear method. The second model additionally includes a radial distortion term in the camera model, and the resulting non-linear equations are solved using an iterative scheme.

4.4.2 The System Model

The Moving Camera Model

The extrinsic camera parameters represent the position and orientation of the camera in space. The initial position and orientation of the camera can be expressed as a 3 component rotation and a 3 component translation. The location of the camera at frame k is given by including an additional translation dependent on the translation step \mathbf{v} . Hence the transformation from coordinates in the external reference frame \mathbf{x} to those in the camera reference frame \mathbf{x}_c is given by

$$\mathbf{x}_c = \mathbf{R} \cdot \mathbf{x} + \mathbf{T} + \mathbf{v}k \quad (4.1)$$

CHAPTER 4. CALIBRATION OF THE INTERFACE LASER SCANNER

where \mathbf{R} is the 3 x 3 rotation matrix and \mathbf{T} is the 3 component translation vector. The rotation matrix \mathbf{R} is the result of rotating around each of the three axes (x, y, z) by the three angles (θ, ϕ, ψ) respectively. The result is the matrix

$$\mathbf{R} = \mathbf{R}_x \cdot \mathbf{R}_y \cdot \mathbf{R}_z = \begin{bmatrix} r_1 & r_2 & r_3 \\ r_4 & r_5 & r_6 \\ r_7 & r_8 & r_9 \end{bmatrix}$$

$$= \begin{bmatrix} \cos \phi \cos \psi & \cos \phi \sin \psi & -\sin \phi \\ -\sin \psi \cos \theta + \cos \psi \sin \phi \sin \theta & \cos \psi \cos \theta + \sin \psi \sin \phi \sin \theta & \cos \phi \sin \theta \\ \sin \psi \sin \theta + \cos \psi \sin \phi \sin \theta & -\cos \psi \sin \theta + \sin \psi \sin \phi \cos \theta & \cos \phi \cos \theta \end{bmatrix} \quad (4.2)$$

The intrinsic camera parameters represent the effective focal length, internal scaling and radial distortion coefficient of the camera. The pinhole perspective model will transform the 3D camera coordinate points $\mathbf{x}_c = (x_c, y_c, z_c)$ into undistorted sensor coordinates (X_u, Y_u) by

$$X_u = f \frac{x_c}{z_c} \quad (4.3)$$

$$Y_u = f \frac{y_c}{z_c} \quad (4.4)$$

where f is the effective focal length of the camera. Radial distortion terms are usually included only up to first order distortion, given by

CHAPTER 4. CALIBRATION OF THE INTERFACE LASER SCANNER

$$X_d = \frac{X_u}{1 + \kappa_1 r_d^2} \quad (4.5)$$

$$Y_d = \frac{Y_u}{1 + \kappa_1 r_d^2} \quad (4.6)$$

where r_d is the distorted radius from the image centre given by

$$r_d^2 = X_d^2 + Y_d^2 \quad (4.7)$$

The measured pixel values (i, j) are then found by translation of the origin to the image centre (C_i, C_j) and by scaling the i axis to compensate for any differential scaling along each axis, i.e.

$$i = X_d s_i + C_i \quad (4.8)$$

$$j = Y_d + C_j \quad (4.9)$$

where s_i is the sensor's i scale uncertainty. The scaling in the j direction is calibrated by the effective focal length. The sensor element size does not affect the calibration as it is masked by the effective focal length f and the i scale uncertainty s_i . These variables will also include any scaling due to the hardware acquisition and internal processing on the PC.

CHAPTER 4. CALIBRATION OF THE INTERFACE LASER SCANNER

Moving Laser Plane Model

The laser plane is modelled as an infinite plane of light with surface normal

$$\mathbf{n} = (\sin \alpha, \cos \alpha \sin \beta, \cos \alpha \cos \beta) \quad (4.10)$$

which travels a distance \mathbf{v} between frames, the same as that of the camera.

This is equivalent to a stationary camera and laser plane, with the scanned object moving on a translation platform a distance $-\mathbf{v}$ between frames. This is represented by

$$\mathbf{n} \cdot \mathbf{x} + n_0 = (\mathbf{n} \cdot \mathbf{v}) k \quad (4.11)$$

where n_0 is a constant, dependent on the position of the plane at frame $k = 0$.

Complete System Model

The moving camera model and the moving laser plane model described above represent a complete description of the laser scanner system. They are combined by noting that all the measured points imaged by the camera lie in the laser plane (Figure 4.2). The model involves the 17 individual parameters shown in Table 4.1.

CHAPTER 4. CALIBRATION OF THE INTERFACE LASER SCANNER

Variable	Description
f	Effective focal length
s_i	Sensor i scale uncertainty
κ_1	Radial distortion coefficient
\mathbf{v}	3 component translation stage velocity vector
(α, β)	2 laser plane angles
n_0	laser plane constant
\mathbf{T}	3 component camera initial translation vector
(θ, ϕ, ψ)	3 camera rotation angles
(C_i, C_j)	2 component image centre (centre of radial distortion)

Table 4.1: The 17 parameters included in the scanner model.

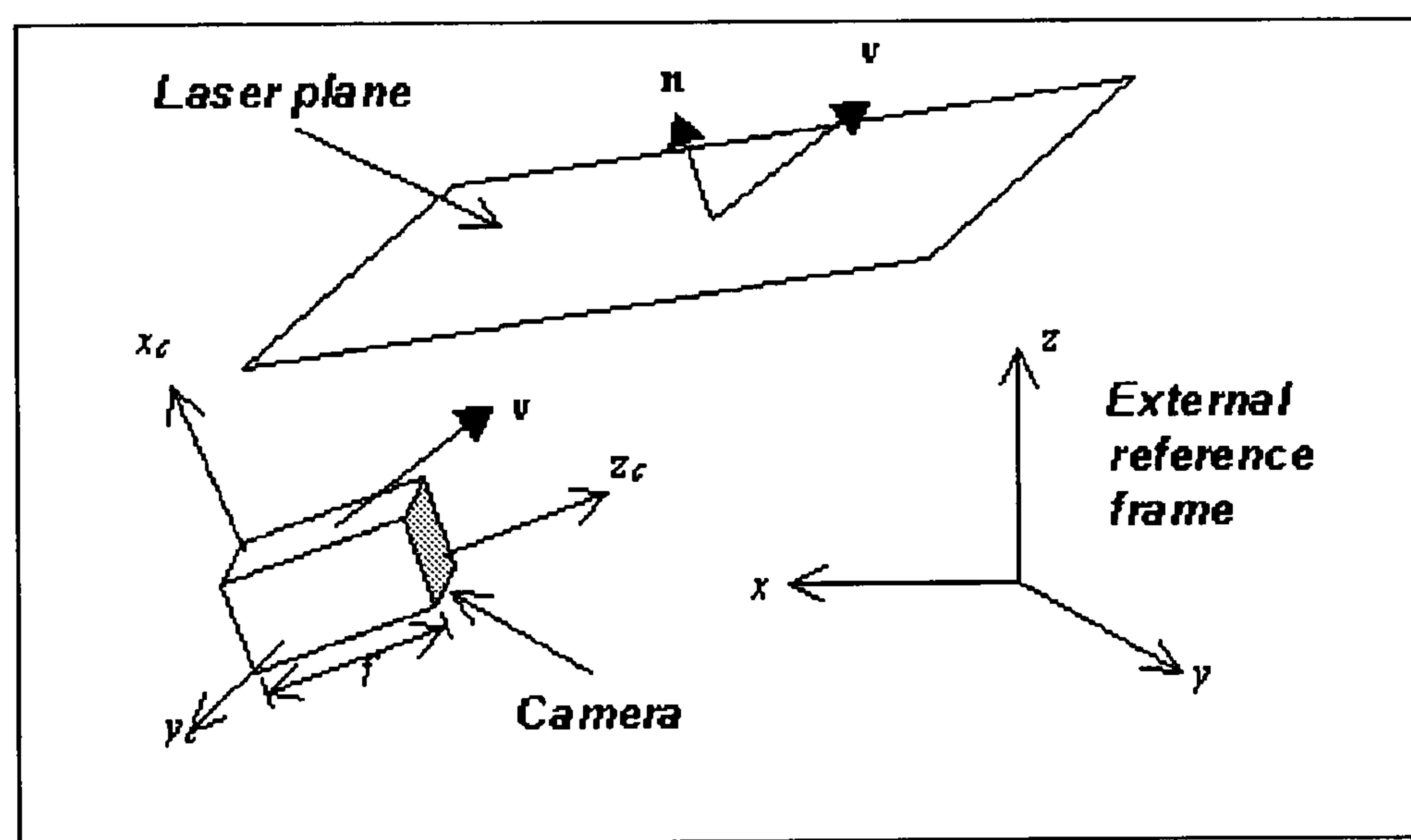


Figure 4.2: A diagram of the Interface laser-video scanner model.

4.4.3 Calibration Methods

Linear Calibration Method

If the radial distortion term is ignored, the equations representing the laser scanning system are given by

$$i = s_i f \frac{r_1 x + r_2 y + r_3 z + T_x + v_x k}{r_7 x + r_8 y + r_9 z + T_z + v_z k} + C_i \quad (4.12)$$

$$j = f \frac{r_4 x + r_5 y + r_6 z + T_y + v_y k}{r_7 x + r_8 y + r_9 z + T_z + v_z k} + C_j \quad (4.13)$$

$$k = \frac{n_x x + n_y y + n_z z}{n_x v_x + n_y v_y + n_z v_z} + n_0 \quad (4.14)$$

By absorbing the image centre (C_i, C_j) into the division expressions, and grouping variables, these can be written in matrix form as,

$$\mathbf{M} \cdot \mathbf{x} = \begin{bmatrix} m_{11} & m_{12} & m_{13} & m_{14} \\ m_{21} & m_{22} & m_{23} & m_{24} \\ m_{31} & m_{32} & m_{33} & m_{34} \\ m_{41} & m_{42} & m_{43} & 1 \end{bmatrix} \begin{bmatrix} x \\ y \\ z \\ 1 \end{bmatrix} = \begin{bmatrix} i' \\ j' \\ k' \\ l' \end{bmatrix} \quad (4.15)$$

and

CHAPTER 4. CALIBRATION OF THE INTERFACE LASER SCANNER

$$\begin{bmatrix} i \\ j \\ k \end{bmatrix} = \begin{bmatrix} i'/l' \\ j'/l' \\ k' \end{bmatrix} \quad (4.16)$$

Because the depth map's vertical component k is not affected by perspective the system is non-linear with respect to the coordinate variables. The model is linear with respect to the model parameters m_{ij} and so linear methods can be used. The coefficients of the matrix \mathbf{M} can be found using at least five non-coplanar points and solving the resulting set of 15 linear equations. Over-defining the equations using 110 calibration points and solving them using singular value decomposition (13) gives a least-squares solution.

To find the reference frame coordinate, (x, y, z) from a measured point (i, j, k) the inverse transform is applied. This is given by,

$$x = \frac{(1 - n_{43}k)(n_{11}i + n_{12}j + n_{14})}{(n_{41}i + n_{42}j + n_{44})} + n_{13}k \quad (4.17)$$

$$y = \frac{(1 - n_{43}k)(n_{21}i + n_{22}j + n_{24})}{(n_{41}i + n_{42}j + n_{44})} + n_{23}k \quad (4.18)$$

$$z = \frac{(1 - n_{43}k)(n_{31}i + n_{32}j + n_{34})}{(n_{41}i + n_{42}j + n_{44})} + n_{33}k \quad (4.19)$$

where $\mathbf{N} = [n_{ij}] = \mathbf{M}^{-1}$. Here the system non-linearity is even more clearly demonstrated.

CHAPTER 4. CALIBRATION OF THE INTERFACE LASER SCANNER

Non-linear Calibration Method

Including radial distortion in the model equations produces a set of non-linear simultaneous equations. These can be solved iteratively using a standard technique such as the Levenberg-Marquardt algorithm (13). This tries to minimise an error function, χ^2 by searching the solution space with a combination of the inverse Hessian and the steepest descent methods. Algorithm 1 finds the three component error χ , given an uncalibrated point and its expected reference frame coordinate.

The variables r_u and r_d are the undistorted and distorted radii from the image centre (C_i, C_j) , (X_u, Y_u) and (X_d, Y_d) are the undistorted and distorted image coordinates, (I, J, K) is the calculated depth map coordinate and (i, j, k) is the corresponding measured coordinate. The cubic polynomial is solved using Cardan's method, selecting the smallest positive real root.

The Levenberg-Marquardt method will only converge to a local minimum and so a reasonable initial guess is required. In order to make such a guess certain assumptions about the scanner can be made as follows.

1. The radial distortion term is small and so can be ignored in a first guess.
2. The image centre is close to the centre of radial distortion.

The linear model parameters along with the approximate image centre are used to establish a first guess.

As with the linear method, the inverse transform can be defined using a matrix transform, provided the radial distortion term is removed first, using

CHAPTER 4. CALIBRATION OF THE INTERFACE LASER SCANNER

Algorithm 1 Calibration Error Function

INPUTS

Model parameters: $\mathbf{n}, \mathbf{v}, s_i, f, \kappa_1, \mathbf{R}, T, C_i, C_j$

Uncalibrated coordinate: (i, j, k)

Reference frame coordinate: $\mathbf{x} = (x, y, z)$

VARIABLES

Scalar $I, J, K, X_u, Y_u, r_d, r_u, X_d, Y_d$

Vector \mathbf{x}_c, χ

BEGIN

Calculate the frame number

$$K = (\mathbf{n} \cdot \mathbf{x}) / (\mathbf{n} \cdot \mathbf{v}) + n_0$$

Calculate the camera coordinates

$$\mathbf{x}_c = \mathbf{R} \cdot \mathbf{x} + \mathbf{T} + K\mathbf{v}$$

Calculate the undistorted sensor coordinates

$$(X_u, Y_u) = \frac{f}{z_c} (x_c, y_c)$$

Calculate the undistorted radius

$$r_u = \sqrt{X_u^2 + Y_u^2}$$

Solve the cubic equation

$$r_u = r_d (1 + \kappa_1 r_d^2)$$

for the distorted radius r_d

Calculate the distorted sensor coordinates

$$(X_d, Y_d) = \frac{r_d}{r_u} (X_u, Y_u)$$

Calculate the image coordinates

$$(I, J) = (X_d s_i + C_i, Y_d + C_j)$$

Calculate the error vector

$$\chi = (I, J, K) - (i, j, k)$$

OUTPUT

Error vector χ

CHAPTER 4. CALIBRATION OF THE INTERFACE LASER SCANNER

$$X_u = X_d (1 + \kappa_1 r_d^2) \quad (4.20)$$

$$Y_u = Y_d (1 + \kappa_1 r_d^2) \quad (4.21)$$

where $r_d^2 = X_d^2 + Y_d^2$, $X_d = (i - C_i)/s_i$ and $Y_d = j - C_j$.

The forward transform matrix is then,

$$\mathbf{M} = \begin{bmatrix} r_1 + v_x n'_x & r_2 + v_x n'_y & r_3 + v_x n'_z & T_x + v_x n'_0 \\ r_4 + v_y n'_x & r_5 + v_y n'_y & r_6 + v_y n'_z & T_y + v_y n'_0 \\ n'_x & n'_y & n'_z & n'_0 \\ r_7 + v_z n'_x & r_8 + v_z n'_y & r_9 + v_z n'_z & T_z + v_z n'_0 \end{bmatrix} \quad (4.22)$$

where $\mathbf{n}' = \mathbf{n}/(\mathbf{n} \cdot \mathbf{v})$. The linear inverse transform is then applied to the coordinates $(X_u/f, Y_u/f, k)$ using the matrix $\mathbf{N} = \mathbf{M}^{-1}$.

4.4.4 Calibration Data Collection

To fit parameters to the models described above, points extracted from two scans of a calibration target (Figure 4.3) are used. The target consists of 55 circular white dots on a black background constructed by writing a raw postscript file and printing on a phototypesetter to an RMS accuracy of 0.09mm. By adjusting the threshold on the video signal intensity used to segment the laser stripe, only the white dots of the target are detected. The calibration range maps therefore have the appearance of a number of approximately circular discs floating in

CHAPTER 4. CALIBRATION OF THE INTERFACE LASER SCANNER

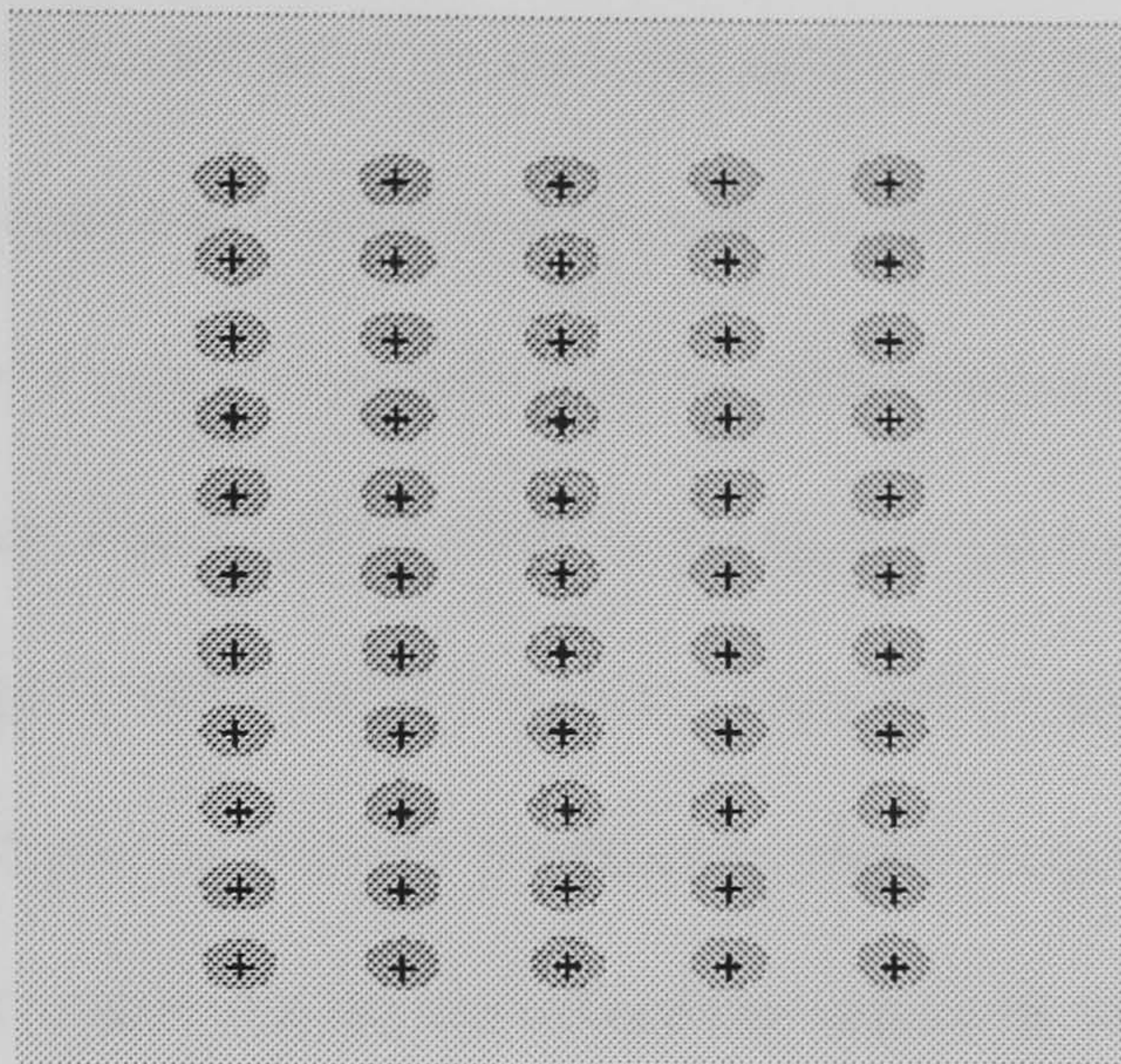


Figure 4.3: The calibration target as captured by the laser scanner. The detected centroids are marked with crosses.

space. For robust calibration, the calibration points range across as much of the scanned volume as possible. The first target is placed in the morphograph's cephalostat, with all points lying in the plane $x = 5mm$, and the second is placed on the back of the morphograph's diffuser in the plane $x = 169mm$. The use of 110 calibration points reduces the effects of random errors in the detected centroids (i.e. due to system vibration and quantisation errors) reducing the need for highly accurate detection of any single point. The dots are detected automatically, by thresholding followed by a nearest neighbour connect routine. The centroids are found by averaging the 3D values over each segmented dot.

4.4.5 Results

The following results demonstrate that reasonable accuracy can be achieved with a one step calibration technique. Results are given for the inverse transform (transforming measured depth-map coordinates into real world points) in Table

CHAPTER 4. CALIBRATION OF THE INTERFACE LASER SCANNER

4.2 and for the forward transform (transforming the expected real world location of a point into the measured coordinate system) in Table 4.3. The distance of the point from the camera (approximately 1m) and the relatively coarse quantisation (approx. $1mm^3$ per voxel) affect the errors in the inverse transform. These results could be improved by using sub-pixel laser stripe segmentation, a higher resolution CCD camera or smaller translation stage steps. The dimensions of the scanner and the voxel size do not affect the errors in the forward transform and so give an indication of the true accuracy. This method predicts the depth-map coordinate to within ± 1 voxel for the vast majority of points and so may be regarded as close to the theoretical limit.

To measure the error away from the calibration points a multi-plane calibration test jig (Figure 4.4), machined on a milling machine accurate to 0.01mm is used. The perpendicular distance of each calibrated point $\mathbf{p} = (x, y, z)$ from the plane $x = ay + bz + c$ was calculated for almost every point in each of the 6 planes. The planes span approximately 60% of the depthmap area, about 50, 000 points. The distribution of errors for the planes (Figure 4.5) obeys a Gaussian model, indicating that the quantisation errors and vibrations are the cause of the large maximum error on some of the planes. The results for the non-linear calibration method are shown in Tables 4.4 and 4.5, giving the results for the inverse and forward transforms respectively.

CHAPTER 4. CALIBRATION OF THE INTERFACE LASER SCANNER

	Linear Method	Non-linear Method
RMS error $(x, y, z)mm$	(0.549, 0.245, 0.0897)	(0.306, 0.0595, 0.00814)
Max. error (mm)	1.38489	0.98138

Table 4.2: The measured error for the inverse transform using the calibration points.

	Linear Method	Non-linear Method
RMS error $(i, j, k)voxels$	(1.382, 0.377, 0.0909)	(1.318, 0.374, 0.0908)
Max. error (voxels)	3.4289	2.4275

Table 4.3: The measured error for the forward transform using the calibration points.

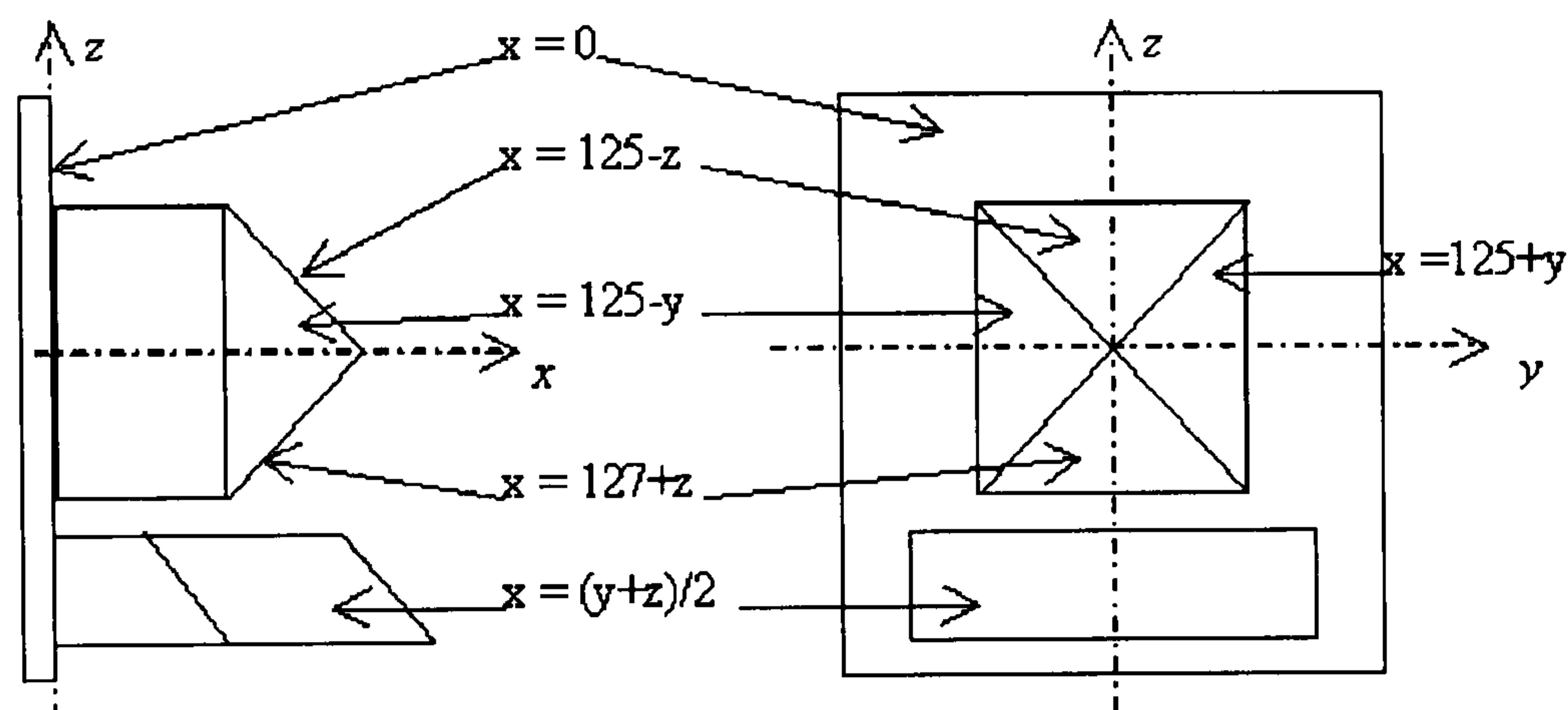


Figure 4.4: A diagram of the multi-plane calibration test object.

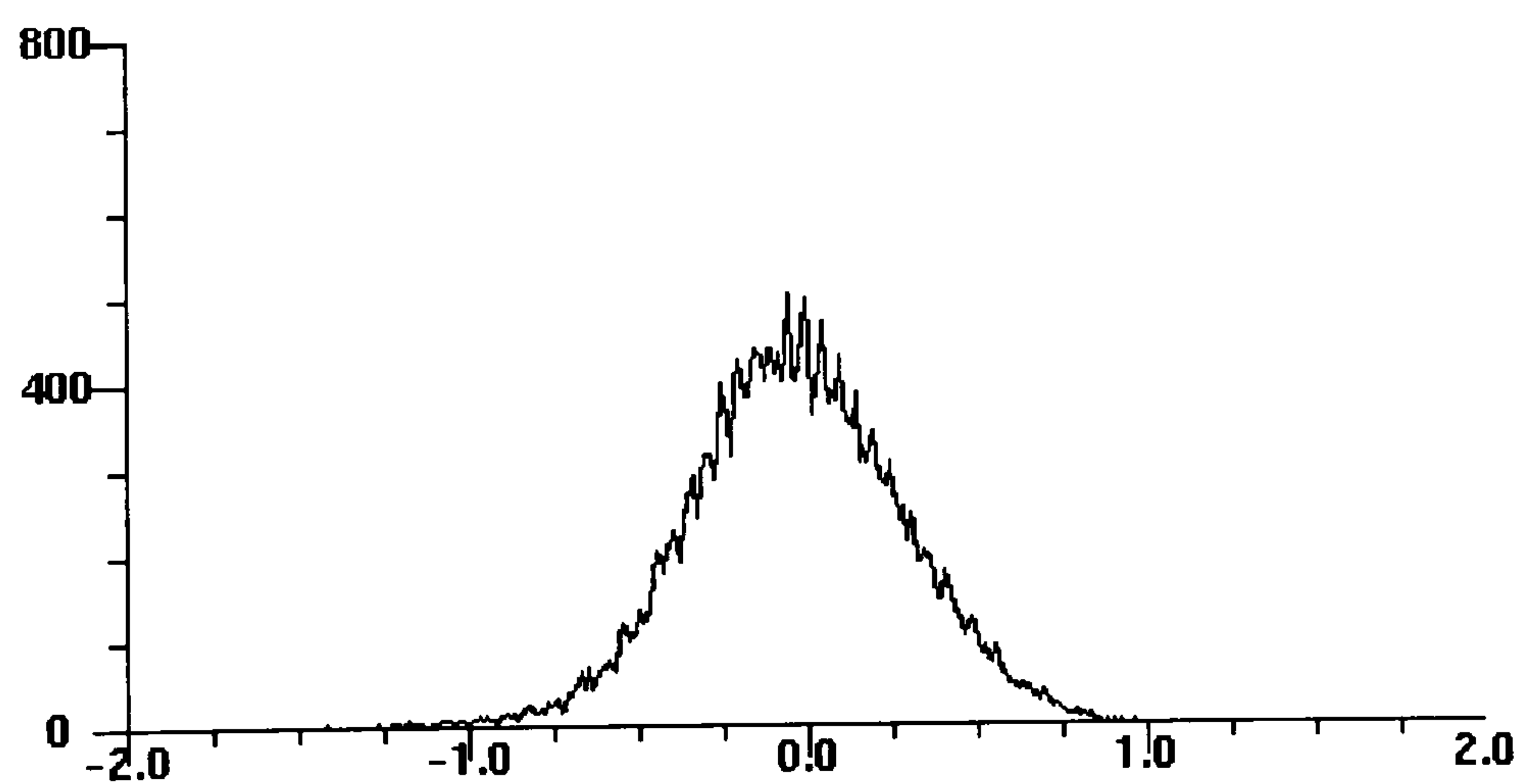


Figure 4.5: A histogram showing the distribution of errors (in mm with 0.01 mm bins) over the six planes of Figure 4.4.

CHAPTER 4. CALIBRATION OF THE INTERFACE LASER SCANNER

Plane	Mean Error	RMS Error	Max. Error
$x = 0$	-0.05	0.388	1.417
$x = 125 - z$	-0.005	0.291	0.972
$x = 125 - y$	-0.117	0.241	0.850
$x = (y + z)/2$	0.007	0.447	1.268
$x = z + 125$	0.081	0.265	0.897
$x = y + 125$	0.011	0.319	1.082

Table 4.4: Errors on planar surfaces for non-linear inverse transform in mm.

Plane	Mean Error	RMS Error	Max. Error
$x = 0$	0.091	0.621	2.501
$x = 125 - z$	0.014	0.465	1.512
$x = 125 - y$	0.237	0.489	1.700
$x = (y + z)/2$	0.044	0.791	2.337
$x = z + 125$	0.127	0.426	1.402
$x = y + 125$	0.015	0.535	1.780

Table 4.5: Errors on planar surfaces for non-linear forward transform in voxels.

4.5 Conclusions

This chapter has demonstrated a new one-stage technique for calibrating the Interface laser-video surface scanner. Although the technique is applicable to scanners with a frame store, it has been designed to solve the calibration problem for a scanner without one. The position and orientation of the camera and the laser stripe, the translation stage movement and the internal camera parameters are all included in a single model. The results show that the method gives an accuracy approaching the resolution of the scanner. For greater accuracy the method could be extended to include more non-linear distortions such as tangential or barrel distortion.

Part III

Inter-Subject Relation

Chapter 5

Inter-Patient Comparison

Methods

5.1 Introduction

The standardised registration and capture of universally relatable surface data via the fixed-relations principle and the new laser-video scanner calibration method assigns a three-dimensional spatial coordinate to each point on the facial surface. The problem discussed in this chapter is how to decide which points are related, anatomically, between different registered images. Some form of labelling is required in order to identify related points between different scans.

Landmarks are point features that are easy to identify and label on a subject or in an image. For example, the intersection of two anatomical contours or the

CHAPTER 5. INTER-PATIENT COMPARISON METHODS

points of maximum curvature in a contour represent useful landmarks (96) (97). The study of landmarks is relatively trivial once all images are standardised to a Cartesian reference frame. The vector displacement between two landmarks is found by subtraction, and the mean of N three-dimensional points is found by summing over each of the coordinate variables separately and dividing the result by N . The ellipsoidal distribution can also be found and is expressed as a three-by-three covariance matrix (98). The problem is that such measures are not well defined for higher dimensional structures. For example given two contours, what do we mean by the distance between them? Should we measure the distance between the ends, and if so, which end to which end? What can we do if the contour is a closed loop?

It can be seen that the comparison problem for contours is really one of finding point to point correspondence between the lines i.e. labelling the contours parametrically. This is true also for surfaces and volumes, where the problem becomes more complex. The solutions presented in the literature range from fully automatic to highly user intensive and are closely linked to the problem of feature extraction (features need to be identified before they can be compared).

At this stage, it is worth noting the relationship between point correspondence and image warping. Warping is defined as a non-rigid deformation of an image, and is usually used to change a shape in one image into a corresponding but different shape in another image. Given two images with corresponding points labelled, the translations between labelled points can be interpolated, and used to warp one image into the shape of the other. The reverse is also

CHAPTER 5. INTER-PATIENT COMPARISON METHODS

true; given the warping transformation between two images one can extract point to point correspondences. In either case, the labelling might not make sense *biologically*, depending on how it is achieved.

5.2 Literature Review

5.2.1 The original morphanalytic solution.

The first to attempt to find a solution to this problem in the context of craniofacial morphology was made by Rabey (4) (6). He reduced the problem of contour matching to a one-dimensional one using the Cartesian grid-lines of the standardised morphanalytic reference frame. Manually extracted contours were compared along each grid-line of the reference frame. If a contour crossed the selected grid-line at an angle greater than 45^0 it was considered acceptable for comparison along the grid line (Figure 5.1). The distance between two contours along the selected grid-line could then be measured. The distribution of many contours along the grid line could be found by counting the number of contours crossing between consecutive pairs of orthogonal grid-lines, along the length of the line (Figure 5.2). The average and standard deviation of points on different grid lines could then be built up into average and standard deviation outlines (Figure 5.3).

The method described above was originally developed before the advent of readily available computing power. For small studies, the method could be performed manually by tracing the contours onto acetate sheets, and overlaying

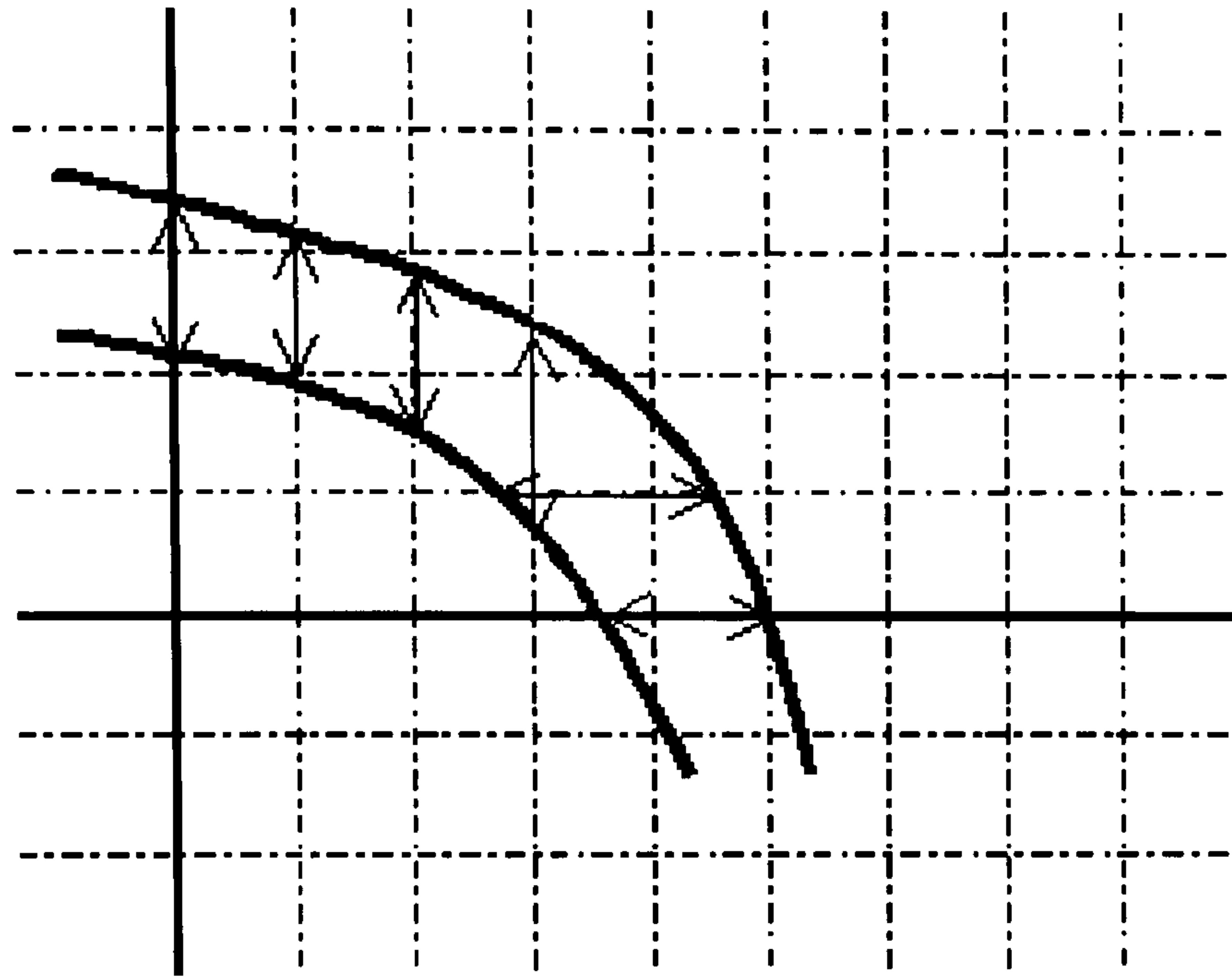


Figure 5.1: Comparison of contours is performed along horizontal or vertical grid lines, depending on the angle at which each contour crosses the line.

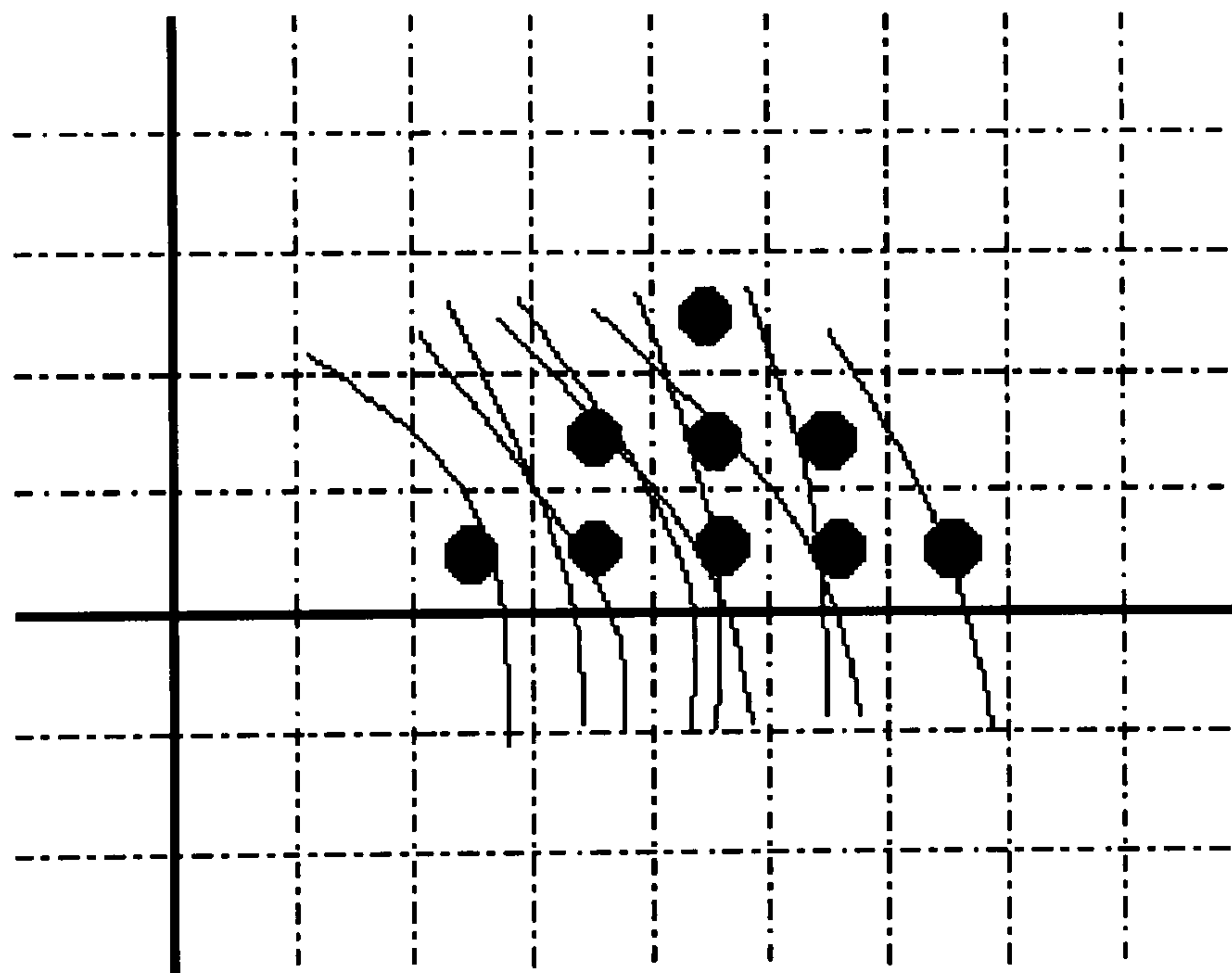


Figure 5.2: The average point of intersection of a set of contours with a grid line is found by summing the number of contours crossing the line between consecutive orthogonal gridlines. This builds up into a histogram, the peak of which is the average.

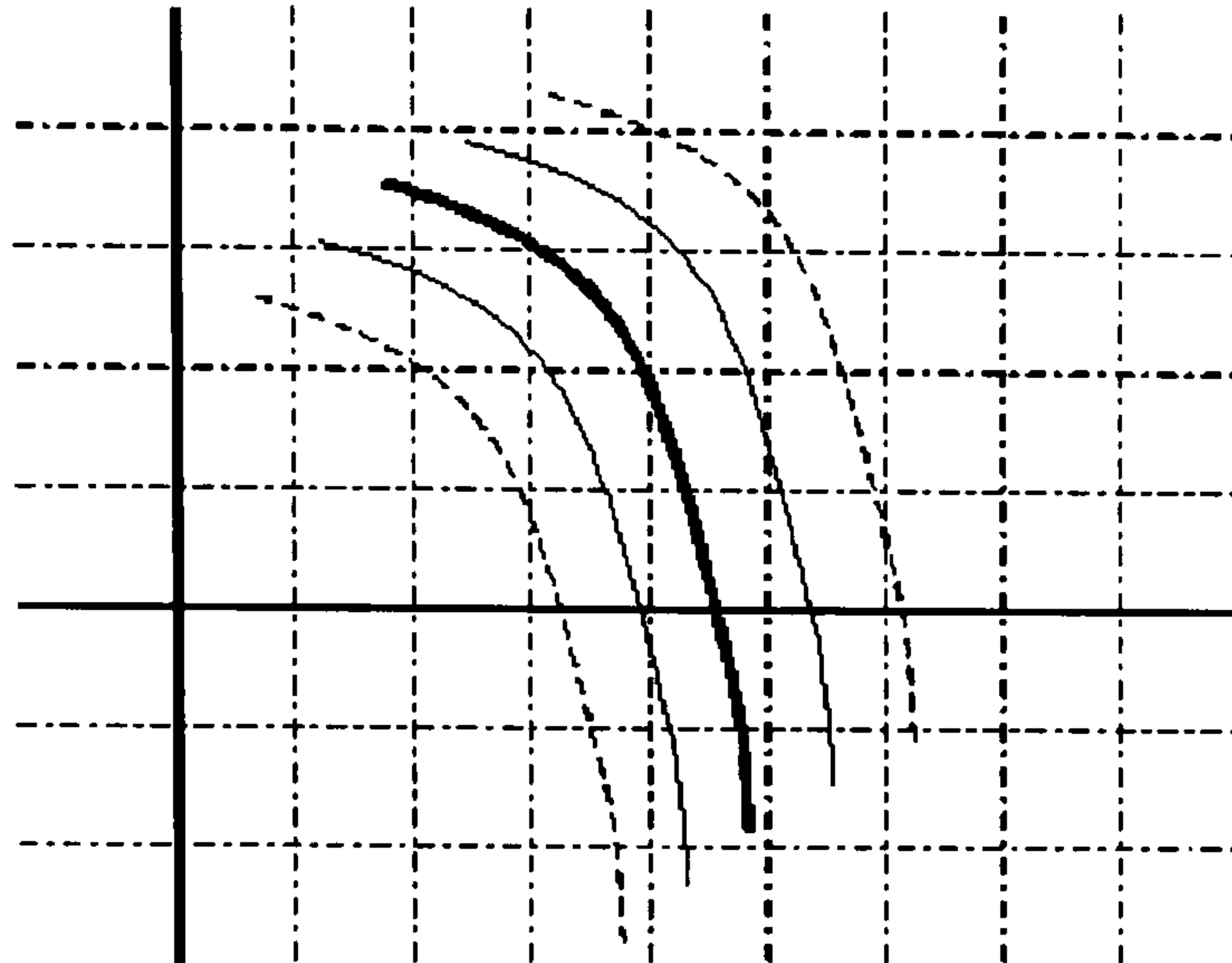


Figure 5.3: The average (bold) first standard deviation (solid) and second standard deviation (dashed) outlines of a contour can be built up by connecting the relevant points at different horizontal and vertical grid lines.

them on the standard reference grid. Later studies (e.g. Rabey et al 1982 (8)) used a digitising table for transferring the contours into a computer for comparison. In the development of computer algorithms for matching contours, several problems were found when matching contours of different topology. For example, consider the two contours shown in Figure 5.4. The bold contour crosses the marked grid-line three times, whereas the solid contour only crosses it twice. Which points should be matched?

The solution to the matching problem was to break the lines into segments labelled according to the direction of travel of the line. This relied on specifying a start and end of the line, which for a closed contour would be at an arbitrary grid-line crossed by both curves. Any additional line segments were discarded by matching the direction and order of the contours. Although this solved the

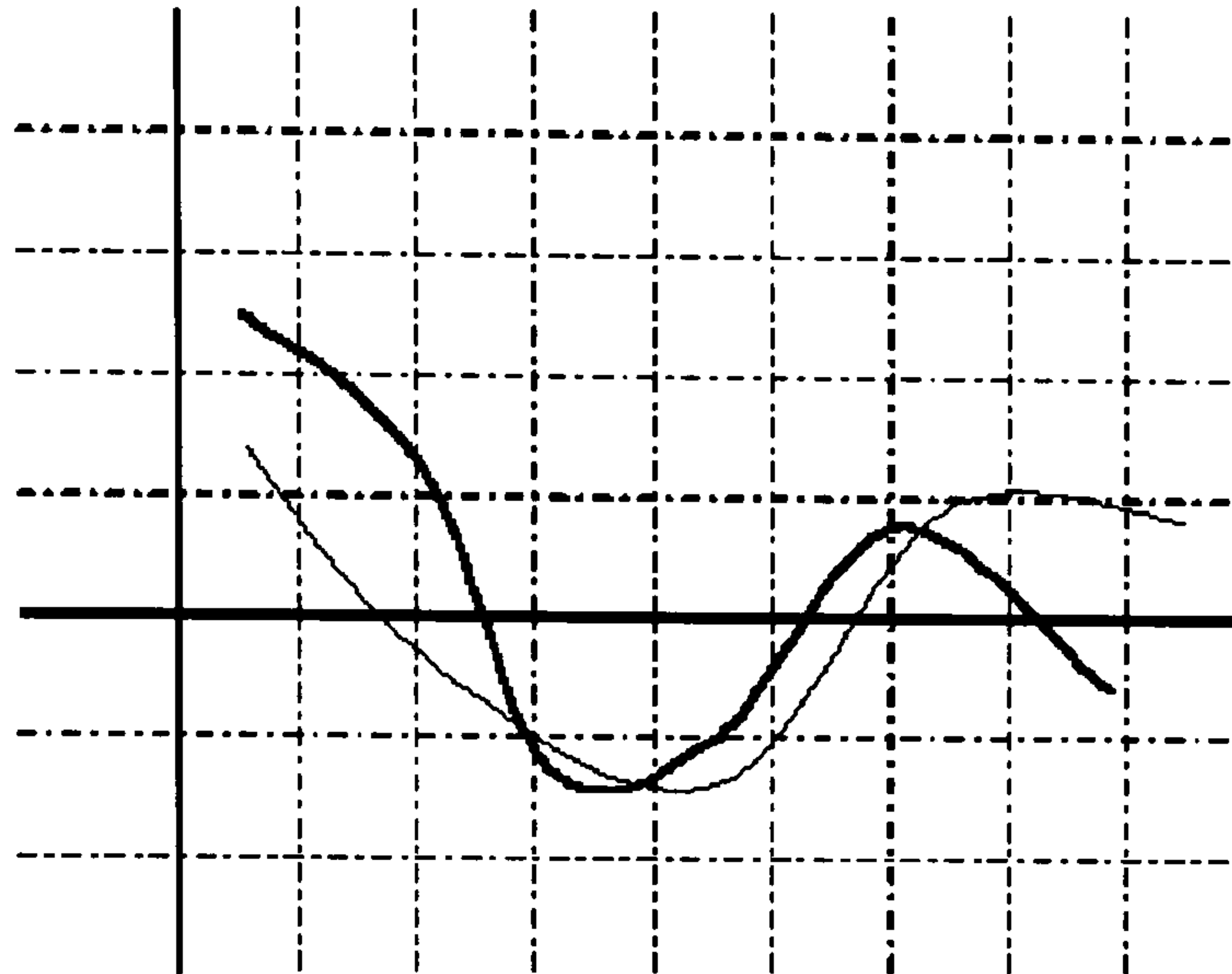


Figure 5.4: Problems with matching lines that cross the same grid line multiple times. The bold contour crosses the bold grid line three times, and the solid contour only crosses it twice. Matching of relevant points is obvious to a human, but a computer needs more information.

problem for the vast majority of contours, it was still possible to get mismatched line segments using this method. Extending this method to surfaces is certainly possible, but is likely to increase rapidly in complexity, especially for surfaces of complex topology.

5.2.2 Depth Averaging

A very simple method for relating two facial scans is to compare depth measurements at each pixel, (x, y) . Unfortunately this method is only able to compare three-dimensional objects in a one-dimensional way. McCance et al (99) (23) (100) (101) use this method for comparison of the facial surface using optically scanned depth data and for the construction of facial average and standard de-

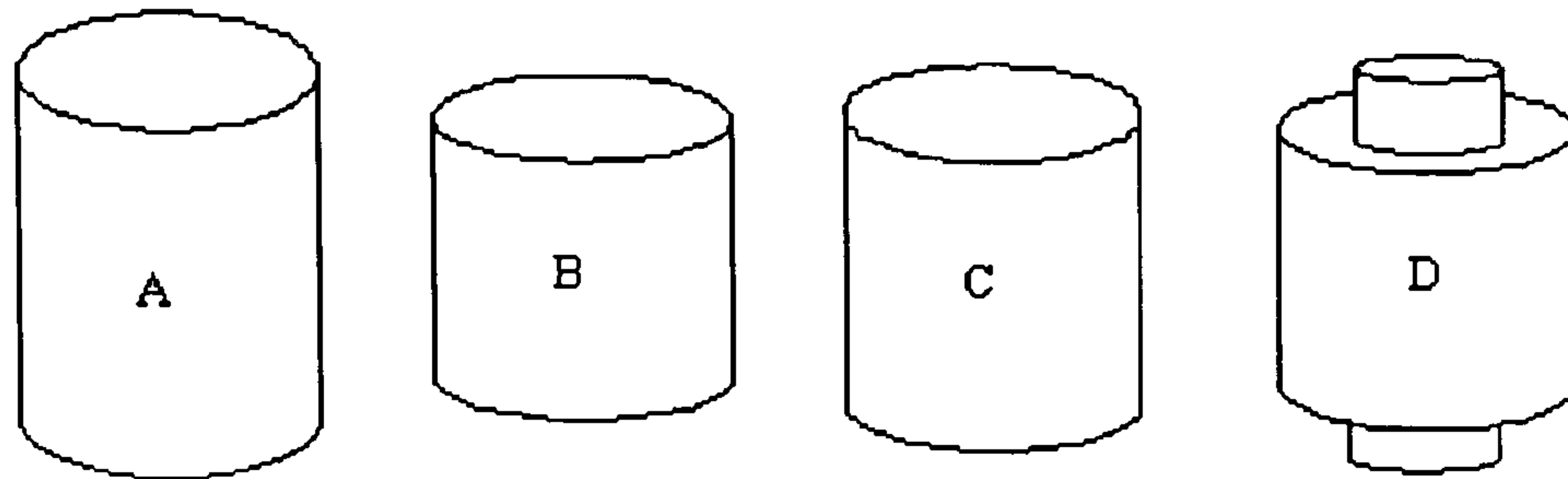


Figure 5.5: Depth-only averaging does not produce the ‘common sense’ shape average in many simple examples. Above the average of two cylinders A and B of equal radius but different height should be C but the cylindrical depth-only average produces D.

viation surfaces. While the average facial images produced look plausible, it is very easy to find examples where averaging radial measurements produces results that are contrary to the common sense solution.

For example, in Figure 5.5 the aim is to find the average of two cylinders with the same radius, R , but different heights H_1 and H_2 . The common sense average of these two is clearly a cylinder radius R , and height $(H_1 + H_2)/2$. Taking a cylindrical laser scan of the registered cylinders and averaging the radial measurements produces a cylinder with a step. The method falls down because the average is only calculated in one dimension. Averaging radial measurements in spherical or polar coordinates may produce more plausible facial averages than averaging along the depth axis of a linear depthmap (because of the somewhat spherical shape of the head) but are equally invalid mathematically.

5.2.3 Feature based warping

In recent years, there has been increasing interest in the area of image warping, the geometrical deformation of images. It is usually combined with cross dissolv-

CHAPTER 5. INTER-PATIENT COMPARISON METHODS

ing for morphing between two images (102) (103) (104) producing visual effects for applications in motion pictures, advertising and music videos. Morphing between two images involves finding a set of intermediate images that change fluidly from one to another in terms of shape and colour. Hence each intermediate image is in a sense a weighted-average of the two source images. These in-between images are found in four stages. First, an animator labels a set of feature primitives, such as points and line segments. Next, the (weighted) average location of these primitives is found. Both images are then warped into this intermediate shape by interpolating the translations from the original positions to the new feature points. Finally the two warped images are cross-dissolved by averaging the colour values at each pixel.

The construction of averages from more than two images has been developed in the field of psychology for the study of facial perception (105) (106) (107). A template of approximately 200 points, at landmarks and around contours, was manually marked on each subject's RGB facial photograph in a database of digital images. The average of these templates was found by calculating the average position of each point in the template. This defines the average two-dimensional shape. To find the average colour at each pixel, each subject's image was warped to this average shape using linear interpolation of the translations between the subject's template and the average template. The average colour at each pixel was then calculated to produce an average facial image.

The first to use image warping in the medical field was Bookstein (108) (96) whose goal was to put the biological warping suggested in D'Arcy Thompson's

CHAPTER 5. INTER-PATIENT COMPARISON METHODS

classic work (109) on a more exact, mathematical footing. Biological landmarks are manually labelled on each medical image under study. The difference between two sets of labelled points is expressed using a warping function known as the Thin-Plate Spline (TPS). This warping method models the two warping surfaces (for the x and y translations) as two thin steel plates, fixed in position at the sample points. The bending energy of the idealised thin plates is minimised to produce the surface that interpolates the translations of the control points across the image. It is essentially the 2D extension of cubic-spline interpolation and so produces smooth, natural deformations.

To minimise the thin-plate bending energy an analytical approach based on constructing a linear combination of radially symmetric logarithmic basis functions was used (110) (111). Measurement of properties of the spline, such as the bending energy and the principal warps, was used as a measure of the difference between the forms. In this way it serves as an extension of the earlier synthetic methods that compared triangles and other Euclidean constructions synthesised between points on biological forms. The method has been extended to three-dimensional images (112) and to points free to slide along piecewise-linear contours(22).

5.2.4 Template Fitting Methods

The feature based warping methods described above are limited to point and simple contour features. For the study of three-dimensional anatomy it is necessary to match not only points but also anatomically identifiable edges and

CHAPTER 5. INTER-PATIENT COMPARISON METHODS

surfaces.

Polygon meshes have long been of interest to the computer graphics community for representing surfaces in a compact form. The fitting of a single, ‘standard’ mesh to a set of surfaces, labels the surfaces with the nodes of the mesh. This allows the comparison of points in the surface, so that displacements, means and standard deviations can be calculated between individual surfaces and across groups. In the medical field, the application of mesh based anatomical modelling has been advanced by Thompson and Toga et al (113) (114) for the study of the cortical (brain) surface. The cortical surface is extracted in parametric form, using an automatic active surface algorithm (115). This uses internal forces in the mesh that preserve smoothness, along with image forces that push the surface towards edges in the volume. A connected system of high-resolution meshes represents the external cortical surface and the sulci (deep folds in the cortical surface), with a separate set of meshes representing the ventricular system. The mean position and covariance matrix of each node in the meshes can be found, and used to compare normal and abnormal anatomy. The method has been extended, using the extracted surfaces to drive a volumetric warp, giving average information throughout the entire volume (116).

Another method for fitting a predefined template to CT images of the human skull has been proposed by Cutting et al (112) (117) and has been extended to MR images of the brain by Dean et al (118). The template is constructed manually using information supplied by an anatomist. To construct an average using

CHAPTER 5. INTER-PATIENT COMPARISON METHODS

the template and a set of surfaces automatically extracted from patient images requires two steps. The first step labels an individual surface using landmarks, ridge and geodesic curves and surface patches identified on the template. (Ridge curves are the most highly curved points on a surface and geodesic curves are the shortest path across a surface between two points.) The second step constructs an average template from the set of adapted templates.

The template is adapted to a single study surface in two stages. First, manually identified landmark points on both the template and the study surface are used to construct a thin-plate spline warp from the template onto the study (Figure 5.6). This brings the template into partial registration with the study, but does not in general register points along the ridge and geodesic contours or surface patches. The ridge curves of the template are fitted locally to the study surface by stepping along the template's ridge curve (Figure 5.7) and finding the intersection of the contour's normal plane at each point. This plane intersects the study surface along a line, which is approximated by a polygon. The equivalent polygon shape on the template is fitted to the study polygon using a least-squares Procrustes method. In the initial stages, no labelling of the surface patches away from ridge curves is performed, so this completes the fitting of the template to a single subject.

In the next stage, an average is created from a set of labelled surfaces. The algorithm proceeds from landmarks, to ridge curves, and finally to surface patches. First each subject's template is warped to the average landmark configuration. Next, to each set of corresponding ridge and geodesic curves a

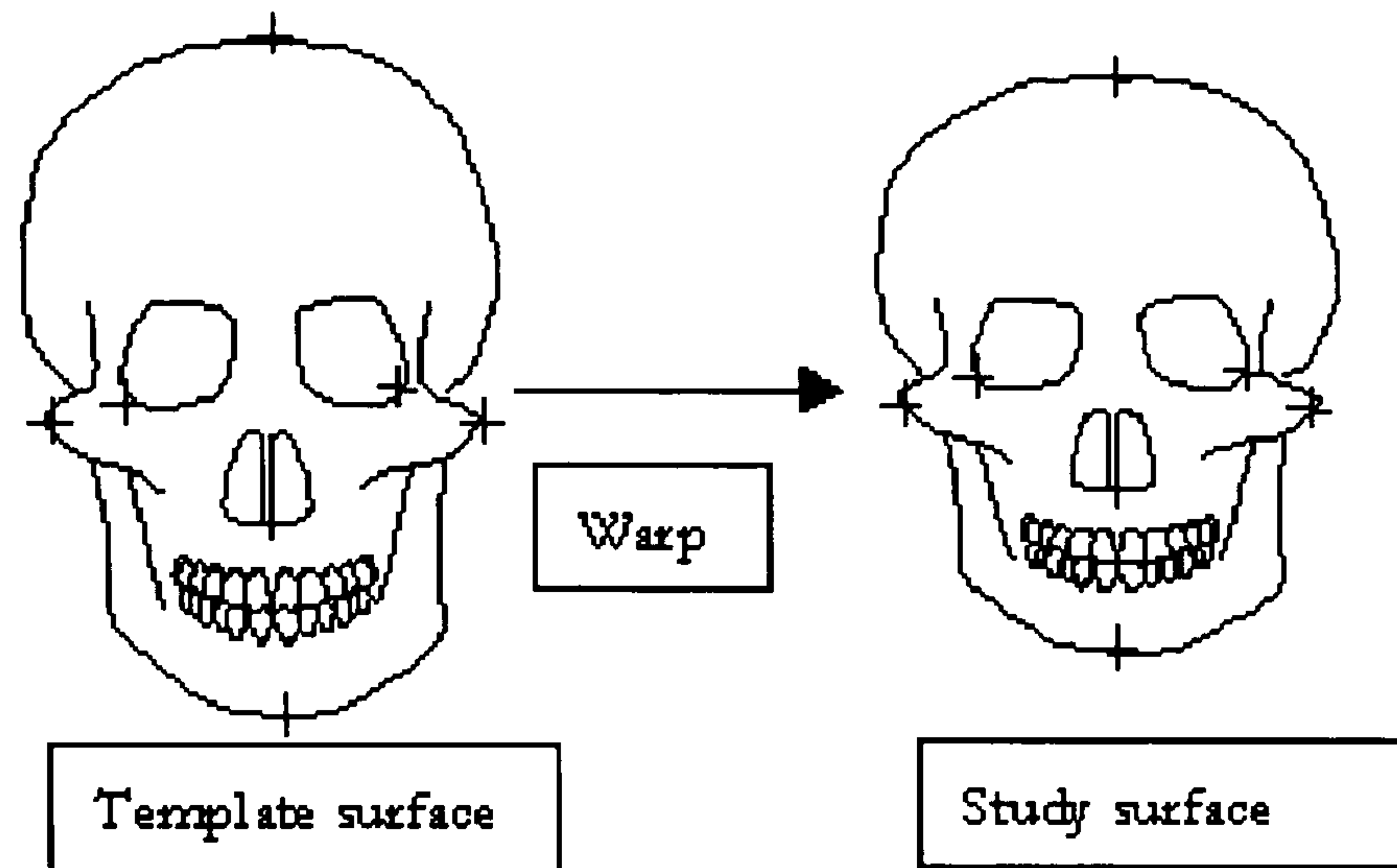


Figure 5.6: Template Matching: Step1. Landmark driven warping of the template onto the study.

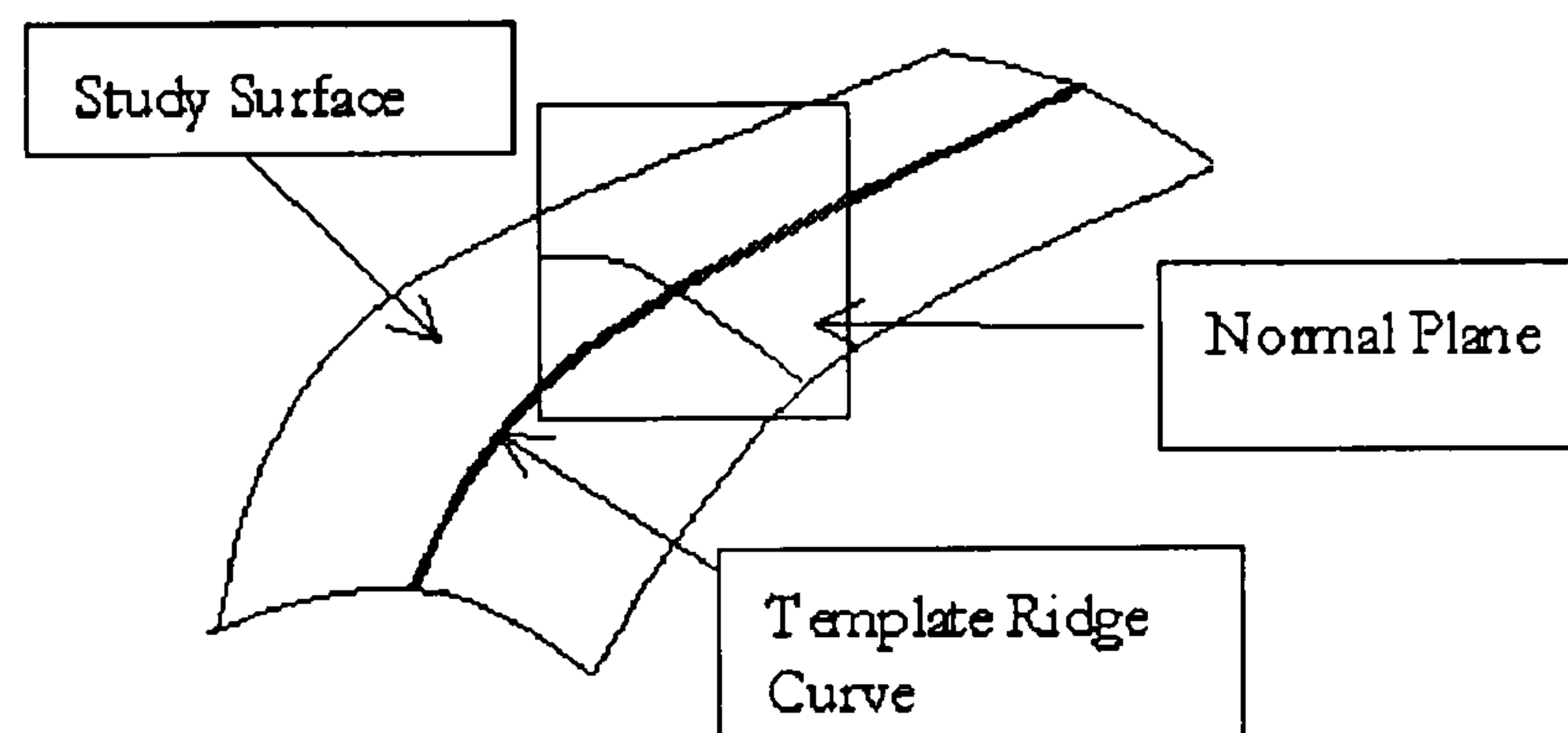


Figure 5.7: Template Matching: Step 2. Translation of the template ridge points onto the study surface by intersection with the normal plane of the template ridge curve.

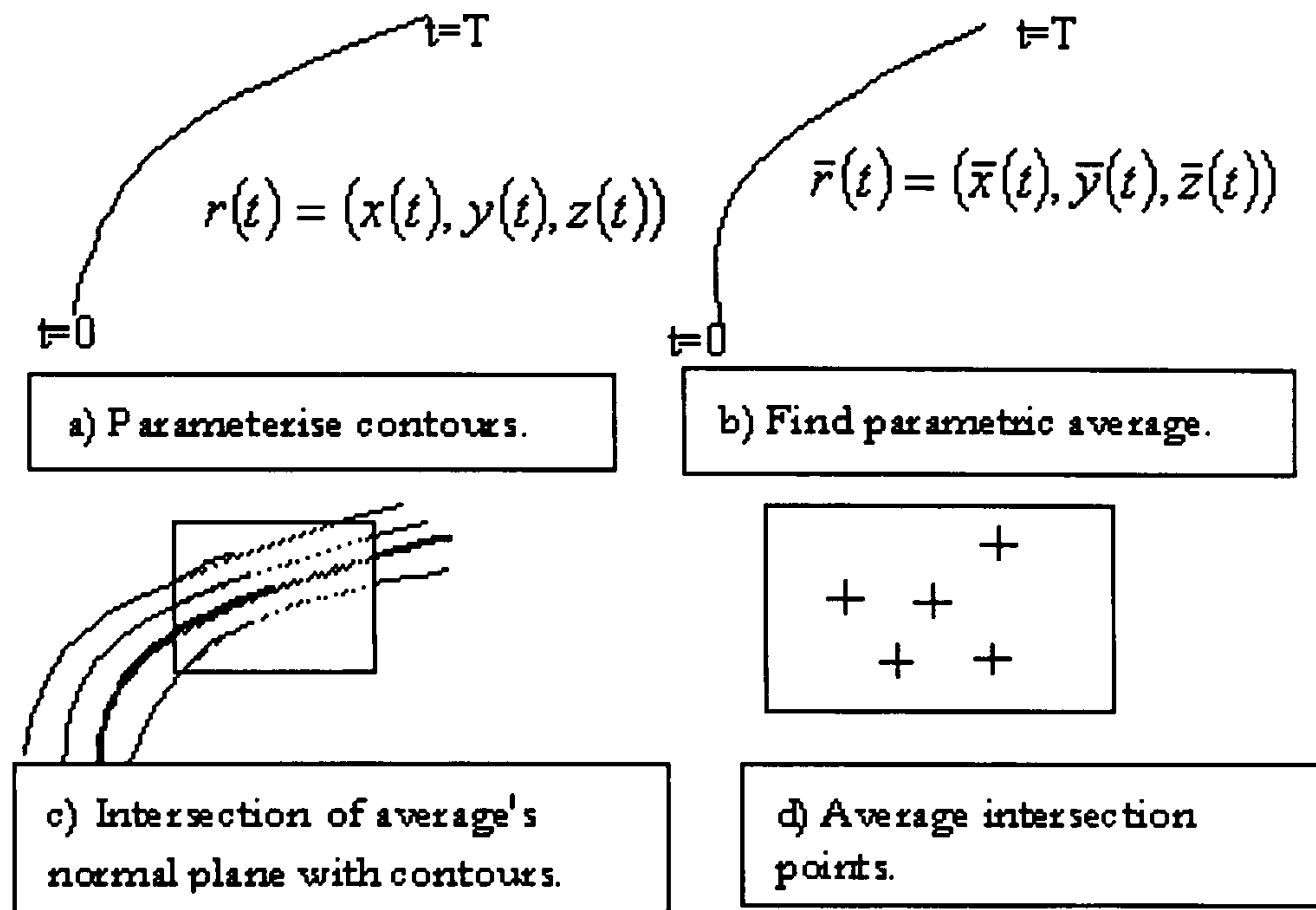


Figure 5.8: Template Matching: Step3. Creation of average ridge lines.

tentative average is created by parameterising the curves by fractions of their arc length. At each point along the tentative average a normal plane exists, and the intersection of this with the set of ridge curves is used to produce a second average (Figure 5.8). Finally, the surface patches are averaged. This requires a parametric description of each surface patch, achieved by constructing a standard Coon's patch (119) over the averaged ridge curves bounding the patch. The average displacement along the direction of each normal vector is then found producing the surface average (Figure 5.9).

The use of template fitting for study of the soft-tissue facial surface has received less attention than for the internal structures of the head. In the medical field, abstracts have appeared very recently that suggest a similar approach to that described above for the facial soft tissue (120). In the field of facial animation, Lee et al (121) adapted a standard face mesh to a radial range-map

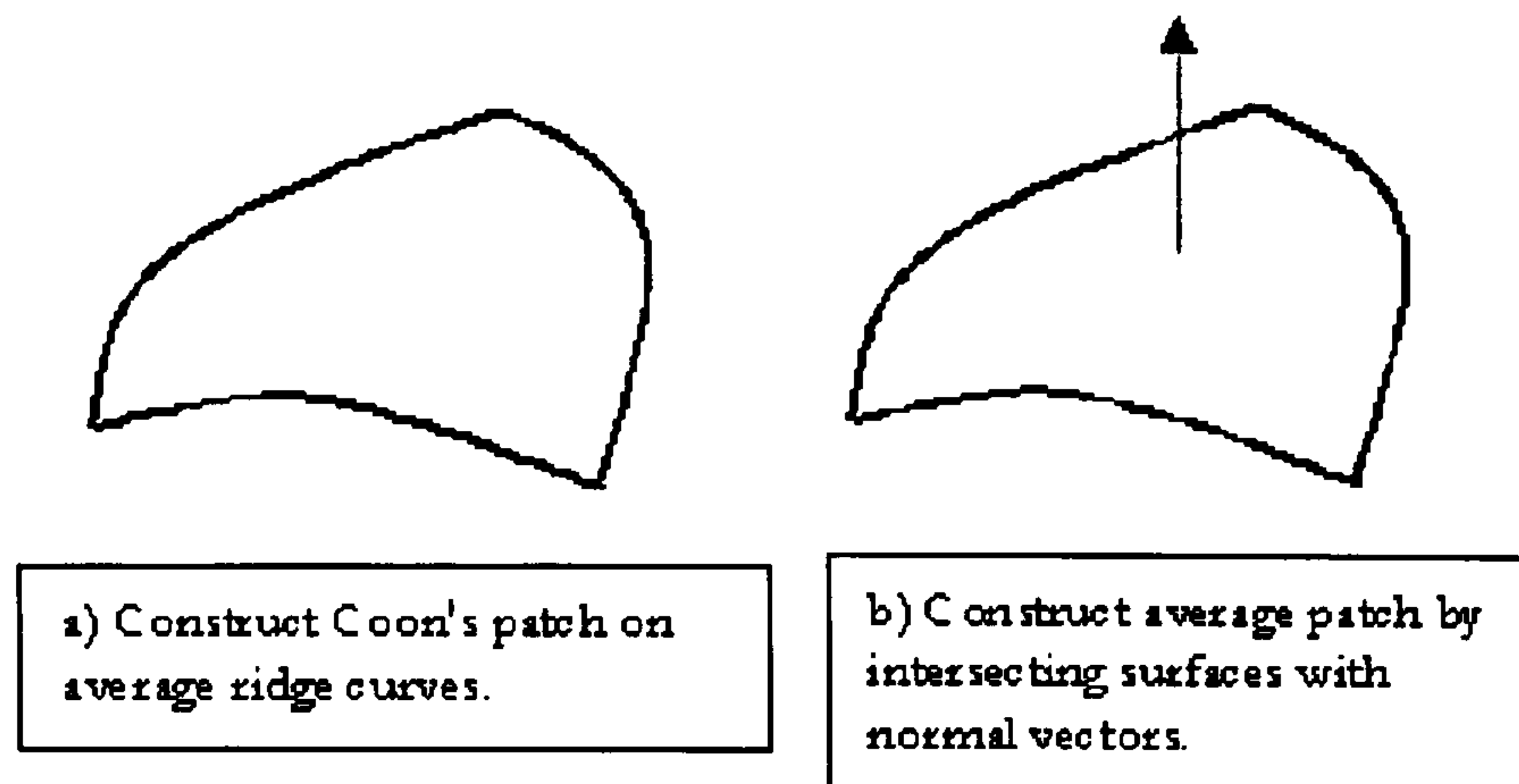


Figure 5.9: Template Matching: Step 4. Construct average surface using Coon's patch on average ridge curves.

and registered RGB image. They used a multi-step method that identified facial features automatically, for example the nose was identified as the highest point in the range-image. For a clean data set, the process could be completed automatically, but for most, some interactive positioning of nodes was required.

5.2.5 Automatic Ridge Line Matching

The methods described above require a pre-defined template, manual or interactive extraction and labelling of landmarks and contours in order to facilitate comparison. Subsol et al (26) (27) have devised a technique for fully automatically matching similar structures in different patients, based on the automatic extraction and non-linear registration of 'crest lines'. At each point on a surface there is a direction in which the surface is curving most and a second direction, orthogonal to the first, in which the surface is curving least. These principal curvatures and the associated principal directions vectors (which are defined mathematically using differential geometry) represent a complete description of a surface's shape. Crest lines are the collection of points that have the greatest

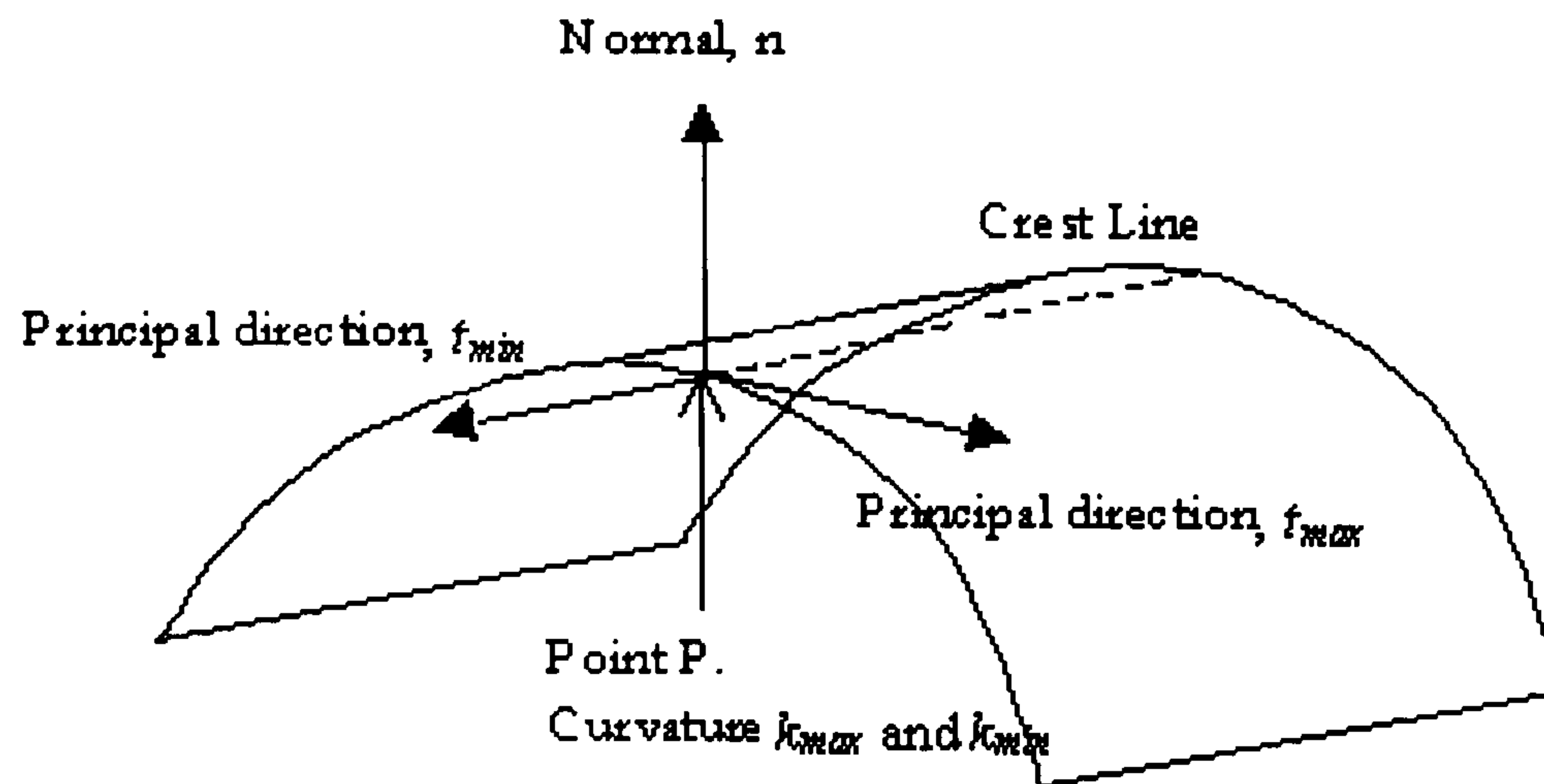


Figure 5.10: Point P is on a crest line if the maximum principal curvature, k_{max} , is a maximum in the principal direction t_{max} .

principal curvature in absolute value in the associated principal direction (Figure 5.10). These correspond closely to what are intuitively considered the most salient lines on a surface. An algorithm called the ‘marching lines’ algorithm (122) (123), closely related to the marching cubes algorithm for surface extraction, was used to automatically find all the crest-lines in a grey-scale volume.

Once the crest-lines had been extracted, the second stage was registration (the method supposes only approximate rigid-body alignment). This was performed automatically using an ‘iterative closest point’ algorithm (24) (25) (Figure 5.11). In registering a study set of crest-lines to a template set, first the nearest point in the template to each point in the study (or vice versa) was found. The direction and connectivity of paired points and lines is used to remove certain points from the matching. Using this subset, a least squares rigid body (translation and rotation) transformation was found and applied to the data. The process was then repeated until a stable position was found. The algorithm was extended to include non-rigid matching. Affine transformations

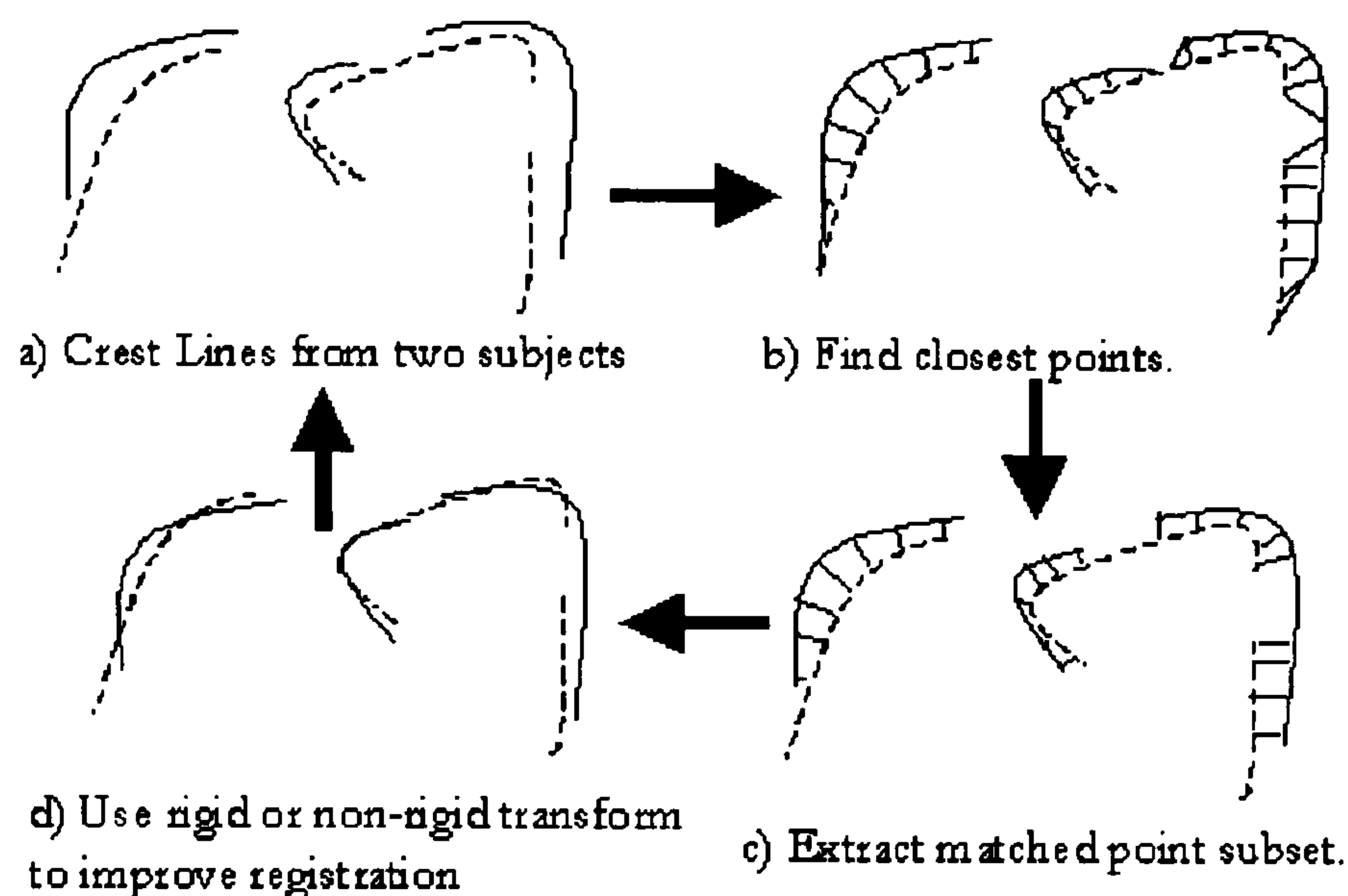


Figure 5.11: The ‘iterative closest point’ algorithm.

(that include scaling and shearing) were followed by least-squares quadratic splines for more natural deformations. A 3-D spline transform was also derived by smoothing the position dependent translation using second order Tikhonov regularisation (124) (smoothing that minimises a particular derivative or derivatives).

After registration, the common features from all the registered sets were extracted. To do this, a topological graph was used, where each node represents a line and each oriented link represents the relation ‘is registered with’ (Figure 5.12). Nodes linked in both directions, and containing at least one line from each set were extracted, as they were thought to represent the subset of features common to all the subjects in the sample.

In order to find average lines from the selected data, modal analysis was used. Given two lines consisting of N matched points each, the difference between them

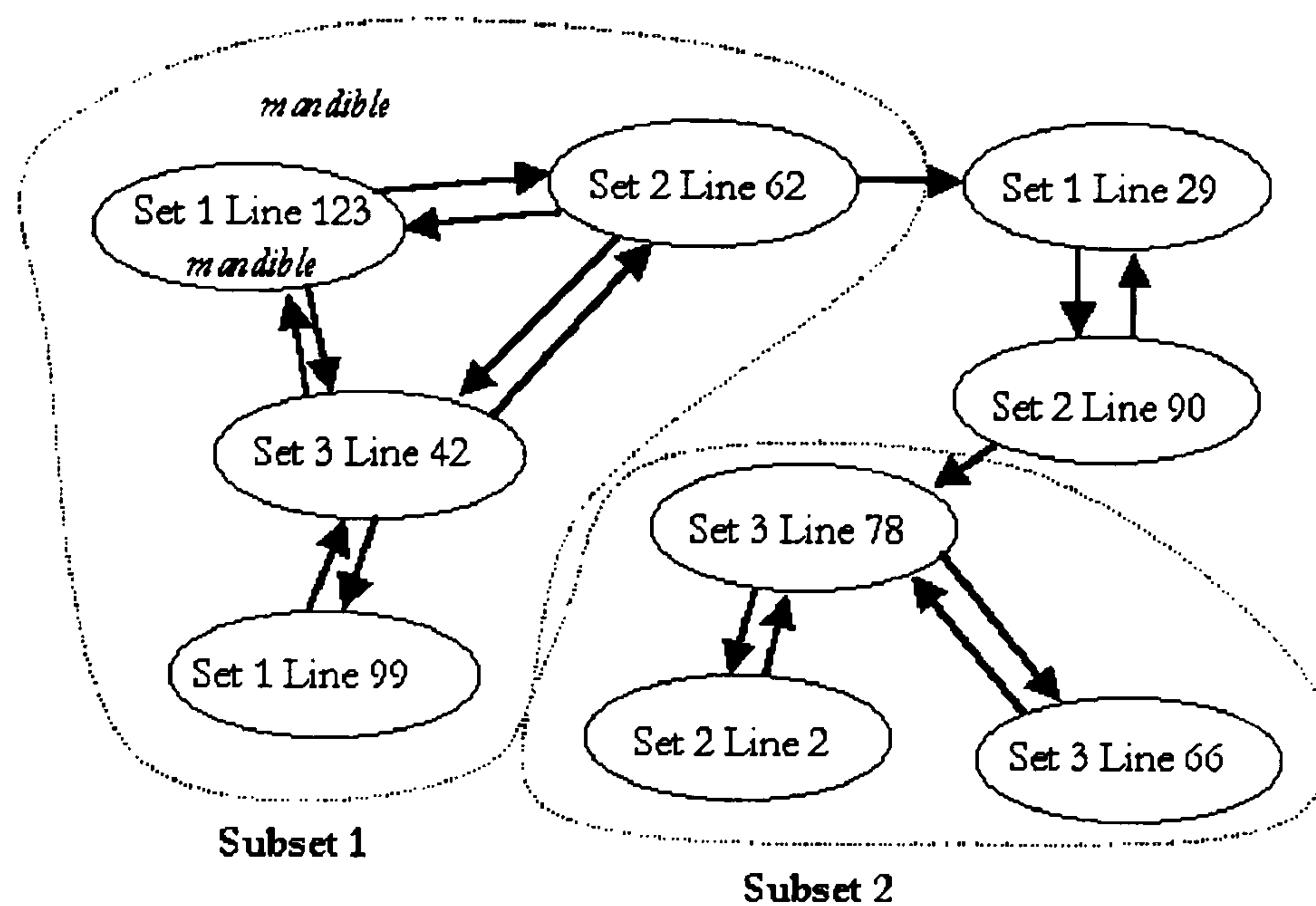


Figure 5.12: Topographical graphs are used for common feature subset extraction

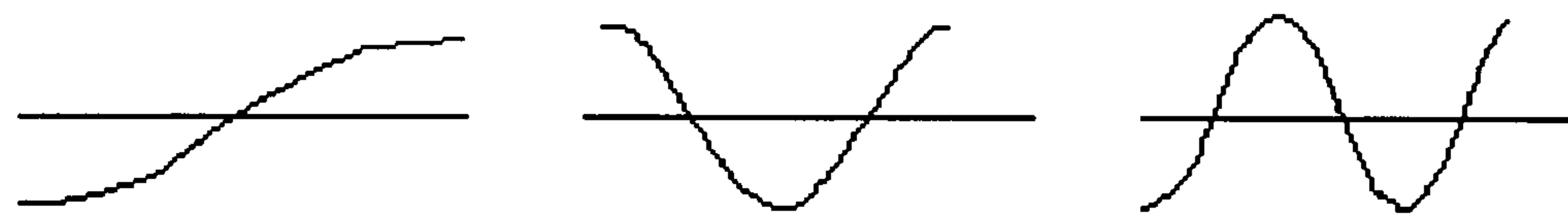


Figure 5.13: Deformations of a straight line created by the first (left), second (middle) and third (right) modes.

can be expressed as a sum of N cosine terms increasing in frequency as shown in Figure 5.13. As with the Fourier series, the sum can be truncated at a number of terms less than N to give a compact description of the deformation. This also tends to smooth the deformation and reduce the effects of noise.

To construct an average, the (truncated) modal transform from the template contour onto each study contour was found and then averaged on a term by term basis. The template was then transformed using the average transformation to give the average contour. The process was repeated with the average replacing

CHAPTER 5. INTER-PATIENT COMPARISON METHODS

the original template to find the standard deviation of the transform.

Once the average anatomical atlas had been found, normal and abnormal anatomy could be compared with it. First the study was registered with the average, and the modal transform between the two found. Comparing the coefficient of each mode to its standard deviation provided an assessment of how abnormal the contour was. An example was given of assessing a Crouzon's disease patient. The deformation of the jaw line was expressed using only five terms, two of which gave notably unusual values. These could be thought of as identifying a typical Crouzon's disease patient.

5.2.6 Intensity Based Matching

Intensity based matching is another automatic method for non-linear image registration. Unlike Subsol's method, it does not involve the extraction of any individual features from the image. Instead, local properties of the grey scale data are used to drive the template into registration with a study image, treating it as an elastic material (125) (126) a viscous fluid (127) or a diffusing gas (128). Although the original algorithms required a massively parallel workstation, recent work has improved the algorithm, achieving similar results on a single processor workstation (129) (130). The main application of this type of automatic warping has been the warping of anatomical atlases into the shape of an individual's anatomy for segmentation, although it has also been used to construct averages.

In order to push the template into the study, the gradient vector of the

CHAPTER 5. INTER-PATIENT COMPARISON METHODS

template is multiplied by grey scale difference between the two images. This produces a force at each point in the template. These forces are largest at sharp edges in the template where the two images differ most in intensity. At each time step the template is deformed, obeying the diffusive, elastic or viscous fluid model. The algorithm is halted when a convergence criterion such as the largest image force falling below a threshold is met. Solving the partial differential equations for elasticity or fluid deformation requires many small time steps and there are a large number of equations to solve per time step. This accounts for the slow convergence of this method.

A similar method has been put forward by Collins et al (131) but they do not use a physics based model of the material. Instead, the deformation field is built up by stepping through the target volume in a 3D grid pattern. At each node in the volume the translation is found that achieves local registration. The process is applied iteratively in a multi-scale hierarchy, with image blurring and grid size reduced between iterations, thus refining the fit.

To ensure accurate registration when using one of these automatic methods, the two images must have the same topology and a similar orientation. Usually, the prior use of rigid body registration and the similar topology between different human subjects leads to very plausible results. In order to constrain the warp further, secondary characteristics such as the surface curvature have been used (132) with limited success.

5.3 Discussion

The original morphanalytic solution was designed for constructing average outlines and contours in two dimensions. As a result it does not guarantee to match identified landmarks and would be difficult to extend to three dimensions. Comparing radial depth measurements does not relate anatomical landmarks and can lead to average three-dimensional shapes that are counter-intuitive as described earlier.

The warping methods all attempt to perform essentially the same task: to label a set of anatomical contours, surfaces or volumes, allowing the comparison of individual points in the images and hence the construction of meaningful averages. The methods represent different compromises between automation and interaction. Automation carries the risk of incorrectly matched features and frequently large computational requirements. High levels of user interaction can be laborious and time consuming and can lead to badly chosen or badly extracted features.

Assessing the validity of the different labelling procedures is not a simple task. The problem is in defining what is meant by a 'good fit' without biasing towards any particular method. For example, if the error measurement is between corresponding landmarks, then a landmark driven spline will give a zero error measurement. Alternatively, if the error is measured in terms of the displacement between ridge-lines, then the ridge line matching method used to measure the error will give the best results.

Thirion, Subsol and Dean (133) have presented a method for cross validating

CHAPTER 5. INTER-PATIENT COMPARISON METHODS

different inter-patient matching methods. These authors represent three of the methods described in the previous sections, intensity matching, automatic crest line matching and template ridge curve matching respectively. They define a distance metric between matching methods by interpolating the translation between two images across the image using a B-spline, then subtracting the translations on a pixel by pixel basis and averaging. The averaging is restricted to a subset of the total image, using only crest lines, crest lines with high curvatures or points in a template defined by an anatomist.

They also assess the error in creating averages using the three different techniques. The averages are constructed by transforming one image into each of the others using one of the techniques. The average transformation is then found, and applied to the initial image to produce the average. To assess the error in constructing the average, the average transformations are compared between matching methods using the same distance measure as for the single image pair.

The results suggest that no particular method gives inconsistent results with respect to the other two. Some of the differences are relatively large, approaching an average of 1cm on the crest lines. The study was performed on a set of anatomically normal skull CT scans. The question remains as to whether similar accuracy can be achieved when comparing normal with abnormal anatomy. Further problems may arise when comparing soft rather than hard tissues. For example, comparing someone with a double chin to someone with a slimmer face may produce incorrectly matched ridge curves around the jaw line.

5.4 Conclusions

The warping methods presented in the literature for inter-patient matching provide a choice between fully automatic and highly interactive schemes. The close relationship between geometrically defined properties of an image and anatomical features indicate that a high degree of automation should be possible. Conversely, the possibility of incorrectly matched features, particularly when considering abnormal anatomy suggests that a degree of interaction is desirable. This could be in the form of suggestions supplied by a user or the opportunity for post registration correction of mismatched features. From the literature there appears to be no clear advantage to any one of these methods. Therefore, for the study of the facial surface *further experimentation is required to select the most suitable method*, as described in subsequent chapters.

Chapter 6

Image Processing Methods

6.1 Introduction

In this chapter the mathematical and image processing techniques required for the experimentation embodied in the following chapters are introduced. These include differential geometry, contour extraction, interpolation and warping. For the problems of interpolation and image warping, new methods are presented and compared with the established methods.

6.2 Basic Image Processing

6.2.1 Introduction

A digital image is a two-dimensional array of dots called picture elements or pixels. Each pixel will have one or more value(s) associated with it that repre-

CHAPTER 6. IMAGE PROCESSING METHODS

sents the information contained in that pixel. For a greyscale image the pixel will have only one value corresponding to the brightness of the pixel. In a colour image there will be three values corresponding to the brightness of the three primary colours, red, green and blue (RGB). For the calibrated laser depth data, the pixel values represent the height, x , of the point (y, z) from the yz -plane.

6.2.2 Convolution and Image Filtering

Convolution is the rolling together of two functions. It is defined for two continuous, one-dimensional functions f and g as the function

$$f * g(x) = \int_{-\infty}^{\infty} f(u - x) g(u) du \quad (6.1)$$

In two dimensions this becomes

$$f * g(x, y) = \int_{-\infty}^{\infty} \int_{-\infty}^{\infty} f(u - x, v - y) g(u, v) dudv \quad (6.2)$$

For discrete functions the integral becomes a summation i.e. for one-dimensional functions

$$f * g(n) = \sum_{i=-a}^b f(n - i) g(i) \quad (6.3)$$

and for two dimensional functions such as digital images

$$f * g(n, m) = \sum_{j=-c}^d \sum_{i=-a}^b f(n - i, m - j) g(i, j) \quad (6.4)$$

CHAPTER 6. IMAGE PROCESSING METHODS

When a digital image $f(x, y)$ is filtered, it is usually performed by convolution with a separable function $g(x, y)$ that has finite support. This means that the function is only non-zero for a small range of pixels, so a , b , c , and d are finite in equation 6.4.

Different filters have different effects on an image. For example, convolution with a filter with an integral of 1 such as $\{0.1, 0.25, 0.3, 0.25, 0.1\}$ will perform some kind of smoothing operation, blurring an image. Alternatively a filter with an integral of zero, such as $\{1, -4, 6, -4, 1\}$ will perform a derivative operation, in this case a fourth derivative finite difference approximation.

6.2.3 Regularisation

Many common computational problems are ill-posed or under-defined in some sense. For discrete functions such as digital images, calculation of derivatives is an ill-posed problem. If a digital signal is converted directly into a continuous function, the derivative will be zero inside each pixel and infinite between pixels. This is clearly not a very useful solution. The usual solution is to convolve the original signal with the sampled derivative of a smooth filter (134). In this way the derivatives of any integrable function are operationally defined and well-posed.

In computational vision the choice of smoothing filter is usually based on Gaussian scale space, regularisation or edge detection. Gaussian scale space (135) (136) (137) is the space of functions each of which is a copy of the original function blurred to a different scale. The blurring filters are all dilations of

CHAPTER 6. IMAGE PROCESSING METHODS

a Gaussian filter, which ensures that variations in the coarse scale images are caused by variations at finer scales. Because the Gaussian function is infinitely differentiable, all derivatives of the function are well defined.

Regularisation theory (124) (138) looks for a differentiable function, which is close to the original function but with one or more derivatives minimised. These two conflicting requirements lead to a functional minimisation approach. For example, to find an approximation to the first derivative of a function $f(x)$ the derivative of the function $g(x)$ that minimises

$$\int (g(x) - f(x))^2 + \lambda \left(\frac{dg(x)}{dx} \right)^2 dx \quad (6.5)$$

is found. The parameter λ controls the relative influence of the original function and the derivative term. This is minimised by taking the variational derivative (i.e. differentiating and treating operators as constants) of this with respect to g and setting the result to zero, i.e.

$$g(x) + \lambda \frac{d^2 g}{dx^2} = f(x) \quad (6.6)$$

For discrete functions the derivative term is replaced with a finite difference filter i.e. $\frac{\delta^2}{\delta x^2} \approx \{-1, 2, -1\}$. This allows equation 6.6 to be written in matrix form as

$$(\mathbf{I} + \lambda \mathbf{K}) \mathbf{g} = \mathbf{f} \quad (6.7)$$

where \mathbf{I} is the identity matrix and \mathbf{K} is the tridiagonal regularisation matrix

CHAPTER 6. IMAGE PROCESSING METHODS

given by

$$\mathbf{K} = \begin{bmatrix} \ddots & & & & \\ & -\lambda & 2\lambda & -\lambda & \\ & & -\lambda & 2\lambda & -\lambda \\ & & & -\lambda & 2\lambda & -\lambda \\ & & & & \ddots \end{bmatrix} \quad (6.8)$$

The function \mathbf{g} can be found by backwards/forwards Gaussian elimination of the stiffness matrix, which for this regular matrix is equivalent to backwards/forwards recursive filtering. Hence regularisation can be implemented using recursive filters (139), which are chosen to optimise a particular derivative or derivatives.

Edge detection requires the choice of filter to guarantee a good signal to noise ratio, localisation, and uniqueness of the detected edge. Frequently the smoothing filter is derived from a piecewise-smooth polynomial spline curve with a finite number of derivatives, such as a cubic spline. This gives good edge localisation and can be implemented with finite support filters for efficiency.

6.3 Differential Geometry

6.3.1 Introduction

For laser-range data, important image features do not necessarily lie at edges (i.e. sudden changes in depth) but at the points of maximum positive and negative curvature, which correspond to the ridges and valleys of the surface



Figure 6.1: The positive curvature (red) and negative curvature (green) of a facial depthmap.

respectively (Figure 6.1). Surface curvature has the desirable property of being view independent, unlike image gradients. Curvature has been widely used to study the shape of craniofacial surfaces in range data (171) (172) (173) (174) and 3D volumetric data (26) (27). In this section a brief review of the basic concepts as embodied in standard texts such as (175) is presented.

6.3.2 Methods

Considering a surface in parametric form, given by $r = r(u, v)$, the first derivatives are denoted by r_u and r_v , and the second derivatives are denoted by r_{uu} , r_{vv} and r_{uv} . Using these derivatives, intrinsic properties of the surface that are independent of the parameterisation can be derived. The unit surface normal is defined as

CHAPTER 6. IMAGE PROCESSING METHODS

$$\mathbf{n} = \frac{\mathbf{r}_u \times \mathbf{r}_v}{|\mathbf{r}_u \times \mathbf{r}_v|} \quad (6.9)$$

The infinitesimal distance, δs , between two points (u, v) and $(u + \delta u, v + \delta v)$ is given by,

$$\delta s^2 = E\delta u^2 + 2F\delta u\delta v + G\delta v^2 \quad (6.10)$$

where $E = \mathbf{r}_u \cdot \mathbf{r}_u$, $F = \mathbf{r}_u \cdot \mathbf{r}_v$ and $G = \mathbf{r}_v \cdot \mathbf{r}_v$. This equation is known as the first fundamental form of the surface. Integrating δs along a path $(u(t), v(t))$ between two points gives the distance along that path on the surface.

The infinitesimal distance δs between neighbouring points is measured in the tangent plane at the point (u, v) . The perpendicular distance, δh , from the tangent plane to the point $(u + \delta u, v + \delta v)$ is given by the second fundamental form of the surface,

$$\delta h^2 = L\delta u^2 + 2M\delta u\delta v + N\delta v^2 \quad (6.11)$$

where $L = \mathbf{n} \cdot \mathbf{r}_{uu}$, $M = \mathbf{n} \cdot \mathbf{r}_{uv}$ and $N = \mathbf{n} \cdot \mathbf{r}_{vv}$. In terms of the first and second fundamental form of the surface the curvature k in the direction (u, v) is given by

$$k = -\frac{\delta h^2}{\delta s^2} = -\frac{Lu^2 + 2Muv + Nv^2}{Eu^2 + 2Fuv + Gv^2} \quad (6.12)$$

and the radius of curvature is $1/k$. The sign convention ensures that a con-

CHAPTER 6. IMAGE PROCESSING METHODS

vex surface has positive curvature and a concave surface negative curvature.

The direction (u, v) in which the curvature obtains extreme values occurs when

$dk/du = 0$ and $dk/dv = 0$ i.e. when,

$$(L + kE)u + (M + kF)v = 0 \quad (6.13)$$

and

$$(M + kF)u + (N + kG)v = 0 \quad (6.14)$$

Solving for k leads to the quadratic equation

$$k^2 - 2Hk + K = 0 \quad (6.15)$$

where K is the Gaussian curvature and H is the mean curvature of the surface defined by

$$K = \frac{LN - M^2}{EG - F^2} \quad (6.16)$$

and

$$H = \frac{2FM - (EN + GL)}{2(EG - F^2)} \quad (6.17)$$

In 1760 Euler discovered that there is always a direction on a surface in which the surface curves least and another direction, orthogonal to the first, in which it curves most. These are given by the equations

CHAPTER 6. IMAGE PROCESSING METHODS

$$k_{max} = H + \sqrt{H^2 - K} \quad (6.18)$$

and

$$k_{min} = H - \sqrt{H^2 - K} \quad (6.19)$$

For the particular case of laser range data the parametric surface is most simply described by,

$$\mathbf{r}(u, v) = \mathbf{r}(x, y) = (x, y, f(x, y)) \quad (6.20)$$

The derivatives are then

$$\begin{aligned} \mathbf{r}_u &= (1, 0, f_x) & \mathbf{r}_v &= (0, 1, f_y) \\ \mathbf{r}_{uu} &= (0, 0, f_{xx}) & \mathbf{r}_{uv} &= (0, 0, f_{xy}) & \mathbf{r}_{vv} &= (0, 0, f_{yy}) \end{aligned} \quad (6.21)$$

The first and second fundamental forms of the surface are given in terms of the variables,

$$\begin{aligned} E &= 1 + f_x^2 & F &= f_x f_y & G &= 1 + f_y^2 \\ L &= \frac{f_{xx}}{1 + f_x^2 + f_y^2} & M &= \frac{f_{xy}}{1 + f_x^2 + f_y^2} & N &= \frac{f_{yy}}{1 + f_x^2 + f_y^2} \end{aligned} \quad (6.22)$$

Substituting these into the equations for H and K gives

$$H(x, y) = \frac{(1 + f_y^2) f_{xx} + (1 + f_x^2) f_{yy} - 2 f_x f_y f_{xy}}{2 (1 + f_x^2 + f_y^2)^{3/2}} \quad (6.23)$$

$$K(x, y) = \frac{f_{xx}f_{yy} - f_{xy}^2}{(1 + f_x^2 + f_y^2)} \quad (6.24)$$

Two approaches have been suggested for calculating these values. Besl and Jain (176) used convolution with finite support filters to approximate the derivatives, but a poor choice of derivative filters caused incorrect classification of surface curvature, particularly near sharply varying regions of the range data. Yokoya and Levine (177) fitted local biquadratic surface patches to the range data using a least-squares method that was later enhanced by Coombes (173) to include variable patch size. In this work the curvature derivatives are approximated using regularisation with recursive filters (139), which is more efficient than patch fitting and provides a more accurate estimation of the derivatives than the filters of Besl and Jain.

The principal curvatures k_{max} and k_{min} can be calculated directly along with the associated principal directions (u, v) denoted by t_{max} and t_{min} respectively. The points in which the principal curvature obtains a maximum value in the direction of the associated principal direction are the curvature extrema. These can be extracted directly in the form of a binary edge image in the same way as the gradient magnitude. Alternatively they can be segmented as contours using the principal curvature image in place of the gradient magnitude image in one of the contour extraction routines described in the next section.

6.4 Edge detection and contour extraction

6.4.1 Introduction

Edges in an image are features where the gradient obtains a maximum value in the direction of the gradient vector. The gradient of an image $f(x, y)$ is the vector valued function given by

$$\nabla f(x, y) = \left(\frac{\partial f}{\partial x}, \frac{\partial f}{\partial y} \right) \quad (6.25)$$

The gradient can be found by convolution with a smoothing filter followed by a finite difference filter. The gradient maxima can then be found locally by testing each pixel's gradient magnitude against its neighbours in the direction of the gradient vector (163). This kind of simple edge detection creates a binary edge image from the image gradient vectors. The problem with edge detectors of this sort is that the edges found do not necessarily correspond to the boundaries of objects. Because the edge detection operators are applied to only a small area around each pixel, the detected edges cannot incorporate larger scale information regarding the desired contour and are easily corrupted by noise. Using a lowpass smoothing operator and placing a lower limit on the magnitude of the detected edges can help to suppress noise and the detection of small edges.

Image edges are generally localised along contours at object boundaries. Extraction of a particular contour rather than a set of unrelated edge points requires some higher level knowledge of the desired contour. This could be given in terms of an initial guess, or the start and end points of the contour.

CHAPTER 6. IMAGE PROCESSING METHODS

Several methods have been proposed for contour extraction, they generally start by highlighting the image edges using filtering operations. For example the gradient magnitude is often used in contour extraction. Once the desired image features have been highlighted they need to be extracted.

6.4.2 Active Contours Methods

Several methods have been proposed for extracting edges based on modelling the contour as a chain of connected nodes (164) (165). The most popular of these are active contours or ‘snakes’ (166). Snakes are energy minimizing splines that are attracted towards strong image features while their bending energy and tension are minimised. The contour is modelled as a set of nodes connected by stiff springs. An initial approximation of the contour is supplied by the user and iterated under external and internal forces until a minimum is found. The external image produced forces are given by the gradient of the edge potential function (the gradient magnitude or maximum or minimum curvature) $P(x, y)$,

$$\mathbf{f}_i = p \nabla P(x, y) + \mathbf{f}_i^u \quad (6.26)$$

Here p is a user defined value that controls the strength of the image forces and \mathbf{f}_i^u are optional user forces that allow the user to interact with the contour. The internal contour forces are determined by the tension and the stiffness. The extension e_i at node i depends on the separation of the nodes, i.e.

$$e_i = |\mathbf{x}_{i+1} - \mathbf{x}_i| - l_i \quad (6.27)$$

CHAPTER 6. IMAGE PROCESSING METHODS

where l_i is the spring's natural length. This extension produces a tension force α_i ,

$$\alpha_i = \frac{a_i e_i}{|\mathbf{r}_i|} \hat{\mathbf{r}}_i \quad (6.28)$$

The relative influence of the tension force is controlled by the variables a_i . The stiffness or bending energy along the contour can be approximated by a five point finite difference method,

$$\beta_i = b_{i+1} (\mathbf{x}_{i+2} - 2\mathbf{x}_{i+1} + \mathbf{x}_i) - 2b_i (\mathbf{x}_{i+1} - 2\mathbf{x}_i + \mathbf{x}_{i-1}) + b_{i-1} (\mathbf{x}_i - 2\mathbf{x}_{i-1} + \mathbf{x}_{i-2}) \quad (6.29)$$

where b_i is the rigidity variable. The entire system is governed by the first order dynamic system

$$\gamma \frac{d\mathbf{x}_i}{dt} + \alpha_i + \beta_i = \mathbf{f}_i \quad (6.30)$$

where γ is a velocity proportional damping coefficient. This can be integrated through time using a numerical method such as the semi-implicit Euler method or a finite element approach. Using a forward finite difference approximation for the derivative,

$$\frac{d\mathbf{x}_i}{dt} \approx \frac{\mathbf{x}_i^{t+\Delta t} - \mathbf{x}_i^t}{\Delta t} \quad (6.31)$$

CHAPTER 6. IMAGE PROCESSING METHODS

and evaluating the linear terms in \mathbf{x}_i at time $t + \Delta t$ and the nonlinear terms at time t leads to a pentadiagonal system of equations,

$$\frac{\gamma}{\Delta t} \mathbf{x}_i^{t+\Delta t} + \beta_i^{t+\Delta t} = \frac{\gamma}{\Delta t} \mathbf{x}_i^t - \alpha_i^t + \mathbf{f}_i^t \quad (6.32)$$

for the new node positions $\mathbf{x}_i^{t+\Delta t}$ in terms of the old node positions \mathbf{x}_i^t . The left hand side of this equation can be represented by a matrix that is time independent. Therefore this matrix can be inverted once at the start and used to efficiently multiply the new right hand side at each time step. This makes snakes a fast and flexible method for contour extraction.

6.4.3 Bayesian Methods

Another approach to the problem of contour extraction is to use probabilistic methods (167). A class of contours is defined, usually using a compact line description such as a Fourier or superquadric model. Each possible contour template t is assigned a probability $Pr(t)$, either by training using a set of contours or by estimating the probabilities from a single initial template. The probability of a particular image i given a particular contour template t , $Pr(i|t)$, is calculated by assuming that the image is a noise corrupted version of the template. Using these two pieces of information, the probability of the template given an image, $Pr(t|i)$, is calculated using Bayes rule,

$$Pr(t|i) = \frac{Pr(i|t) Pr(t)}{Pr(i)} \quad (6.33)$$

CHAPTER 6. IMAGE PROCESSING METHODS

where the probability of the image, $Pr(i)$, is taken as a constant. This probability (after some mathematical manipulation) is maximised over t using a standard nonlinear optimisation routine such as continuous gradient ascent or a nonlinear conjugate gradient algorithm (13).

6.4.4 Graph Searching Methods

Another class of edge extraction methods views the problem as one of searching for the most optimal route through a graph represented by the image. The ‘cost’ of traveling from one pixel to the next through the image is minimised at each point by adjusting the position of the contour points. The cost between two image points is calculated from edge detection filtering so that traveling along sharp edges (motorways) will be cheapest and traveling across flat image areas (cross country) is most expensive. Early methods performed this optimization along the contour given an initial estimate of the curve (168) (169). More recently a method has been devised (170) that does not require an initial estimate of the curve but only an initial seed point. From a user-selected point a cost wavefront expands. At each iteration the cheapest point to reach from the seed is expanded to its neighbouring pixels outside the wavefront to create a new wavefront. Within the wavefront the cost from the seed point is analogous to a ditch, with the lowest point at the seed. Selecting a destination point is like placing a ball at a point on the walls of this ditch and allowing it to roll down the slope to the bottom. This allows fast interactive selection of the contour, without requiring an initial guess. The destination point can be moved at

CHAPTER 6. IMAGE PROCESSING METHODS

interactive rates until the desired edge is selected.

6.4.5 Choice of Method

In the current study snakes have been employed to assist in the edge extraction. Snakes allow a single template to be interactively adapted to many different facial images, whereas graph searching methods are more suited to segmenting a single image in a unique way. Snakes are fast and easy to implement, being considerably less complex than probabilistic approaches.

6.5 Two-dimensional Interpolation

6.5.1 Introduction

Interpolation of scattered data involves finding a function that passes through a given, finite set of discrete points (140) (141) (142). Clearly, there exists an infinite number of functions that could satisfy this condition and so the problem is ill-defined. Further information is required, usually in the form of a model of the expected solution.

6.5.2 Energy minimisation methods

Regularisation is one of the best known interpolation theories (143) (144) (145) (146) (147) (148) which leads to an energy minimisation problem. For one-dimensional interpolation, the interpolated curve is expected to follow the shape that a thin rigid beam would adopt if fixed at the control points. Minimising

CHAPTER 6. IMAGE PROCESSING METHODS

the bending energy of a theoretical thin beam leads to the classical cubic spline interpolation. For the two-dimensional interpolation problem the surface is expected to take the shape of a thin steel plate fixed in position at the control points. The resulting function $f(x, y)$ will minimise the integral square bending energy of the surface given by

$$\int \int_{\mathbb{R}^2} \left(\frac{\partial^2 f}{\partial x^2} \right)^2 + 2 \left(\frac{\partial^2 f}{\partial x \partial y} \right)^2 + \left(\frac{\partial^2 f}{\partial y^2} \right)^2 dx dy \quad (6.34)$$

while satisfying the border constraints. Taking the variational derivative of this function gives the biharmonic equation

$$\Delta^2 f \equiv \left(\frac{\partial^2}{\partial x^2} + \frac{\partial^2}{\partial y^2} \right)^2 f \propto \delta(x, y) \quad (6.35)$$

where $\delta(x, y)$ is the Dirac delta function, which takes the value 1 at $(0, 0)$ and is zero elsewhere. This equation has a solution in terms of the functions (110) (111)

$$U(r) = -r^2 \log r^2 \quad (6.36)$$

where $r^2 = x^2 + y^2$ is the distance of the point from the origin. The interpolant is a linear combination of these radial logarithmic basis functions $U(|r_i - (x, y)|)$ and linear (affine) terms that satisfies the border constraints.

The analytical solution to thin-plate spline interpolation has proved popular for image warping in the medical imaging literature (108) because it produces apparently ‘natural’ deformations with only a few control points. The method is

CHAPTER 6. IMAGE PROCESSING METHODS

fast for a small number of constraints but very slow for large numbers of points and for interpolation across large images. The reasons for this are that

- a) finding the coefficient of each logarithmic and linear term involves the inversion of an $(N + 3)^2$ matrix and
- b) building the interpolant involves summing over N logarithmic terms at each pixel.

An alternative to the analytical solution given above is to use numerical methods. The interpolated function needs to be found at each point on a two-dimensional digital function, i.e. a digital image. The derivatives in the bi-harmonic equation are formed into discrete filters e.g. $\frac{\partial^2}{\partial x^2} \approx \{-1, 2, -1\}$ and $\frac{\partial^4}{\partial y^4} \approx \{1, -4, 6, -4, 1\}$. Convolution with the derivative filters is equivalent to multiplication by an $N \times N$ matrix \mathbf{K} and combining this with the border constraints leads to the system of linear equations,

$$(\lambda \mathbf{K} + \mathbf{S}) \mathbf{u} - \mathbf{d} = 0 \quad (6.37)$$

The $N \times 1$ vector \mathbf{u} is the desired solution and \mathbf{d} is the $N \times 1$ vector whose non-zero entries contain the measured border constraints. \mathbf{S} is an $N \times N$ diagonal sampling matrix with 1's at the border constraints and 0's at all other points. The scalar parameter λ controls the relative influence of the border constraints and the regularising stiffness constraint.

Theoretically the above equation can be solved directly by inverting the matrix $(\lambda \mathbf{K} + \mathbf{S})$ and multiplying \mathbf{d} by the result. In practical problems however,

CHAPTER 6. IMAGE PROCESSING METHODS

this matrix is huge, e.g. for a 256×256 pixel image the matrix has $65536^2 \cong 4.3 \times 10^9$ values, and so direct inversion is not possible. Instead iterative methods, such as the conjugate gradient method or the full multi-grid method are used. These only reference the sparse matrix $(\lambda K + S)$ and not its inverse. Even so, the process can be slow, with the algorithms taking hundreds or even thousands of iterations to converge. Transforming the matrix into a wavelet basis (13) (149) can improve the rate of convergence but the fastest algorithm (150) is not appropriate for exact interpolation i.e. for very small λ .

6.5.3 Triangulation based methods

Many other interpolation schemes exist in the literature that do not depend on energy minimisation, but take a more direct route to the interpolated function. The simplest such method is linear interpolation over triangles. This is the two dimensional extension of simple linear interpolation in one dimension. The points in the data set are formed into triangles using a triangle optimisation routine (151). For example, Delaunay triangulation maximises the size of the smallest angle in each triangle. The three points of each triangle specify a unique plane that is constructed over the triangle. This is a simple method for interpolation, but the resulting function is only continuous and not smooth. Higher order smoothness can be achieved by fitting quadratic, cubic or higher order polynomials over the points or using finite element methods (151) (152) (153), but this increases the complexity of the algorithm and reduces the speed. The major drawback to triangulation based approaches is that the result de-

CHAPTER 6. IMAGE PROCESSING METHODS

depends critically on the nature of the triangulation, and long thin triangles cannot always be avoided.

6.5.4 Weighted average approaches

Other methods construct a surface by using a weighted-average approach. Each point in the interpolated function is set to a weighted-average of the control points, with the influence of each control point falling off as a function of distance. Shepard's method (154) (155) uses the inverse of the distance from the control point raised to the power, n , specified by the user. This produces smooth surfaces but suffers from flattening of the interpolated function at the control points i.e. the partial derivatives of the surface are zero at the control points. Improvements have been made to overcome this problem(142) (116), but they require knowledge of the partial derivatives at the control points or some method to approximate them. It can also be a relatively slow method for very large numbers of control points, as each control point influences the entire function.

6.5.5 Grid based methods

Approximate interpolating functions can be constructed over a rectangular grid for some simple models, such as the least-squares fitting of quadratic or cubic polynomial functions. These can be applied locally and then a smooth global function found by blending the functions together using smooth blending functions. The most popular example of this kind of interpolation is known as free-

CHAPTER 6. IMAGE PROCESSING METHODS

form deformation (FFD) (156) (157), which has proved popular for modelling surface shape in three dimensions. In two dimensions this is a cubic B-spline surface constructed over a lattice of control points defined by

$$f(x, y) = \sum_{k=i}^{i+3} \sum_{l=j}^{j+3} B_k(x) B_l(y) \phi_{kl} \quad (6.38)$$

where $i = \lfloor x/\text{gridsize} \rfloor$, $j = \lfloor y/\text{gridsize} \rfloor$, ϕ_{kl} is the value of the control lattice at point (k, l) and $B_k(x)$ and $B_l(y)$ are the k^{th} and l^{th} B-spline basis functions evaluated at x and y respectively.

Each lattice control point will influence the resulting function in a square area 4 times the grid size surrounding the control point. If the surface given above is required to satisfy a single border constraint z_i within this square, an infinite number of possible choices for the control lattice values, ϕ_{kl} , exist. The choice,

$$\phi_{kl}(z_i) = \frac{w_{kl} z_i}{\sum_{a=i}^{i+3} \sum_{b=j}^{j+3} w_{ab}^2} \quad (6.39)$$

where $w_{ab} = B_a(x)B_b(y)$, will minimise the control lattice displacements in the least squares sense (156).

In general there will be more than one border constraint within each area of four-by-four grid-squares. It may not be possible to satisfy all of the constraints exactly, but the error can be minimised in the least squares sense using lattice values ϕ_{kl} given by (158)

$$\phi_{kl} = \frac{\sum_i w_{kli}^2 \phi_{kl}(z_i)}{\sum_i w_{kli}^2} \quad (6.40)$$

where $w_{kli} = B_k(x_i)B_l(y_i)$.

6.5.6 Multilevel B-splines

For a small grid size the standard B-spline interpolation given above will satisfy the border constraints accurately, but will show sharp local variations. Alternatively a large grid size will have smoother local variations but may not accurately satisfy the border conditions. In order to overcome this drawback, multilevel B-spline interpolation has been proposed (158) (159). The function is first interpolated using a large grid, then the grid is reduced (usually by a factor of two) and any remaining error in the control points is interpolated and added to the result. The process is repeated until the lattice is of size 1 and the border conditions are exactly satisfied. The whole algorithm is implemented efficiently using B-spline refinement to construct the control point displacements at finer scales, without reconstructing the entire function.

6.6 A New Multiscale Method

6.6.1 Introduction

The analytical thin-plate spline method described above is efficient for very sparse data (i.e. tens of points) and the multi-level B-spline method is efficient for sparse data (i.e. thousands of points) but neither is suitable for relatively

CHAPTER 6. IMAGE PROCESSING METHODS

dense data with only a few holes (i.e. tens of thousands of points). This kind of problem occurs for example due to occlusion of the laser stripe when scanning subject's faces. Numerical thin-plate spline methods can be used but require thousands of iterations to converge. This section presents a new method that is completely independent of the number of border constraints and does not require iteration.

6.6.2 Method

The method proposed here is similar in some respects to both the multi-level B-spline method and the weighted-average approach. The smoothness of a digital image will depend on its resolution. A function that is smooth at a fine scale can show sharp variations at a coarser scale. A set of scattered measurements can be digitised onto a set of images at different resolutions, placing each measurement at the nearest pixel at the chosen resolution. If more than one border constraint falls within a single pixel, a sensible compromise is to take the average of the border constraints. As the resolution decreases the accuracy of the digitised measurement will also reduce. At a coarse enough scale all the pixels will be allocated one or more measured values. Hence beyond a certain image resolution no interpolation is necessary. By expanding this image to a finer scale, this information can be used to fill in the missing data at the finer resolution. Provided the interpolated function is smooth up to the scale of the next resolution image, the resulting function will remain smooth. Continuing this process up to the finest scale will then produce a smoothly interpolated

CHAPTER 6. IMAGE PROCESSING METHODS

surface satisfying the border constraints.

Two functions are initialised with the measured border constraints. The first $f_0(x, y)$ contains the border conditions themselves, and the second $s_0(x, y)$ will contain a 1 at sample points and 0 elsewhere, i.e.

$$f_0(x, y) = \begin{cases} z_i & \text{if } (x, y) = (x_i, y_i) \\ 0 & \text{otherwise} \end{cases} \quad (6.41)$$

$$s_0(x, y) = \begin{cases} 1 & \text{if } (x, y) = (x_i, y_i) \\ 0 & \text{otherwise} \end{cases} \quad (6.42)$$

The reduced images are then found by filtering, sub-sampling at every other pixel and dividing the resulting functions,

$$f_j(x, y) = \frac{\sum_{n,m} h(n) h(m) f_{j-1}(2x - n, 2y - m)}{\sum_{n,m} h(n) h(m) s_{j-1}(2x - n, 2y - m)} \quad (6.43)$$

and

$$s_j(x, y) = \frac{\sum_{n,m} h(n) h(m) s_{j-1}(2x - n, 2y - m)}{\sum_{n,m} h(n) h(m) s_{j-1}(2x - n, 2y - m)} \quad (6.44)$$

and setting $0/0 = 0$. To reconstruct the smooth function at a finer resolution, the images are up-sampled by pixel doubling and filtered with a smooth spatial filter,

$$g_j(x, y) = \begin{cases} \sum_{n,m} h(n) h(m) g_{j+1}(\lfloor (x-n)/2 \rfloor, \lfloor (y-m)/2 \rfloor) & \text{if } s_j(x, y) = 0 \\ f_j(x, y) & \text{if } s_j(x, y) = 1 \end{cases} \quad (6.45)$$

The filter $h(n)$ is chosen so that repeated applications of this filter at all scales along a dyadic sequence converges to a cubic spline filter, i.e. in the Fourier domain,

$$\phi(\omega) = \prod_{j=0}^{\infty} H\left(\frac{\omega}{2^j}\right) \quad (6.46)$$

The choice of coefficients $h = \{0.1, 0.25, 0.3, 0.25, 0.1\}$ have been used in this work, which gives rise to the piecewise cubic spline curve shown in figure 6.2. The borders are treated using $2N$ periodic wrap-around border constraints. After expansion the sample border constraints may not be exactly satisfied. Therefore the function is adjusted by replacing the interpolated function with the stored border constraint where necessary.

6.6.3 Results

The interpolation method described above has been tested on a range of real and artificial data. The results are shown in figures 6.3, 6.4 and 6.5. These demonstrate that the multi-scale filter method produces smooth interpolated functions and by definition the border constraints are always satisfied exactly. The reconstructed functions suffer from the flattening problem at the sample

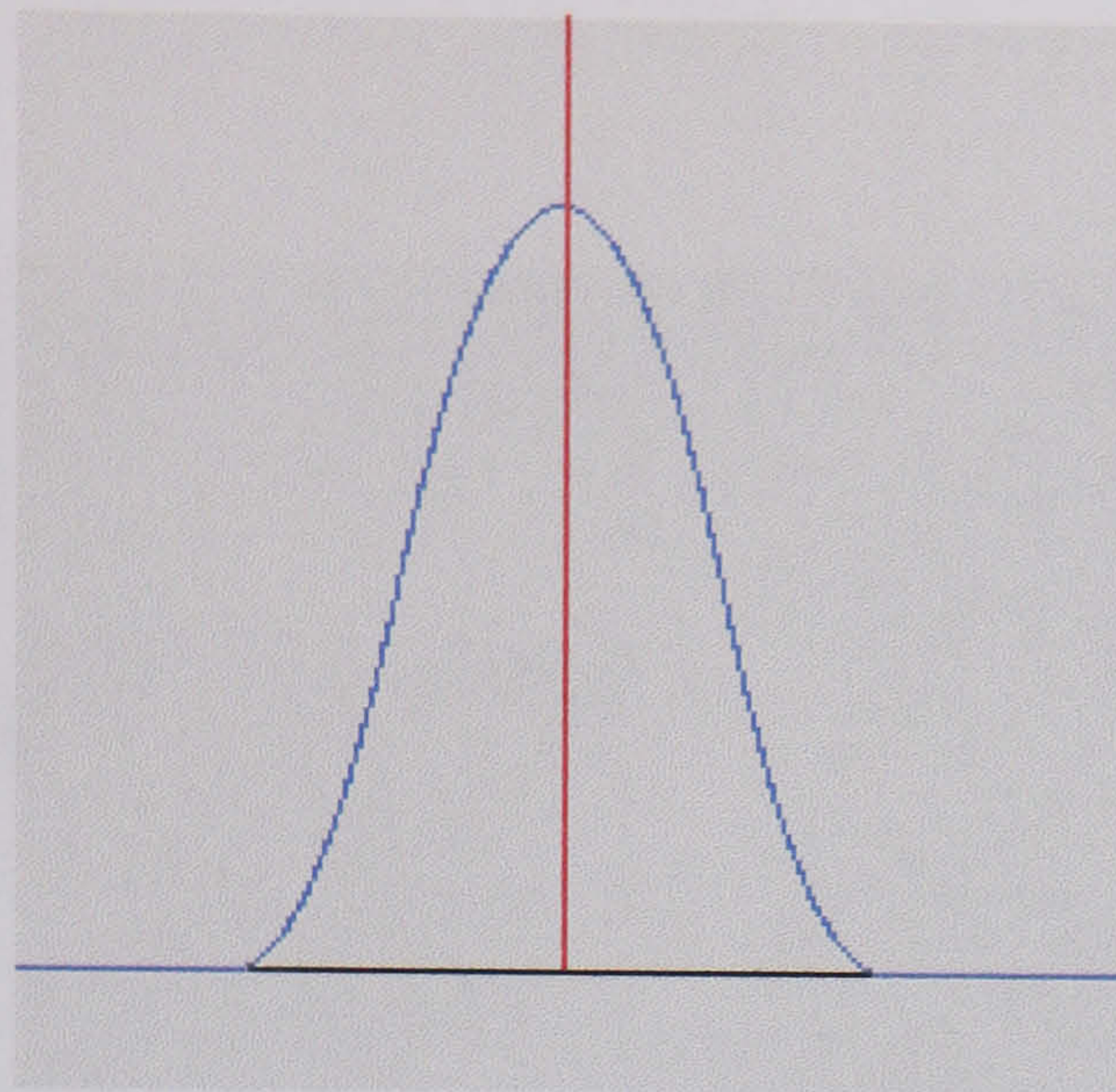


Figure 6.2: The piecewise smooth cubic spline curve generated using the filters described in the text.

points in the same manner as Shepard's method, but unlike Shepard's method the function is continuous and smooth at the sample points. The interpolation speed is independent of the number of border constraints and is $O(N \log N)$ for an N -pixel image. The time required for a 256 by 256 interpolation problem is difficult to assess on a multi-tasking operating system, but is typically less than 1 second.

6.6.4 Conclusions

For interpolation problems that are critically dependent on satisfying a particular model, such as the thin-plate bending model, the numerical or analytical solution of the resulting regularisation problem is recommended. For many problems however it is more desirable to have an efficiently calculated solution that 'looks right' in some sense. The multi-level B-spline method produces scale-invariant, C^2 -continuous interpolating functions very rapidly, with only a small

CHAPTER 6. IMAGE PROCESSING METHODS

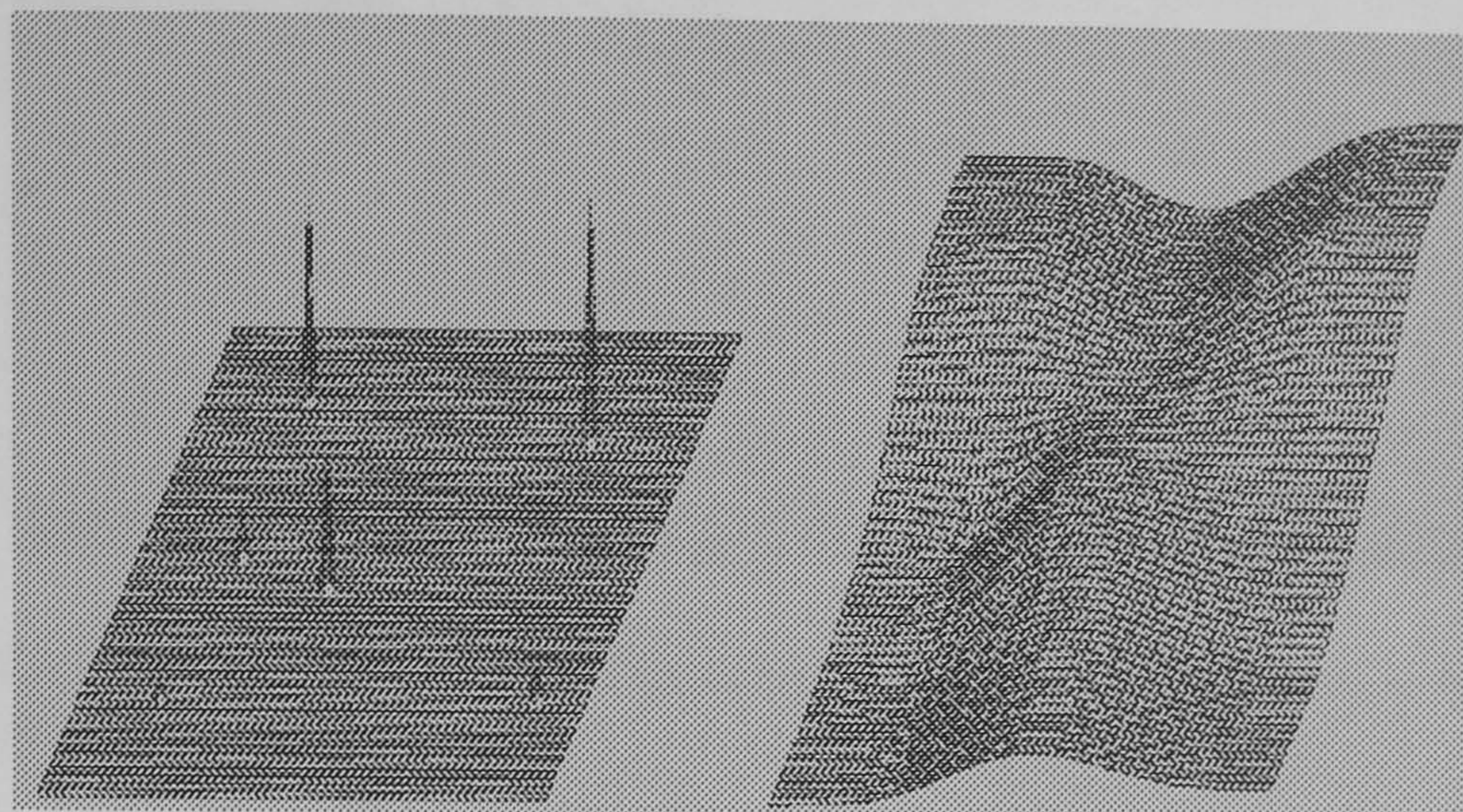


Figure 6.3: A typical sparse interpolation problem (left) and the solution constructed using the multiscale method (right).

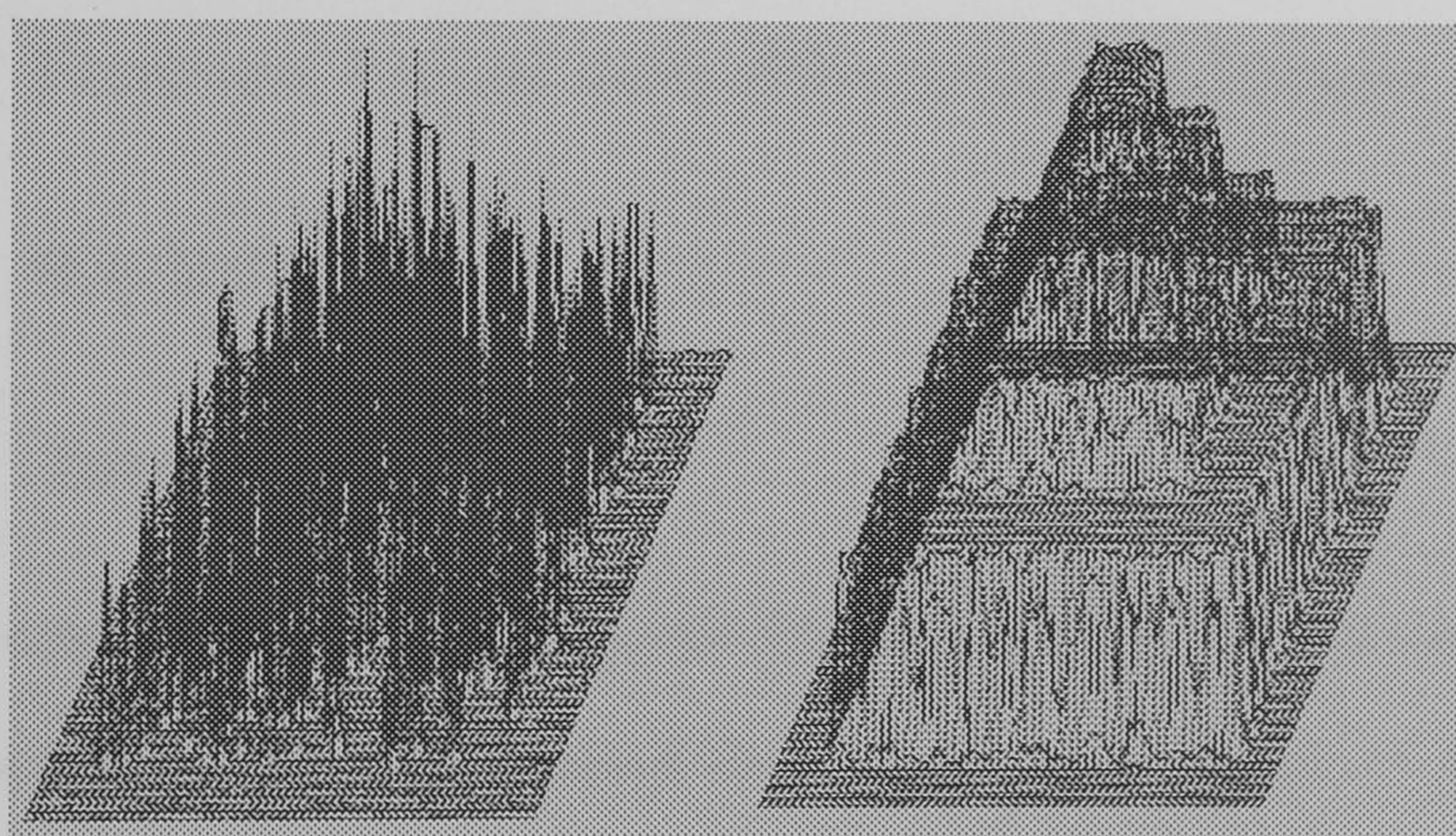


Figure 6.4: 10% sampling of a 'wedding cake' function (Left). Reconstruction by interpolation with the multiscale method (Right).

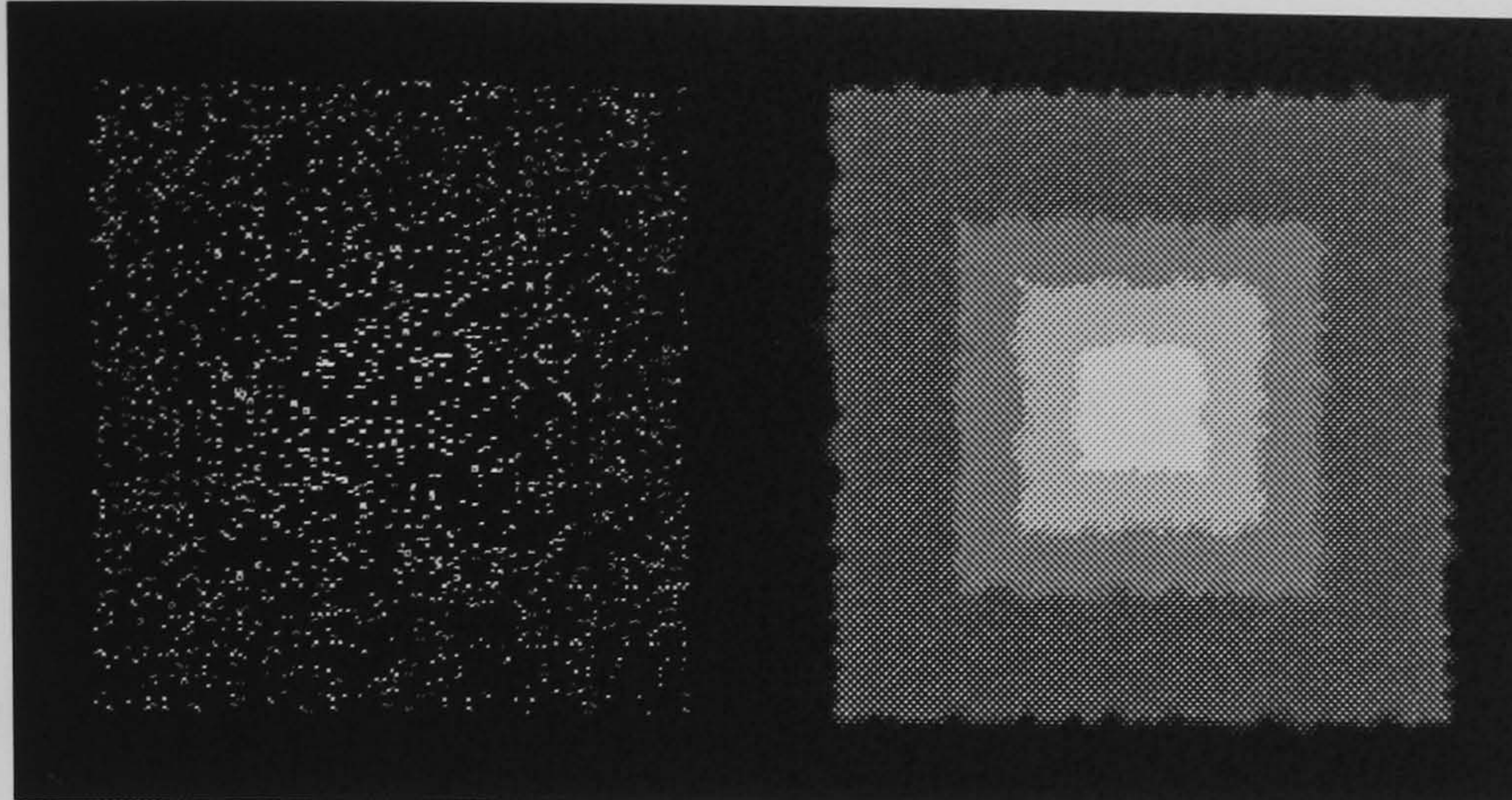


Figure 6.5: The same problem (left) and solution (right) as shown in Figure 6.4 displayed as images.

time penalty for a large number of border conditions or large image size. The new multi-scale approach also produces a C^2 -continuous interpolating function very efficiently, but the flattening of the function at the control points makes this a less desirable solution.

6.7 Feature based two-dimensional image warping

6.7.1 Introduction

As described in chapter 5, the majority of methods for inter-subject comparison have used image warping to extend the comparison of a small set of points across the entire image. The warping methods used have generally involved interpolating the translations in the direction of each coordinate axis separately. In some cases this can lead to the image not only stretching, but also folding,

CHAPTER 6. IMAGE PROCESSING METHODS

even when the individual interpolating functions are smooth and continuous. In this section a new general solution to the problem of preventing folding in image warping is presented.

6.7.2 The one-to-one property

The problem of image warping given a set of matching point sets is essentially the problem of interpolating two functions simultaneously. One function is for the translation in the direction of the x -axis and the other for the translation in the direction of the y -axis. An additional problem is maintaining the one-to-one property of the warping transformation. Each point in the transformed image should correspond to only one point in the original image and vice-versa. If the one-to-one property is not satisfied the warped function will have the appearance of being folded, rather than only stretched.

In Figure 6.6 the three points are mapped according to,

$$(x, y) \rightarrow (f(x, y), g(x, y)) \quad (6.47)$$

$$(x + \delta x, y) \rightarrow (f(x + \delta x, y), g(x + \delta x, y)) \quad (6.48)$$

$$(x, y + \delta y) \rightarrow (f(x, y + \delta y), g(x, y + \delta y)) \quad (6.49)$$

In the limit as $\delta x \rightarrow 0$ and $\delta y \rightarrow 0$ the direction of the vectors \mathbf{a} and \mathbf{b} are given by

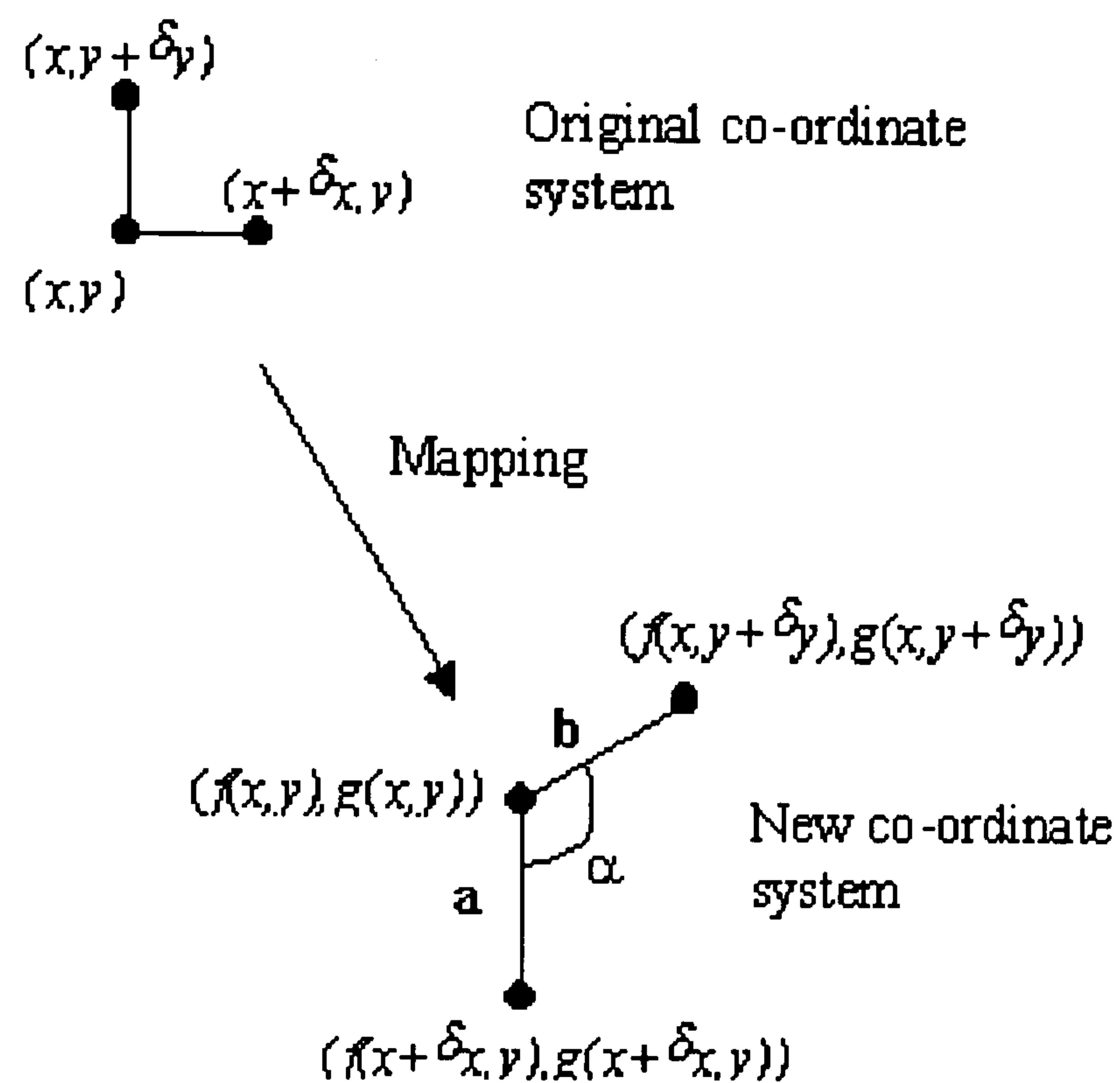


Figure 6.6: A mapping function will be one-to-one provided the angle α is between 0 and π . This is only true if the cross product of the vectors \mathbf{a} and \mathbf{b} points out of the page. Taking the limit as $\delta x \rightarrow 0$ and $\delta y \rightarrow 0$ this becomes equivalent to the Jacobian of the transform remaining positive.

$$\mathbf{a} \propto \left(\frac{\partial f}{\partial x}, \frac{\partial g}{\partial x} \right) \quad (6.50)$$

$$\mathbf{b} \propto \left(\frac{\partial f}{\partial y}, \frac{\partial g}{\partial y} \right) \quad (6.51)$$

The mapping will not flip when the angle $0 < \alpha < \pi$, or equivalently when $\sin(\alpha) > 0$. The cross-product of \mathbf{a} and \mathbf{b} will be a vector perpendicular to the page, given by

$$\mathbf{a} \times \mathbf{b} = |\mathbf{a}| |\mathbf{b}| \sin \alpha \hat{\mathbf{n}} \quad (6.52)$$

hence the Jacobian, J , of the transformation, given by

$$J = \frac{\partial (f, g)}{\partial (x, y)} = \frac{\partial f}{\partial x} \frac{\partial g}{\partial y} - \frac{\partial f}{\partial y} \frac{\partial g}{\partial x} \quad (6.53)$$

will have the same sign as $\sin \alpha$. Therefore if the Jacobian becomes negative the mapping will fold-over (160).

6.7.3 Previous solutions

Previously derived methods for preventing fold-over have been specifically designed for a small subset of interpolation methods. For the numerical solution of the thin-plate stiffness equations, an additional constraint (in addition to the thin-plate stiffness and the border constraints) can be placed on the solution, forcing the Jacobian to remain positive (161) (162). For the case of multilevel

CHAPTER 6. IMAGE PROCESSING METHODS

B-splines a clipping of the border constraints whose magnitude is above 0.48 can ensure the one-to-one property (159).

6.7.4 A new general solution

The one-to-one property of the change of variables can be preserved using two simple facts. Firstly, the concatenation of two one-to-one maps must be one-to-one, i.e. given two one-to-one mappings

$$(x, y) \rightarrow (f, g) \tag{6.54}$$

with Jacobian $J_1 > 0$ and

$$(f, g) \rightarrow (u, v) \tag{6.55}$$

with Jacobian $J_2 > 0$, then the combined mapping

$$(x, y) \rightarrow (u, v) \tag{6.56}$$

will (by the chain rule of differentiation) have Jacobian

$$J_3 = J_1 J_2 > 0 \tag{6.57}$$

and so be one-to-one.

The second point to note is that an overlapping function of the form

CHAPTER 6. IMAGE PROCESSING METHODS

$$(x, y) \rightarrow (x + f, y + g) \quad (6.58)$$

can be made one-to-one by scaling the functions f and g by an appropriate constant α satisfying $0 \leq \alpha < \beta$ so that the mapping

$$(x, y) \rightarrow (x + \alpha f, y + \alpha g) \quad (6.59)$$

is one-to-one. The constant $\beta \leq 1$ is the limit on the parameter α , chosen so that the smallest value of the Jacobian becomes zero, i.e.

$$J = (\beta f_x + 1)(\beta g_y + 1) - \beta^2 f_y g_x = 0 \quad (6.60)$$

where the subscripts denote partial derivatives. This quadratic equation can be solved for β at the point where the Jacobian is smallest. This point can be found using finite difference approximations for the partial derivatives across the image.

Using these two facts, a simple method for eliminating overlap is to construct a set of one-to-one warps by interpolation and scaling, which are then concatenated into a single one-to-one warp. Interpolation is first carried out using the raw interpolation method, and then the warping function is scaled by a fraction α calculated using equation 6.60. This will translate the border constraints a fraction α of the desired amount. The remaining translation is then interpolated, scaled if necessary and concatenated with the original. This

CHAPTER 6. IMAGE PROCESSING METHODS

is repeated until $\beta > 1$ and the border constraints are satisfied or $\beta \leq 0$ and the border constraints are forcing an overlap. In the latter case, a choice must be made between satisfying the border constraints and overlapping, or having a one-to-one warp and not satisfying the border conditions.

6.7.5 Results

This method is independent of the type of interpolation being performed, so it can be applied to any feature based warping method. An example image and specified translations (Figure 6.7) are used to demonstrate the effect of warping with and without overlap control. Figure 6.8 shows the results of interpolating using the new multiresolution method. The effects of overlap can be seen, particularly on the central white square, which has been split at the four corners. Figure 6.9 demonstrates constraining this warp to be one-to-one. The central white square now stretches smoothly out to the corners. Figures 6.10 and 6.11 demonstrate an analytically interpolated thin-plate spline warp without and with overlap control respectively. Again the folding of the image is particularly notable around the central white square, with the image completely inverted at the borders when overlap control is not used.

6.7.6 Conclusion

For interpolation problems with only a small number of border constraints, combining the analytical solution to the thin-plate energy minimisation with the overlap prevention method presented above gives a robust and efficient method.

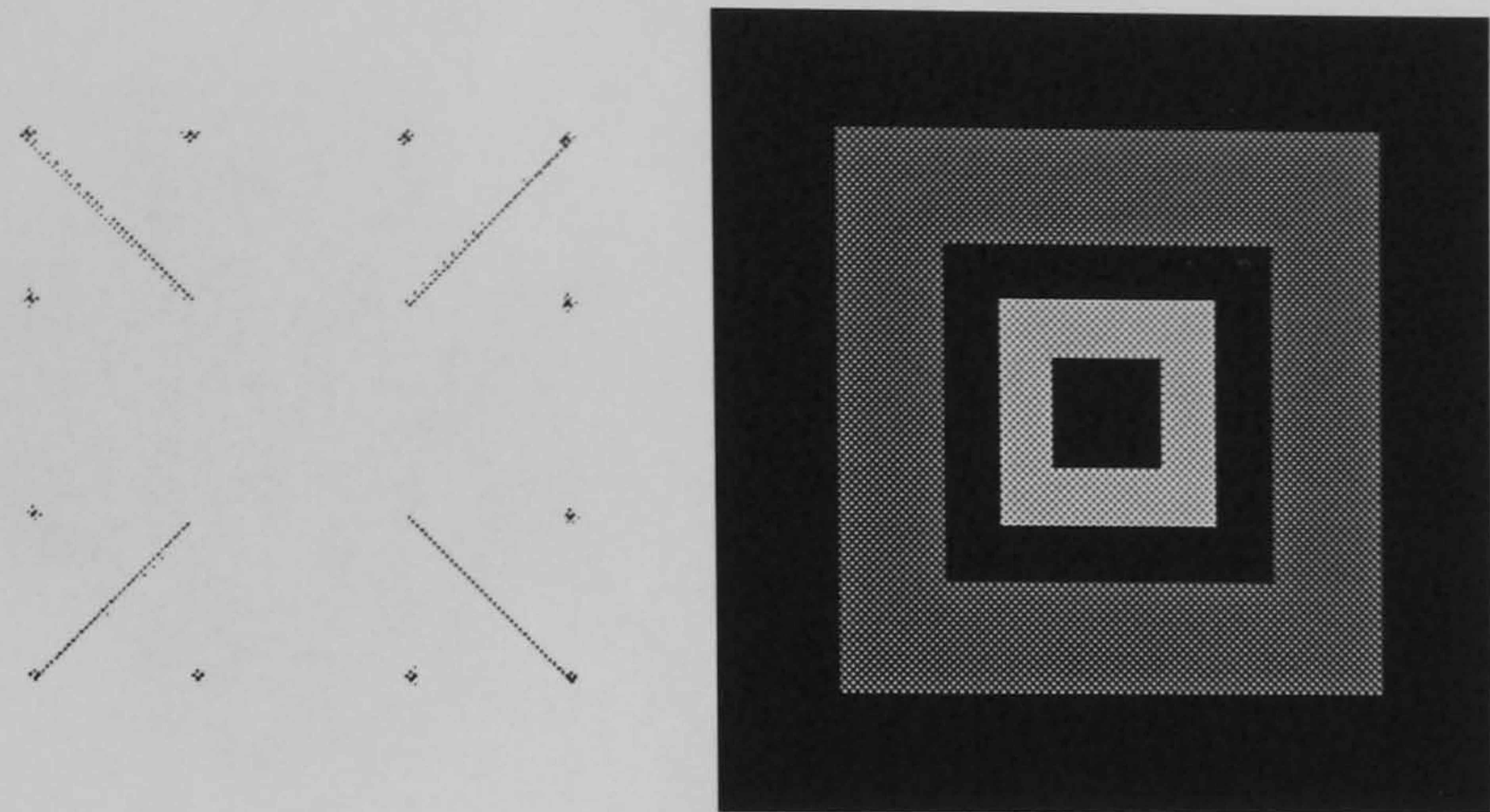


Figure 6.7: The example translations (left) and image (right) used in the warping examples.

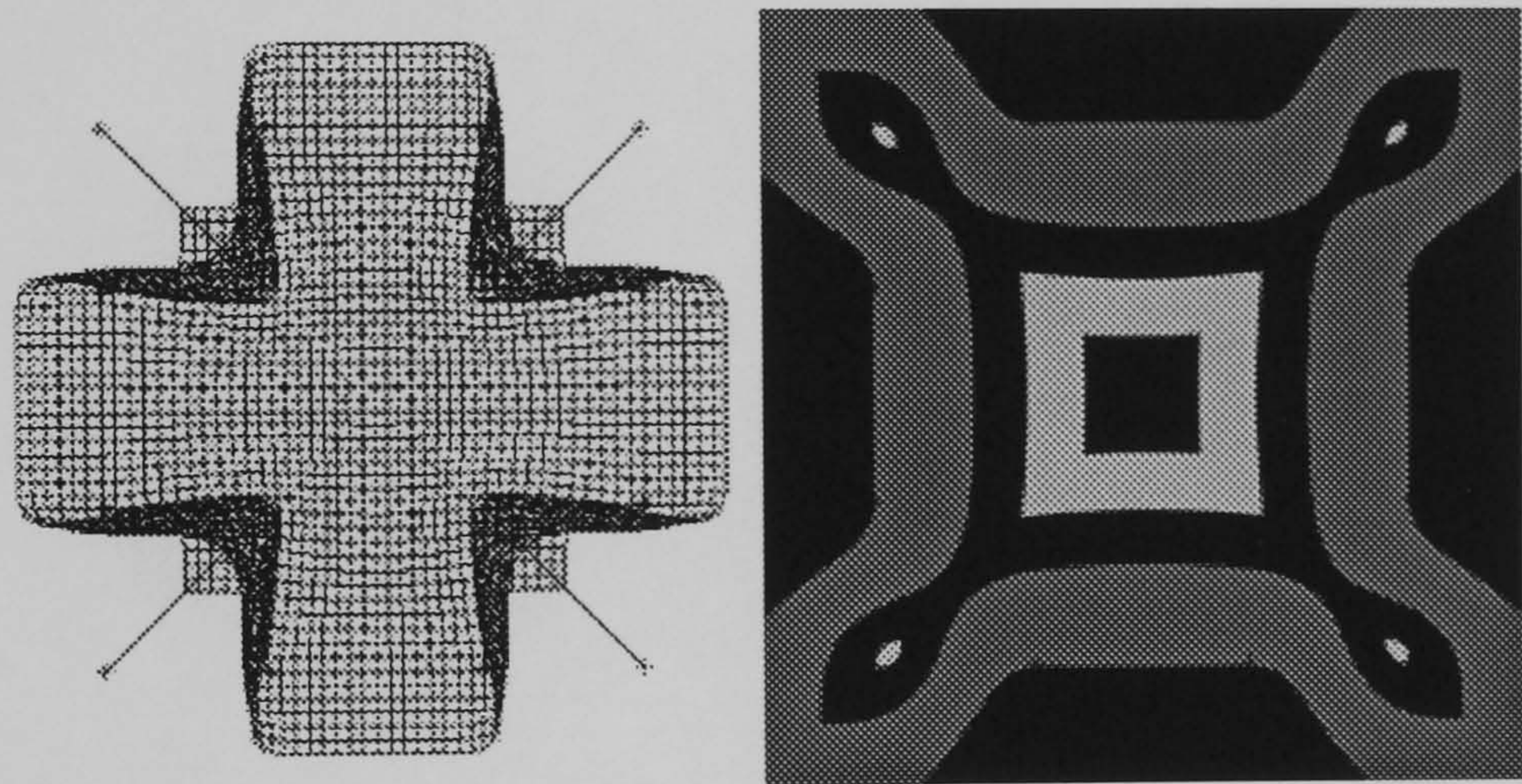


Figure 6.8: The warping function interpolated using the multiscale method without overlap control (left) and the resulting transformed image (right).

For larger problems, where the choice of interpolating function is less critical, the MFFD method with control point clipping provides the most efficient solution.

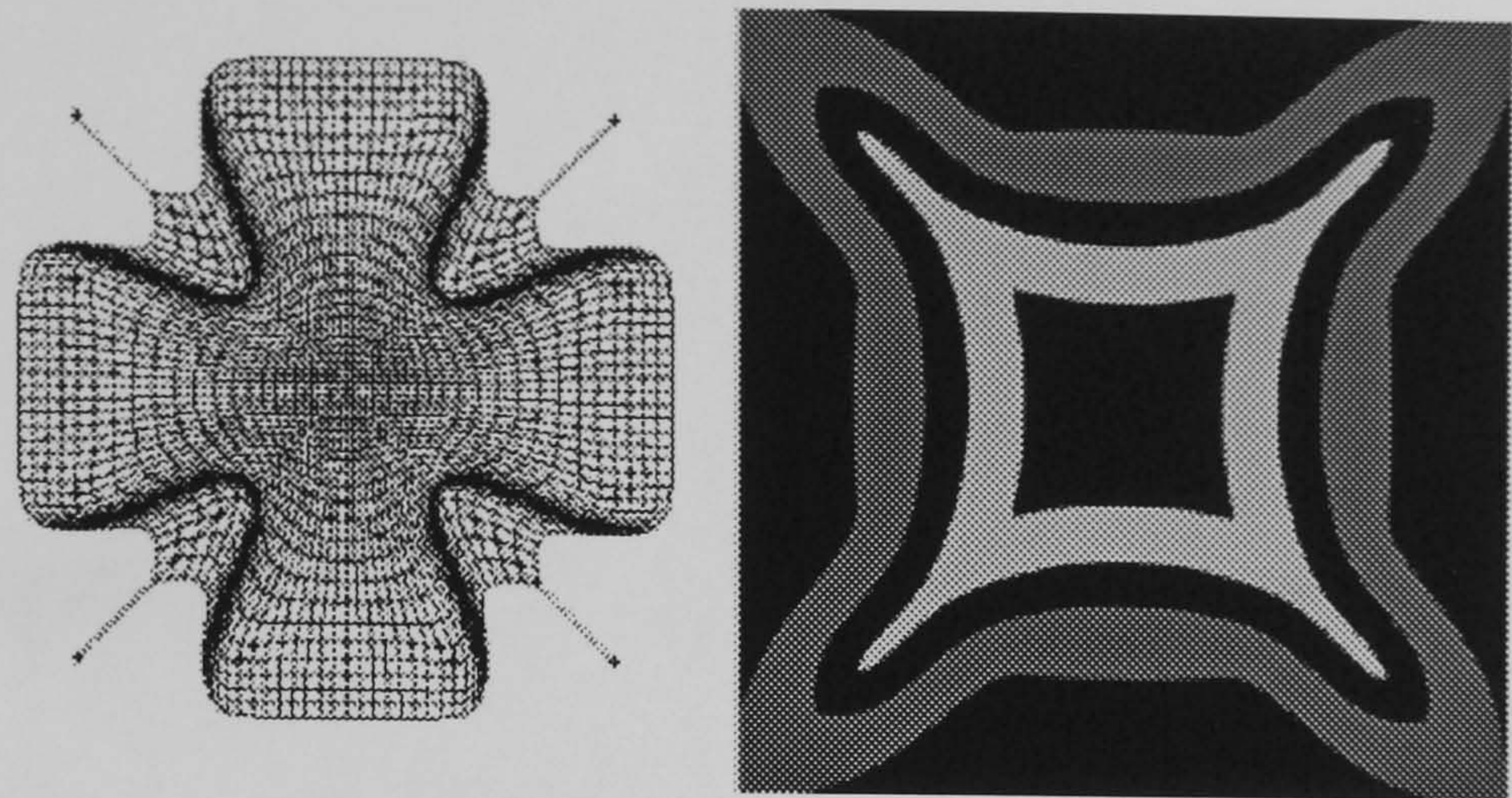


Figure 6.9: The same problem as figure 6.8 solved with the multiscale interpolation method with overlap control.

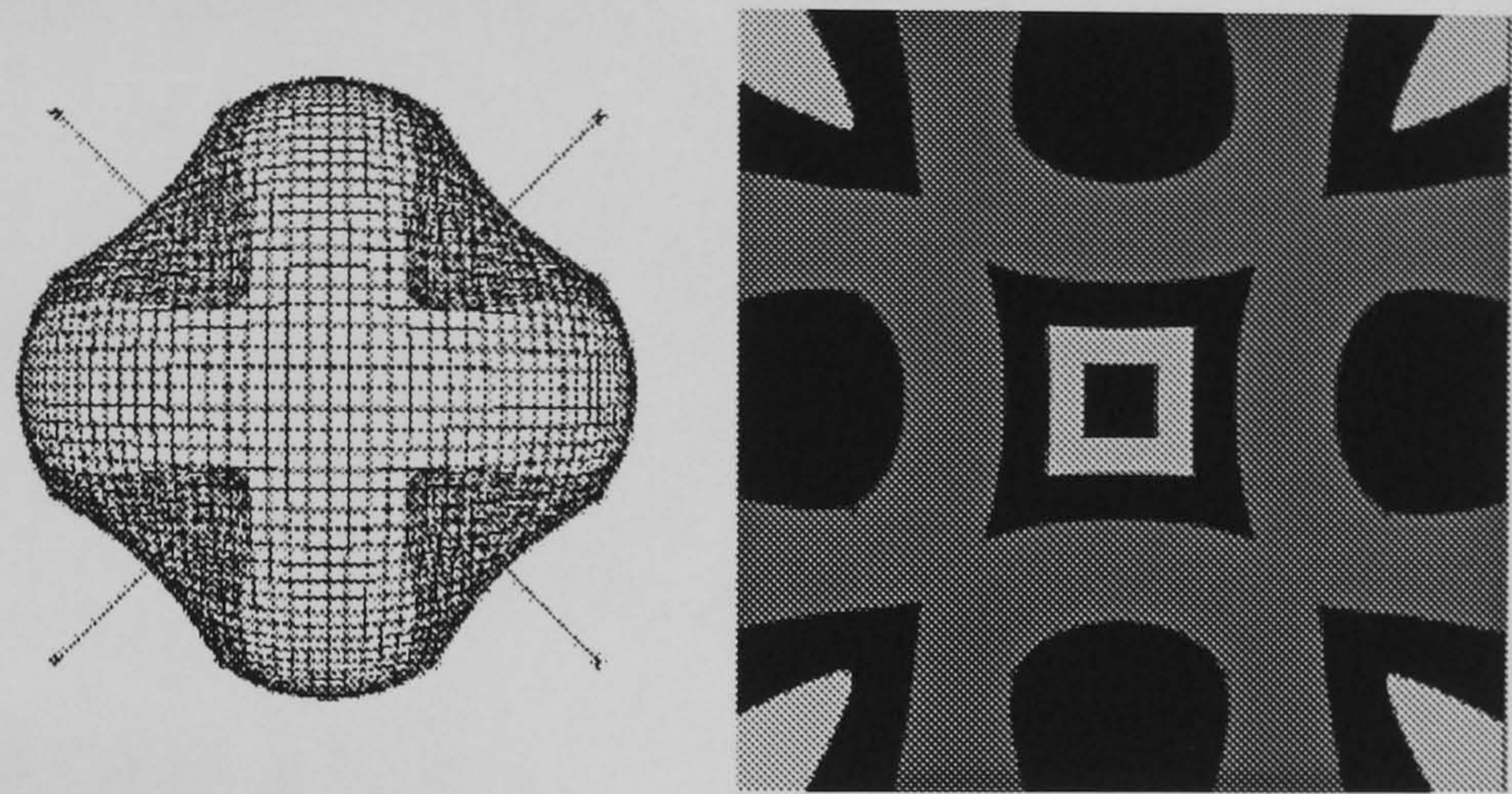


Figure 6.10: The same warping problem interpolated using analytical thin-plate splines without overlap control.

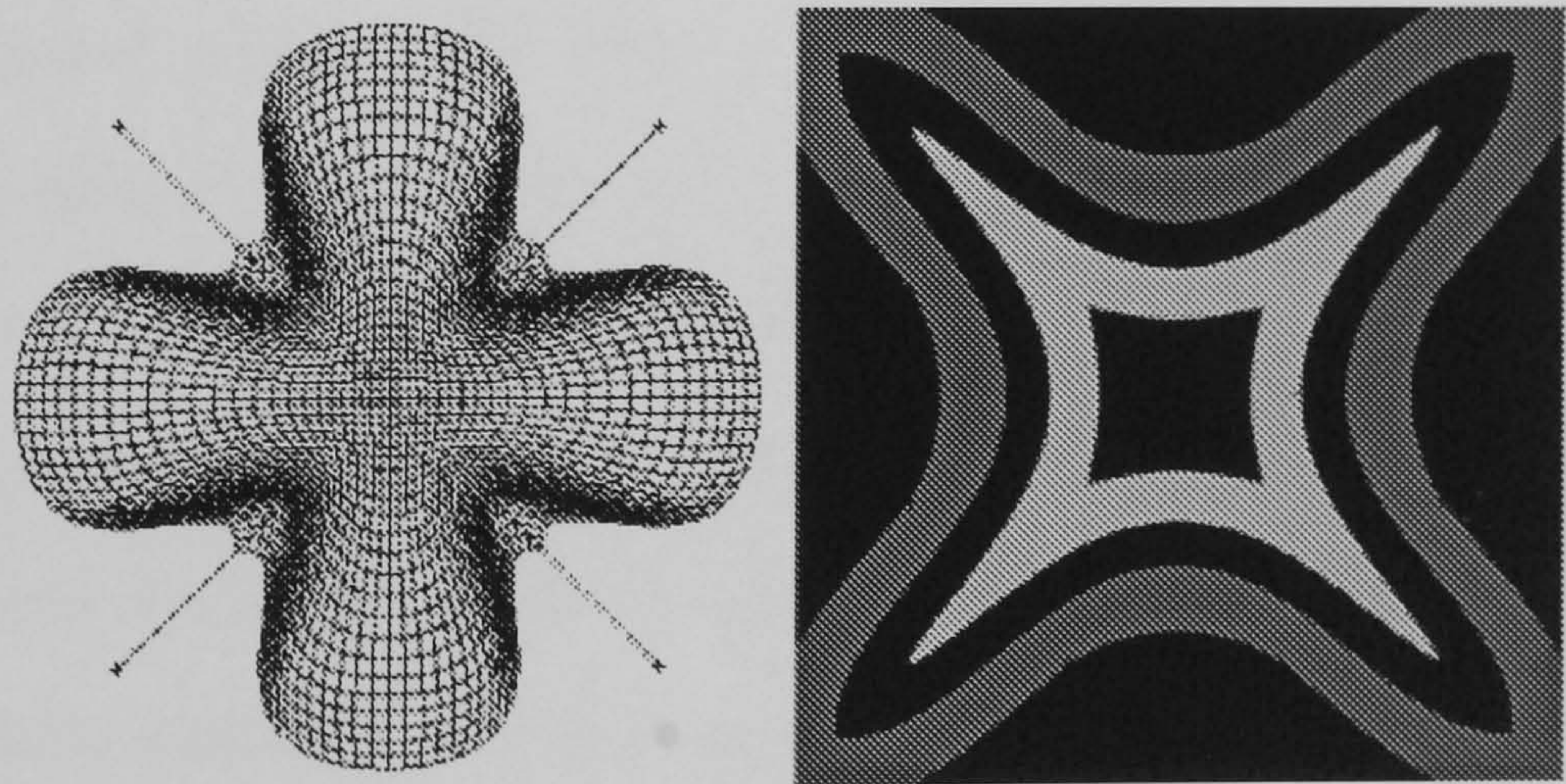


Figure 6.11: The same problem solved using analytical thin-plate splines with overlap control.

Chapter 7

Inter-Surface Comparison Study

7.1 Introduction

Analysis of the differences between facial images can aid diagnosis, treatment planning and research. Registration to a Cartesian reference frame using the fixed relations principle assigns a spatial coordinate to each point on the facial surface. Comparison of three-dimensional facial landmark points between subjects can then be made via this independent reference convention. Landmark points only represent a tiny fraction of the available data and so methods are required for extending the matching to featureless areas of the face away from landmark points, such as the cheeks or forehead.

CHAPTER 7. INTER-SURFACE COMPARISON STUDY

In chapter 5 the various available methods for inter-patient matching were reviewed. From the current literature it is unclear which of the available methods produces the most useful results and which is the most suited to laser-range data. Therefore, in this chapter, three new methods for the inter-patient comparison of laser-scanned facial surfaces and a registered photograph are described and tested.

The first method uses depth variation and the surface normal vectors to match facial points automatically, in a manner similar to the automatic elastic matching of volume data. Because this method does not make use of the photographic data or secondary surface features it can lead to incorrect matching of anatomical features such as the nose, the eyes etc. This is demonstrated by warping the registered facial photograph using the matching information from this method.

To overcome these problems the other two methods use matching of extracted features, principally points and contours. The first of these methods uses a fully automatic algorithm based on the automatic extraction and matching of edge and curvature maxima points. The edge extraction is performed with standard edge and curvature extraction routines, and the matching by an iterative closest point algorithm. Feature-based warping driven by the matched points is used to match points away from the extracted edges. While this method produces an accurate matching in most cases, individual scans may be matched incorrectly. Also, it has only been tested on our database of normal, white, adults and it is possible that faces with differently coloured skin or a particu-

CHAPTER 7. INTER-SURFACE COMPARISON STUDY

larly unusual shape (i.e. patients) may be incorrectly matched.

To overcome the problems of incorrect matching in the automated methods, the final method uses interactive segmentation of curvature and surface features followed by interpolation-based warping. ‘Snakes’ are used to assist in the segmentation of contours in a manually defined template. A new snake implementation, for contours connected at landmarks, ensures that the template landmarks are properly placed as well as the contours. Other landmarks not associated with contours are placed manually. Because the template is adapted interactively, the user can easily deal with unusually shaped or coloured faces. This leads to very accurate matching of subjects with an acceptable level of user interaction.

7.2 Data Capture

To provide data for the experiments contained in this and subsequent chapters facial images were captured of volunteer subjects. Thirty male and thirty female adult Caucasian volunteers from the staff at Stoke Mandeville Hospital, Aylesbury, had a frontal photograph and laser-video scan of their face captured in the analytic morphograph. The subjects were first registered to the morphograph’s reference frame in the manner described in chapter 2. For ‘belt-and-braces’ safety eye patches were placed over the subject’s closed eyes prior to capturing the laser surface scans. Holes in the scans due to occlusion, low beam intensity and scatter were later interpolated using the multiscale method described in

CHAPTER 7. INTER-SURFACE COMPARISON STUDY

section 6.6.

The eye patches were removed after scanning and then a photograph of each subject was captured with their eyes open . The photographic images were captured on Polaroid instant (chemical) film in the usual manner for morphanalytic photographs. These images were then digitised at a resolution of 100 dpi. This rather coarse image resolution was considered sufficient for testing the new methods, whilst conserving limited storage space. The images can become rotated slightly in the digitisation process and so they were aligned by manually locating two markers on the cephalostat's ear rods. The left point (x_l, y_l) and the right point (x_r, y_r) should be at equal distances from the morphanalytic origin (x_0, y_0) given by,

$$(x_0, y_0) = \frac{(x_l, y_l) + (x_r, y_r)}{2} \quad (7.1)$$

The images were then scaled and rotated to conform to a standard size and resolution. The rotation angle, θ , is given by

$$\theta = \arctan \left(\frac{y_r - y_l}{x_r - x_l} \right) \quad (7.2)$$

The scale of the original image points in the morphanalytic yz -plane is the combination of a 10% enlargement coupled with a one third reduction. Combining this with the 100dpi ($\simeq 0.253mm/pixel$) scanning resolution gives the scale of

CHAPTER 7. INTER-SURFACE COMPARISON STUDY

the scanned points as,

$$resolution = 0.253 \times \frac{3}{1.1} mm/pixel = 0.69 mm/pixel \quad (7.3)$$

The photographic images are also distorted by perspective and so a final stage is used to remove the perspective from the images. This is achieved by using the depth data from the laser scans and knowledge of the camera parameters. Because the 10% enlargement has already been removed the perspective equations are given by

$$y = \frac{(169 - x)Y}{169} \quad (7.4)$$

$$z = \frac{(169 - x)Z}{169} \quad (7.5)$$

for image pixel (Y, Z) (scaled and centred to the morphanalytic coordinate frame) and morphanalytic coordinate (x, y, z) , derived from the laser scan.

7.3 Method 1: Automatic surface matching

7.3.1 Method Overview

In this section a simple warping method for automatically matching two laser-range scans is described. The method is based on matching two surfaces using only the relative depths and the surface normals. The algorithm is derived from similar algorithms for 3D scalar data based on matching intensities using the

CHAPTER 7. INTER-SURFACE COMPARISON STUDY

gradient vector and a smooth elastic model. The algorithm traces the surface normal from each point in the target scan until it intersects the study scan. These vectors represent the displacements between the two registered scans, which can be used to warp the study image into the shape of the target image.

It is important to realise that tracing any vector from the target to the study will create a warp that will correctly transform the study into the template, but it may make no biological sense. In order to improve the registration the warping functions need to be defined more precisely. To this end a further criterion is imposed, namely that the warping function must be smooth. Regularising the warping function using recursive filters imposes a thin-plate-like smoothness constraint.

Regularising the warp can lead to a warp that does not exactly satisfy the border constraints i.e. does not warp the study range-map exactly into the shape of the target. To improve the registration a new target range map is created, by inverting the warping function and applying it to the original target image. This new target will be more similar to the study range-map than the original. Repeating this process and concatenating the resulting functions at each iteration produces a smooth warp from the original target to the study. Once the change in the largest translation in the warp between iterations falls below a threshold the algorithm is halted. Algorithm 2 describes the entire process in pseudo-code.

CHAPTER 7. INTER-SURFACE COMPARISON STUDY

Algorithm 2 Automatic depth warping

Inputs: Target scan T , Study scan S
Begin
 $TotalWarp = 0$
 $Iteration = 0$
repeat
 $Warp = \text{trace surface normals from } T \text{ to } S$
 Regularise ($Warp$)
 $TotalWarp = TotalWarp + Warp$
 $InverseWarp = \text{Invert}(Warp)$
 $T = \text{Warp } T \text{ with } InverseWarp$
 $Max = \text{Magnitude of Largest vector in } Warp$
 $Iteration = Iteration + 1$
until $Max < Threshold$ OR $Iteration > MaxIteration$
Output: $TotalWarp$
End

7.3.2 Implementation

Surface Normal Calculation

The first stage in constructing the warping function using this method is to calculate the surface normal vectors in the range image. In this implementation the surface normals are calculated as the normal to the least-squares fit plane over each 3 by 3 surface patch. The equation of this plane is given by

$$x = ay + bz + c \quad (7.6)$$

and the surface normal is given by

$$\mathbf{n} = (1.0, -a, -b) \quad (7.7)$$

The least squares surface patch will find the parameters a , b and c that

CHAPTER 7. INTER-SURFACE COMPARISON STUDY

minimise the sum of square errors

$$\chi^2 = \sum_{i,j} (ay_i + bz_j + c - x(y_i, z_j))^2 \quad (7.8)$$

This is minimised by setting its partial derivatives with respect to these parameters to zero, i.e.

$$\frac{\partial \chi^2}{\partial a} = \sum_{i,j} 2y_i (ay_i + bz_j + c - x(y_i, z_j)) = 0 \quad (7.9)$$

$$\frac{\partial \chi^2}{\partial b} = \sum_{i,j} 2z_j (ay_i + bz_j + c - x(y_i, z_j)) = 0 \quad (7.10)$$

$$\frac{\partial \chi^2}{\partial c} = \sum_{i,j} 2 (ay_i + bz_j + c - x(y_i, z_j)) = 0 \quad (7.11)$$

This results in a set of linear simultaneous equations for the surface normals, written in matrix form as

$$\begin{bmatrix} \sum y_i^2 & \sum y_i z_j & \sum y_i \\ \sum y_i z_j & \sum z_j^2 & \sum z_j \\ \sum y_i & \sum z_j & \sum 1 \end{bmatrix} \begin{bmatrix} a \\ b \\ c \end{bmatrix} = \begin{bmatrix} \sum y_i x(y_i, z_j) \\ \sum z_j x(y_i, z_j) \\ \sum x(y_i, z_j) \end{bmatrix} \quad (7.12)$$

The surface normal is not affected by a change of coordinate system to centre the surface patch on the origin i.e. $x = -1$ to 1 and $y = -1$ to 1 . Inserting

CHAPTER 7. INTER-SURFACE COMPARISON STUDY

these values into equation 7.12 gives

$$\begin{bmatrix} 6 & 0 & 0 \\ 0 & 6 & 0 \\ 0 & 0 & 9 \end{bmatrix} \begin{bmatrix} a \\ b \\ c \end{bmatrix} = \begin{bmatrix} \sum y_i x(y_i, z_j) \\ \sum z_j x(y_i, z_j) \\ \sum x(y_i, z_j) \end{bmatrix} \quad (7.13)$$

and hence

$$a = \frac{1}{6} (z(1, -1) + z(1, 0) + z(1, 1) - z(-1, -1) - z(-1, 0) - z(-1, 1)) \quad (7.14)$$

and

$$b = \frac{1}{6} (z(-1, 1) + z(0, 1) + z(1, 1) - z(-1, -1) - z(0, -1) - z(1, -1)) \quad (7.15)$$

and the unit surface normal is then given by

$$\hat{\mathbf{n}} = \frac{(1.0, -a, -b)}{\sqrt{1 + a^2 + b^2}} \quad (7.16)$$

Ray-Tracing Surface Normals

Ray-tracing is used to calculate the intersection of the first surface's normal vectors with the second surface. The equation of the ray, \mathbf{r} , is given in terms of the starting point \mathbf{r}_0 and the unit normal vector $\hat{\mathbf{n}}$ by

CHAPTER 7. INTER-SURFACE COMPARISON STUDY

$$\mathbf{r} = \mathbf{r}_0 + \lambda \hat{\mathbf{n}} \quad (7.17)$$

for scalar parameter λ . For efficiency, nearest-pixel ray tracing is performed using the Bresenham line algorithm. A further speed improvement can be implemented by tracing the ray in two dimensions rather than three. The ray is traced across the (y, z) dimensions of the depth map and the current x coordinate found at each pixel. The direction of the ray is chosen to be in the positive normal direction if the surface point is inside the second surface and in the negative normal direction if the surface point is outside the second surface. The ray is terminated when it crosses the second surface or exits a bounding box surrounding the depth map.

Regularisation

Even when the least-squares surface normal is used, the surface normal vectors can vary a great deal from point to point. In order to construct a smooth warping function the surface normal vectors are smoothed both before and after the ray-tracing stage. This is performed using second-order Tikhonov regularisation, implemented using backwards-forwards recursive filters (139).

Calculating the Inverse Warping Function

The forward warping function defines a translation vector at every pixel in the destination image. These are used to ‘collect’ image values (colour or depth) from the source image, ensuring that the destination image is properly defined

CHAPTER 7. INTER-SURFACE COMPARISON STUDY

at every pixel. If the same warping function were used to ‘place’ the destination pixel values at the nearest pixel in the source image, this would (in general) not define the transformed function at every pixel. Interpolation is used to ensure that the inverse warping does not leave gaps in the transformed image.

7.3.3 Results

To test the automatic surface warping method several of the images of subjects in our database were used. For example figure 7.1 shows two scans from the database and figure 7.2 shows the results of warping the source scan into the shape of the target scan and the result of applying the inverse of this transformation to the target scan. These subjects have quite similarly shaped faces and the result of warping the registered photographic image produces reasonable results (figure 7.3). For less similarly shaped faces (e.g. figure 7.4) warping of the range images can produce incorrect matching (figure 7.5) which is clearly demonstrated by warping the registered RGB image with the warp found with this method (figure 7.6).

7.4 Method 2: Automatic edge based warping

7.4.1 Method Overview

This method aims to overcome the potential problem of incorrectly matching facial features by using an edge-based approach. Three kinds of image edges

CHAPTER 7. INTER-SURFACE COMPARISON STUDY

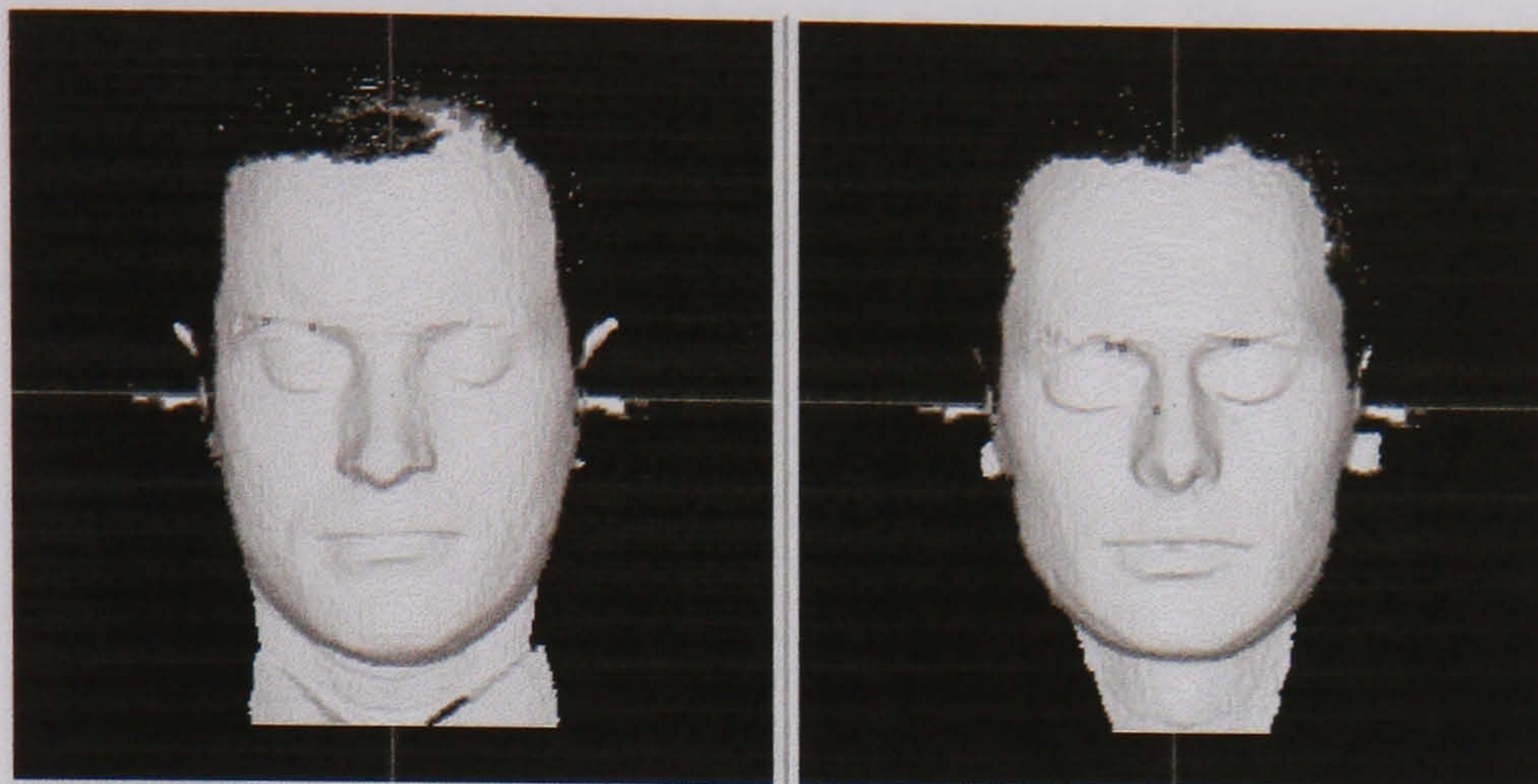


Figure 7.1: The rendered target (left) and source (right) range images used for testing method 1.

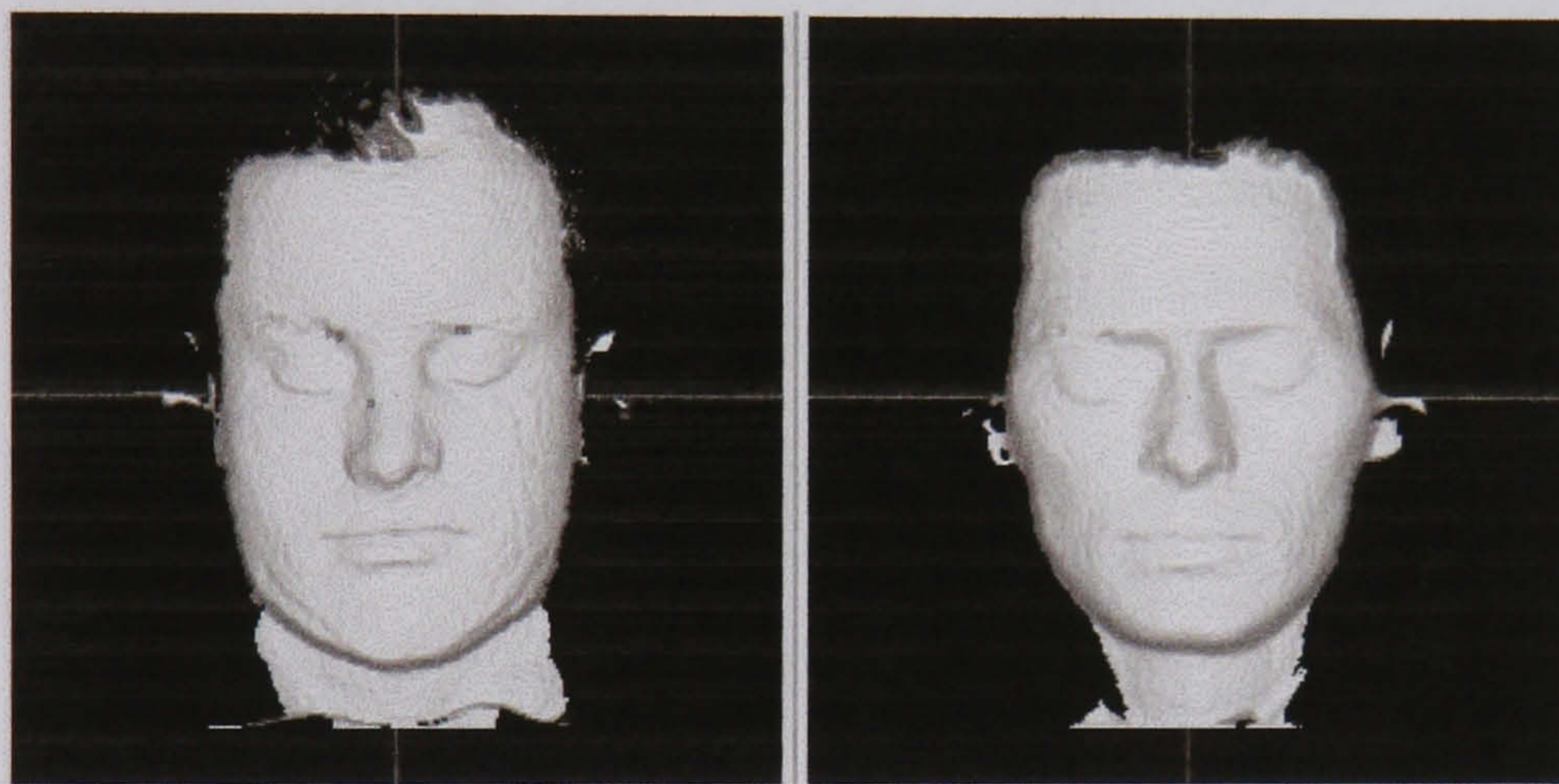


Figure 7.2: The rendered source (left) and target (right) range images after warping with method 1.



Figure 7.3: The target image (right), source image (left) and warped source image (centre) using method 1.

CHAPTER 7. INTER-SURFACE COMPARISON STUDY

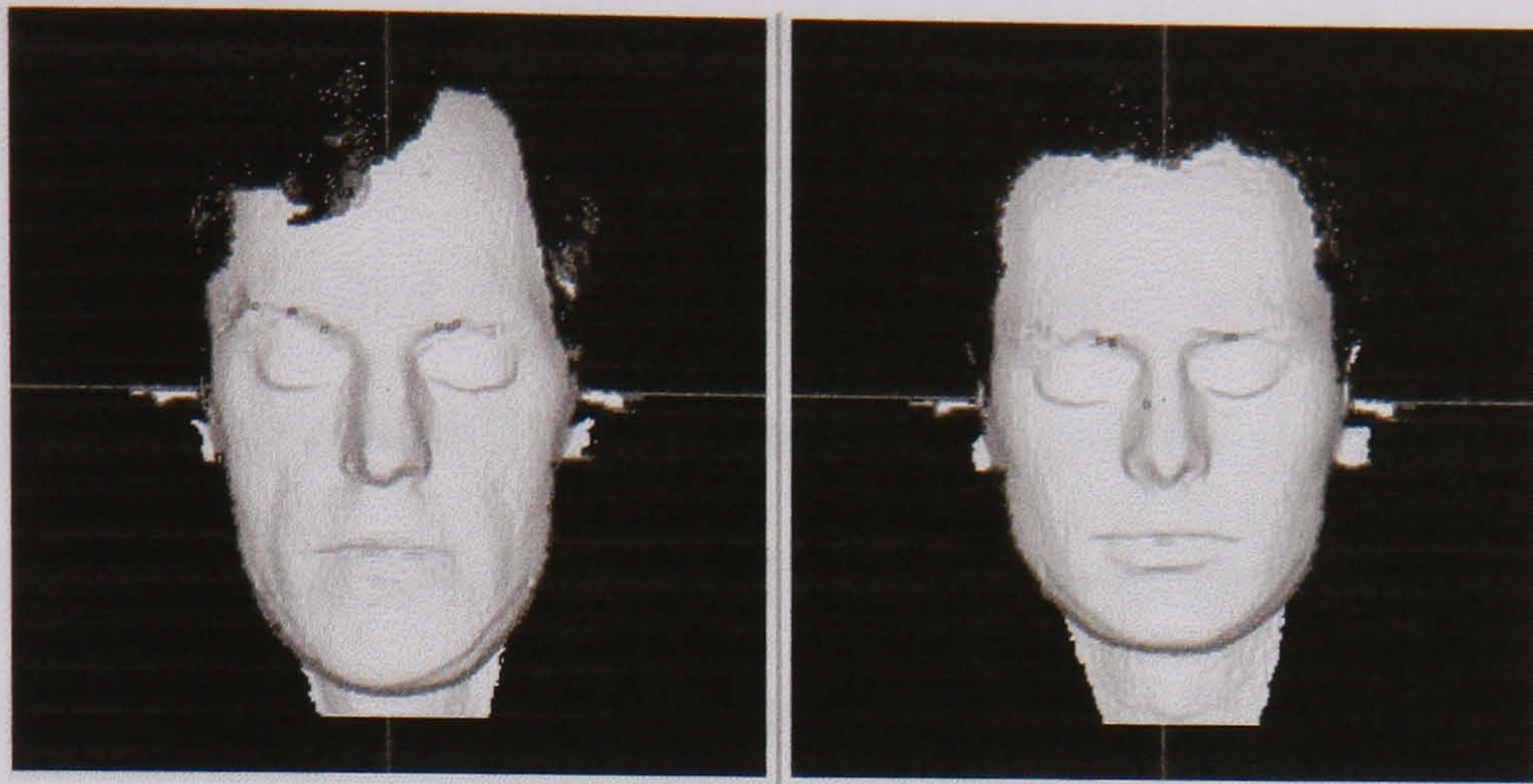


Figure 7.4: The rendered source (left) and target (right) range images before matching.

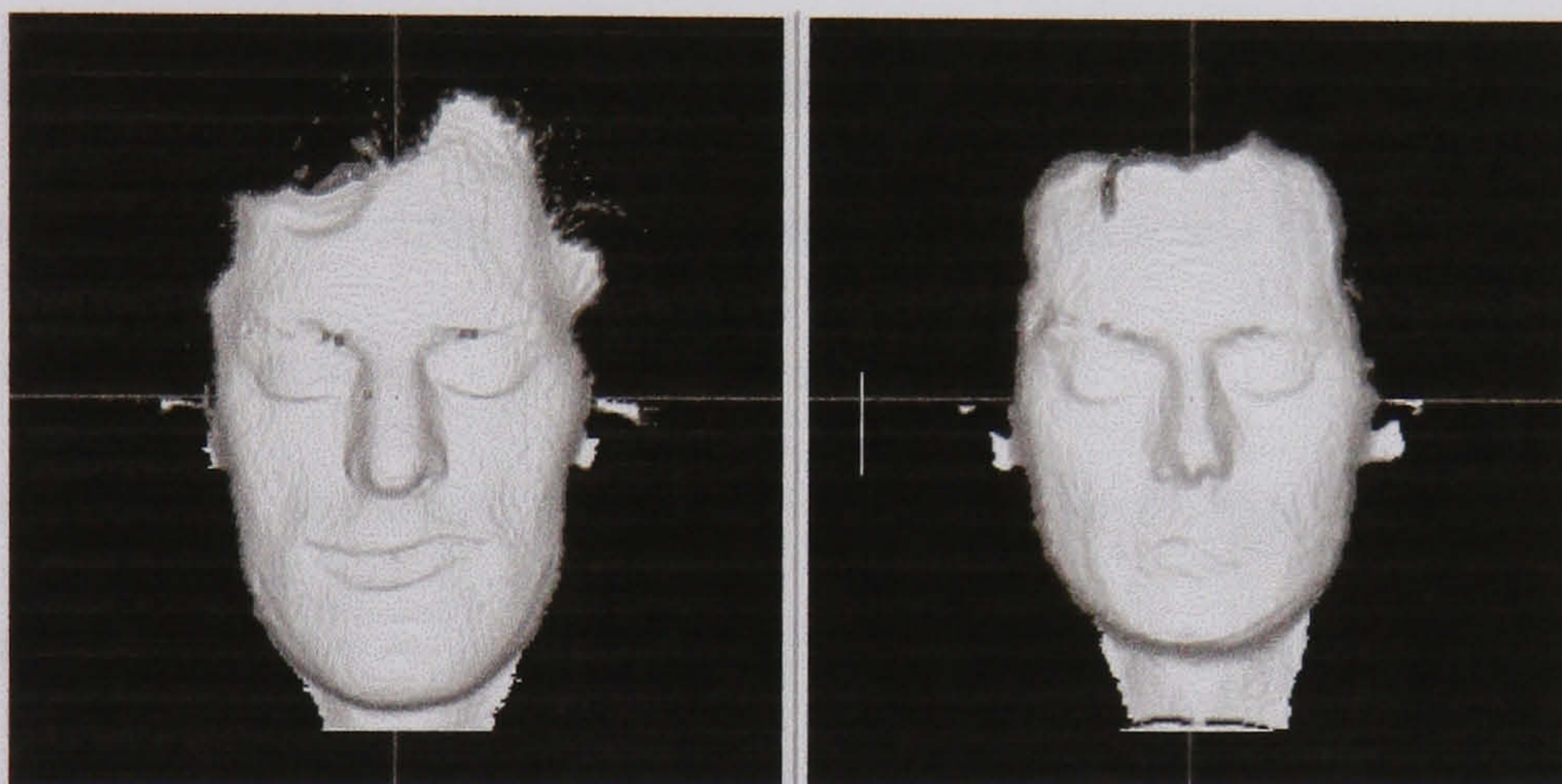


Figure 7.5: The rendered source (right) and target (left) range images after warping with method 1. Incorrect matching of the mouth is notable.

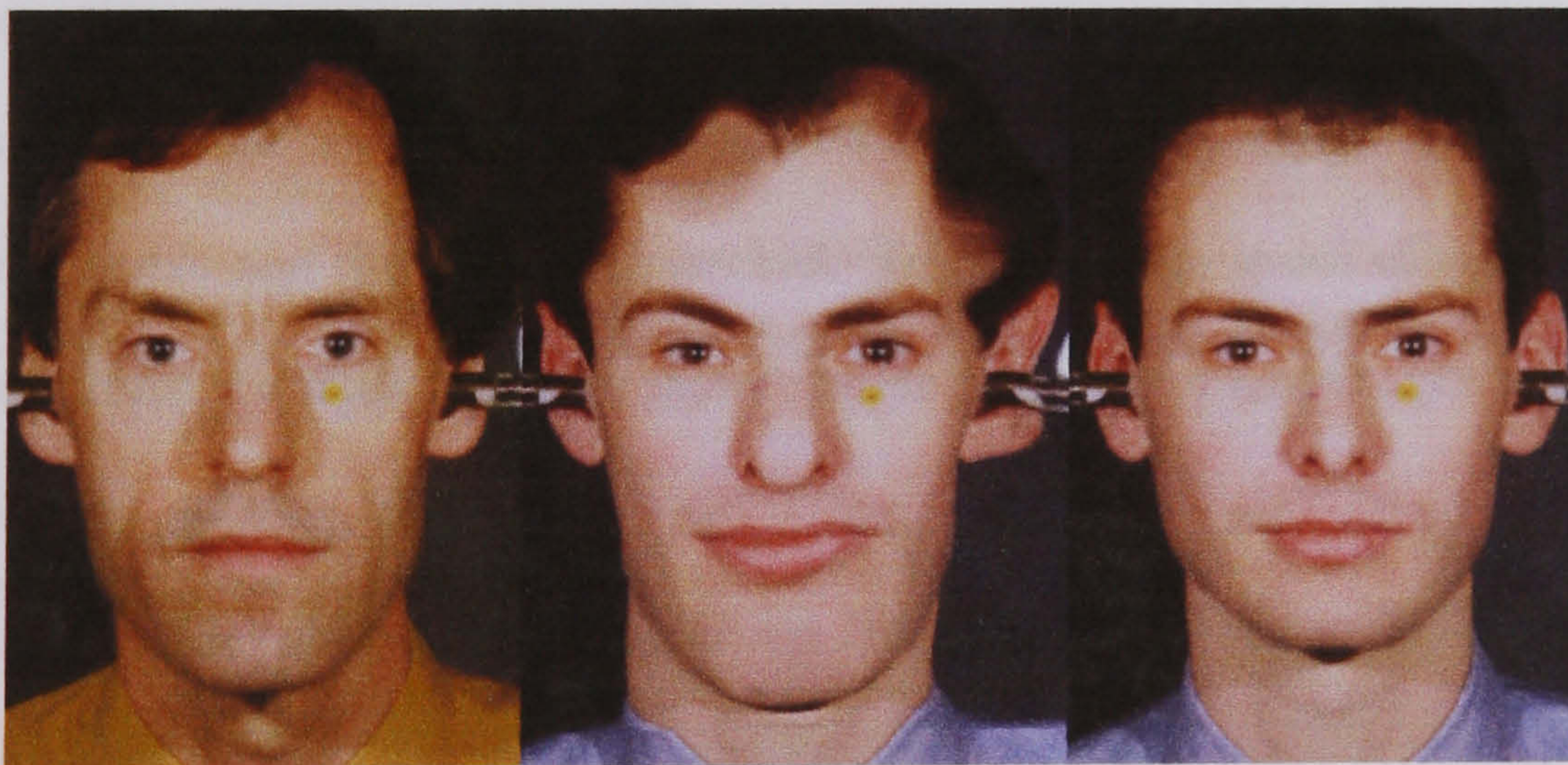


Figure 7.6: The target RGB image (left), source image (left) and warped source image (centre) after warping with method 1.

CHAPTER 7. INTER-SURFACE COMPARISON STUDY

are extracted, the gradient maxima of the facial photograph and the positive and negative curvature maxima of the laser range scan. These points are then automatically matched using a version of the iterative closest point (ICP) algorithm. The original ICP algorithm was designed for rigid-body registration using rotations and translations (24) (25). It was extended to non-rigid deformations by using a variety of approximating interpolants including quadratic spline and B-spline based approximations (178) (179). Rigid-body registration has already been achieved in the morphograph via the fixed relations principle, and so no further rigid-body constraints are imposed on the data. Instead a hierarchy of B-spline surfaces are defined on progressively finer grids to construct the warping transform.

Initially the extracted points are matched by finding the mutually closest points. Two points, a in set A and b in set B , are matched if a is the closest point in A to b and b is the closest point in B to a . Additionally points must be of the same type i.e. image gradient maxima, positive curvature maxima or negative curvature maxima. To prevent incorrect matching of gradient edges an additional constraint is imposed so that only edge points with a similar magnitude and direction are matched. To improve the speed of matching the search for the closest point is performed only in a small neighbourhood of each point.

Using the list of matched points a free-form deformation (FFD) is derived and used to warp one point set towards the other. Initially this is applied on a coarse grid to produce a smooth interpolating function that does not accurately

CHAPTER 7. INTER-SURFACE COMPARISON STUDY

satisfy the border constraints. To ensure the one-to-one property of the transformation the warping grid control-points are clipped so that they are less than 0.48 in magnitude. The process is applied iteratively, with the grid size reduced by a factor of two every time the change in maximum distance between closest points falls below a threshold. The closest-point search-area is also reduced by a factor of two along with the grid size to increase the speed of the algorithm and reduce the chances of sharp variations in the final matching. The method is presented more concisely in algorithm 3.

Algorithm 3 ICP with FFD

Inputs: Point sets $P = \{p_i\}$ and $Q = \{q_i\}$
Begin
Set initial scale $s = smax$
 $R = 0$
repeat
 Find closest point subsets S in P and T in Q
 Find maximum distance between matched points D
 Find W the FFD from S to T at scale s
 Warp points in P using W
 if $NOT(clipped)$ **AND** $(R - D) < threshold$ **then**
 $s = s/2$
 end if
 $R = D$
until $s < 1$
Outputs: Point sets S and T
End

This algorithm produces a set of matched points between the study and the subject. These can be interpolated using a multi-level free-from-deformation (MFFD) to warp the study range and colour images into the shape of target range and colour image.

CHAPTER 7. INTER-SURFACE COMPARISON STUDY

7.4.2 Implementation

Edge and Curvature Maxima Detection

The edge points used from the photographic image are found from the (greyscale) gradient as the points that obtain a maximum value in the direction of the gradient vector. The partial derivatives along the x and y axes are found by convolution with smoothed finite-difference filters ∂_x and ∂_y respectively. This is known as Canny edge detection (163) and is described in algorithm 4.

For the laser-range data important image features do not only lie at the gradient maxima but also at the points of highest curvature. An algorithm similar to Canny edge detection is used to calculate the points at which the curvature obtains maximum values in the associated principal direction as shown in algorithm 5. The curvature is calculated using finite difference filters for the derivatives as explained in section 6.3.

Algorithm 4 Canny edge detection

```
INPUT: Image  $f(x, y)$ 
Begin
Calculate gradient  $\nabla f(x, y) \approx (\partial_x * f(x, y), \partial_y * f(x, y)) =$ 
 $(u(x, y), v(x, y)) = G(x, y)$ 
Point list  $P = \{\}$ 
for  $y = 0$  to  $height$  do do
  for  $x = 0$  to  $width$  do do
    if  $|G(x, y)| > |G(x + u(x, y), y + v(x, y))|$  AND  $|G(x, y)| >$ 
 $|G(x - u(x, y), y - v(x, y))|$  then
      Append  $(x, y)$  to  $P$ 
    end if
  end for
end for
End
OUTPUT: Point list  $P$ , Gradient images  $(u(x, y), v(x, y))$ 
```

Algorithm 5 Curvature edge detection

INPUT: Range image $f(x, y)$
 Begin
 Calculate curvature $k(x, y)$ and principal direction $(u(x, y), v(x, y))$
 Point list $P = \{\}$
 for $y = 0$ to $height$ do do
 for $x = 0$ to $width$ do do
 if $|k(x, y)| > |k(x + u(x, y), y + v(x, y))|$ AND $|k(x, y)| > |k(x - u(x, y), y - v(x, y))|$ then
 Append (x, y) to P
 end if
 end for
 end for
 End
 OUTPUT: Point list P , Curvature image $k(x, y)$, principal direction images $(u(x, y), v(x, y))$

Closest Point Matching

The edge and curvature maximum points are matched to points (within a specified distance) of the same type and with a similar magnitude. For edge points an additional restriction is imposed so that the gradients have a similar direction, in order to prevent matching of light-to-dark edges with dark-to-light edges. Algorithm 6 describes this method more precisely.

7.4.3 Results

Figure 7.7 shows a typical example of the iterative closest point matching (corresponding to figure 7.9). Figures 7.8, 7.9 and 7.10 show the results of warping individuals to a target image using this method. In most cases the matching produced is excellent, but occasional errors (for example around the eyes in Figure 7.10) suggest that the method may have difficulty in matching differently coloured faces or those with a markedly different shape.

Algorithm 6 Match closest points

INPUT: Point lists P and Q , magnitude images $M_p(x, y)$, $M_q(x, y)$ and angle images $A_p(x, y)$, $A_q(x, y)$

Begin

$S = \{\}, T = \{\}$

for all i do

$min = \infty, J = -1$

 for all j do

 if $|p_i - q_j| < min$ AND $|M_p(p_i) - M_q(q_j)| < magthresh$ AND $|A_p(p_i) - A_q(q_j)| < angtresh$ then

$min = |p_i - q_j|$

$J = j$

 end if

 end for

 if $min < distthresh$ AND $J > -1$ then

$min = \infty, I = -1$

 for all j do

 if $|p_j - q_J| < min$ AND $|M_p(p_j) - M_q(q_J)| < magthresh$ AND $|A_p(p_j) - A_q(q_J)| < angtresh$ then

$min = |p_j - q_J|$

$I = j$

 end if

 end for

 if $I = i$ then

 Append p_i to S

 Append q_J to T

 end if

 end if

end for

End

OUTPUT: Matched point lists S and T

CHAPTER 7. INTER-SURFACE COMPARISON STUDY

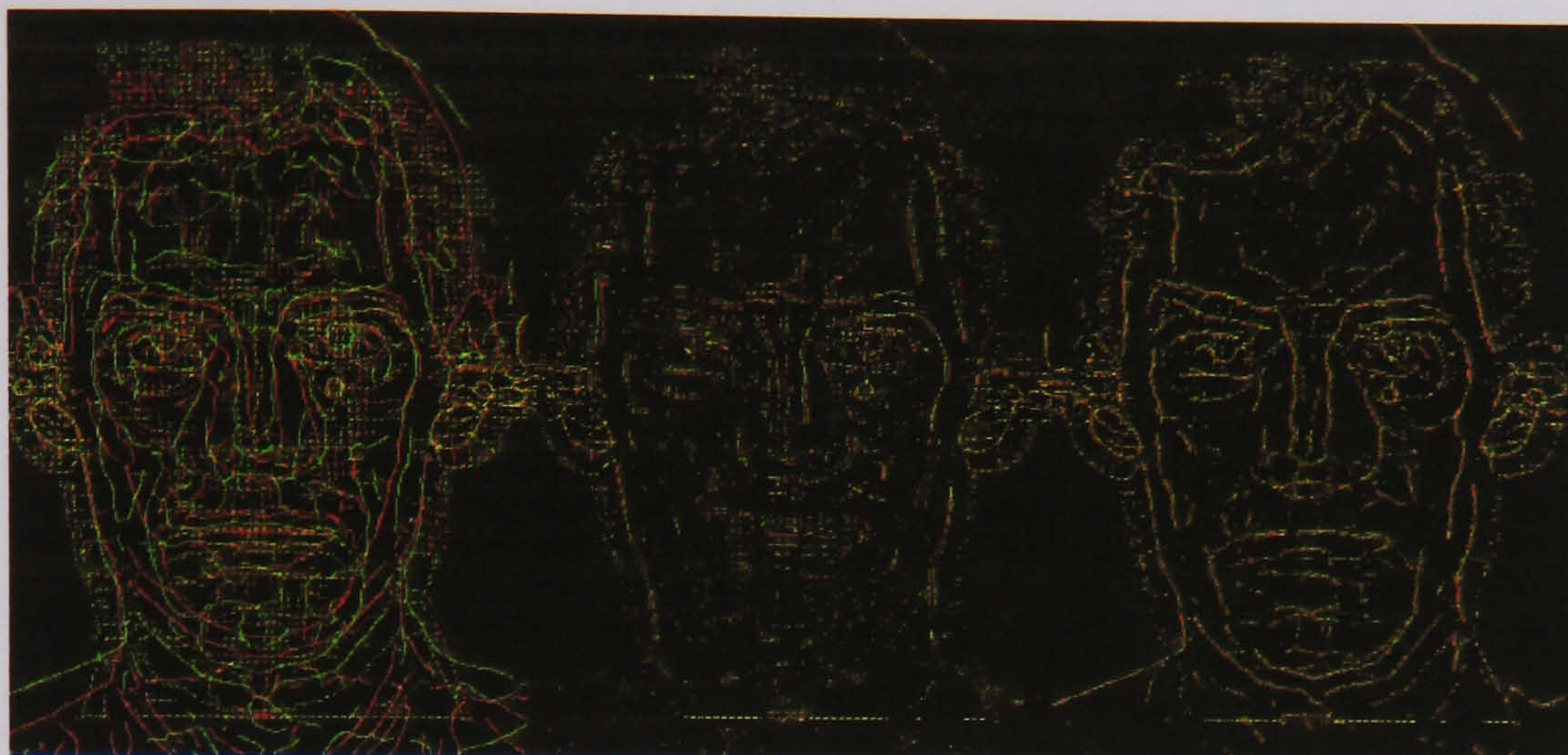


Figure 7.7: Edge points are shown as green in the target image and red in the source image. The edges extracted from both images are shown on the left. At the start of the process 4605 points are matched (centre) and by the end 6590 points are matched (right).

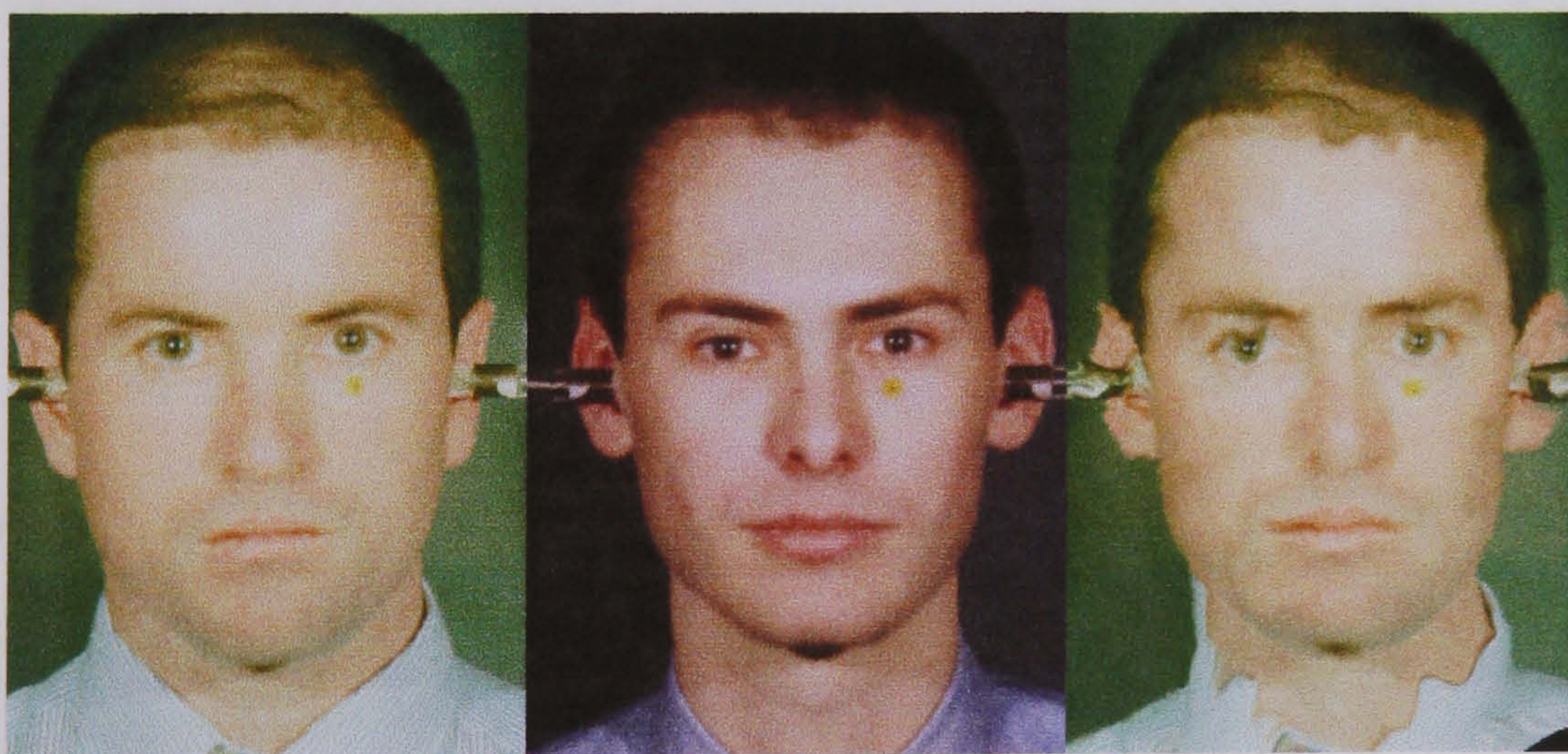


Figure 7.8: Automatic matching of the source image (left) to the target image (centre) gives the warped source (right).

CHAPTER 7. INTER-SURFACE COMPARISON STUDY

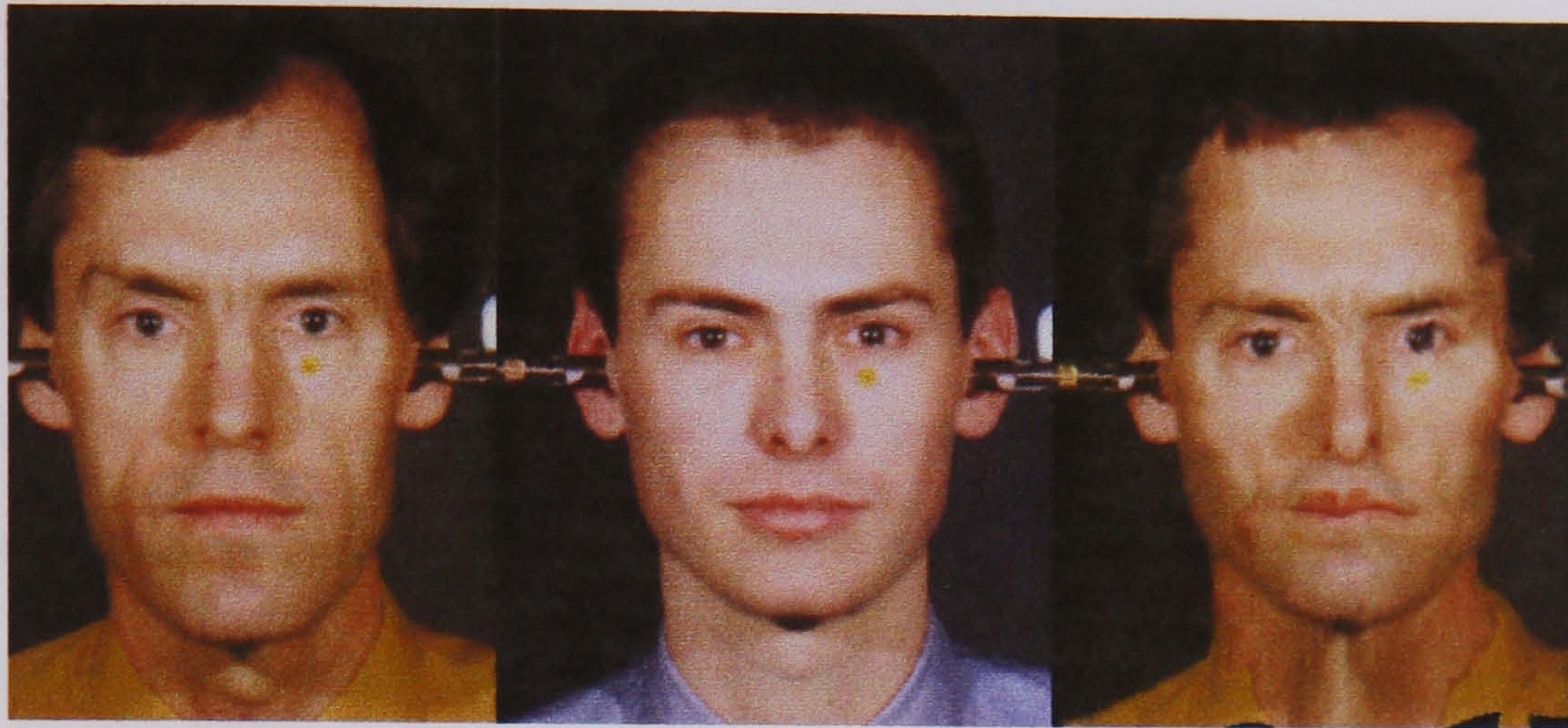


Figure 7.9: Another automatic maxima matching example.

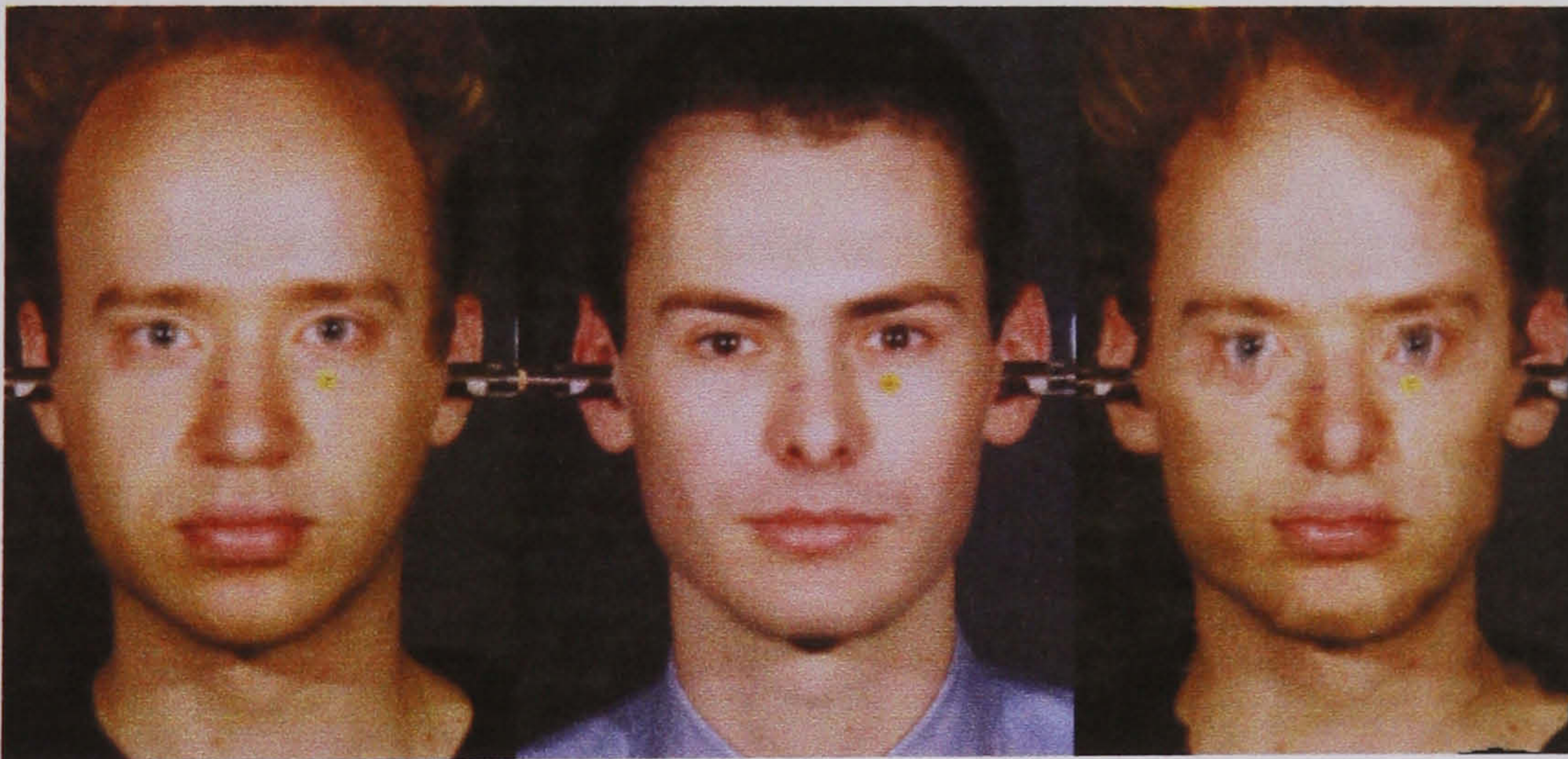


Figure 7.10: Another automatic maxima matching example.

7.5 Method 3: Feature based warping with interactive labelling

7.5.1 Method overview

This method uses interactively labelled features to compare individuals. Two types of facial features are used: point landmarks and facial contours. The facial image contours used are further divided into three kinds: those with a large gradient magnitude, a large positive curvature or a large negative curvature. The edge extraction is performed with snakes attracted to one of these feature types, which is specified by the user. Points at the end of a contour or at the junction of two or more contours represent important anatomical features or landmarks. The template used is constructed from a set of contours connected at landmarks. Hence the optimisation of the boundaries to the desired image features will also tend to constrain the landmarks to the correct locations. Using a connected set of contours also helps to prevent accidentally crossing contours which could cause the image to twist or fold-over. Other landmarks not associated with image contours, such as the centres of the pupils and the orbitale marker are placed manually. The template used in the current study is shown in figure 7.11. This is not intended as a de facto standard, but has proved useful in testing the new methods.

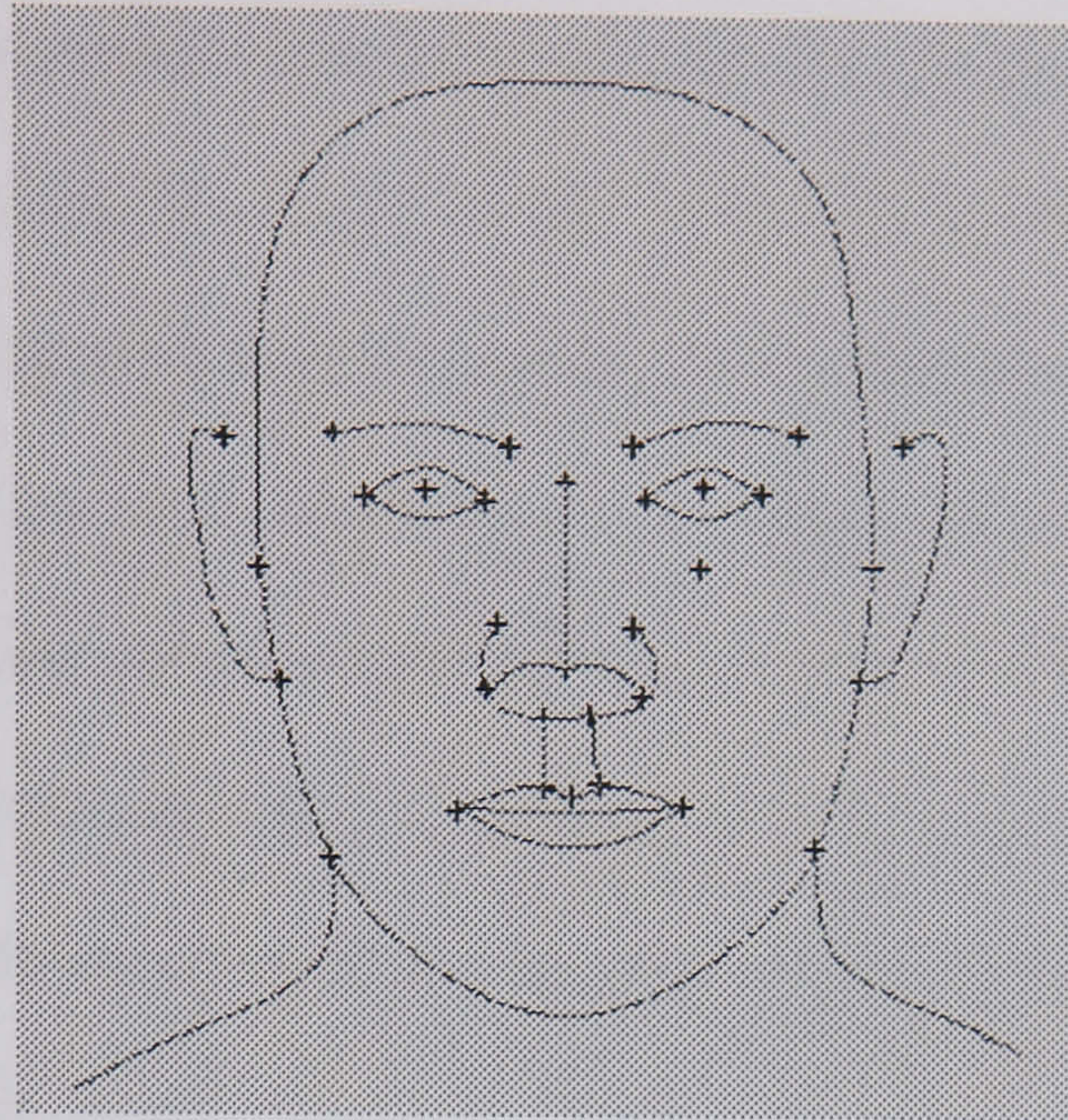


Figure 7.11: The feature template used in method 3.

7.5.2 Implementation

Template fitting

A template is defined manually by an operator using landmark points, open contours and closed contours. The contours are constructed using cubic spline curves, with the operator adding control points along the contour. If the operator clicks on a landmark point while constructing a contour, that contour will be attached to that landmark. Several contours may be attached to a single landmark.

The first stage in fitting the template to a subject is to manually move the landmarks and the contour control points so that the template approximately fits the individual's facial data. Moving a landmark also adjusts all the contours connected to it. The second stage improves this fitting automatically using snakes.

CHAPTER 7. INTER-SURFACE COMPARISON STUDY

The basic snake method has been adapted for use in this work in several ways. Firstly, because the contours are *connected* at the landmarks all the contours must be iterated simultaneously. To do this efficiently the contours' stiffness equations are all inverted during the initialisation stage, then during each iteration the contours are adjusted one at a time. The different contours connected at a landmark will all attempt to pull the landmark in different directions. The displacement of the landmark is calculated as the average of these displacements.

The second alteration attempts to increase the influence of the initial suggestion supplied by the user. Traditional snakes try to minimise the bending energy of the spline even in its initial position, i.e. an initially curved contour on a featureless image will eventually become straight. To prevent this behaviour, rather than regularising the *positions* of the contour points, the *displacements* along the contour are regularised. This means that the contour will have minimum bending energy in its initial shape, however twisted.

Snakes can occasionally become 'distracted' from a small local edge by a larger edge nearby. Such a snake will gradually move completely away from the local edge. An additional parameter is included in the snake model so that the displacements from the original position are also minimised. This means that, ignoring image forces, the contour will have its energy minimised in its original position.

The final modification to the original snake model exploits the fact that the initialising cubic polynomial curve is always sampled at regular intervals

CHAPTER 7. INTER-SURFACE COMPARISON STUDY

along its length. Hence the terms involving the calculation of the current spring lengths can be eliminated. By regularising the *displacement* along the contour, rather than the position, all the nonlinear elastic terms can be eliminated. This allows the use of regularising filters along the contour length, rather than more computationally expensive matrix inversion and so allows the contours to be initialised and iterated very quickly.

Contour comparison

To relate points along different contours, the contours are parameterised using the fraction of length along the contour from one end to the other. If a contour is closed it can be split into open contour segments provided it contains one or more clear landmarks along its length. If it does not contain a landmark, an end point can be chosen so as to minimise the total displacement from points in a corresponding contour. In order to perform comparisons and statistics between a set of contours, the line's length in the parametric coordinate system is normalised to 1 by dividing by the total length. This ensures that a point fraction t from one end of a line is related to the corresponding point fraction t from the same end of every other line. Hence the problem of relating contours is reduced to the problem of relating a set of labelled points, for which measurements and statistics are well defined.

CHAPTER 7. INTER-SURFACE COMPARISON STUDY

Surface comparison

In order to compare points across the range-map surface, corresponding points need to be labelled. The labels should correspond on the points that have already been labelled as landmarks or along the parametric contours and should vary smoothly between them. Therefore a smooth parametric description of the surface is required, with border constraints at the landmark and contour points. This requires interpolation of the specified border constraints. The large number of points generated along the parametric contours means that analytical thin-plate spline methods are too slow for solving this interpolation problem. Instead multi-level free-form deformations are used, which guarantees C^2 continuity and the one-to-one property of the mapping without compromising efficiency.

7.5.3 Results

The snake based method can adapt a feature template to an individual, given a reasonable initial guess, as shown in figure 7.12. Given two such templates this method reliably warps the corresponding individual's images. Examples are shown in figures 7.13 and 7.14.

7.6 Conclusions and Choice of Method

All three of the matching algorithms are capable of credibly matching individual facial images in the majority of cases. This is consistent with the results presented in the literature for the equivalent methods for three-dimensional vol-

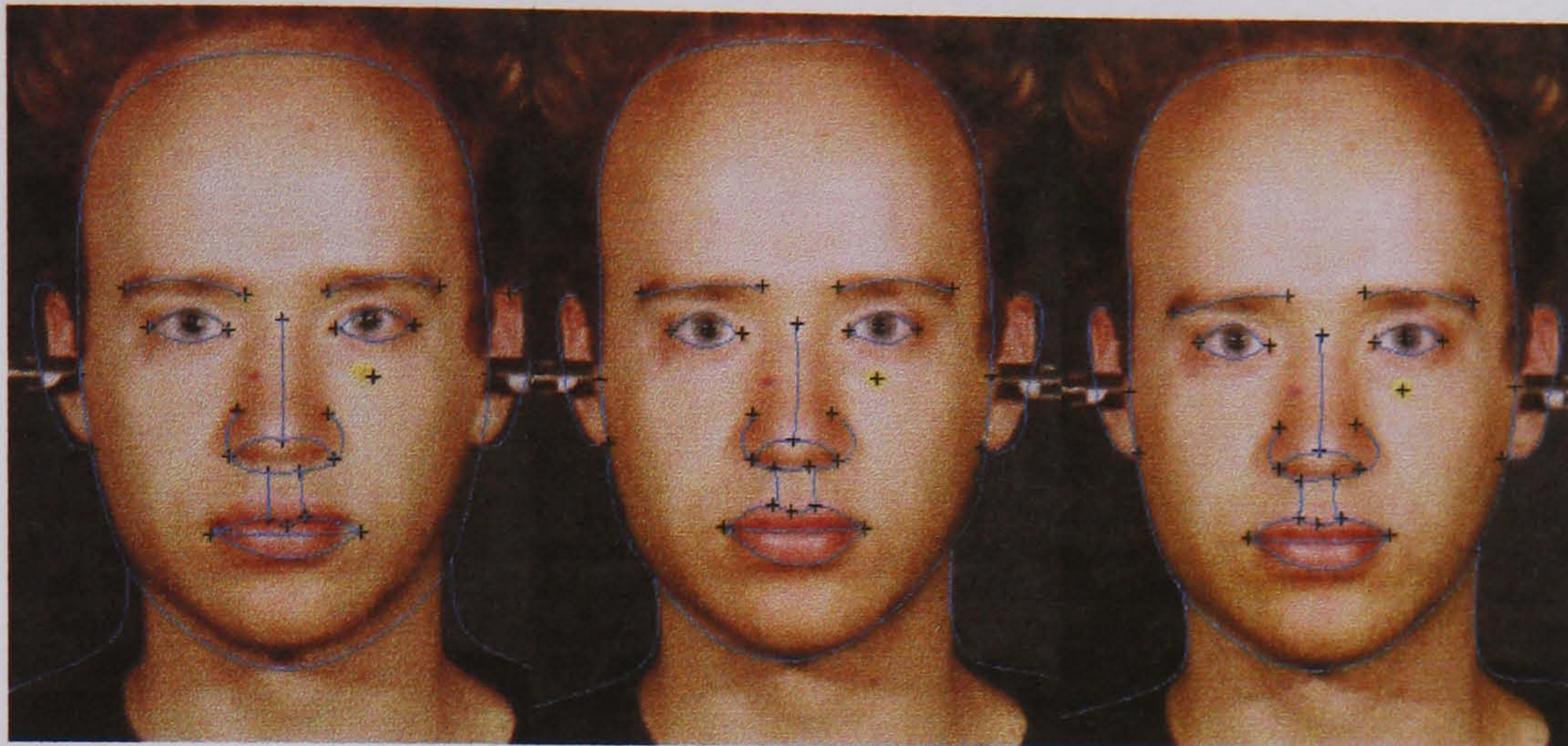


Figure 7.12: Adaptation of the template to an individual. The original template (left) is adapted manually to approximate the shape of the individual face shape (centre) and then snakes are used to refine the fit (right).



Figure 7.13: An example of matching a source image (left) to a target (centre) to give the warped source image (right) using feature based warping.

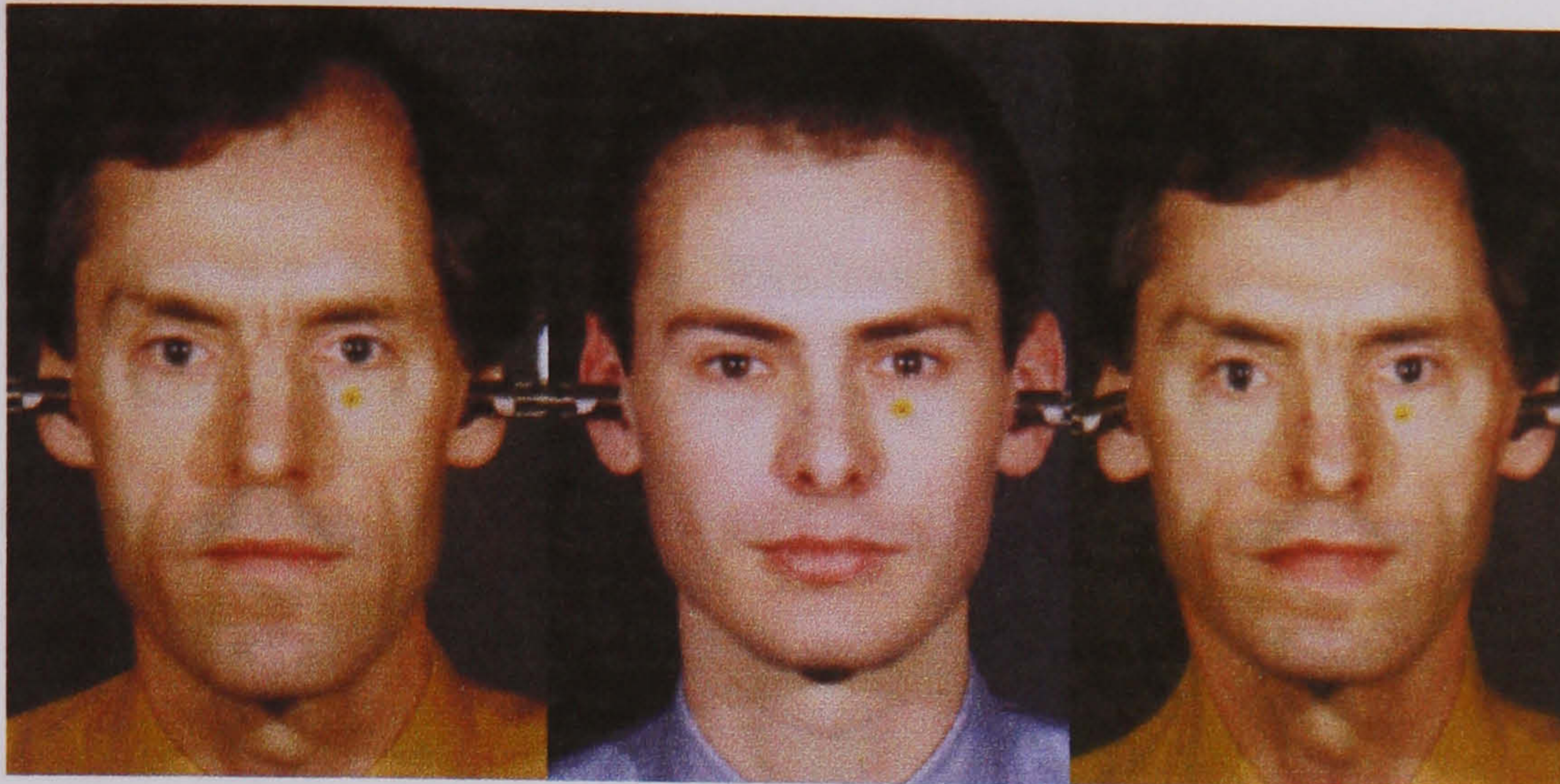


Figure 7.14: An example of matching a long-faced subject (left) to a target image (centre) to give the warped source image (right) using the feature based warping method.

umetric data. Method 1 did have difficulty correctly matching in one case (the long-faced subject). It is impossible to test the matching of every possible face to every other, but failure in this case suggests that the algorithm is not robust and so will fail in many other cases. The surface shapes of many facial features are too subtle for this algorithm to identify, and hence match them correctly.

Methods 2 and 3 both involve the identification and matching of edge and curvature points. This means that they are more likely to correctly match facial features. Method 2 automatically extracts edges and curvature maxima points and matches them automatically using an iterative closest point method. In the tests with our database of (mainly) normal, white adults the algorithm proved robust. Further testing is required on patients with abnormal or differently coloured faces, to ensure that the matching remains robust.

Method 3 matches contours defined by the user in a template and interactively adapted to each subject using snakes. This ensures that unusual faces,

CHAPTER 7. INTER-SURFACE COMPARISON STUDY

or those from diverse ethnic groups can easily be accommodated. The use of snakes to assist in segmenting the selected facial contours reduces the burden on the user and improves accuracy. This level of interaction should give clinicians confidence in the method, whereas fully automatic methods may give the impression of being a 'black-box' with unpredictable output. The only drawback is that a user must define the initial template, a procedure which could be subject to subconscious bias as to the most important facial features.

The mixture of user interaction with a degree of automation makes method 3 a more robust and more flexible method than the fully automatic methods (methods 1 and 2). As a result, method 3 was chosen as the inter-subject comparison method for the remainder of this thesis.

Part IV

Statistics, Results and Applications

Chapter 8

Surface Statistics

8.1 Introduction

In Part III the various available methods for inter-subject matching of corresponding anatomical features were reviewed. Three methods were then adapted for texture-mapped laser-range facial surface data and tested. This section extends the application of surface comparisons from individuals to statistical groups. To do this, methods for constructing facial mean and distribution data need to be devised. Because of the close relationship between one-to-one and statistical comparisons the essentials of these ideas have already been reviewed in chapter 5.

In this chapter two new methods for constructing facial averages are described and tested. These represent different compromises between complexity and the quality of the results.

CHAPTER 8. SURFACE STATISTICS

The first method calculates the probability that each 3D point in the morphanalytic reference frame has of lying inside the human head. Points near the morphanalytic origin are certain to lie inside the head and points at a large distance (e.g. 1m) from the origin are certain not to. Between these two extremes there is a gradual decrease in probability that depends upon the shapes of the heads in the sample. This method requires little processing and no user interaction, but does not allow the construction of averages from small samples.

The second method uses feature-based warping to construct an average consisting of the mean surface depth and colour and the distribution. The inter-subject comparison methods described in chapter 7 label related points in different scans. Finding the mean 3D position and colour of each related point allows the construction of the mean surface. The normal distribution about this mean can also be found in terms of the covariance matrix, calculated at each point.

8.2 Method 1: Probability histomorphogram

8.2.1 Method description

The first technique is a very simple and quick method for constructing mean and distribution facial data. This method treats the laser-range data as a simple surface, ignoring secondary surface characteristics such as curvature extrema contours, intensity change maxima contours or landmarks. The goal is to produce a 3D probability histogram in which the value in each 3D bin represents the probability of that point lying inside the head. The algorithm starts with an

CHAPTER 8. SURFACE STATISTICS

empty 3D volume (i.e. all voxels set to zero) and a single height map is added using the pseudo-code algorithm 7.

Algorithm 7 Add to histomorphogram

```
INPUT:
Volume  $V(x, y, z)$ , Height Image  $h(x, y)$ , Sample Size  $S$ 
BEGIN
 $S = S + 1$ 
for all  $(x, y)$  in  $h$  do
  for  $z = 0$  to  $h(x, y)$  do
     $V(x, y, z) = V(x, y, z) + 1$ 
  end for
end for
End
```

The variable S keeps a record of the number of facial scans that have been added to the volume. This can then be used to convert the frequency values to probabilities via division when required.

The mean facial surface is given by the volume's isosurface where the probability is equal to 0.5. i.e the surface given by the implicit equation,

$$V(x, y, z) = 0.5 * S \quad (8.1)$$

for volume data set $V(x, y, z)$ and sample size S . Other isosurfaces correspond to the various univariate standard deviations (u.s.d.). For example 68.5 % of a sample lies within ± 1 univariate standard deviation of the mean. This corresponds to a probability of 0.5 ± 0.342 . Hence one standard deviation smaller than the mean is given by the isosurface with probability 0.842 and one standard deviation larger than the mean by the isosurface with probability 0.158. Similarly the second univariate standard deviation isosurfaces are given by $0.5 \pm 0.477 =$

CHAPTER 8. SURFACE STATISTICS

0.977 or 0.023 and the third by $0.5 \pm 0.4985 = 0.9985$ or 0.0015. These surfaces can be visualised by volume rendering the histomorphogram with the intensity threshold set to the appropriate fraction of the sample size.

In order to assess an individual surface visually, the probability is calculated for each point in the laser-range surface dependent on its position in the histomorphogram. These probabilities are converted to colours using a look-up-table, which are used to produce a texture map that is pasted onto the rendered surface.

8.2.2 Results

Figure 8.1 shows the mean and standard deviation surfaces from the sample of male subjects and figure 8.2 shows the mean and standard deviation surfaces from the sample of female subjects. These look like plausible faces of individuals even though the sample size is quite small. This implies that the sample of faces are in some sense normally distributed about the mean. Figure 8.3 shows the results of comparing an adult cleft palate subject, a long-faced subject and a normal subject to the male histomorphogram using the texture mapping method. Figure 8.4 shows the results of comparing three female subjects to the female histomorphogram.

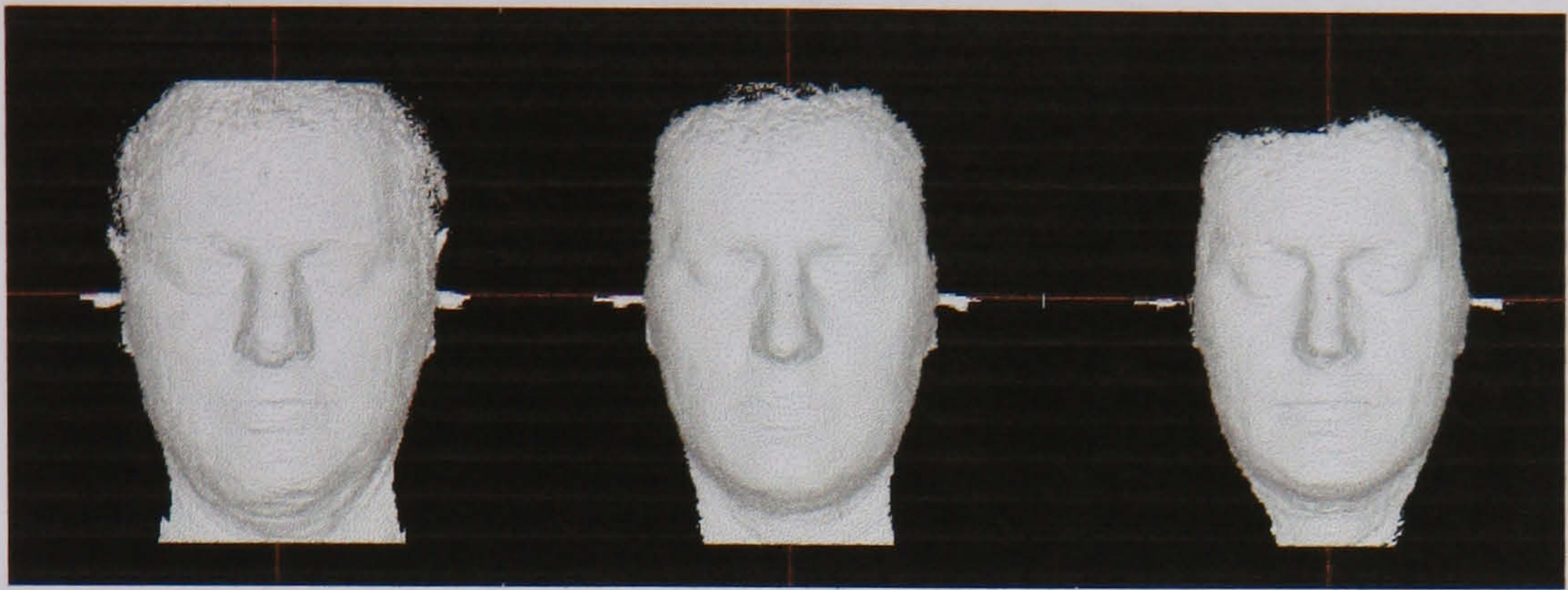


Figure 8.1: The mean (centre), minus one standard deviation (right) and plus one standard deviation (left) isosurfaces of the male probability histomorphogram.

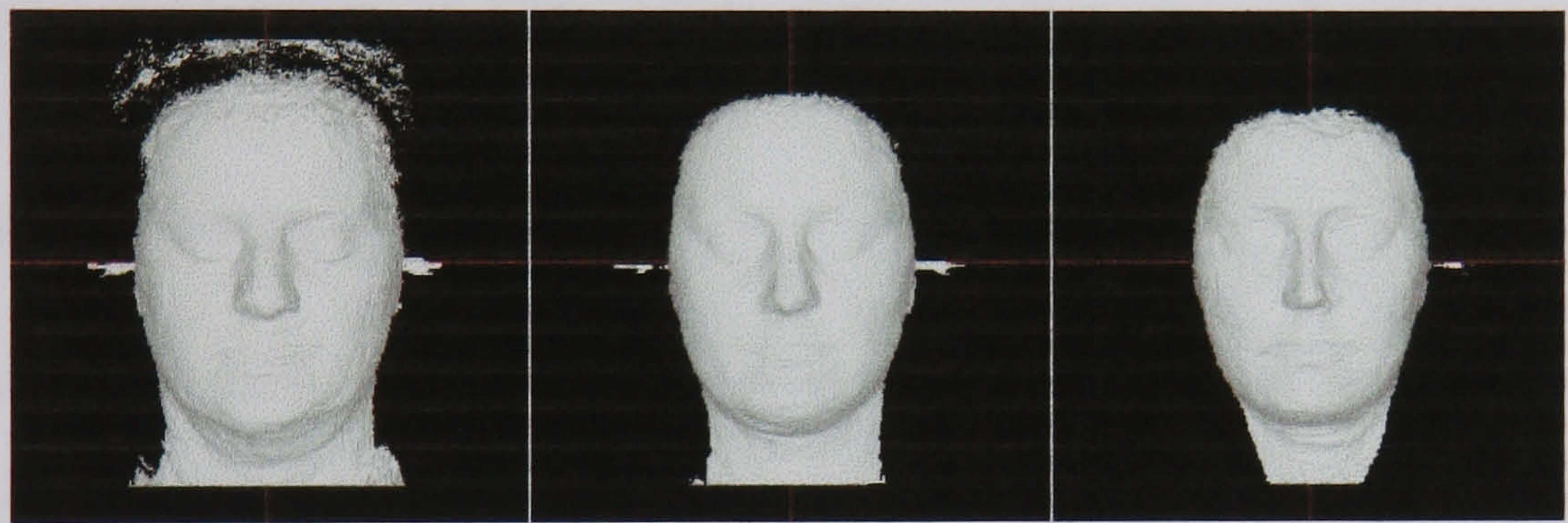


Figure 8.2: The mean (centre), minus one standard deviation (right) and plus one standard deviation (left) isosurfaces of the female probability histomorphogram.

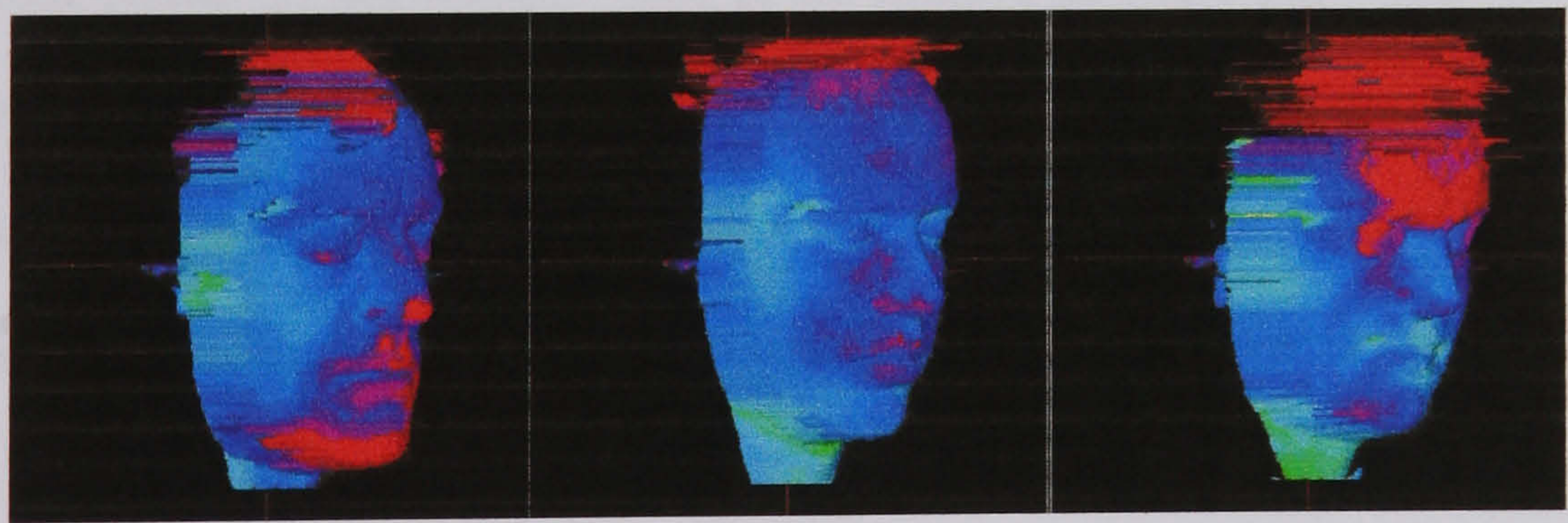


Figure 8.3: Comparison of a long faced subject (right), a normal subject (centre) and an adult cleft palate subject (right) to the male histomorphogram.

Key: Probability 0.0 0.2 0.4 0.6 0.8 1.0
U.S.D +1 0 -1

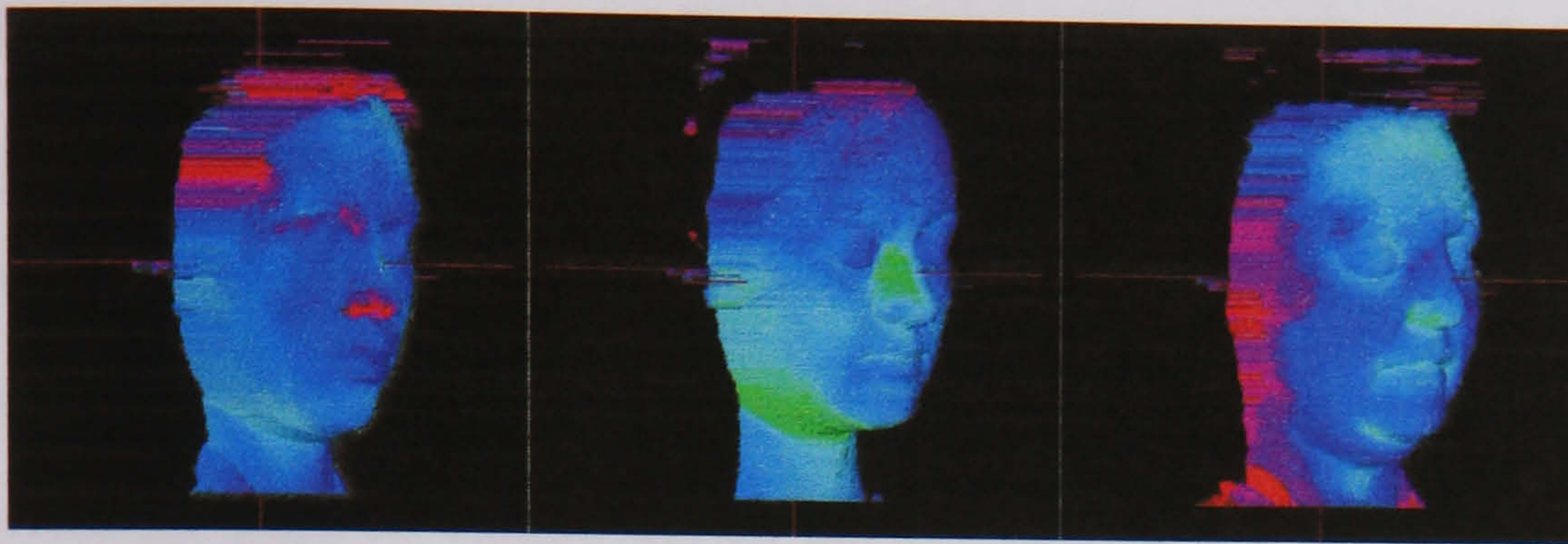


Figure 8.4: Comparison of three of the female volunteers to the female histogram.

Key: Probability 0.0 0.2 0.4 0.6 0.8 1.0
 U.S.D +1 0 -1

8.3 Method 2: Warping based averaging

8.3.1 Method overview

Due to the fixed relations registration system, each point in the laser-range data has a 3D coordinate with respect to the external reference frame. The problem is to compare the position of three-dimensional points between individuals and statistically across population samples. In order to make credible comparisons, related points on the surfaces need to be labelled in some way. The warping based matching method described in section 7.5 allows facial image points from different subject's images that possess the same parametric coordinate to be related. Hence point-based measurements and statistics can be used to create facial image averages. Section 8.3.2 describes the tools necessary for the measurement and statistical analysis of three-dimensional points (98).

The construction of the average facial surfaces consists of four steps. The first step labels the facial images using a template of connected contours. The second

CHAPTER 8. SURFACE STATISTICS

step calculates the mean template by parameterising the contours by fraction of arc length. The third step warps each subject's images into the mean (2D) shape by interpolating the translations between the subject's template and the mean template. Finally the images are averaged on a pixel by pixel basis to create the mean 3D surface and 2D photographic image. Using the mean, the distribution can be calculated in terms of the covariance matrix at each point. To create an average facial surface, distribution and colour image, algorithm 8 is used.

Individual range scans can be compared with the average by calculating the spatial probability relative to the corresponding point and distribution in the average. These probabilities are converted into colours using a look-up table and then pasted onto the surface using a texture mapping approach.

Algorithm 8 Create average with template

Inputs: Photographic images I_i , Depth maps H_i , Feature template T

Begin

for all subject's i **do**

$T_i = \text{Adapt the template } T \text{ to images } H_i \text{ and } I_i \text{ using snakes}$

end for

$\bar{T} = \text{Average templates } T_i \text{ by parameterising the contours}$

Zero average images \bar{H} , \bar{I} and \bar{D}

for all subject's i **do**

$W_i = \text{Find warp from } \bar{T} \text{ to } T_i$

$\bar{H} = \bar{H} + (\text{Warp } H_i \text{ using } W_i)$

$\bar{I} = \bar{I} + (\text{Warp } I_i \text{ using } W_i)$

$\bar{D} = \bar{D} + (\text{Convert } W_i \text{ and } H_i \text{ to distribution sums})$

end for

$\bar{H} = \bar{H}/n$

$\bar{I} = \bar{I}/n$

$\bar{D} = \text{Convert } \bar{D} \text{ to covariance matrices}$

End

Outputs: Average depth map \bar{H} , Average image \bar{I} , Distribution \bar{D}

CHAPTER 8. SURFACE STATISTICS

8.3.2 Multivariate Statistical Methods

Displacement

Measuring the displacement between two 3D points is trivial i.e.

$$\mathbf{d}_{ij} = \mathbf{r}_i - \mathbf{r}_j \quad (8.2)$$

where \mathbf{d}_{ij} is the vector displacement of the point whose position vector is \mathbf{r}_i relative to the point whose position vector is \mathbf{r}_j .

Mean

The mean of a set of N 3D points is defined as

$$\bar{\mathbf{r}} = \frac{1}{N} \sum_{i=0}^{N-1} \mathbf{r}_i \quad (8.3)$$

for points $\mathbf{r}_i = (x_i, y_i, z_i)$ and mean $\bar{\mathbf{r}}$.

Distribution

The normal distribution of 3D points can be expressed in terms of the covariance matrix

$$\mathbf{C} = \begin{bmatrix} c_{xx} & c_{xy} & c_{xz} \\ c_{yx} & c_{yy} & c_{yz} \\ c_{zx} & c_{zy} & c_{zz} \end{bmatrix} \quad (8.4)$$

CHAPTER 8. SURFACE STATISTICS

where

$$c_{ij} = \frac{1}{N-1} \sum_{n=0}^N (i_n - \bar{i}) (j_n - \bar{j}) \quad (8.5)$$

for a point $\mathbf{r} = (x, y, z)$. The probability of lying at a point \mathbf{r} is given by

$$p(\mathbf{r}) = \frac{1}{(2\pi)^{\frac{3}{2}} |\mathbf{C}|^{\frac{1}{2}}} \exp \left[-\frac{1}{2} (\mathbf{r} - \bar{\mathbf{r}})^t \mathbf{C}^{-1} (\mathbf{r} - \bar{\mathbf{r}}) \right] \quad (8.6)$$

The probability of lying at any single point in a 3D distribution is very small, even at the average position itself. A more useful measure is the probability of lying within a certain volume around the average. The normal probability distribution in three dimensions has nested ellipsoidal isosurfaces centred on the average. The probability of lying within a particular ellipsoid, E is given by the integral

$$P(R) = \int \int \int_E p(\mathbf{r}) d\mathbf{r} \quad (8.7)$$

Where the integral is performed over the ellipsoidal domain E given by

$$(\mathbf{r} - \bar{\mathbf{r}})^t \mathbf{C}^{-1} (\mathbf{r} - \bar{\mathbf{r}}) = R^2 \quad (8.8)$$

for some Mahalanobis distance R . By a change of variables

$$\mathbf{x} = \mathbf{C}^{-\frac{1}{2}} (\mathbf{r} - \bar{\mathbf{r}}) \quad (8.9)$$

The integral can be performed over a spherical domain, given by,

CHAPTER 8. SURFACE STATISTICS

$$p(R) = \frac{1}{(2\pi)^{\frac{3}{2}}} \int \int \int_R \exp\left(-\frac{1}{2}|\mathbf{x}|^2\right) d\mathbf{x} \quad (8.10)$$

A further change of variables into spherical polar coordinates gives,

$$p(R) = \frac{1}{(2\pi)^{\frac{3}{2}}} \int_0^{2\pi} d\phi \int_0^\pi \sin\theta d\theta \int_0^R r^2 e^{-\frac{r^2}{2}} dr \quad (8.11)$$

The first two integrals are trivial leaving

$$p(R) = \frac{2}{\sqrt{2\pi}} \int_0^R r^2 e^{-\frac{r^2}{2}} dr \quad (8.12)$$

This integral cannot be expressed in terms of elementary functions and so numerical solutions or standard tables must be used. Although technically the probability of lying within Mahalanobis distance $R = 1$ is analogous to the probability of a one-dimensional distribution lying within one standard deviation of the mean, it is not equivalent numerically. In order to correlate results more easily with the previous work, values of R are chosen to correlate to a one dimensional ‘four sigma rule’ i.e. $p(1.878) = 0.683$, $p(2.833) = 0.954$, $p(3.762) = 0.997$ and $p(4.696) = 0.999936$ corresponding to the probability of lying within 1, 2, 3 and 4 univariate standard deviations respectively.

Significance Tests

Statistical significance tests are used to calculate the probability that two samples are drawn from the same population. The standard multivariate test is Hotelling’s T^2 test, which is the multivariate equivalent of Student’s t-test for

CHAPTER 8. SURFACE STATISTICS

univariate data. Given two samples of n_1 and n_2 points, with means $\bar{\mathbf{r}}_1$ and $\bar{\mathbf{r}}_2$ and covariance matrices \mathbf{C}_1 and \mathbf{C}_2 , the pooled estimate for the covariance matrix is

$$\mathbf{C} = \frac{(n_1 - 1) \mathbf{C}_1 + (n_2 - 1) \mathbf{C}_2}{n_1 + n_2 - 2} \quad (8.13)$$

and Hotelling's T^2 statistic is defined as,

$$T^2 = \frac{n_1 n_2}{n_1 + n_2} (\bar{\mathbf{r}}_1 - \bar{\mathbf{r}}_2)^t \mathbf{C}^{-1} (\bar{\mathbf{r}}_1 - \bar{\mathbf{r}}_2) \quad (8.14)$$

A significantly large value of T^2 indicates that the mean vectors are different for the two populations. The significance or lack of significance of T^2 is determined by using the fact that in the null hypothesis case of equal population means, the transformed statistic

$$F = \frac{n_1 + n_2 - 4}{3(n_1 + n_2 - 2)} T^2 \quad (8.15)$$

follows an F distribution with 3 and $n_1 + n_2 - 4$ degrees of freedom.

8.3.3 Implementation

The fitting of the feature template to each subject has already been described in section 7.5.2. The mean template is found given a set of adapted templates simply by averaging each related point in the templates. The number of samples along a contour is defined when the template is created, so the template points already have a one-to-one relationship between each other and no further

CHAPTER 8. SURFACE STATISTICS

sampling is required.

The warping transformation from each subject's template to the mean template is constructed using MFFD's as the warping interpolation function. To find the average RGB image, each subject's RGB image is warped to this mean template shape and the average colour at each pixel is found by summing and division. The average depth image is found in the same way, replacing the RGB images with the laser-range images and averaging the depth at each warped pixel.

The distribution is calculated in terms of the covariance matrices at each point. This matrix can be found at each point in the average given the 3D displacement from the average point to the corresponding point in each subject using equations 8.4 and 8.5. For small samples or for points only free to slide along an axis or in a plane the covariance matrix can be singular. To prevent this the matrix is inverted as though it was only 2D or 1D when one or two rows are zero.

8.3.4 Results

The male surface mean is shown without texture mapping in figure 8.5 and with the corresponding average RGB image texture mapped in figure 8.6. The corresponding female mean is displayed without and with texture mapping in figures 8.7 and 8.8 respectively.

Statistical comparison with the average is performed by calculating the spatial probability of each point on the surface of the subject's scan relative to the

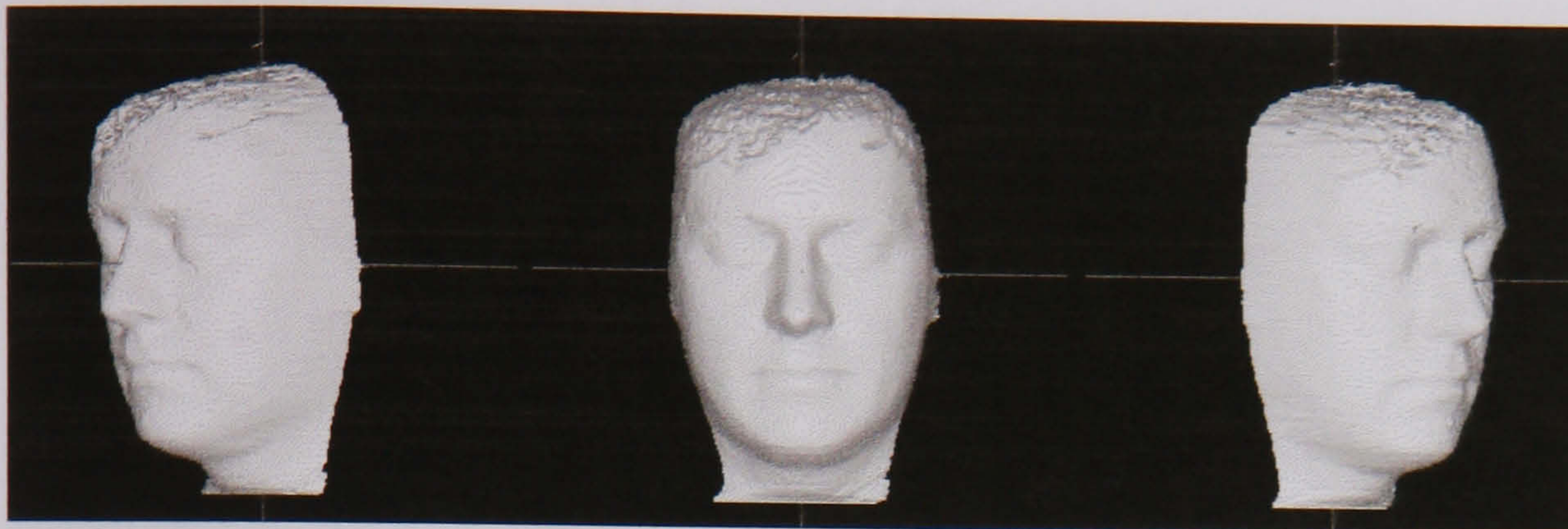


Figure 8.5: The male average rendered without texture mapping.

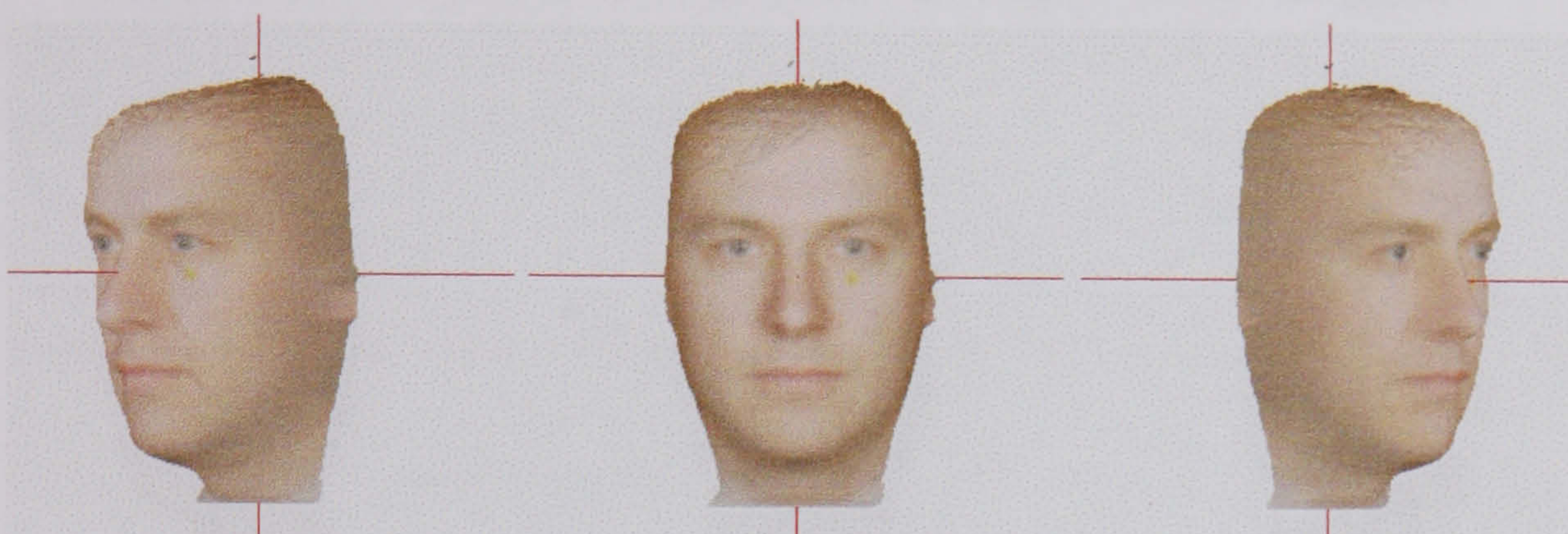


Figure 8.6: The male average rendered with texture mapping.

corresponding point in the average. These probabilities are converted to colours in a texture map (via a look up table) that is pasted on to the rendered surface. Two examples are shown, one comparing a normal male to the male average (figure 8.9) and one comparing a normal female to the female average (figure 8.10).

8.4 Conclusion and Choice of Method

The advantage of the probability histomorphogram method is its simplicity and speed, as it requires little processing and no user interaction. It can also be easily extended to segmented 3D scalar data, where the probability represents

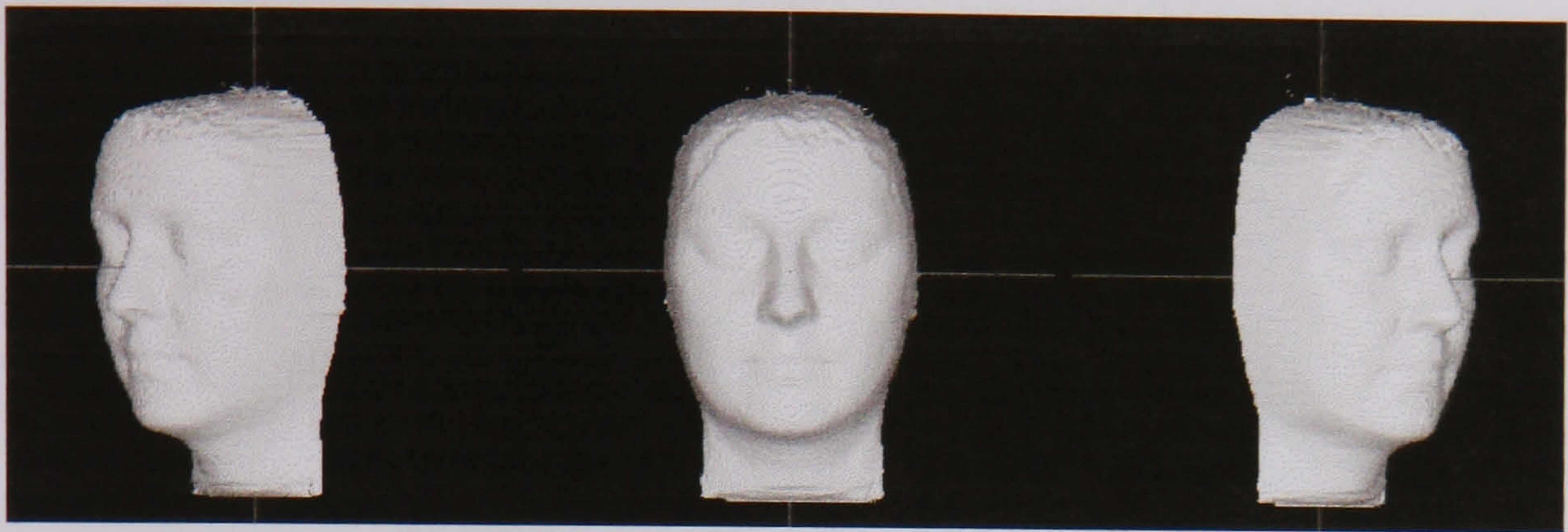


Figure 8.7: The female average rendered without texture mapping.



Figure 8.8: The female average rendered with texture mapping.

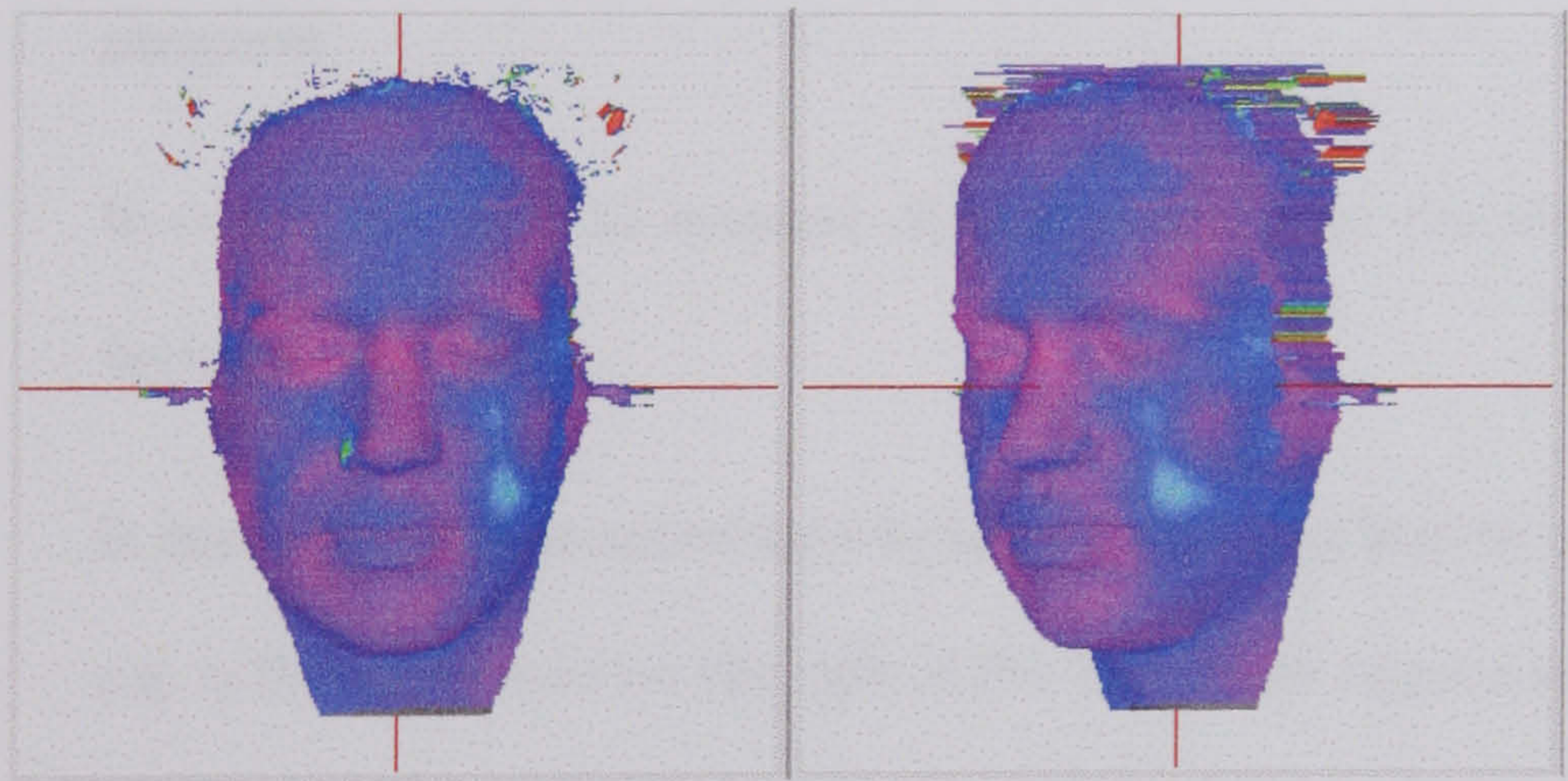
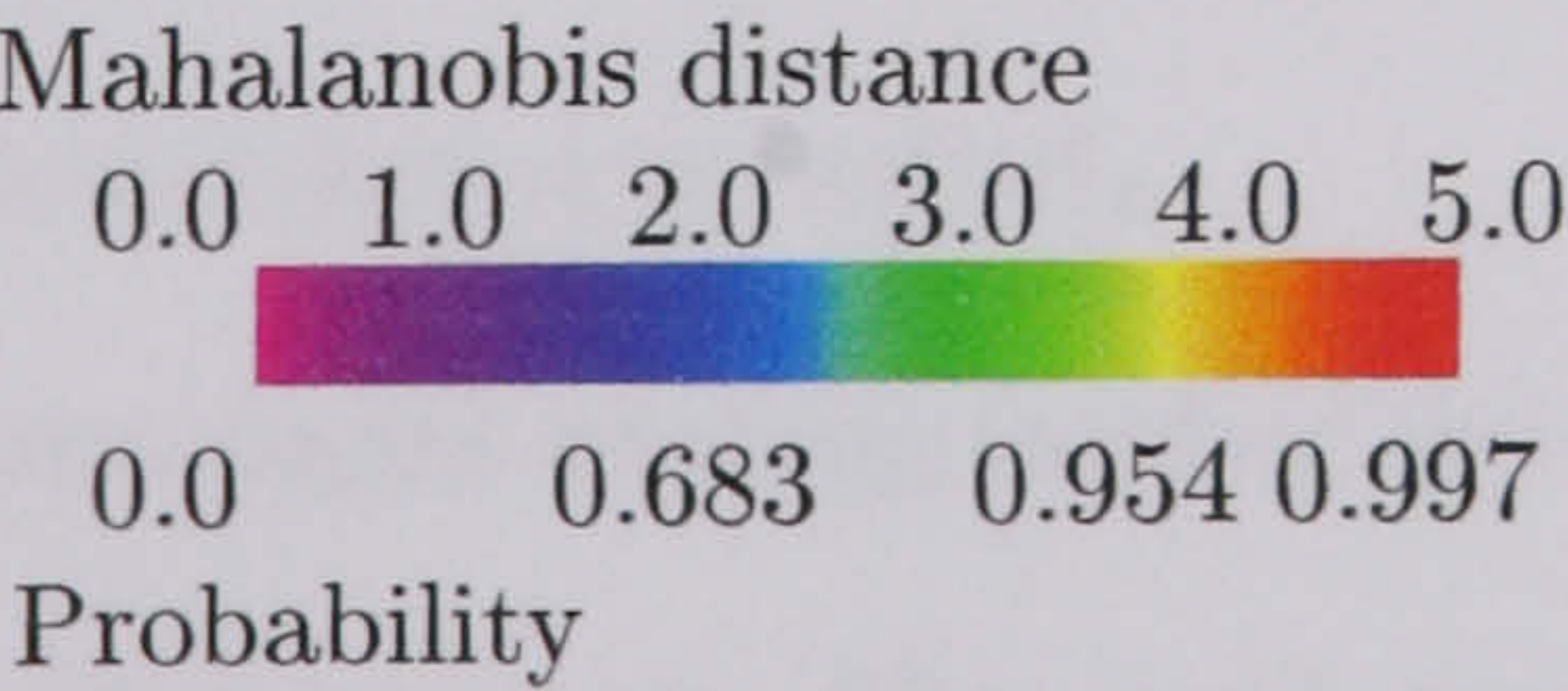


Figure 8.9: Comparison of a normal male subject with the male average.
Key:



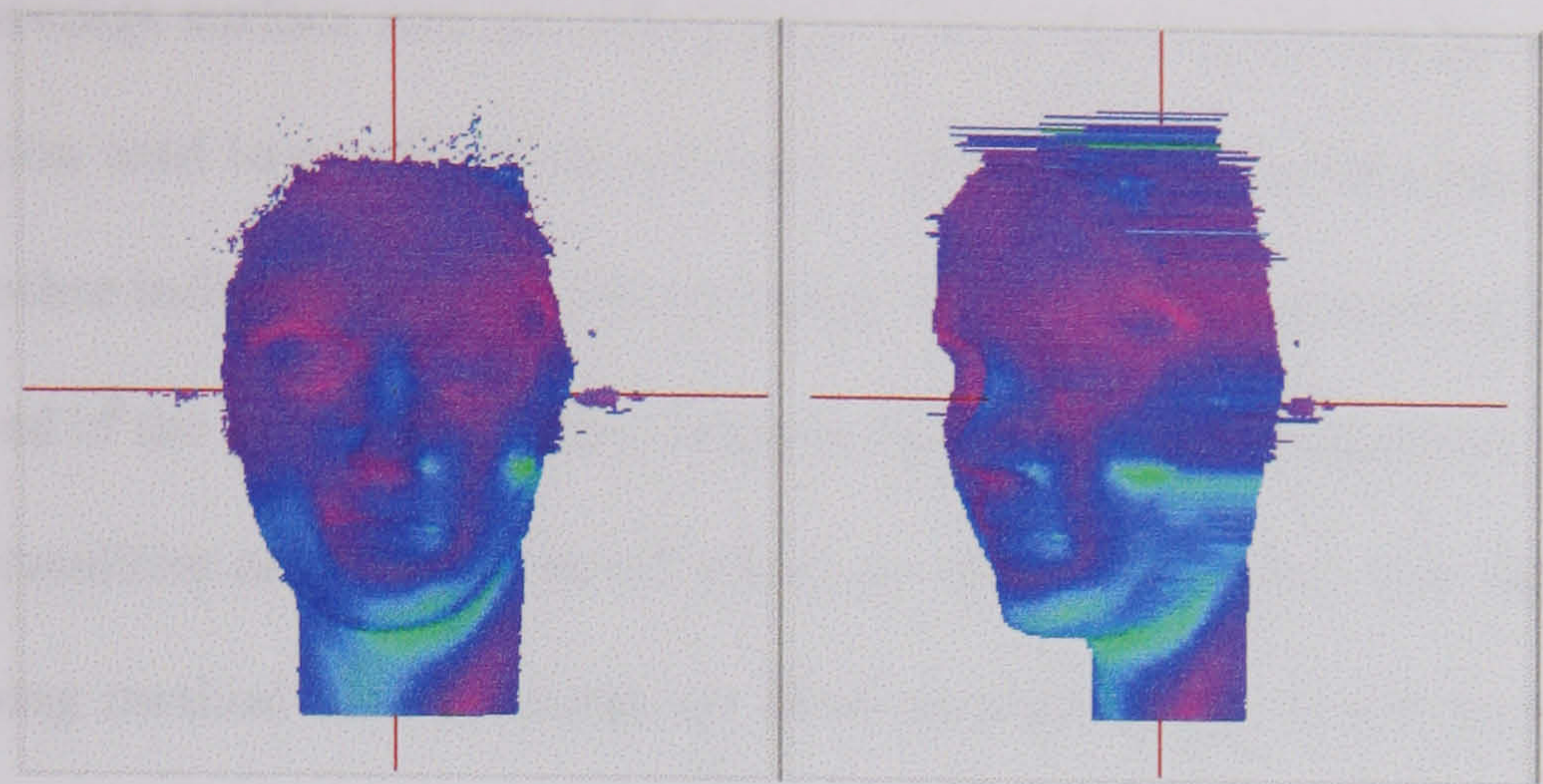
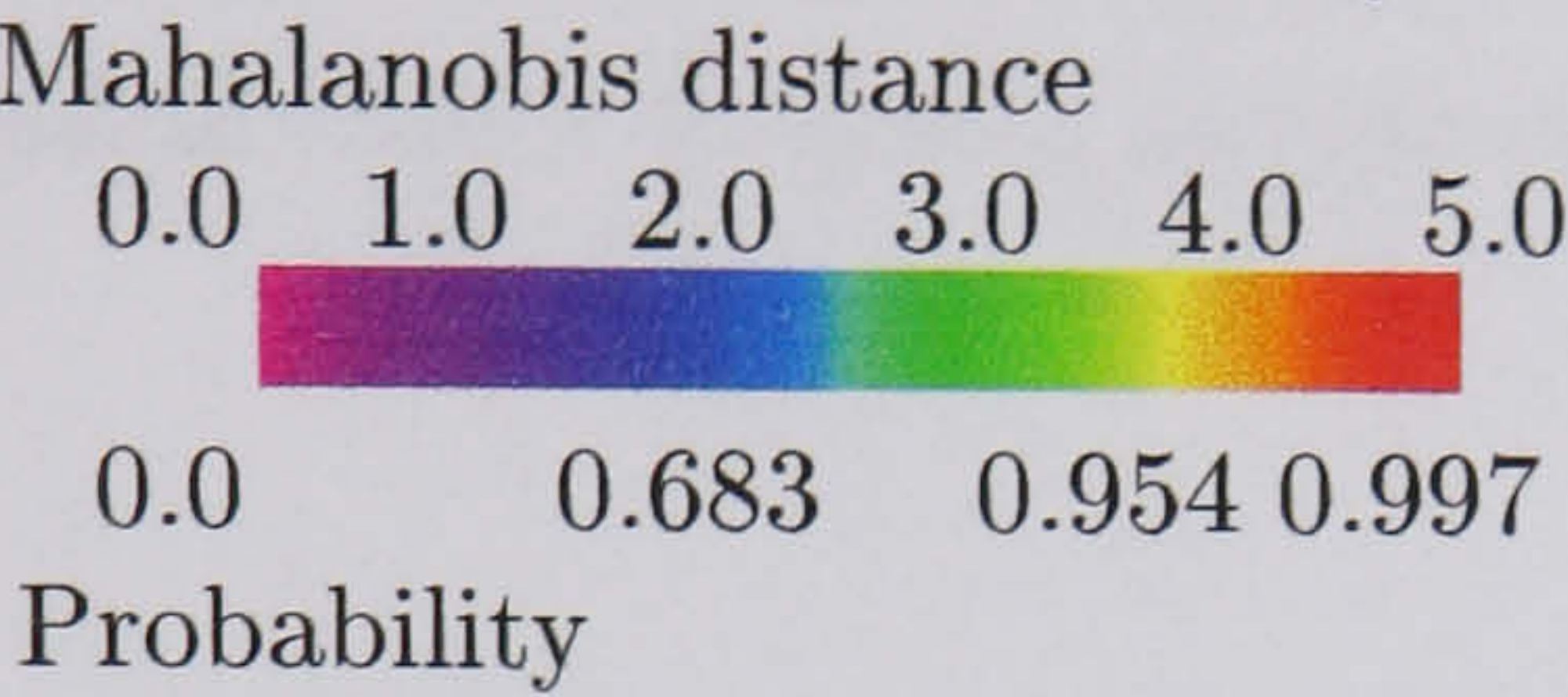


Figure 8.10: Comparison of a normal female subject with the female average.
Key:



the likelihood of lying inside the segmented 3D structure. The disadvantages are,

- a) A large sample is required to produce a smoothly varying histomorphogram.
- b) It cannot be used to measure displacements from the average or between individuals.
- c) It does not use anatomical knowledge and thus may lead to problems e.g. a flattened nose on the side of the face might appear normal!

In conclusion, this method is efficient and simple but the amount of useful information that can be extracted is limited.

In contrast the feature-based warping method does not require a large sample to produce a lifelike facial average. The displacement between each point on

CHAPTER 8. SURFACE STATISTICS

the average surface and an individual in the sample is defined by the warping function used to construct the average. The displacements between the average and other individuals can be found using the feature based warping method described in the previous chapter. Because facial features are matched, anatomical abnormalities as discussed in (c) above are dealt with easily. The feature-based warping method also produces an RGB average image, which provides additional visual information about the average face. Hence the feature-warping method is the method of choice for facial average construction.

Chapter 9

Results and Applications

9.1 Introduction

In the previous chapter two methods for constructing average three-dimensional facial surfaces and distributions were described. The method chosen is based on interactively adapting a template of contours and landmarks to each subject using snakes, then using the average template to set up a parametric coordinate system for each face based on image warping (method 2). This chapter demonstrates and discusses some of the possible future applications of this method, using examples drawn from the small test database. Further testing on real clinical subjects is required before these methods can be adopted clinically, but their feasibility is clearly demonstrated.

The probabilistic assessment of individual facial scans has already been demonstrated and further examples are given. The comparison of two averages

CHAPTER 9. RESULTS AND APPLICATIONS

using significance testing is demonstrated using the male and female averages.

The potential application of probabilistic assessment for pre-surgical planning is enhanced by combining it with surgical simulation. To demonstrate this, a new, fast, high resolution surgical simulator has been developed that is optimised for laser-range surface data. This allows prediction of changes in the facial surface given the corresponding movements of connected CT hard tissue data.

Finally, face-space transformations, which can transform individual's between statistical groups are demonstrated for three-dimensional laser-range data. These have application in studying growth and transformation of patients between their patient group and the corresponding normal group. This could provide surgeons with a more individual surgical goal.

9.2 Patient Assessment

The use of standardised images will allow a clinician to compare patients analytically with other patients, or with an average facial surface. In the orthogonal two-dimensional morphanalytic work, these kinds of comparisons have already led to improvements in diagnosis and the identification of new craniofacial anomalies. In the previous chapter, examples have been shown of comparing normal faces from the small test database to the corresponding averages. Further examples of comparing a subject with a long face and an adult cleft-palate subject are shown in figures 9.1 and 9.2 respectively. Visualisation of the spatial

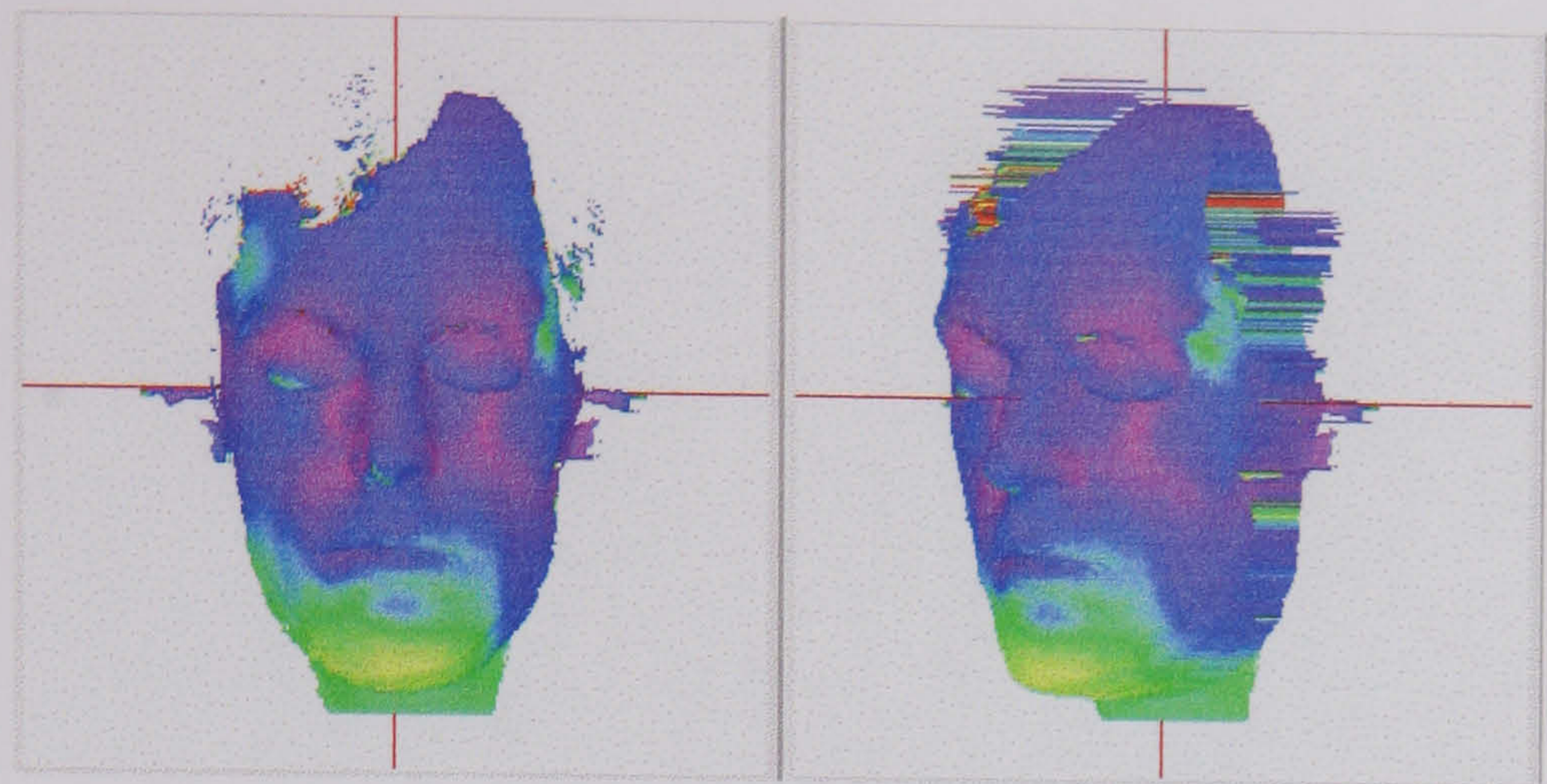
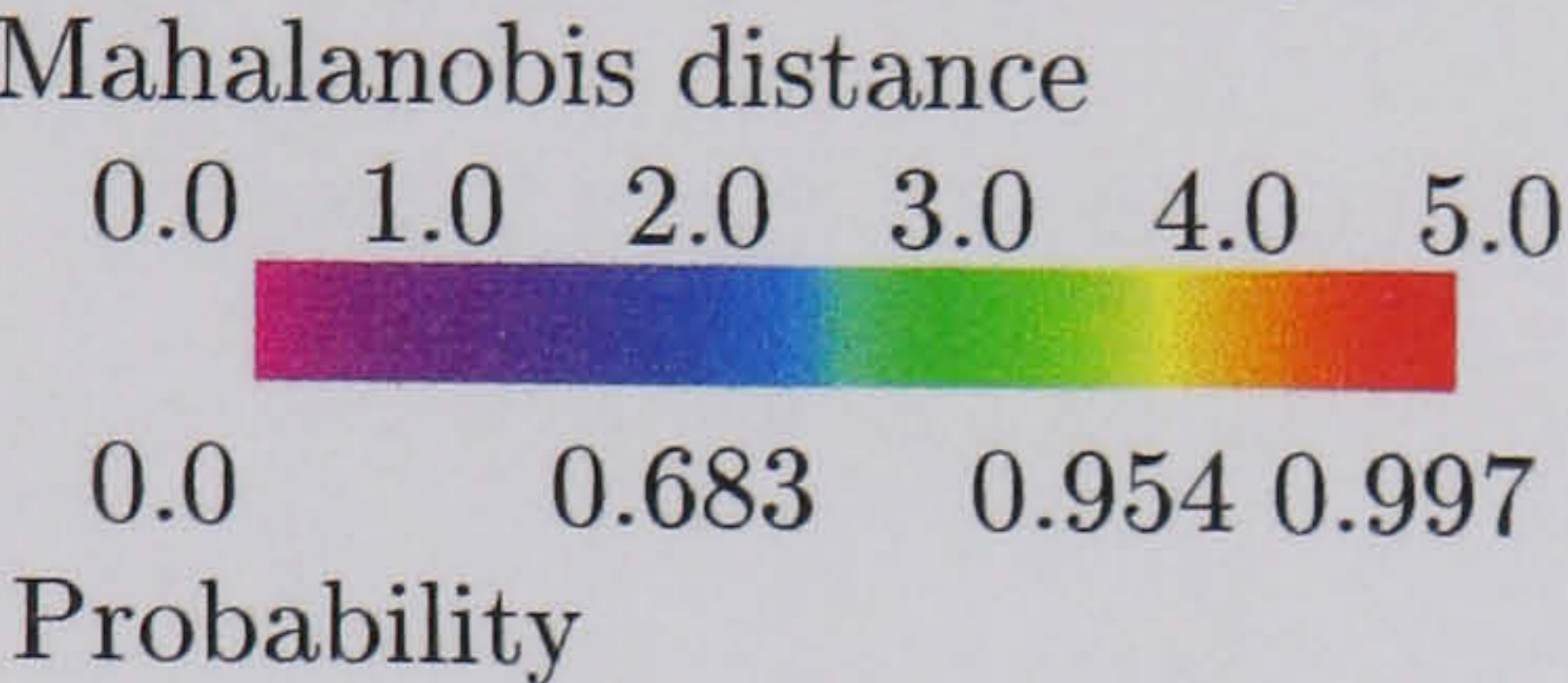


Figure 9.1: Comparison of a long-faced subject with the male-average.
Key:



probability of each surface point is achieved by converting it into a colour value and displaying the results as a texture map.

9.3 Assessing averages

In the previous chapter, methods were presented for the analytic comparison of averages in terms of vector displacement, spatial probability and statistical significance. The potential clinical and research applications for these kinds of quantitative assessments of statistical groups are numerous. For example, suppose two sets of patients undergo different treatments for the same craniofacial condition. A clinician planning future treatment might ask questions such as,

- a) Which treatment's average is closer to the normal average for this group?

CHAPTER 9. RESULTS AND APPLICATIONS

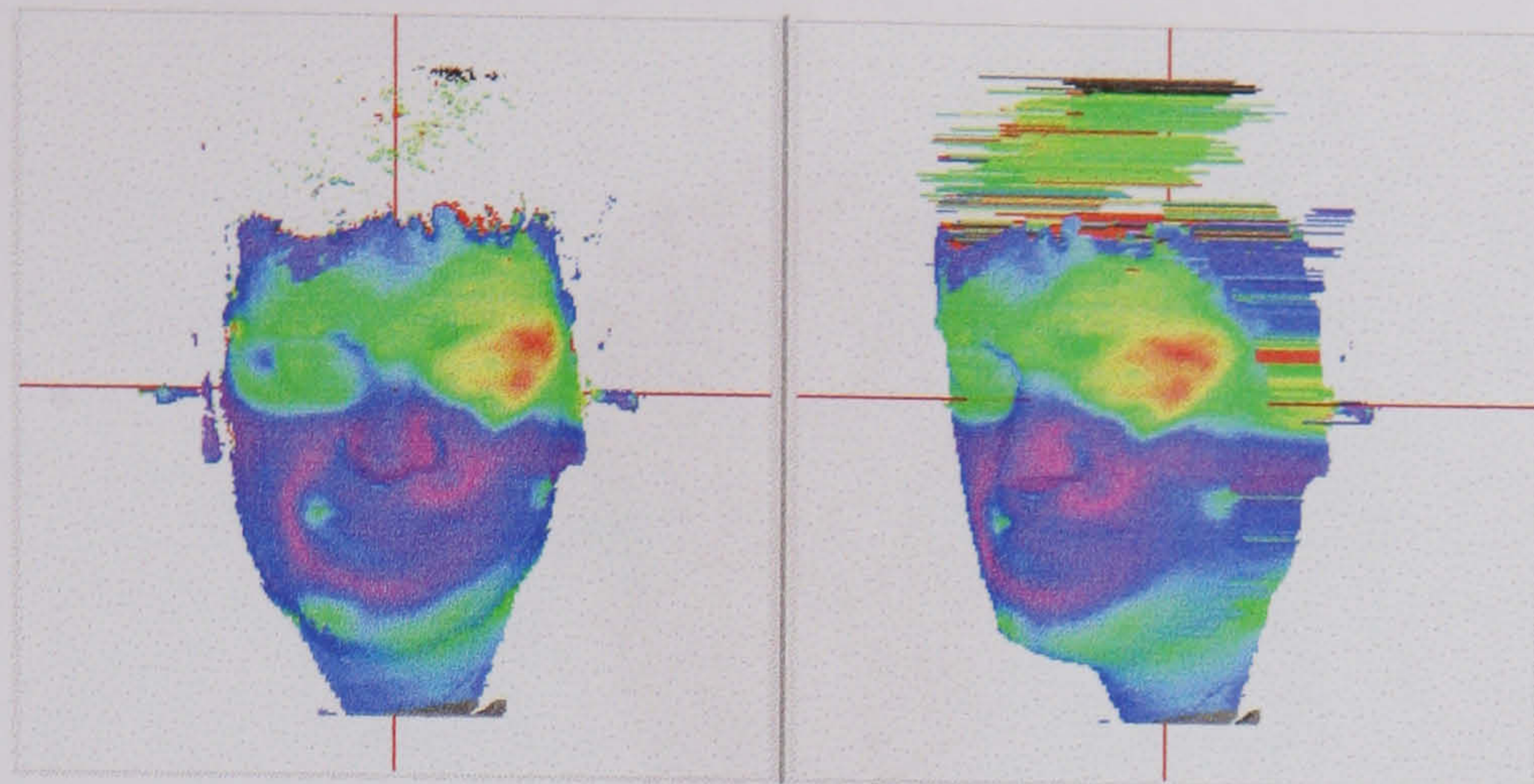
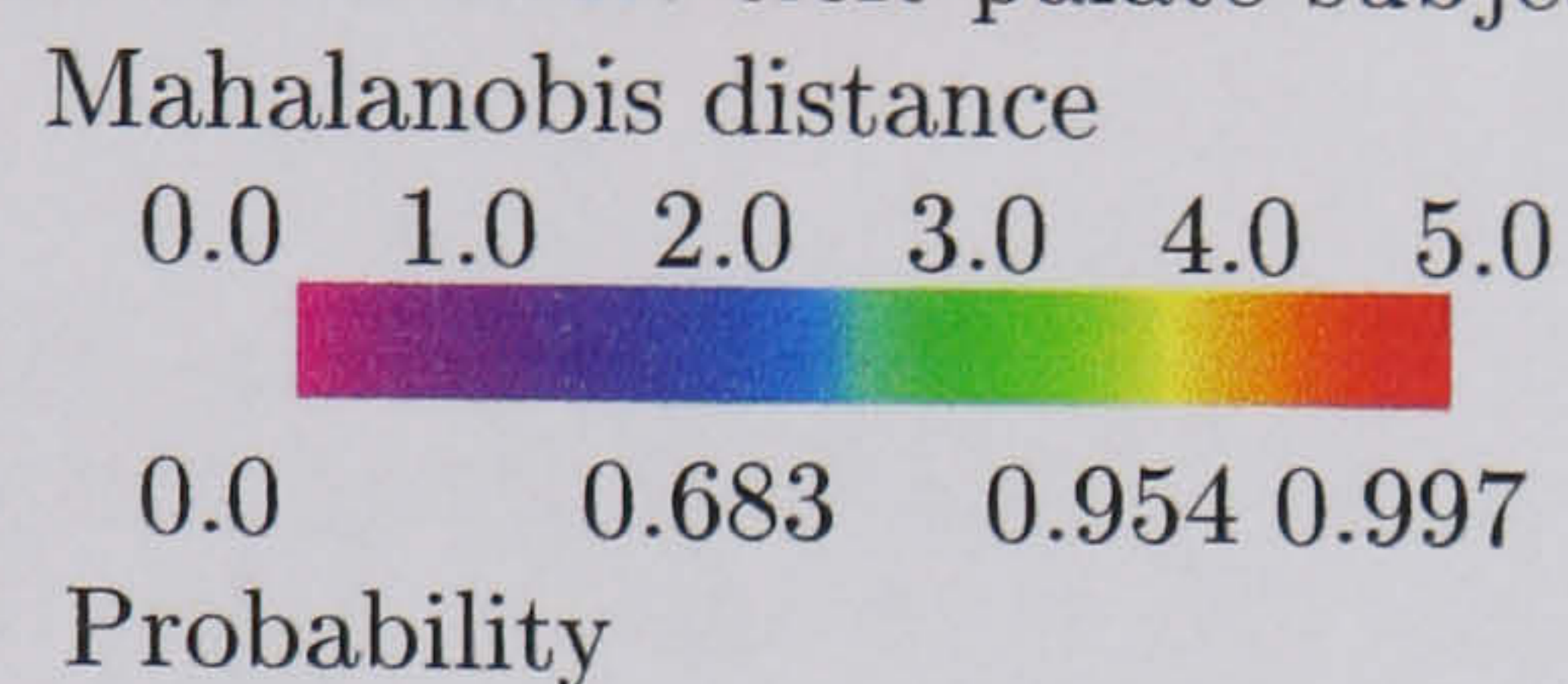


Figure 9.2: Comparison of an adult cleft-palate subject with the male average.
Key:



- b) Do these treatments produce significantly different results?
- c) Was there any statistically significant difference between these groups before treatment?

Comparison of averages can be performed using the same spatial probability mapping as for an individual facial surface. Alternatively, the significance of the difference between each mean facial point can be calculated using Hotelling's T^2 -test and the results displayed as a texture map. An example showing the comparison of the male and female averages using this method is shown in figure 9.3. Not surprisingly, the result shows that the two averages are significantly different. The null-hypothesis of equal distribution means is rejected at the 1% level for most of the facial surface, and at the 5% level on the cheeks.

CHAPTER 9. RESULTS AND APPLICATIONS

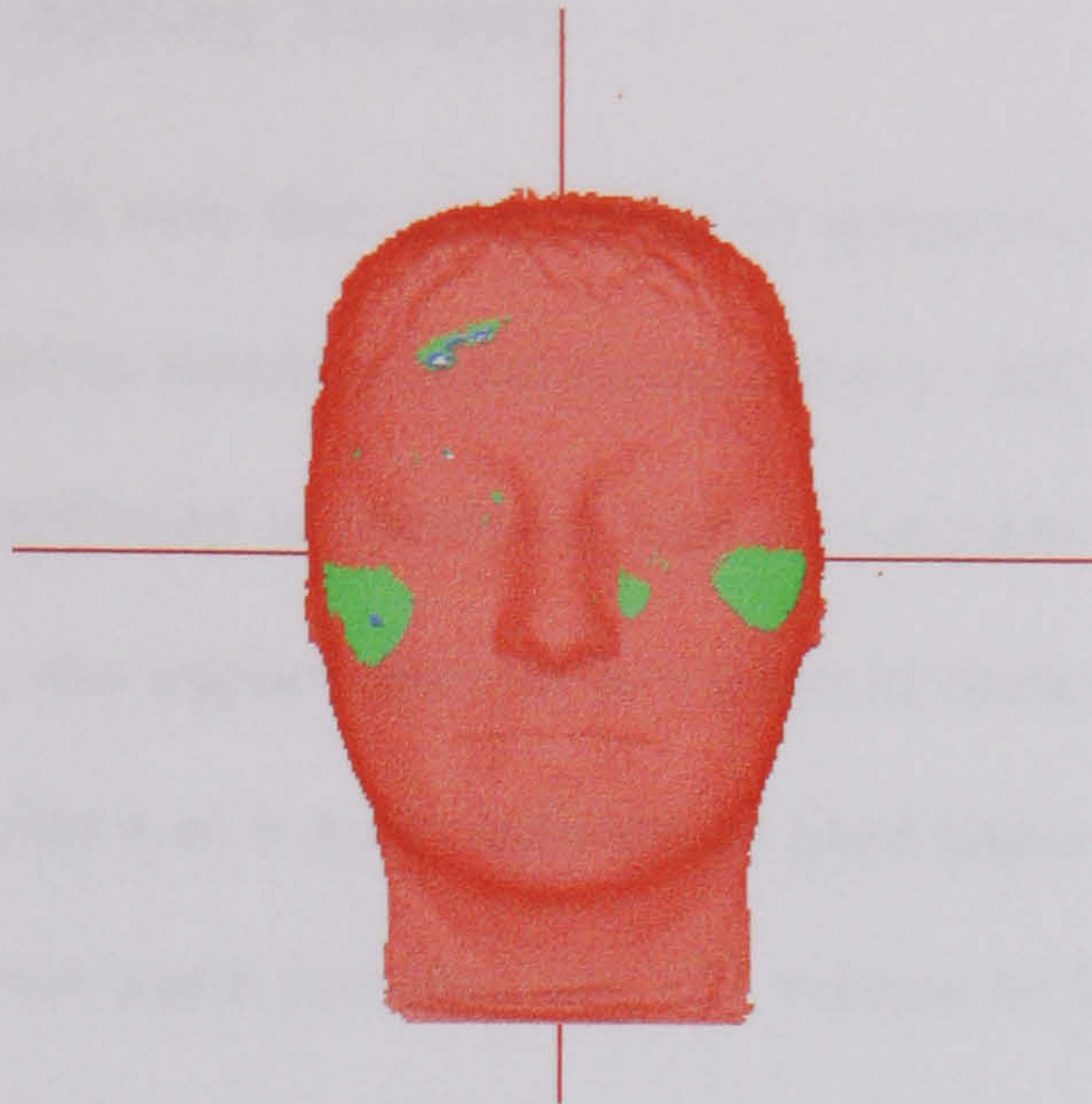


Figure 9.3: The significance of the difference between the male and female averages displayed as a texture map. Red areas are rejected at the 1% level, green at the 5% level, blue at the 10% level and white are rejected at less than the 10% level.

9.4 Assessing surgical models

9.4.1 Background

When planning craniofacial surgery it is often instructive to have a clear idea of the possible outcome. Several groups have proposed the use of soft tissue models that deform naturally under the action of user supplied forces or the movement of the underlying hard tissue. These allow a surgeon to experiment with different treatments before surgery begins. The simulation generally proceeds in two steps. The first sets up the model and the second solves the tissue model equations given an external mechanical force or tissue movement. The two most popular approaches for solving the model equations in the literature are finite element methods and mass spring models integrated numerically.

9.4.2 Mass Spring Models

Mass spring models were first used for facial animation (180) (181) (121) and have been adapted to simulate craniofacial surgery (182). To set up the model, first the facial depthmap is converted into a triangular mesh. From each vertex in the mesh, the surface normal is projected inwards until it intersects a registered CT volume at a point labelled as hard tissue. The three vertices of each triangle in the mesh intersect the CT volume at three points, forming a new triangle at the opposite end of an irregular triangular prism. This forms the basic volume element. The edges of this volume are treated as springs that attempt to maintain their original length. The force \mathbf{f}_s in a spring of stiffness k and natural length l due to an extension e is

$$\mathbf{f}_s = \frac{ke}{l}. \quad (9.1)$$

Each spring will produce an equal and opposite force at each end, pushing together or pulling apart the two vertices. The total spring force, \mathbf{F}_s , at each node is the sum of the forces due to all the springs connected to it. Human skin has a non-linear stress-strain relationship, with the stiffness increasing with extension. This can be modelled using a biphasic linear function, a quadratic function or a higher order polynomial function to approximate the behaviour.

The volume elements also attempt to maintain their original volume. This is achieved by producing additional forces at each surface node due to the difference between the original and current volume. This force is transmitted in the

CHAPTER 9. RESULTS AND APPLICATIONS

direction from the centre of mass of the prism to the surface point. The magnitude of the force f_v for an element of natural volume V and current volume V_c is given by,

$$f_v = \lambda \frac{(V - V_c)}{V} \quad (9.2)$$

where λ is the coefficient of the volume dependent term. This force is shared equally between each of the surface triangle's vertices. The forces due to all of the volume elements connected to a vertex are added to produce a force \mathbf{F}_v . The volume of the irregular triangular prisms can be calculated as the sum of three triple vector products. The entire system is then governed by the dynamic system

$$m \frac{d^2 \mathbf{x}}{dt^2} + \gamma \frac{d\mathbf{x}}{dt} + \mathbf{F}_v + \mathbf{F}_s = 0 \quad (9.3)$$

where m is the mass of the node and γ is the coefficient of the velocity proportional damping term. This system is integrated numerically to find the new position of each node when external forces are applied at each time step. By moving the underlying hard tissues, the surface nodes deform to take on new positions \mathbf{x} that minimise the forces at each vertex due to the connected springs and volume elements.

Mass spring models are reasonably fast for relatively low-resolution meshes. Keeve et al (182) report that for a 3080 triangle mesh, the surface resulting from the movement of internal hard tissues takes approximately 1 minute to

CHAPTER 9. RESULTS AND APPLICATIONS

calculate on an SGI High Impact workstation. The algorithm is $O(N^2)$ for N -nodes, so for the laser scans used in this paper to be integrated at full resolution (approximately 60000 facial triangles) would require 400 minutes on a similar workstation.

9.4.3 Finite element models

Finite element models were originally designed for modelling the stresses and strains of rigid structures in engineering design (183) (184). They have been applied to modelling human tissue for surgical simulation (185) (186) (187) (188) (189) (190) including craniofacial surgical simulation (191) (182). The idea is to minimise the internal and surface bending energy and stretching caused by external forces. The deformation energy of structure Ω can be written as

$$E_{def} = \int_{\Omega} (\alpha \text{stretching} + \beta \text{bending}) d\Omega \quad (9.4)$$

where α and β are the tensors representing the stretching and bending properties of the material respectively. If external forces $\mathbf{f}(u, v)$ are applied to the surface $\mathbf{w}(u, v)$ the surface energy can be written as

$$E_{surf} = \int_{\Omega} \frac{\alpha_{11}\mathbf{w}_u^2 + \alpha_{12}\mathbf{w}_u\mathbf{w}_v + \alpha_{22}\mathbf{w}_v^2}{\beta_1\mathbf{w}_{uu}^2 + \beta_2\mathbf{w}_{vv}^2 + \beta_3\mathbf{w}_{uv}^2} - 2\mathbf{f}\mathbf{w}d\Omega \quad (9.5)$$

where the subscripts denote partial derivatives. The stretching and bending tensors are given by

CHAPTER 9. RESULTS AND APPLICATIONS

$$\alpha = \begin{bmatrix} \alpha_{11} & \alpha_{12} \\ \alpha_{12} & \alpha_{22} \end{bmatrix} \quad (9.6)$$

and

$$\beta = \begin{bmatrix} \beta_1 \\ \beta_2 \\ \beta_3 \end{bmatrix} \quad (9.7)$$

By dividing the surface into small patches, the so called finite elements, the energy function given above collapses into a matrix equation of the form,

$$\mathbf{K}\mathbf{u} = \mathbf{F} \quad (9.8)$$

where \mathbf{K} is the global system stiffness matrix, \mathbf{u} is the vector of unknown surface displacement coefficients and \mathbf{F} is the external force vector. The vector \mathbf{u} is used to multiply a set of basis functions at each node in order to define the solution throughout the volume, and not just at the nodes. In this way the finite element method is different to finite difference methods, where the solution is only defined at the nodes. The continuity of the basis functions denotes the continuity of the finite elements, for example C^0 finite elements are continuous, C^1 finite elements have a continuous first derivative and so on.

The matrix \mathbf{K} is usually large and sparse and sophisticated libraries have been developed for solving this kind of inverse problem. Keeve et al (182) used a public domain finite element package (DIFFPACK (192)) to perform the finite

CHAPTER 9. RESULTS AND APPLICATIONS

element calculations. This took approximately 10 minutes to solve the equations for a 3080 triangle mesh using an SGI High Impact workstation, which translates to approximately 4000 minutes for our 60000-triangle face mesh. Speed can be improved by exploiting the fact that the result only needs to be computed on the visible surface and not at internal nodes (187) (188) (189) (190). Modern implementations of the finite element method allow real-time interaction with the deformable models, provided that the model does not contain a large number of nodes and a very fast workstation is used.

9.4.4 A New Method

In this section a simple elastic facial tissue model is described that is based on finite difference methods. The model allows the movement of hard tissues extracted from a registered CT scan and uses this to calculate the deformation of the connected surface. The predicted surface is generated by minimising the surface tension and the internal tension simultaneously using regularisation.

The finite element method views the problem of tissue modelling as an energy minimisation approach. Recently the use of backwards and forwards recursive filters has been proposed for solving energy minimisation problems in image processing (139). These regularisation problems are formulated as a linear inverse problem for the unknown solution vector \mathbf{f} in terms of the given function \mathbf{g} written in matrix form as

$$(\mathbf{I} + \lambda\mathbf{K}) \mathbf{f} = \mathbf{g} \quad (9.9)$$

CHAPTER 9. RESULTS AND APPLICATIONS

where \mathbf{K} is the stiffness matrix, \mathbf{I} is the identity matrix and the scalar parameter λ controls the relative influence of these two terms. The stiffness matrix contains finite-difference approximations to derivative terms. For example, second-order derivatives minimise the first derivatives for membrane stiffness and fourth-order derivatives are used to minimise the third derivative for thin-beam stiffness.

The matrix \mathbf{K} is an n -diagonal matrix, with each row simply a shifted copy of the previous row. Inversion of this kind of matrix is possible with Gaussian elimination. Due to the extremely regular nature of the matrix, the forward and backward Gaussian elimination can be performed directly on the image data, avoiding storage of the large inverse matrix. This is equivalent to a forward and backward recursive filtering of the image with appropriate filters.

The similarity between image regularisation and finite element models suggests that solution of the finite difference linear system should be possible, at least approximately, using recursive filtering. Furthermore, because the matrix is not stored or inverted directly the method should be considerably faster than direct inversion methods. The increase in speed and decrease in storage requirements would allow far larger (and hence more accurate) models to be simulated, which is important in the medical field.

9.4.5 The model

The surface model is constructed on a discrete two-dimensional grid. Each node in the grid contains a single depth value that will form a node in the final solution. From each node, the surface normal is projected into the registered CT

CHAPTER 9. RESULTS AND APPLICATIONS

data set until it intersects a segmented bone structure. The distance from the internal bone node to the external surface node is stored as $L(x, y)$. The natural lengths of the surface springs between horizontally and vertically separated nodes are also calculated and stored as $l_h(x, y)$ and $l_v(x, y)$ respectively. At equilibrium the tension in the internal springs will be equal to the tension in the external springs. Along the horizontal axis (i.e. for constant y) this problem can be represented as inverting the linear system

$$\alpha(x-1) \frac{f(x) - f(x-1)}{l_h(x-1)} - \alpha(x) \frac{f(x+1) - f(x)}{l_h(x)} = \beta(x) \frac{g(x) - f(x)}{L(x)} \quad (9.10)$$

where $g(x)$ is the known internal node displacement and $f(x)$ is the unknown surface node displacement. The stiffness of the external and internal springs are given by $\alpha(x)$ and $\beta(x)$ respectively. This can be seen as an approximation to the differential equation

$$f(x) + \lambda \frac{d^2 f}{dx^2} = g(x) \quad (9.11)$$

that also accounts for variability in the spring length and stiffness across the surface. The solution to this equation will minimise the stretching energy integral

$$\int (f(x) - g(x))^2 + \lambda \left(\frac{df(x)}{dx} \right)^2 dx \quad (9.12)$$

CHAPTER 9. RESULTS AND APPLICATIONS

This leads to a tridiagonal system of equations that are solved using forward and backward elimination of the matrix system directly on the image vector along each row. A similar tridiagonal system is established and solved along each column. The surface found after filtering along both rows and columns will minimise the integral

$$\int \int (f - g)^2 + \lambda \left(\frac{\partial f}{\partial x} \right)^2 + \lambda \left(\frac{\partial f}{\partial y} \right)^2 + \lambda^2 \left(\frac{\partial^2 f}{\partial x \partial y} \right)^2 dx dy \quad (9.13)$$

and so minimises several of the terms in equation 9.5. Solution of this energy minimisation can be implemented separately along rows and columns, which is not true of equation 9.5. Inverting the linear system along rows and columns separately allows much lower storage requirements and more efficient solution.

The bending energy of the surface can be added as 4th ordered linear terms without compromising the efficiency of the algorithm. This leads to a solution that minimises an integral of the form

$$\int \int (f - g)^2 + \frac{\lambda f_x^2 + \lambda f_y^2 + \lambda^2 f_{xy}^2 + \gamma f_{xx}^2 + \gamma f_{yy}^2 + \gamma^2 f_{xxyy}^2}{\gamma f_{xx}^2 + \gamma f_{yy}^2 + \gamma^2 f_{xxyy}^2} dx dy \quad (9.14)$$

Again, using a modification of the exact energy minimisation to allow separable solution along rows and columns opens the potential for much faster solution. Varying the tension λ and the stiffness γ across the image allows different tissue strengths to be simulated. For example, the springs connecting across the mouth

CHAPTER 9. RESULTS AND APPLICATIONS

opening could be made very weak, or the internal springs in the nose could be strengthened to simulate cartilage.

9.4.6 Results

To test the algorithm given above, a CT scan of a dry skull was captured and aligned manually, using translations, rotations and non-uniform scaling, to approximate the hard tissues of one of the subjects in our database. The CT data were segmented using the thresholding and cutting tools in the *ANALYZEtm* biomedical-visualisation software package(193). The surface scan was then connected to the segmented data by ray tracing the surface normal vectors. The surface displacements were initialised with the displacement of the connected internal structures. The adaptive filtering converts these to the surface displacements that are used to modify the surface node positions.

Figure 9.4 shows the original segmented CT skull data on the left, the original facial surface in the centre and the probabilistic assessment of the facial surface on the right. In figure 9.5 the left-hand image shows the CT data after the mandible has been translated forward 10mm, and the resulting change in the facial surface is displayed in the central image. The result is a smooth, plausible deformation of the soft tissue that takes only a few seconds to set up and calculate on an ordinary PC. A second example showing the effects of a maxillary advancement is shown in figure 9.6 along with the new soft tissue profile. The nose is less severely effected than the surrounding tissue, probably because the internal springs from the nose are very long. This increases the regularisation

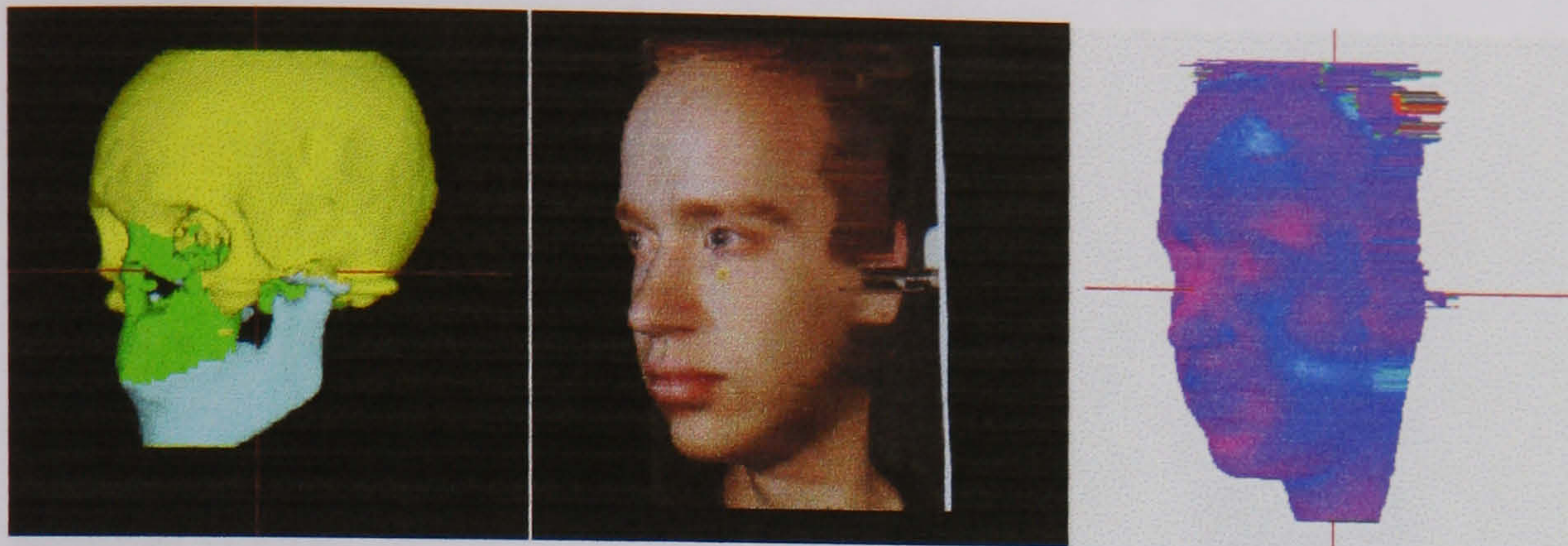


Figure 9.4: The segmented CT data (left) aligned to the surface scan (centre) with the probabilistic assessment (right).

Key:

Mahalanobis distance					
0.0	1.0	2.0	3.0	4.0	5.0
0.0	0.683	0.954	0.997		
Probability					

of these surface points, resulting in smaller translations. Stiffening the internal springs by decreasing λ in this area could avoid this problem.

9.4.7 Validation of Surgical Models

In the past, the accuracy of the predictions provided by surgical models has been based on visual assessment. The three-dimensional morphanalytic methods described in this thesis allow the quantitative comparison of the predicted model with the surgical outcome. This could help in validating the quality of the simulation, although it may not always be possible to carry out a surgical plan precisely in the operating theatre.

Another problem lies in the assessment of the quality of the predicted surgical results generated by the simulation i.e. which surgical plan produces the most satisfactory results. In previous work, this assessment has been performed

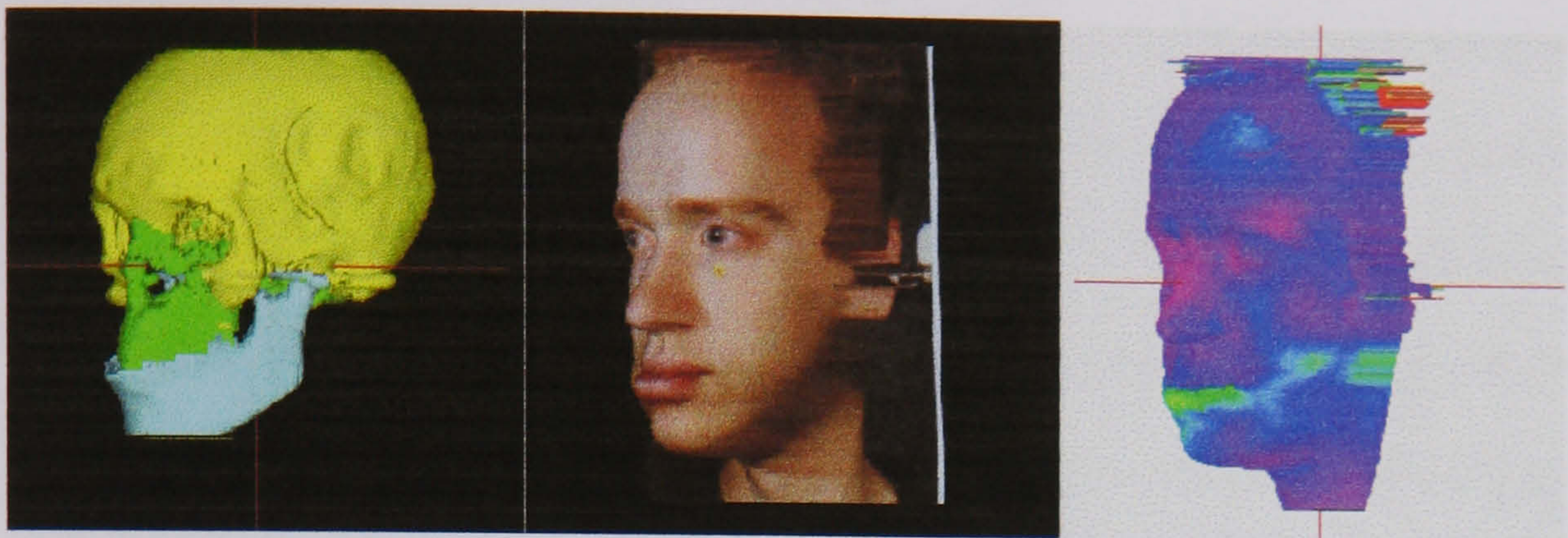


Figure 9.5: Movement of the mandible of the CT data (left) produces the predicted movement of the facial soft tissues (centre) and the resulting change in surface probability (right).

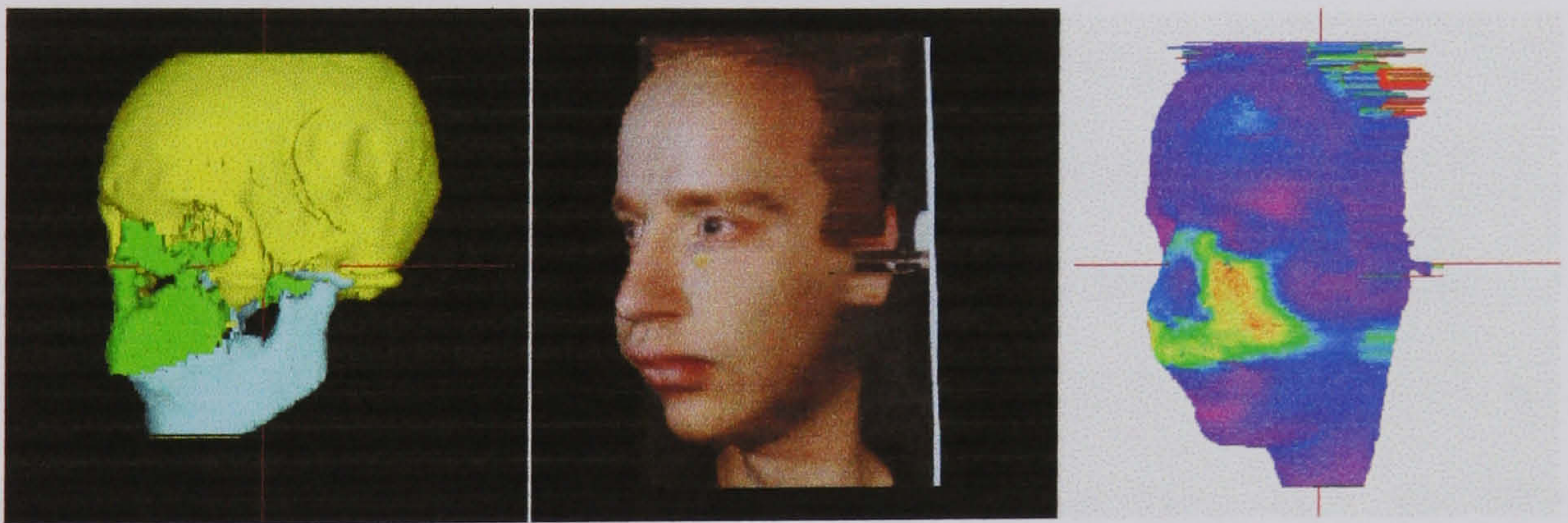
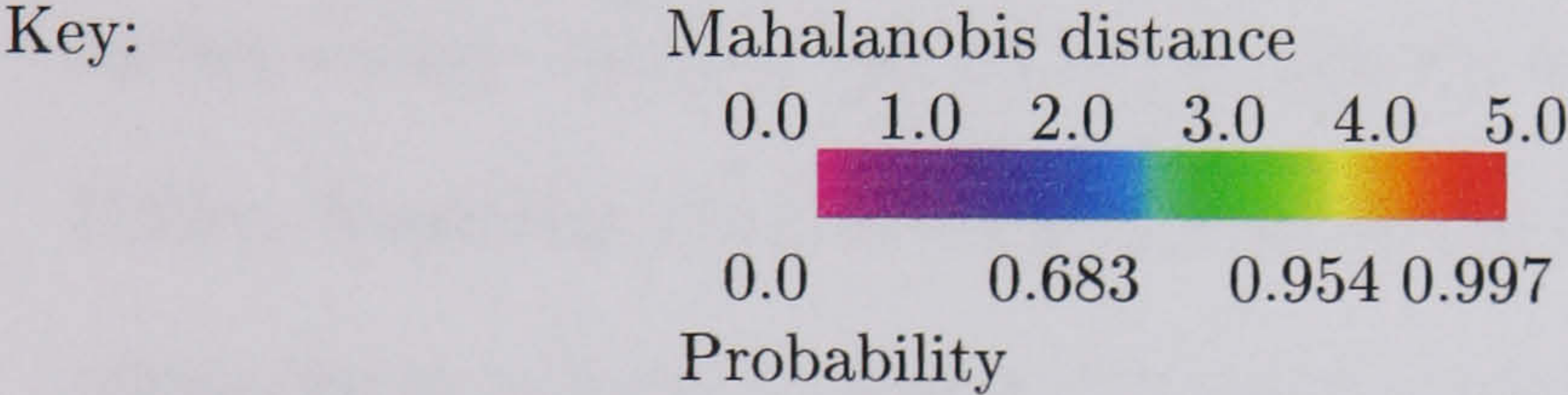
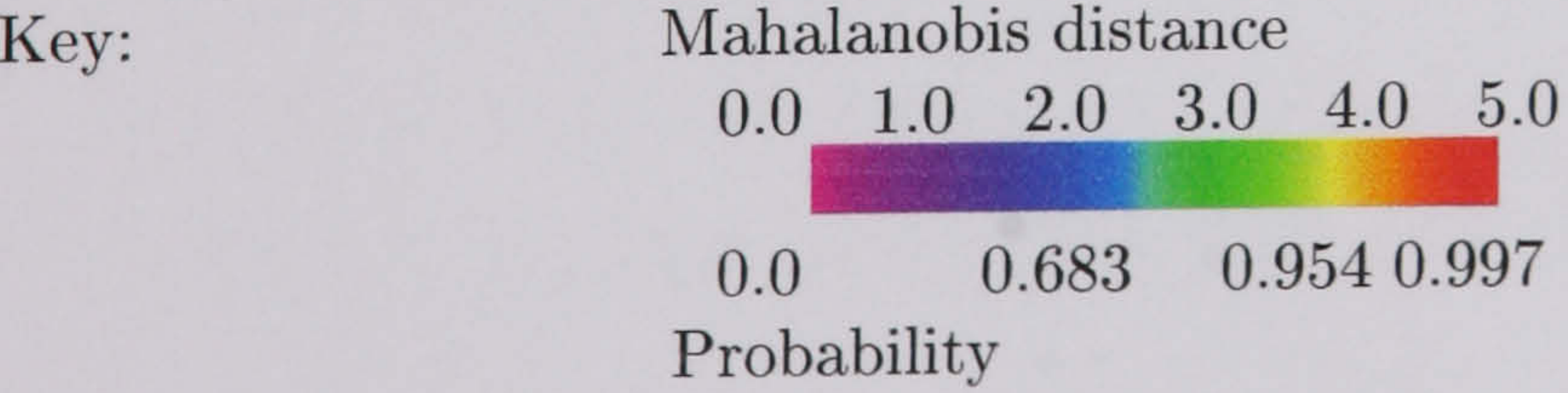


Figure 9.6: Movement of the maxillae of the CT data (left) produces the predicted movement of the facial soft tissues (centre) and results in a change in the surface probabilities (right).



CHAPTER 9. RESULTS AND APPLICATIONS

subjectively by the clinician using the simulator. The morphanalytic methods described in this thesis allow the quantitative assessment of predicted models by their comparison with the normal average for the subject's population group.

The right-hand images of figures 9.4, 9.5 and 9.6 show the surgical simulation described in the previous section compared with the male average for the database. By varying the surface colour to reflect the spatial probabilities, a direct assessment of the relative benefit of the procedure can be made. The surface probability in figure 9.4 is within normal limits across the entire facial surface, so any change in the surface is expected to decrease the spatial probabilities. Reassessment of the surface probability after simulation of mandibular advancement in figure 9.5 shows that surface points are more abnormally situated than in the undeformed original. The simulation of maxillary advancement in figure 9.6 produces an even more significant decrease in the spatial probability of points in the affected area. Although the maxillae are advanced by only the same size translation as the mandible, the resulting face has far more abnormally situated points. Many points around the nose are approaching 4 u.s.d, although the nose itself is relatively normal. This could be because the nose's internal springs have only been assigned the same stiffness as the surrounding tissue, but are in fact far longer.

9.5 Face Space Transformations

9.5.1 Growth Studies

In addition to modelling the effects of surgery, craniofacial research would also benefit from an increased understanding of the effects of growth. The growth of some craniofacial structures has been shown to alter following surgery. Accurate prediction of the long-term effects of surgery, particularly in young patients, is desirable to avoid repeated surgery later in life. The best treatment may be the one that allows correct growth rather than the one that looks the best immediately following surgery. Prediction of growth could allow a surgeon to identify abnormal growth patterns earlier, allowing more time to be devoted to treatment planning. To facilitate such advanced treatment planning, new tools are required.

9.5.2 Background

Rowland and Perrett (194) have demonstrated a method for transforming facial photographs of individuals between different statistical groups, whilst maintaining individuality and even expression. The original application was in psychological studies, experimenting with facial beauty and ageing using two-dimensional photographs (107). Essentially the method involves finding the difference between two statistical groups in terms of 2D shape and colour. This can then be added to an individual in one of these groups, transforming them into the other group.

CHAPTER 9. RESULTS AND APPLICATIONS

To construct the averages, first a large set of points labelling features (such as contours around the face, eyes, mouth etc.) was manually placed on each facial image. The average 2D shape was found by averaging the location of each labelled point. Each subject's photograph was then warped into this average shape by interpolating the point translations. The average colour was found at each pixel in the warped shape to produce an average colour image.

The shape difference between two averages of different statistical groups (separated by age, sex or any other statistical device), was found by subtracting corresponding points in the two templates. Warping the two average images into the mean 2D shape and subtracting produced the colour difference at each pixel. To apply this difference to an individual, first the translation vectors were added to each point in the individual template to define the new 2D shape. The individual's facial image and the colour difference image were then warped into this new shape and added to produce the new facial image. Experiments were performed, transforming between gender and age, with extremely believable results. Additional experiments scaled the difference data so that partial or exaggerated transformations could also be performed.

9.5.3 A New Method

The method for laser range data can be implemented as a direct extension of the two-dimensional method, by simply treating the laser range data as an additional colour channel to the red, green and blue components of the registered photograph. First, the translations between each point in the two average

CHAPTER 9. RESULTS AND APPLICATIONS

templates are found by subtraction. Next the two images are warped into the same shape (one of the two is chosen and the other warped to that shape) and subtracted to find the colour and depth differences.

Once the 3D shape and colour differences have been found they can be applied to an individual. Adding the group's template translations to each point in the individual's template creates a new template. The individual's RGB and range images are then warped into this new shape. This first change only accounts for the two-dimensional geometry change and not the change in surface depth or colour. The colour and depth difference images are then also warped into the shape of the new template and added to complete the transformation.

9.5.4 Results

This section demonstrates the application of three-dimensional face-space transformations by transforming an individual between the male and female groups already created. Figure 9.7 shows the construction of the difference between the male and female averages in terms of depth and colour. An example of applying this transformation to an individual female subject is shown in figure 9.8. The resulting surface and colour changes produce a very plausible male equivalent to the subject. A second example finds the shape and colour difference between an individual male subject and the male average (Figure 9.9). Adding this difference to the subject produces a caricature of the individual, exaggerating anything 'unusual' about their face. Subtracting the difference from the male

CHAPTER 9. RESULTS AND APPLICATIONS

average produces the ‘opposite’ of the subject.

In future, the hope is to test this method for the prediction of growth in normal subjects, cleft palate patients and patients with other common facial deformities. By constructing accurate averages of different age groups, the face-space transformation of an individual into an older age group could allow the growth pattern to be predicted. Alternatively, extrapolation of the differences between an individual’s facial scans at different ages could help to predict growth in a more individual way. Face-space transformations could also be used to transform individuals from deformed facial groups into their normal equivalent as an alternative to physically-based surgical models.

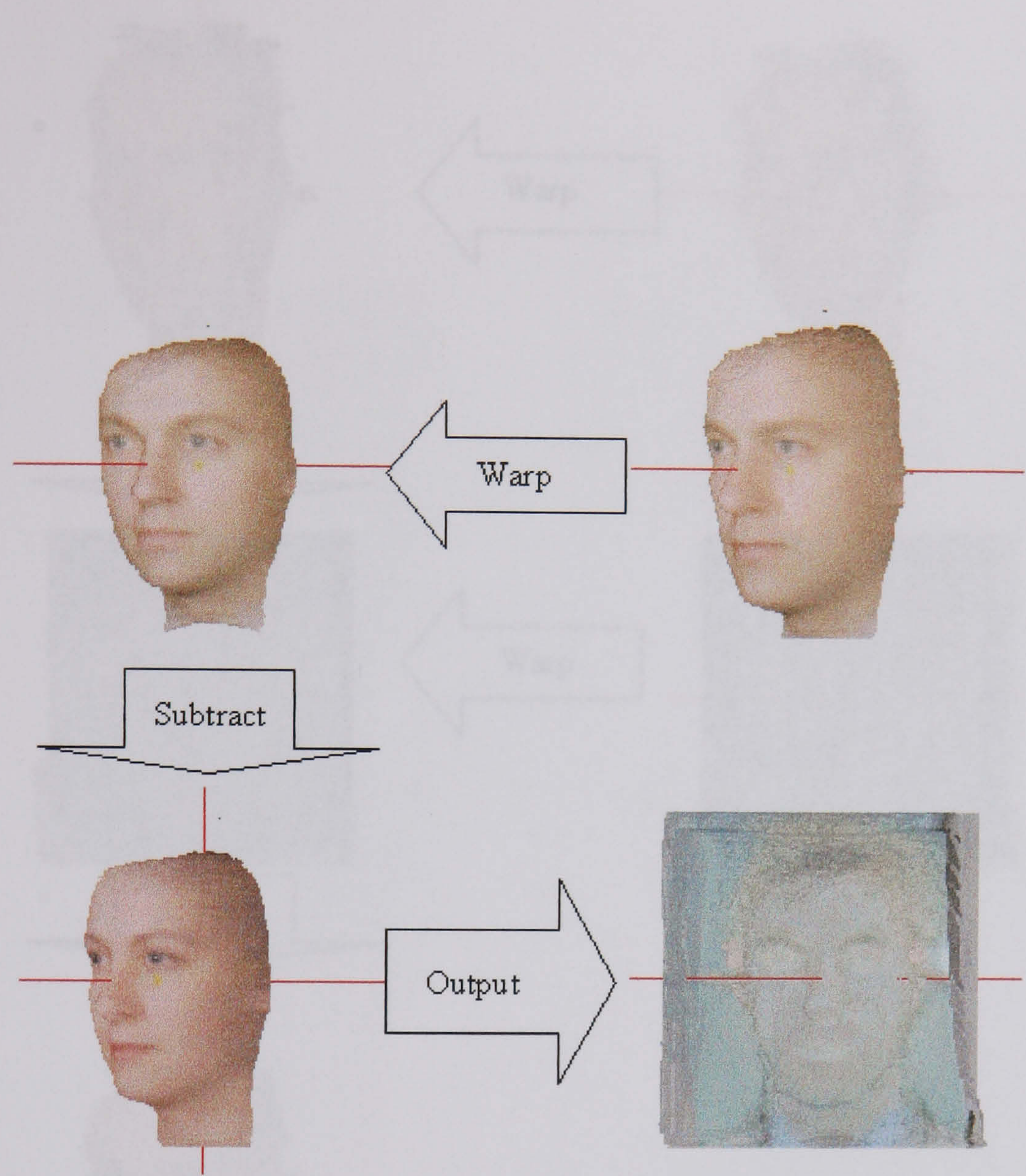


Figure 9.7: A diagram showing the steps used to find the face space transformation between the male and female averages. First the male average depth and RGB images are warped to the same 2D shape as the female. Then the female depth and colour is subtracted to give the depth and colour differences.

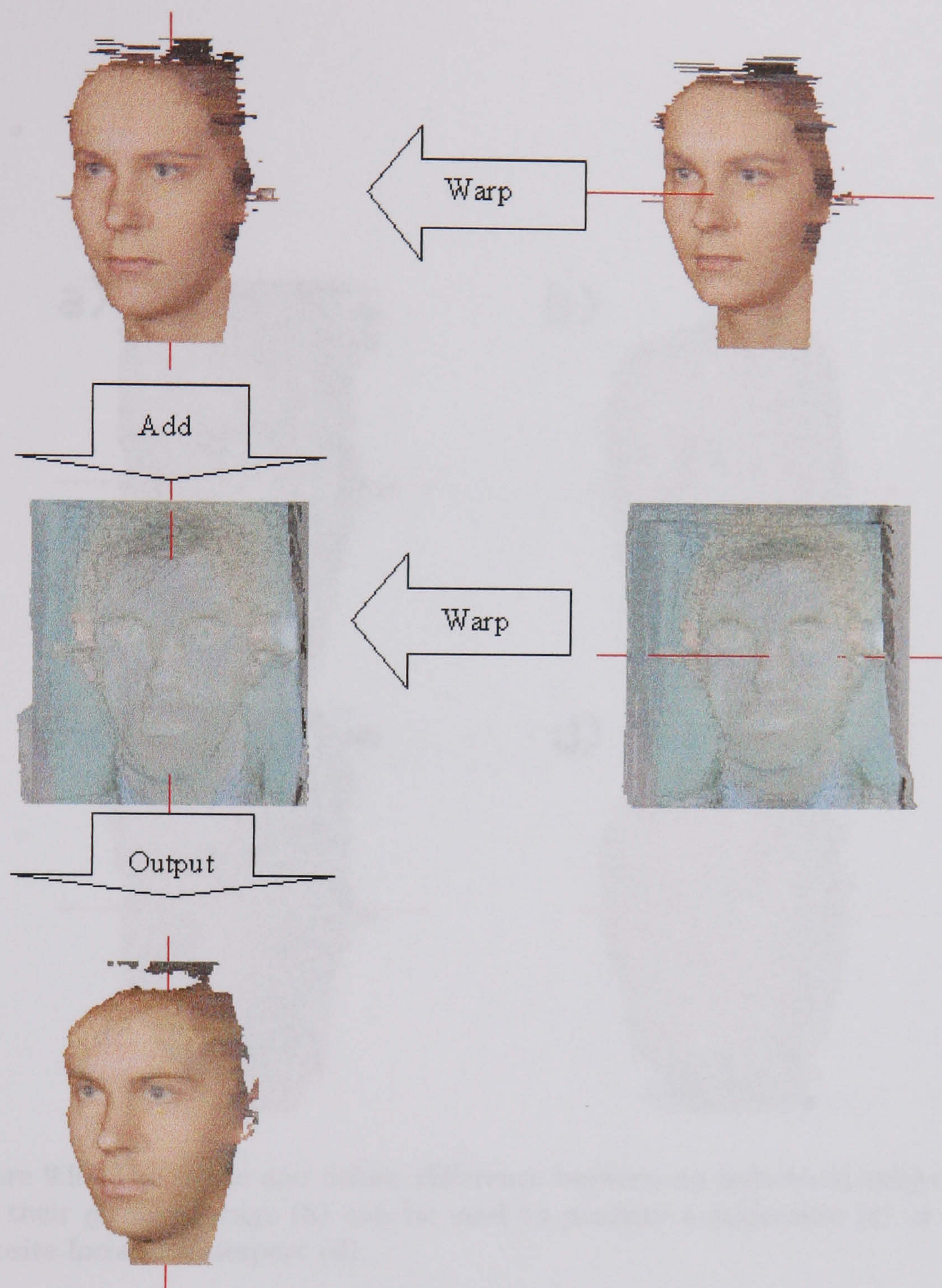


Figure 9.8: This diagram shows the application of a female-to-male face-space transformation. A new template is defined by adding the translation vector differences to the individual's template. The individual's colour and depth images are warped into the new shape along with the colour and depth difference images. These two are added to produce the altered subject.

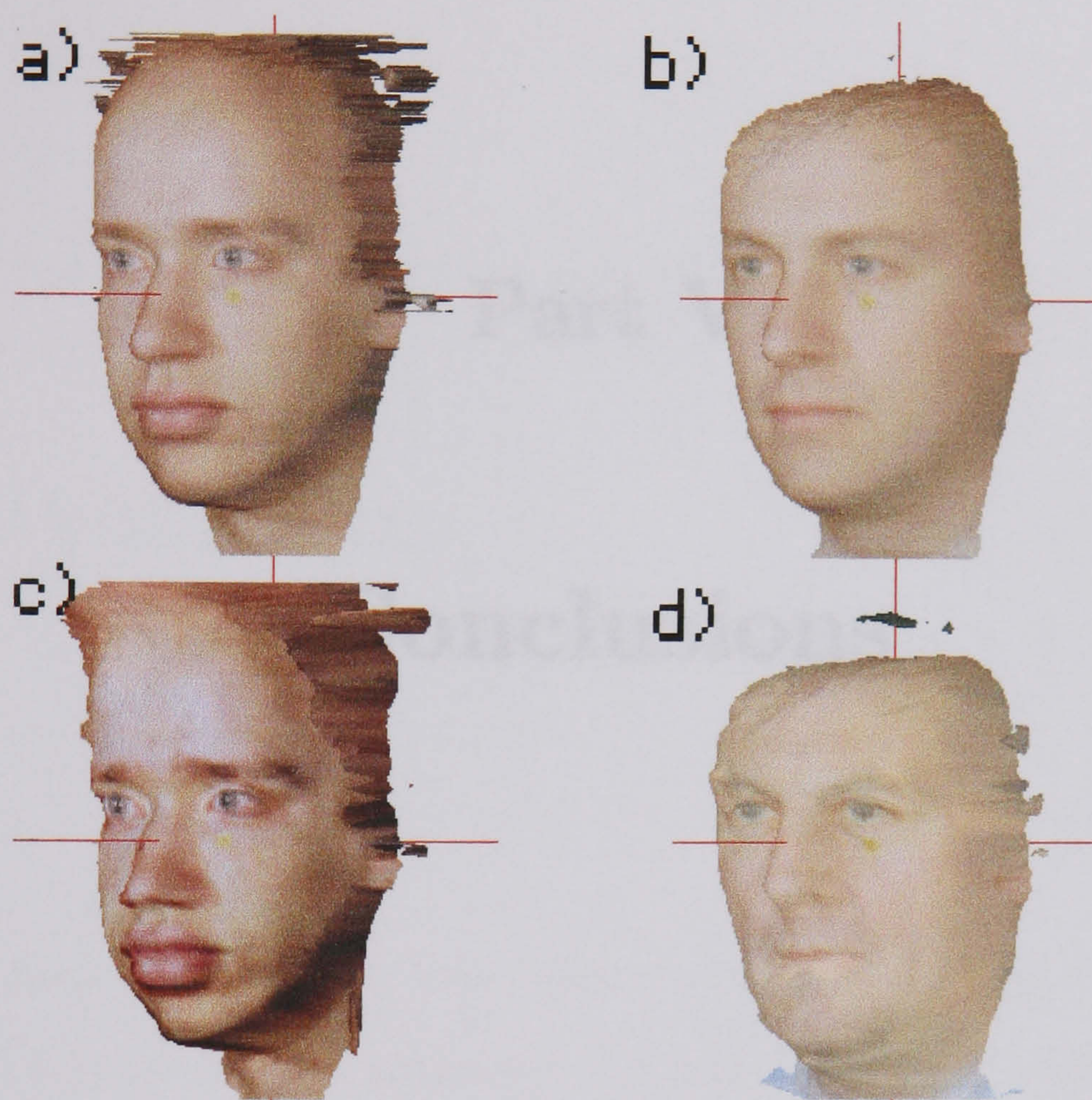


Figure 9.9: The shape and colour difference between an individual subject (a) and their group average (b) can be used to produce a caricature (c) or their opposite facial counterpart (d).

Part V

Conclusions

Chapter 10

Conclusions and Future Directions

10.1 Summary

The *overall objective* of the work reported in this thesis has been to determine the extent to which the established principles of two-dimensional orthogonal morphanalytic (universally relatable) craniofacial imaging might be extended into the realm of computer-based three-dimensional imaging.

The *overall conclusion* is gratifyingly positive. It is clear that it is not only possible to extend the principles in this way, but that the extension has also enhanced the established principles and led to advances in the field. The development of the extended principles and the emergence of the advances may

CHAPTER 10. CONCLUSIONS AND FUTURE DIRECTIONS

be summarised as follows.

Chapter 1 explained the need expressed by clinicians and researchers for quantitative analytical methods for the study of facial shape in three dimensions. To achieve this a three stage plan was devised involving rigid-body registration, standardised data capture and inter-subject comparisons.

The first stage required the alignment of subjects to a Cartesian reference frame using a rigid-body registration method. This registration assigns a 3D spatial coordinate to every point on the surface scan of each subject. Chapter 2 reviewed the available rigid-body registration methods and explained the choice of the fixed relations principle to achieve the rigid alignment.

The second stage required the capture of standardised images of the facial surface. Chapter 4 describes a new laser-video-scanner calibration method, which facilitated the capture of *universally relatable* laser-range data of the face.

The final stage required the comparison of different standardised images. Surface points in patient images are inter-related by a feature-based parametric labelling. Chapter 5 reviewed the available methods for parametric anatomical labelling and demonstrated the diversity of methods available for inter-subject comparisons. As no method showed a clear advantage in the literature, it was decided that more than one method should be tested. Chapter 6 reviewed the mathematical methods required for inter-patient matching. Along the way a new multi-scale interpolation method and a new overlap control method were devised. Chapter 7 tested three methods for inter-relating facial laser-scans and photographic data and concluded that feature based interpolation provides the

CHAPTER 10. CONCLUSIONS AND FUTURE DIRECTIONS

most reliable results, with an acceptable level of user interaction.

The three stage morphanalysis of the facial surface allows the comparison of individual faces and the construction of probabilistic facial averages. Chapter 8 described two methods for the construction of probabilistic facial averages and selected the method based on feature based warping as the preferred method. The average facial surfaces constructed consist of the mean depth, colour and the covariance matrix at each point in the mean.

Three-dimensional morphanalytic records have many potential applications beyond the construction of average facial surfaces. Chapter 9 described the potential applications of probabilistic facial averages and gave several examples. These included the comparison of individuals to the average to give a probabilistic assessment of the different areas of the face and the comparison of different averages in the form of significance tests. These significance tests present the opportunity to validate different treatments and identify new conditions.

In recent years there has been considerable interest in modelling surgery using computer graphic techniques. The standardisation inherent in morphanalytic records provides a unique opportunity for the validation of surgical simulations. Chapter 9 included the description of a new soft tissue simulation system. This method is designed for speed using an approximation to the surface stiffness and bending energy. The results showed that this method can produce realistic surgical changes to the facial surface for high resolution range images at a fraction of the speed of other methods. Examples with a normal subject showed how the probabilistic assessment of the simulations can provide

CHAPTER 10. CONCLUSIONS AND FUTURE DIRECTIONS

additional information to assist the selection of the most appropriate treatment.

An alternative method for modifying the facial surface was also given in chapter 9. Three-dimensional face-space transformations allow application of facial differences between groups or individuals to be applied to individuals. This could allow quantitative assessment of facial changes in order to improve understanding of both normal and abnormal growth and the effects of surgery. Face space transformations also open the possibility of transforming abnormal individuals into their normal equivalent, which would present both surgeons and patients with realistic surgical goals.

10.2 New Advances

The major innovations that have emerged from the research reported in this thesis are as follows.

- 1) A new calibration method for morphanalytic laser-video scanned surface data.
- 2) A new interpolation method for scattered 2D measurements.
- 3) A new overlap control method for ensuring the one-to-one property of mapping functions (for image warping).
- 4) Three new methods for inter-subject matching of laser-video surface data that offer compromises between speed, robustness and user interaction.

CHAPTER 10. CONCLUSIONS AND FUTURE DIRECTIONS

- 5) Two new methods for constructing average and distribution facial data.
- 6) A new method for the probabilistic assessment of individual faces compared with average and distribution facial data.
- 7) A new method for the significance testing of two average and distribution facial images.
- 8) A new, fast, high-resolution method for soft-tissue modelling of laser-scanned surface data in craniofacial surgery simulation.
- 9) The extension of face-space transformations to texture-mapped laser surface data.

10.3 Future Work

10.3.1 Introduction

The work reported in this thesis has been a self-contained project within the larger collaborative enterprise called the Interface Project, and has inevitably revealed many opportunities for future enhancements. Further testing and evaluation of the software will be required, with real patients in a clinical setting. The methods have been tested on a database of normal subjects and some subjects with more unusual faces. By using an established registration method (the fixed relations principle) and an interactive inter-subject matching method, the

CHAPTER 10. CONCLUSIONS AND FUTURE DIRECTIONS

risk of errors due to a subject having a very different face from those in our small sample is minimised.

10.3.2 Clinical Trials

For several years now, the Interface Project has been involved in the development of new computer graphic craniofacial imaging techniques and their applications as described in this thesis. The next stage of this research is to test and apply these methods clinically. This will involve several threads including the following.

- a) The construction of probabilistic average and distribution facial data for a range of statistical groups, arranged according to sex, race, age and facial deformity.
- b) The assessment of individual patients via probabilistic comparison with the average and distribution data.
- c) The comparison of means from different facial groups and different treatment histories via surface significance testing.
- d) Further evaluation of the surgical simulation approach using real subjects, probabilistic comparison with the mean and comparison with the actual outcome.
- e) Evaluation of the three-dimensional face-space transformations for growth prediction and for setting pre-surgical goals.

CHAPTER 10. CONCLUSIONS AND FUTURE DIRECTIONS

10.3.3 Computer Graphic and Imaging Enhancements

The thrust of the Interface Project must continue to be towards clinical assessment and research, to prevent it becoming detached from clinical reality. Because of the rapid advances in medical imaging it is also important that parallel progress continues to be made on the computational front. As with the clinical research, many avenues exist for improving and enhancing the current methods. These include the following.

- a) Extension of universally relatable imaging to include Computed Tomography (CT) and Magnetic Resonance Imaging (MRI). Progress towards this has already been made with the construction of a prototype head jig. As explained in chapter 2, rigid alignment of three-dimensional images of a single patient using least-squares methods is robust and valid. Therefore it may be possible to avoid the use of a head jig, instead registering the 3D scalar data-set to the morphanalytically aligned laser surface scan.
- b) Improvements in imaging time. The laser scanner used in this paper takes approximately 5 seconds to capture a surface scan. Modifications made to a similar scanner have allowed the capture of real time surfaces (88). Other methods using white light projection and fast image capture also offer the opportunity to capture moving 3D facial images. Moving three-dimensional facial data could be used to study the dynamics of the facial structure, improving the study

CHAPTER 10. CONCLUSIONS AND FUTURE DIRECTIONS

of functionality in addition to static shape.

- c) The laser range scanner, like most other range scanning systems, captures only from a particular viewpoint. The combination of scans from several views would provide a more realistic face model. Several methods have been put forward in the literature, and these will need to be reviewed and adapted for morphanalytic laser-video data.

Again, many more potential improvements are likely to be suggested when the software is used in clinical situations.

10.4 Concluding Remarks

As with all clinically motivated research, the goal of this Project is to help improve the quality of people's lives. The psychological burden of growing up with a major craniofacial deformity, particularly on young people, is well documented. A severe facial deformity can affect personality, sexual success and even employment prospects. It is my sincere hope that the work contained in this thesis will contribute in some small way to improving the treatment, and hence the lives, of these patients.

References

- [1] Cutting C., 'Applications of computer graphics to the evaluation and treatment of major craniofacial malformations,' *Proceedings Conference on 3D Imaging in Medicine*, Chapter 6, November 16-19, Coronado CA, 1989.
- [2] Rabey G.P., *Morphanalysis*, H.K. Lewis, London, 1968.
- [3] Rabey G.P., 'Craniofacial Morphanalysis, *Proceedings of the Royal Society of Medicine*, Vol. 64, pp 103-111, 1971.
- [4] Rabey G.P., 'Current principles of morphanalysis and their implications in oral surgical practice,' *British Journal of Oral Surgery*, Vol. 15, pp97-109, 1977-78.
- [5] Rabey G.P. 'Current and Future Practice in Craniofacial Morphanalysis,' in *Surgical Correction of Dentofacial Deformities: New Concepts*, Ed. William H. Bell, W.B. Saunders Co., pp715-731, 1985.
- [6] Rabey, G.P., 'Morphanalysis of craniofacial dysharmony,' *British Journal of Oral Surgery*, Vol. 15, pp. 110-120, 1977.

REFERENCES

- [7] Rabey G.P., 'Bilateral mandibular condylolysis - a morphanalytic diagnosis,' *British Journal of Oral Surgery*, Vol. 15, pp. 121-134, 1977.
- [8] Rabey G.P., Hodgkinson P.D., Svensgaard M., and Wolff G.S., 'Computer-graphic three-dimensional morphanalysis of long-term cleft palate results in the soft and hard tissues of the craniomaxillofacial complex,' in Huddart A.G. and Ferguson M.J.W. (eds) *Cleft lip and palate: Long term results and future prospects*, Proc. 1st Int. Meeting of the Craniofacial Soc. of G.B., 1983, Vol. 2, Manchester University Press, 1990.
- [9] Huang T.S., Blostein S.D., Margerum E.A., 'Least-squares estimation of motion parameters from 3-D point correspondences', in *Proc. IEEE Conf. Computer Vision and Pattern Recognition*, Miami Beach, FL, June 24-26, 1986.
- [10] Faugeras O.D. and Hebert M., 'A 3-D recognition and positioning algorithm using geometrical matching between primitive surfaces,' in *Proc. Int. Joint Conf. Artificial Intelligence*, Karlsruhe, West Germany, pp. 996-1002, Aug. 1983.
- [11] Faugeras O.D. and Hebert M., 'The representation, recognition and locating of 3-D objects,' *Int. J. Robotic Res.*, vol. 5, no. 3, pp. 27-52, 1986.
- [12] Fright W.R. and Linney A.D., 'Registration of 3-D surfaces using multiple landmarks,' *IEEE Tans. Medical Imaging*, Vol. 12, pp 515-520, 1993.

REFERENCES

- [13] Press W.H., Teukolsky S.A., Vetterling W.T., Flannery B.P., *Numerical Recipes in C: The Art of Scientific Computing*, 2nd Ed., Cambridge University Press. 1994.
- [14] Arun K.S., Huang T.S. and Blostein S.D., 'Least-squares fitting of two 3-D point sets,' *IEEE Transactions on Pattern Analysis and Machine Intelligence*, Vol. 9, No. 5, Sept. 1987.
- [15] Schonemann P.H., 'A generalized solution to the orthogonal Procrustes problem,' *Psychometrika*, vol. 31, no.1, 1966.
- [16] Golub G.H. and Van Loan C.F., *Matrix Computations*, Baltimore, MD, John Hopkins Univ. Press, 1983.
- [17] Bookstein F.L., 'Biometrics, biomathematics and the morphometric synthesis,' *Bulletin of Mathematical Biology*, 58:313-365, 1996.
- [18] Bookstein F.L., 'Shape and the information in medical images: A decade of morphometrics,' Vol. 66, No. 2, pp. 97-118, 1997.
- [19] Hill D.L.G, Hawkes D.J., Crossman J., Gleeson M.J., Cox T.C.S., Bracey E.E.C.M.C., Strong A.J. and Graves P., 'Registration of MR and CT images for skull base surgery using point-like anatomical features,' *The British Journal of Radiology*, Vol. 64, No. 767, pp 1030-1035, Nov. 1991.
- [20] Lemoine D., Barillot C., Gibaud B. and Pasqualini E., 'An anatomical based 3-D registration of multimodality and atlas data in neurosurgery,' in

REFERENCES

- Colchester A. and Hawkes D. (eds) *Proc. 12th Int. Conf. on Information Processing in Medical Imaging*, pp. 154-164, Springer-Verlag, 1991.
- [21] Maguire G.Q., Noz M., Rusinek H., Jaeger J., Kramer E.L., Sanger J. and Smith G., 'Graphics applied to medical image registration,' *IEEE Computer Graphics and Applications*, Vol. 11 pp. 20-28, 1991.
- [22] Bookstein F.L., 'Visualizing Group Differences in Outline Shape: Methods from Biometrics of Landmark Points,' in *Proceeding Visualization in Biomedical Computing (VBC '96)*, Springer-Verlag, pp 406-410, 1996.
- [23] McCance A.M., Moss J.P., Fright W.R., Linney A.D. and James D.R., 'Three-dimensional analysis techniques - Part 2: Laser scanning: A quantitative three-dimensional soft-tissue analysis using a color-coding system,' *The Cleft Palate - Craniofacial Journal*, Vol. 34, No. 1, pp 46-51, January 1997.
- [24] Besl P.J. and McKay N.D., 'A method for registration of 3-D shapes,' *IEEE Transactions on Pattern Analysis and Machine Intelligence*, Vol. 14, pp. 239-256, Feb. 1992.
- [25] Zhang Z., 'On local matching of free-form curves,' in David Hogg and Roger Boyle (eds), *British Machine Vision Conf.*, (Leeds UK), pp. 347-356, Springer-Verlag, Sept. 1992.
- [26] Subsol G., Thirion J-P. and Ayache N. 'A General Scheme for Automatically building 3D Morphometric Anatomical Atlas: Application to a Skull Atlas,' INRIA research report 2586, [ftp.INRIA.fr/INRIA/tech-reports/RR/RR-2586.ps.gz](ftp://INRIA.fr/INRIA/tech-reports/RR/RR-2586.ps.gz), 1995.

REFERENCES

- [27] Subsol G., Thirion J-P. and Ayache N., 'Application of an Automatically Built 3D Morphometric Brain Atlas: Study of Cerebral Ventricular Shape,' *Proc. 4th Int. Conf. On Visualization in Biomedical Computing (VBC'96)*, pp373-382, 1996.
- [28] Pelizzari C.A., Chen G.T.Y., Spelbring D.R., Weichselbaum R.R. and Chen C-T., 'Accurate three-dimensional registration of CT, PET and/or MR images of the brain,' *Journal of Computer Assisted Tomography*, Vol. 13, No. 1, pp. 20-26, 1989.
- [29] Jiang H., Robb R. and Holton K., 'A new approach to 3-D registration of multimodality medical images by surface matching,' in *Proc. Visualization in Biomedical Computing* (Chapel Hill NC), pp. 196-213, SPIE Press, Bellingham WA, 1992.
- [30] Hill D.L.G and Hawkes D.J., 'Medical Image Registration using knowledge of adjacency of anatomical structures,' *Image and Vision Computing*, 12, pp173-178, 1994.
- [31] Van den Elsen P.A., Pol E.J.D., Sumanawaeera T.S., Hemler P.F., Napel S. and Adler J.R., 'Grey value correlation techniques used for automatic matching of CT and MR brain and spine images,' in *Proc. Visualisation in Biomedical Computing*, Rochester, MN, pp 227-237, SPIE Press, Bellingham WA, 1994.

REFERENCES

- [32] Woods, R.P., Mazziotta J.C. and Cherry S.R., 'MRI-PET registration with automated algorithm,' *J. Computer Assisted Tomography*, vol. 17, pp536-546, 1993.
- [33] Hill D.L.G., Hawkes D.J., Harrison N.A. and Ruff C.F., 'A strategy for automated multimodality image registration incorporating anatomical knowledge and imager characteristics,' in *Proc. Information Processing in Medical Imaging* (Flagstaff AZ), pp 182-196, Springer-Verlag, 1993.
- [34] Collignon A., Vandermeulen, Suetens P. and Marchal G., '3-D multimodality medical image registration using feature space clustering,' in *Proc. 1st Int. conf. on Computer Vision, Virtual Reality and Robotics in Medicine*, Nice, pp195-204, Springer, Berlin, 1995.
- [35] Studholme C., Hill D.L.G and Hawkes D.J., 'Multiresolution voxel similarity measures for MR-PET registration' in Bizais Y., Barrillot C. and Di Paola R. (eds), *Proc. Information Processing in Medical Imaging*, Brest, pp287-298, Kluwer, Dordrecht, 1995.
- [36] Collignon A., Maes F., Delaere D., Vandermeulen D., Suetens P. and Marchal G., 'Automated multimodality image registration using information theory,' in Bizais Y., Barillot C. and Di Paola R. (eds), *Information Processing in Medical Imaging* (Brest), pp. 263-274. Kluwer, Dordrecht, 1995.
- [37] Viola P.A. and Wells W.M., 'Alignment by maximisation of mutual information,' in *Proc. 5th Int. Conf. on Computer Vision*, Boston, pp15-23, IEEE Press, 1995.

REFERENCES

- [38] Wells W.M., Viola P. and Kikinis R., 'Multimodal volume registration by maximization of mutual information,' in *Proc. 2nd annual Int. Symp. On Medical Robotics and Computer Assisted Surgery*, Baltimore, MD, pp55-62, Wiley, New York, 1995.
- [39] Studholme C., Hill D.L.G. and Hawkes D.J., 'Automated 3-D registration of MR and CT images of the head,' *Medical Image Analysis*, Vol. 1, No. 2, pp. 163-175, 1996.
- [40] Broadbent B.H.(Snr), 'A new X-ray technique and its application to orthodontia,' *Angle Orthodontist*, vol. 1, pp 45-66, 1931. (Reprinted, *Angle Orthodontist*, vol.51, p93, 1981).
- [41] Moyers R.E. and Bookstein F.L., 'The inappropriateness of conventional cephalometrics,' *Am. J. of Orthodontics*, Vol. 75, No. 6, June 1979.
- [42] Besl, P.J., 'Active optical range imaging sensors,' *Machine Vision Appl.*, 1, (2), pp.127-152., 1988.
- [43] Jarvis, R.A., 'A perspective on range finding techniques for computer vision,' *IEEE Trans. Pattern Analysis and Machine Intelligence*, 5, pp.122-139, 1983.
- [44] Strand, T.S., 'Optical three-dimensional sensing for machine vision,' *Opt. Eng.*, 24, (1), pp. 33-40, 1985.

REFERENCES

- [45] Mansbach M., 'Die Stereophotogrammetrie Hilfsmittel in der Orthodontie', *Deutsche Zeitschrift Zahnartzliche Orthopadie*, vol. 14, 105 (in German), 1922.
- [46] Zeller M., *Textbook of Photogrammetry*, Translation by Miskin A.E. and Powell R., London, H.K.Lewis & Co. Ltd, 1939.
- [47] Thalmaan-Degen P., 'Die Stereo-photogrammetrie, ein diagnostisches Hilfsmittel in der Kieferorthopadis,' Doctoral Dissertation, University of Zurich, 1944 (in German).
- [48] Bjorn H., Lundquist C. and Helmstrom P., 'A photogrammetric method of measuring the volume of facial swelling,' *Journal of Dental Research*, vol.33, pp295-308, 1954.
- [49] Haga M., Ukiya M., Koshihara Y. and Ota Y., 'Stereophotogrammetric study of the face,' *Bulletin Tokyo Dental Collection*, vol.5, pp10-24, 1964.
- [50] Burke P. H. and Beard L. F. H., 'Stereophotogrammetry of the face,' *American Journal of Orthodontics*, vol. 53, no. 19, pp769-782, 1967.
- [51] Dixon D.A. and Newton I., 'Minimal forms of the cleft palate syndrome demonstrated by stereophotogrammetric surveys of the face,' *British Dental Journal*, vol. 132, pp183-189, 1972.
- [52] Berkowitz S. and Cuzzi J., 'Biostereometric analysis of surgically corrected abnormal faces,' *American Journal of Orthodontics*, vol. 72, no. 6, pp526-538, 1977.

REFERENCES

- [53] Ras F., Habets L.L.M.H., Vanginkel F.C., Prahlandersen B., 'Method for quantifying facial asymmetry in 3 dimensions using stereophotogrammetry,' *Angle Orthodontist*, Vol.65, No.3, pp.233-239, 1995.
- [54] Ras F., Habets L.L.M.H., Vanginkel F.C., Prahlandersen B., 'Quantification of facial morphology using stereophotogrammetry - Demonstration of a new concept,' *Journal of Dentistry*, Vol.24, No.5, pp.369-374, 1996.
- [55] Stevens W.P., 'Reconstruction of three-dimensional anatomical landmark coordinates using video-based stereophotogrammetry,' *Journal of Anatomy*, Vol.191, No.Pt2, pp.277-284, 1997.
- [56] Ozanian T., 'Approaches for stereo matching,' *Modelling Identification and Control*, Vol.16, No.2, pp.65-94, 1995
- [57] Siebert P., Niblett T., Jin J. and Urquhart C., 'C3D-clinical: A Vision-based 3D Digitization System for Medical Applications,' Craniofacial Society of GB, CIRCA meeting, NEL Glasgow, 1995.
- [58] Ju X. and Naftel A., 'Active shape model-assisted stereo matching for 3D recovery of facial features,' Craniofacial Society of GB, CIRCA meeting, Keeble college, Oxford, 1998.
- [59] Takasaki H., 'Moiré topography,' *Applied Optics*, vol 12, pp854-850, 1970.
- [60] Takasaki H., 'Moiré topography', *Proc. Symposium of Commission V, International Society for Photogrammetry*, Biostereometric '74, pp590-607, 1974.

REFERENCES

- [61] Groves D., Dangerfield P.H. and Pearson J., 'Advanced computer analysis of Moiré contour images of the human back,' *Proceedings 5th International Symposium on Surface Tomography and Body Deformity*, Neugebauer H. and Windischbauer G. editors, Vienna, Austria, Gustav Fischer Verlag, Stuttgart, New York, pp107-114, 1990.
- [62] Burwell R.G., Patterson J.F., Webb J.K. and Wojcik A.S., 'School screening for scoliosis - The multiple ATI system of back shape appraisal using the scoliometer with observations on sagittal declive angle,' *Proceedings 5th International Symposium on Surface Tomography and Body Deformity*, Neugebauer H. and Windischbauer G. editors, Vienna, Austria, Gustav Fischer Verlag, Stuttgart, New York, pp17-24, 1990.
- [63] Neugebauer H. and Windischbauer G., 'School Screening using Moiré fringes,' *Proceedings 5th International Symposium on Surface Tomography and Body Deformity*, Neugebauer H. and Windischbauer G. editors, Vienna, Austria, Gustav Fischer Verlag, Stuttgart, New York, pp45-48, 1990.
- [64] Xenofos S.S. and Jones C.H., 'Theoretical aspects and practical applications of Moiré topography,' *Physics and Medical Biology*, vol.24, no.2, pp250-261, 1979.
- [65] Marshall S.J., Dixon R.C., Whiteford D.N., Cumming J.T., Wells P.J. and Powell S.J., 'Projection Moiré Fringe Contouring for 3-D Clinical and Anthropometric Imaging,' Craniofacial Society of GB, CIRCA meeting, NEL Glasgow, 1995.

REFERENCES

- [66] Hierholzer E. and Frobin W., 'Automatic measurement of body surfaces using rasterstereography,' *Biostereometrics*, pp125-131, 1982.
- [67] Turner-Smith A.R., 'A television/computer three dimensional surface shape measurement system,' *Journal Biomechanics*, vol. 21, no. 6, pp 515-529, 1988.
- [68] Kanazawa E. and Kamiishi H., 'Evaluation of facial osteotomy with the aid of Moiré contourography,' *Journal of Maxillofacial Surgery*, vol. 6, pp233-238, 1978.
- [69] Halioua M. and Liu H-C., 'Optical sensing techniques for 3-D machine vision,' *Conference on optical sensing techniques for 3-D machine vision*, Proceedings SPIE, vol. 665, pp150-161, 1986.
- [70] Elad D. and Einav S., 'Three dimensional measurement of biological surfaces,' *ISPRS Journal of Photogrammetry and Remote Sensing*, vol. 45, pp247-266, 1990.
- [71] Takeda M. and Mutoh K., 'Fourier transform profilometry for the automatic measurement of 3-D object shapes,' *Applied Optics*, vol. 22, pp3977-3982, 1983.
- [72] Halioua M. and Liu H-C., 'Optical three-dimensional sensing by phase measuring profilometry,' *Optics and Lasers in Engineering*, vol. 11, pp185-215, 1989.

REFERENCES

- [73] Halioua M., Liu H-C., Chin A. and Bowins T.S., 'Automated topography of the human form by phase measuring profilometry and model analysis,' *Proceedings 5th International Symposium on Surface Tomography and Body Deformity*, Neugebauer H. and Windischbauer G. editors, Vienna, Austria, Gustav Fischer Verlag, Stuttgart, New York, pp91-100, 1990.
- [74] Will P.M. and Pennington K.S., 'Grid coding: Preprocessing technique for robot and machine vision,' *Artificial Intelligence*, 2(3) pp 319-329, 1971.
- [75] Popplestone R.J., Brown C.M., Ambler A.P. and Crawford G.F., 'Forming models of plane-and-cylinder faceted bodies from light stripes,' in *Proc. 4th Int. Joint Conf. Artificial Intelligence*, pp. 669-673, 1975.
- [76] Crawford G.F., 'The stripe finder hardware,' Dept. Artificial Intelligence, University of Edinburgh, 1974.
- [77] Duffy N.D. and Yau J.F.S., 'Facial image reconstruction and manipulation from measurements obtained using a structured lighting technique,' *Pattern Recognition Letters*, Vol. 7, pp 239-243, 1988.
- [78] Arridge S., Moss J.P., Linney A.D. and James D.R., 'Three dimensional digitization of the face and skull,' *J.max.-fax. Surg.*, 13, pp 136-143, 1985.
- [79] Linney A.D., Tan A.C., Richards R., Gardener J., Grindrod S. and Moss J.P., 'Three-dimensional visualization of data on human anatomy: diagnosis and surgical planning,' *Journal of Audiovisual Media in Medicine*, Vol. 16, pp 4-10, 1993.

REFERENCES

- [80] Cyberware Laboratory Inc., *4020/RGB 3D Scanner with Colour Digitizer*, Monterey, U.S.A., 1990.
- [81] Duffy N.D. and Crawley T., 'Intascan Laser Safety Audit,' Interface internal report, 1996.
- [82] Short A., Mutch M., Andersom J. and Grover R.D., 'The direct measurement and display of human shape,' *Proceedings Symposium of Commission V, International Society for Photogrammetry*, Biostereometrics '74, pp583-587, 1974.
- [83] Lindstrom K., Mauritzson L., Benoni G., Svedman P. and Willner S., 'Applications of air-borne ultrasound to biomedical measurements,' *Medical Biology Engineering Computing*, vol. 20, pp393-400, 1982.
- [84] Gallup B., Cotton C., Schewchenko N., Filoso S. and Hidson D., 'Evaluation of 3-D human shape monitoring techniques,' *Proceedings 5th International Symposium on Surface Tomography and Body Deformity*, Neugebauer H. and Windischbauer G. editors, Vienna, Austria, Gustav Fischer Verlag, Stuttgart, New York, pp119-127, 1990.
- [85] Ansley D.A., 'Techniques for pulsed laser holography of people,' *Applied Optics*, vol. 9, pp815-821, 1970.
- [86] Cobb J., 'A projected grid method for recording the shape of the human face,' *Royal Aircraft Establishment Technical Report*, no71184, 1971.

REFERENCES

- [87] Tiddeman B., Duffy N.D., Rabey G.P. and Lokier J., 'Laser-video scanner calibration without the use of a frame store,' *IEE Proc. Vision, Image and Signal Processing*, accepted 1998.
- [88] Duffy N.D., Drummond G.D., McGowan S. and Dessesard P., 'A real time optical scanning system for measurement of chest volume changes during anaesthesia,' *Biostereometric Technology and Applications*, SPIE Vol. 1380, 1990.
- [89] Vernon, D., *Machine vision: automated visual inspection and robot vision*, Prentice Hall, UK, 1991.
- [90] Tsai R.Y., 'An efficient and accurate camera calibration technique,' *Proc. IEEE Comp. Soc. Conf. Computer Vision and Pattern Recognition*, pp 364-374, Miami Beach Florida, 1986.
- [91] Tsai R.Y., 'A versatile camera calibration technique for high accuracy 3D machine vision metrology using off-the-shelf TV cameras and lenses,' *IEEE J. Robotics Autom.*, RA-3(4) pp323-344, 1987.
- [92] Theodoracatos V.E. and Calkins D.E., 'A 3-D vision system model for automatic object surface sensing,' *International Journal of Computer Vision*, 11:1 pp75-79 1993.
- [93] Vannier M.W., Pilgram T., Bhatia G. and Brunsten B., 'Facial Surface Scanner,' *IEEE Computer graphics and applications*, pp 72-80, November 1991.

REFERENCES

- [94] Manthey D.W., Knapp K.N. II and Lee D., 'Calibration of a laser range-finding coordinate-measuring machine,' *Optical Engineering*, 33(10), pp3372-3380 October 1994.
- [95] Trucco E. and Fisher R.B., 'Acquisition of consistent range data using local calibration,' *Proc. IEEE International Conference on Robotics and Automation*, pp3410-3415, San Diego California, 1994.
- [96] Bookstein, F.L., *Morphometric Tools for Landmark Data*, Cambridge University Press, New York, 1991.
- [97] Rolf, F.J and Bookstein F.L. *Proceedings of the Michigan Morphometrics Workshop*, University of Michigan Museums, Ann Arbor, MI 1990.
- [98] Manly B.F.J., *Multivariate statistical methods: A primer*, 2nd Edition, Chapman and Hall, 1994.
- [99] McCance A.M., Moss J.P., Fright W.R., Linney A.D. and James D.R., 'Three-dimensional analysis techniques - Part 1: Three-dimensional soft tissue analysis of 24 adult cleft palate patients following Le Fort I maxillary advancement: A preliminary report,' *The Cleft Palate - Craniofacial Journal*, Vol. 34, No. 1, pp 36-45, January 1997.
- [100] McCance A.M., Moss J.P., Fright W.R., Linney A.D. and James D.R., 'Three-dimensional analysis techniques - Part 3: Color-Coded system for three-dimensional measurement of bone and ratio of soft-tissue to bone: The analysis,' *The Cleft Palate - Craniofacial Journal*, Vol. 34, No. 1, pp 52-57, January 1997.

REFERENCES

- [101] McCance A.M., Moss J.P., Fright W.R., Linney A.D. and James D.R.,
‘Three-dimensional analysis techniques - Part 4: Three-dimensional analysis
of bone and soft-tissue to bone ratio of movements in 24 cleft palate pa-
tients following Le fort I osteotomy: A preliminary report,’ *The Cleft Palate*
- *Craniofacial Journal*, Vol. 34, No. 1, pp 58-62, January 1997.
- [102] Ruprecht D. and Muller H., ‘Image warping with scattered data interpo-
lation,’ *IEEE Computer Graphics and Applications*, Vol. 15, No. 2, pp 37-43,
1995.
- [103] Wolberg G., *Digital Image Warping*, IEEE Computer Society press, Los
Alamitos, CA, 1990.
- [104] Beier T. and Neely S., ‘Feature-based image metamorphosis,’ *Computer*
Graphics (SIGGRAPH '92), Vol 26, No. 2, pp 32-42, 1992.
- [105] Benson P.J. and Perrett D.I. ‘Synthesizing Continuous Tone Caricatures,’
Image and Visual Computing, Vol. 9, pp123-129, 1991.
- [106] Benson P.J. and Perrett D.I., ‘Extracting prototypical facial images from
exemplars,’ *Perception*, Vol. 22, pp 257-262, 1993.
- [107] Perrett D.I., May K.A. and Yoshikawa S., ‘Facial shape and judgements
of female attractiveness,’ *Nature*, Vol. 368, pp. 170-178, 1994.
- [108] Bookstein F.L., ‘Principal warps: Thin-plate splines and the decomposi-
tion of deformations,’ *IEEE Trans. on PAMI*, Vol. 11, No. 6, pp. 567-585,
June 1989.

REFERENCES

- [109] Thompson D'Arcy W., *On Growth and Form*, 1917, abridged edition, J. T. Bonner. Cambridge University Press, 1961.
- [110] Duchon J., 'Splines minimizing rotation-invariant semi-norms in Sobolev spaces,' Chui C., Schumaker L. and Ward J. (eds), *Multivariate Approximation Theory*, Birkhauser (Basel, Switzerland), pp 85-100, 1975.
- [111] Meinguet J., 'Multivariate interpolation at arbitrary points made simple,' *Zeitschrift fur Angewandte Mathematik und Physik (ZAMP)*, 30:292-304, 1979.
- [112] Cutting C.B., Bookstein F.L., Haddad B., Dean D. and Kim D., 'A spline-based approach for averaging three-dimensional curves and surfaces,' *SPIE Mathematical Methods in Medical Imaging*, Vol. 2035, pp29-44, 1993.
- [113] Thompson P. and Toga A.W., 'Visualization and mapping of anatomical abnormalities using a probabilistic brain atlas based on random fluid transformations,' *Proc. Visualization in Biomedical Computing (VBC '96)*, pp 384-392, Springer, 1996.
- [114] Thompson P. M., Schwartz C., Lin R.T., Khan A.A. and Toga A.W. 'Three-Dimensional Statistical Analysis of Sulcal Variability in the Human Brain,' *Journal of Neuroscience*, Vol. 16, No. 13, pp 4261-4274, July 1996.
- [115] MacDonald D., Avis D. and Evans A.C., 'Automatic Parameterization of Human Cortical Surfaces,' *Annual Symp. Information Processing in Medical Imaging (IPMI)*, 1993.

REFERENCES

- [116] Thompson P.M. and Toga A.W. 'A Surface-Based Technique for warping Three-Dimensional Images of the Brain,' *IEEE Transactions on Medical Imaging*, Vol. 15, No. 4, August 1996.
- [117] Cutting C.B., Dean D., Bookstein F.L., Haddad B., Khorrambadi D. and Zonneveld F. 'A three-dimensional smooth surface analysis of untreated Crouzons disease in the adult,' *Journal of Craniofacial Surgery*, Vol. 6, pp 444-453, 1995.
- [118] Dean D., Buckley P., Bookstein F.L., Kamath, J., Kwon D., Friedman L. and Lys C. 'Three-dimensional MR-Based Morphometric Comparison of Schizophrenic and Normal Cerebral Ventricles,' *Proc. 4th Int. Conf. On Visualization in Biomedical Computing (VBC'96)*, pp363-372, 1996.
- [119] Forrest A.R. 'On Coon's and other methods for the representation of curved surfaces,' *Computer Graphics and Image Processing*, Vol. 1, pp 341-359, 1972.
- [120] Hawk J., Dean D., Kalarickal Z., Masri N., Kamath J., Haaga J., Mardia K.V., Linney A.D., Goldberg J., Luce E. and Hans M., 'A Template for 3D soft tissue face analysis,' *Journal of Dental Research*, Vol.76, No.SISI, p.903, 1997
- [121] Lee Y., Terzopoulos D. and Waters K., 'Constructing Physics based models of individuals,' *Proc. Graphics Interface '93*, pp 1-8, 1993.

REFERENCES

- [122] Thirion J-P. and Gourdon A. 'The 3D Marching Lines Algorithm and its Application to Crest Lines Extraction,' *INRIA Research Report*, NO. 1672, <ftp.INRIA.fr/INRIA/tech-reports/RR/RR-2586.ps.gz>, 1995.
- [123] Thirion J-P. and Gourdon A. 'The Marching Lines Algorithm: new results and proofs,' *INRIA Research Report*, Nos. 1881-1 and 1881-2, <ftp.INRIA.fr/INRIA/tech-reports/RR/RR-1881-1.ps.gz>, 1995.
- [124] Tikhonov A.N. and Arseninn V.Y., *Solution of Ill-Posed Problems*, V.H. Winston & Sons, John Wiley, 1977.
- [125] Bajcsy R. and Kovacic S., 'Multiresolution Elastic Matching,' *Computer vision, Graphics and Image Processing* Vol. 46, pp1-21, 1989.
- [126] Miller M. I., Christensen G. E., Amit Y. and Grenander U. 'Mathematical textbook of deformable neuroanatomies,' *Proc. National Academy of Sciences*, 90(24) pp11944-48, December 1993.
- [127] Christensen G. E., Rabbitt R. D. and Miller M. I., '3D Brain Mapping Using a Deformable Neuroanatomy,' *Physics in Medicine and Biology*, Vol. 39, pp 609-618, 1994.
- [128] Thirion J-P. 'Non-rigid matching using demons,' *Proc. Int. Conf. Computer Vision and Pattern Recognition (CVPR'96)*, San Francisco, June 1996.
- [129] Bro-Nielson M. and Gramkow C., 'Fast Fluid Registration of Medical Images', *Proc. 4th Int. Conf. on Visualization in Biomedical Computing (VBC'96)*, pp267-276, 1996.

REFERENCES

- [130] Schormann T. Henn S. and Zilles K., 'A new approach to fast elastic alignment with application to human brains,' *Proc. 4th Int. Conf. on Visualization in Biomedical Computing (VBC'96)*, pp337-342, 1996.
- [131] Collins D.L., Holmes C., Peters T. and Evans A., 'Automatic 3D model-based neuro-anatomical segmentation,' *Human Brain Mapping*, Vol. 3(3), pp 190-208, 1996.
- [132] Collins D.L., Le Goualher G., Venugopal R., Caramanos A., Evans A.C. and Barillot C., 'Cortical Constraints for Non-Linear Cortical registration,' *Proc. 4th Int. Conf. on Visualization in Biomedical Computing (VBC'96)*, pp307-316, 1996.
- [133] Thirion J-P., Subsol G. and Dean D., 'Cross Validation of Three Inter-Patient Matching Methods,' *Proc. 4th Int. Conf. on Visualization in Biomedical Computing (VBC'96)*, pp327-336, 1996.
- [134] Schwarz L., 'Theorie des Distributions,' *Vol. I, II of Actualités Scientifiques et Industrielles*, Publications de l'institute de Mathématique de l'Université de Strasbourg, 1950-51.
- [135] Witkin A.P., 'Scale Space Filtering,' *Proc. of IJCAI*, Karlsruhe, Germany, 1983.
- [136] Konderink J. J., 'The Structure of Images,' *Biol. Cybern.*, vol. 50, pp 363-370, 1984.

REFERENCES

- [137] Florack J., *The Syntactical Structure of Scalar Images*, PhD Thesis, University of Utrecht, 1993.
- [138] Poggio T., Voorhees H. and Yuille A., 'A regularized solution to edge detection,' *A.I. Memo 883*, MIT, May 1985.
- [139] Nielsen M., Florack L. and Deriche R., 'Regularization and scale-space,' *INRIA Research Report*, No. 2352, [ftp.INRIA.fr/INRIA/tech-reports/RR/RR-2352.ps.gz](ftp://ftp.INRIA.fr/INRIA/tech-reports/RR/RR-2352.ps.gz), 1994.
- [140] Spath H., *Two dimensional spline interpolation algorithms*, publisher A.K. Peters, Wellesley, Massachusetts, 1995.
- [141] Barnhill R., 'Representation and approximation of surfaces,' *Mathematical software III*, J.R.Rice (ed.), Academic Press (New York), pp. 68-119, 1977.
- [142] Franke R. and Nielsen G.M., 'Scattered data interpolation of large sets of scattered data,' *International Journal of Numerical Methods in Engineering*, Vol. 15, pp. 1,691-1,704, 1980.
- [143] Blake A. and Zisserman A., *Visual Reconstruction*, Cambridge, M.A., M.I.T. Press, 1987.
- [144] Boult T. and Kender J., 'Visual surface reconstruction using sparse depth data,' in *Proceedings IEEE Conference on Computer Vision and Pattern Recognition '86*, Miami Beach, FL. pp. 68-76, 1986.

REFERENCES

- [145] Grimson W.E.L., 'An implementation of a computational theory of visual surface interpolation,' *Computer Vision, Graphics and Image Processing*, Vol. 22, pp. 36-69, 1983.
- [146] Poggio T., Torre V. and Koch C., 'Computational vision and regularisation theory,' *Nature*, Vol. 317, pp. 314-319, Sept 26, 1985.
- [147] Terzopoulos D., 'The computation of visible surface representations,' *IEEE Trans. Pattern Analysis and Machine Intelligence*, Vol. 10, No. 4, pp. 417-439, 1988.
- [148] Terzopoulos D., 'Multilevel computational processes for visual surface reconstruction,' *Computer Vision, Graphics and Image Processing*, Vol. 24, pp. 52-96 1983.
- [149] Yaouh M.H. and Chang W.T., 'Fast surface interpolation using multiresolution wavelet transform,' *IEEE Transactions on Pattern Analysis and Machine Intelligence*, Vol.16, No.7, pp.673-688, 1994.
- [150] Pentland A.P., 'Interpolation using wavelet bases,' *IEEE Transactions on Pattern Analysis and Machine Intelligence*, Vol.16, No.4, pp.410-414, 1994.
- [151] Lawson C., 'Software for C^1 surface interpolation,' *Mathematical software III*, J.R.Rice (ed.), Academic Press (New York), pp. 161-194, 1977.
- [152] McLain D., 'Two-dimensional interpolation from random data,' *Computer Journal*, Vol. 19, pp. 178-181, 1976.

REFERENCES

- [153] Clough R. and Trocher J., 'Finite element stiffness matrices for analysis of plates in bending,' *Proc. Conf. Matrix Methods in Structural Mechanics*, pp. 515-545, 1965.
- [154] Crain I. and Bhattacharyya K., 'Treatment of non-equispaced two-dimensional data with a digital computer,' *Geoexploration*, Vol. 5, pp. 173-194, 1967.
- [155] Shepard D., 'A two dimensional interpolation function for irregularly spaced data,' *Proc. ACM 23rd National Conference*, pp. 517-524, 1968.
- [156] Hsu W.M., Hughes J.F. and Kaufman H., 'Direct manipulation of free-form deformations,' *Computer Graphics (Proceedings SIGGRAPH '92)*, Vol. 26, No. 2, pp. 177-184, 1992.
- [157] Welch W. and Witkin A., 'Variational surface modelling,' *Computer Graphics (Proceedings SIGGRAPH '86)*, Vol. 26, No. 2, pp. 157-166, 1992.
- [158] Lee S-Y., Wolberg G. and Shin S. Y., 'Scattered data interpolation with multilevel B-splines,' *IEEE Transactions on Visualization and Computer Graphics*, Vol. 3, No. 3, pp. 229-244, 1997.
- [159] Lee S.-Y., Chwa K-Y., Shin S.Y. and Wolberg G., 'Image metamorphosis using snakes and free-form deformations,' *Computer Graphics (SIGGRAPH '95 Proceedings)*, pp. 439-448, 1995.

REFERENCES

- [160] Meisters G.H. and Olech C., 'Locally one-to-one mappings and a classical theorem on Schlicht functions,' *Duke Mathematics Journal*, Vol. 30, pp. 63-80, 1963.
- [161] Lee S.-Y., Chwa K.-Y., Hahn J. and Shin S. Y., 'Image morphing using deformable surfaces,' in *Proceedings of Computer Animation '94*, Geneva, Switzerland, IEEE Computer Society Press, pp. 31-39, 1994.
- [162] Litwinowicz P. and Williams L., 'Animating images with drawings,' *Computer Graphics (SIGGRAPH '94 Proceedings)*, pp 409-412, 1994.
- [163] Canny J., 'A computational approach to edge detection,' *IEEE Trans. PAMI*, Vol. 8, pp 679-698, 1986.
- [164] Gritton C.W.K and Parish (Jnr) E.A., 'Boundary location from an initial plan: The bead chain algorithm,' *IEEE Trans. PAMI*, Vol. 5, No. 1, pp.8-13, Jan. 1983.
- [165] Cooper D.B., 'Maximum likelihood estimation of Markov-process blob boundaries in noisy images,' *IEEE Trans. PAMI*, Vol. 1, No. 4, pp. 372-384, Oct. 1979.
- [166] Kass M., Witkin A. and Terzopoulos D., 'Snakes: Active contour models,' *Int. J. Computer Vision*, Vol. 1, No. 4, pp. 321-331, 1988.
- [167] Staib L.H. and Duncan S., 'Boundary Finding with Parametrically Deformable Models,' *IEEE Transactions on PAMI*, Vol. 14, No. 11, pp 1061-1075, 1992.

REFERENCES

- [168] Montanari U., 'On the optimal detection of curves in noisy pictures,' *Commun. ACM*, vol. 14, No. 5, pp. 335-345, May 1971.
- [169] Martelli A., 'An application of heuristic search methods to edge and contour detection,' *Commun. ACM*, vol.19, No. 2, pp 73-83, Feb 1976.
- [170] Mortensen E.N. and Barrett W.A., 'Intelligent Scissors for Image Composition,' *Computer Graphics (Proceedings SIGGRAPH '95)*, pp 191-198, 1995.
- [171] Coombes A.M., Linney A.D., Richards R. and Moss J.P., 'A method for the analysis of the 3D shape of the face and changes in the shape brought about by facial surgery,' *SPIE Biostereometric Technology and Applications*, Vol. 1380, pp 180-189, 1990.
- [172] Coombes A.M., Moss J.P., Linney A.D., Richards R. and James D.R., 'A mathematical method for the comparison of three-dimensional changes in the facial surface,' *European J. of Orthodontics*, Vol. 13, pp 95-110, 1991.
- [173] Coombes A.M., *Shape Classification: Towards a Mathematical Description of the Face*, PhD Thesis (UCL), 1993.
- [174] Gordon G.G., 'Face recognition based on depth maps and surface curvature,' *Proc. SPIE*, Vol. 1570, San Diego, 1991
- [175] Lipshultz M.M., *Differential Geometry*, McGraw-Hill, New York, 1969.
- [176] Besl P.J. and Jain R.C., 'Segmentation through variable order surface fitting,' *IEEE PAMI*, Vol. 10, pp167-192, 1988.

REFERENCES

- [177] Yokoya N. and Levine M.D., 'Range image segmentation based on differential geometry: A hybrid approach,' *IEEE-PAMI*, Vol. 11, No. 6, pp. 643-649, 1989.
- [178] Greitz T., Bohm C., Holte S. and Erikson L., 'A computerized brain atlas: construction, anatomical content and some applications,' *Journal of Computer Assisted Tomography*, Vol. 15, No. 1, pp. 26-38, 1991.
- [179] Declerck J., Subsol G., Thirion J-P. and Ayache N., 'Automatic retrieval of anatomical structures in 3D medical images' in Nicolas Ayache (ed.) *CVRMed '95*, Volume 905 of *Lecture Notes in Computer Science*, Springer-Verlag, pp 153-162, April 1995.
- [180] Terzopoulos D. and Waters K., 'Physically-based facial modelling, analysis and animation,' *Visualisation and Computer Animation*, Vol. 1, pp. 73-80, 1990.
- [181] Waters K., 'A physical model of facial tissue and muscle articulation derived from computer tomography data,' *SPIE Visualization in Biomedical Computing*, Vol. 1808, pp. 574-583, 1992.
- [182] Keeve E., Girod S. and Girod B., 'Craniofacial surgery simulation,' *Proc. Visualization in Biomedical Computing (VBC '96)*, pp 541-546, Springer, 1996.
- [183] Bathe K.-J., *Finite Element Procedures in Engineering Analysis*, Prentice Hall (New Jersey), 1982.

REFERENCES

- [184] Zienkiewicz O.C., *The Finite Element Method*, fourth edition, vol. 1-2, McGraw-Hill, 1994.
- [185] Bro-Nielsen M., 'Modelling elasticity in solids using active cubes - application to simulated operations, in *Computer Vision, Virtual Reality and Robotics in Medicine (CVRMed '95)*, pp. 535-541, 1995.
- [186] Cover S.A., Ezquerro N.F., O'Brien J.F., Rowe R., Gadacz T. and Palm E., 'Interactively deformable models for surgery simulation,' *IEEE Computer Graphics and Applications*, pp68-75, November 1993.
- [187] Bro-Nielsen M., 'Surgery simulation using fast finite elements,' *Proc. Visualization in Biomedical Computing (VBC '96)*, pp 529-534, Springer, 1996.
- [188] Cotin S., Delingette H. and Ayache N., 'Real time volumetric deformable models for surgical simulation,' *Proc. Visualization in Biomedical Computing (VBC '96)*, pp 535-540, Springer, 1996.
- [189] Bro-Nielsen M., 'Finite element modelling in surgery simulation,' *Proceedings of the IEEE*, Vol. 86, No. 3, pp.490-503, 1998.
- [190] Bro-Nielsen M. and Cotin S., 'Real-time volumetric deformable models for surgery simulation using finite-elements and condensation,' *Computer Graphics Forum*, Vol.15, No.3, p.C 57, 1996.
- [191] Koch R.M., Gross M.H., Carls F.R., von Buren D.F., Frankhauser G. and Parish Y.I.H., 'Simulating facial surgery using finite element models,' *Computer Graphics (SIGGRAPH '96 Proceedings)*, pp 421-428, 1996.

REFERENCES

- [192] Langtangen H.-P., 'A solver for the equations of linear thermoelasticity,'
The Diffpack Report Series, SINTEF, 1995.
- [193] Robb R.A., 'A software system for interactive and quantitative analysis
of biomedical images,' in *3D Imaging in Medicine*, K.H. Hohne et al (eds.),
Springer-Verlag (Berlin, Heidelberg), pp. 333-361, 1990.
- [194] Rowland D.A. and Perrett D.I., 'Manipulating facial appearance through
shape and color,' *IEEE Computer Graphics and Applications*, pp 70-76,
September 1995.